Computational and Experimental Investigation of Conventional and Cryogenic Cooling in Milling Operations

Eleanor Jane Harvey

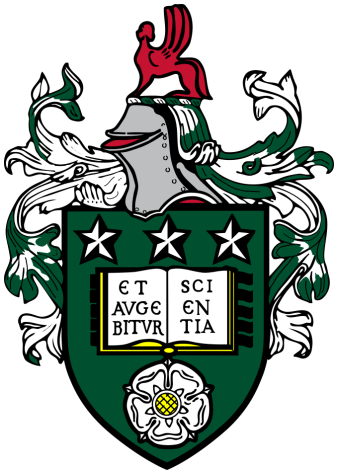

Submitted in accordance with the requirements for
the degree of Doctor of Philosophy

The University of Leeds
EPSRC Centre for Doctoral Training in Fluid Dynamics

January 2023

Declaration of Authorship

The candidate confirms that the work submitted is their own, except where work which has formed part of jointly authored publications has been included. The contribution of the candidate and the other authors to this work has been explicitly indicated below. The candidate confirms that appropriate credit has been given within the thesis where reference has been made to the work of others.

Acknowledgements

Firstly I would like to thank my supervisor Harvey Thompson for his invaluable guidance, encouragement, and support during the course of my PhD. Thanks go to Nik Kapur and Sam Flint for their support and advice in the experimental work conducted. A special thanks to Sandvik Coromant for providing industry support to this project, in particular to Gaetano Pittala and Adam Johns, for their continuous support and enthusiasm. I have enjoyed working with each one of my supervisors and am very appreciative of their encouragement and experience.

This worked was funded by the UK Engineering and Physical Sciences Research Council (EPSRC) grant EP/L01615X/1 for the University of Leeds Centre for Doctoral Training in Fluid Dynamics. I'd also like to thank the CDT friends I've made throughout this process, who have also provided advice and support.

Above all, I would like to thank my family for their unwavering support.

Abstract

In machining, high thermo-mechanical loads which limit tool life and efficiency are often managed using coolants. Appropriate coolant selection and well targeted application can transport significant thermal loads away from the cutting region, along with providing lubrication and aiding in chip evacuation. In this work, numerical and experimental studies of coolant applications contribute to both increasing fundamental understanding of coolant behaviours and supporting the design of improved cutting tools.

A multiphase conjugate heat transfer computational fluid dynamics (CFD) model is developed in OpenFOAM to study both the coolant coverage and tool temperatures during the application of an oil-water emulsion coolant in milling processes via through-tool channels. Utilising this model to investigate a standard tool design has shown the coolant jet is targeted near to the cutting edge, with coolant spreading out to cover the tool and workpiece surfaces to provide good coverage along the cutting edge. To support the development of improved tool designs, the CFD model has been further utilised in an exploration of the coolant channel design space and optimisation study. As well as providing new tool designs with minimised tool temperatures and maximised coolant coverage in this study of the design space, key physical features such as a shift in coolant spreading behaviour and the presence of designs with significant levels of splashing have been identified for the first time.

Cryogenic coolants provide a cleaner alternative to oil-water emulsion coolants in cutting operations. Liquid CO_2 is one such coolant which has shown promise in experimental machining tests. To build towards the development of a CO_2 CFD model which can support innovation of tool designs to maximise the benefits of this new coolant, fundamental experimental and modelling work is presented in this thesis. An experimental rig design has been developed to analyse heat transfer when using CO_2 coolants in a simplified setting and this has been used to successfully validate a CFD model capturing the conjugate heat transfer when using liquid CO_2 coolant.

Contents

List of Figures

List of Tables

Chapter 1

Introduction

Contents

Over the last century, continuous developments in industries such as the aerospace, automotive and energy sectors have contributed to an ever-increasing demand for efficient manufacturing with advanced engineering materials. All these applications have increasing demands for high strength and heat resistant metals to build components for extreme environments like the interior of combustion engines and along turbine blades (Donachie & Donachie, 2002). As these advanced engineering materials are developed, manufacturing tools and techniques must undergo continuous innovation to match the challenge of cutting these materials into the necessary forms efficiently (Fan et al., 2020).

In machining processes, cutting tools are used to remove material from a less resistant workpiece material. These tools can be subjected to extremely high stresses and thermo-mechanical loads (Aggarwal et al., 2008), with a large proportion of the energy used transformed into heat (Huang & Yang, 2016). Effective application of coolants is often essential since high temperatures at the cutting zone can cause significant problems in both the workpiece and the tool, such as reducing dimensional accuracy, introducing micro-scale cracks that can impact the life of the component, and significantly shortening tool lifespans (Richardson et al. (2006a), Shokrani et al. (2012b)). Appropriate coolant selection and well targeted application can directly cool both the tool edge and workpiece, along with providing lubrication which reduces cutting forces and aiding in chip evacuation. Providing the coolant directly through internal channels in the tool can result in high pressure jets towards the cutting edge and increase the effectiveness of the coolants (Bermingham et al., 2014).

An improved understanding of the fluid flow and heat transfer when using coolants can be used to support the tool design process and analysis of machining tool wear in testing. It can be difficult to observe coolant flow in industrial machining due to the visual obstructions and the high temperatures and stresses creating a hostile environment. Computational Fluid Dynamics (CFD) has been used in this thesis to

provide insight into the coolant's behaviour. Tool design parameters have been investigated using CFD models of coolant coverage (Johns et al., 2018) and heat transfer (Fallenstein & Aurich, 2014) for drilling operations, illustrating that CFD modelling has excellent potential for improving the tool design process. The above studies have highlighted the benefits of applying CFD in machining operations. There is a breadth of applications which would benefit from CFD analysis, such as intermittent cutting operations like milling, which can have more complex reactions to coolant behaviours due to increased thermal shock (Uhlmann et al., 2017). Extending previous work in the literature, CFD models can be developed to combine pre-existing models so that coolant coverage and heat transfer can be studied concurrently.

Along with the widely used oil and water based emulsion coolants, often referred to as conventional coolants, which are well established in industrial machining, there is ongoing research into cleaner and more efficient coolants which are cheaper and more environmentally friendly (Shokrani et al., 2012b). Alternatives, such as cryogenic coolants like carbon dioxide and nitrogen, have shown promise in experimental machining tests (Sadik et al. (2016), Pittalà (2018)). Further to being a cleaner, less hazardous coolant, cryogenic CO_2 can provide increased cooling when it expands from high pressure due to a cold sublimating solid-gas jet (Pursell, 2012).

Development towards the extension of conventional coolant modelling to a validated CO_2 CFD model, which can support innovation of tool designs to maximise the benefits of this new coolant, would be a significant contribution to the literature. The fundamental understanding of how cryogenic CO_2 coolant cools and interacts with the heated surfaces under machining conditions is less well understood than when using conventional cooling (Pušavec et al., 2019), where there is a wealth of knowledge and testing experience (Shokrani et al., 2012b). Expansion to atmospheric pressure and the presence of three phase flow in the CO_2 coolant make the modelling much more challenging, and more fundamental studies and simplified models are needed to make it viable for modelling in machining settings.

1.1 Research aims

The aim of this thesis is to develop CFD models to contribute towards an improved understanding of coolant application in milling processes. To deliver this aim, the problem has been split into two distinct parts: firstly the modelling of conventional water based coolant, and secondly the development of a simplified model for cryogenic CO_2 cooling. The objectives are as follows:

1.1. Implement an approach which can be used to investigate both coolant coverage

and tool temperatures, using multiphase and conjugate heat transfer modelling in OpenFOAM.

  - Build on models described in the literature (Johns et al. (2018), Fallenstein & Aurich (2014)) to combine coolant coverage and conjugate heat transfer into one model.
  - Perform validation and verification of this model through comparison to both commercial software and experimental data in the literature for an appropriate set of heat transfer results.

1.2. Explore the coolant supply and channel design parameter space to study their effects on coolant supply to the cutting edge and the subsequent cooling of the tool.

  - Determine key parameters to include in studies of the design space, run CFD models across a set of sample points and use the results to predict values of output parameters across this design space.
  - Analyse the variation of key output parameters to provide observations and optimal solutions which can be of use in tool design processes.

2. Extend the modelling of coolants to a simplified model of cryogenic CO_2 cooling which can capture the heat transfer capabilities of this new coolant.

  - Design and build an experimental rig to make fundamental observations of CO_2 cooling and provide a validation data set.
  - Using experimental observations, propose and validate a simplified model for cooling with liquid supply CO_2 jets.
  - Apply the CO_2 CFD model to a machining pilot study to provide initial results and show that the model can be efficient and compatible with machining geometries and meshes.

1.2 Thesis layout

This thesis consists of nine chapters, including this introduction. A brief outline for each chapter is provided for the reader:

- Chapter 2 provides a review of the conventional coolant use in milling and machining processes. Coolant types and application methods are discussed with studies from the literature spanning a range of cutting conditions. A review of CFD modelling of conventional coolant is also provided.

- Chapter 3 contains the details of the CFD modelling for conventional coolants. Both visualisations of the simulation results and quantitative data are presented and discussed.
- Chapter 4 applies the CFD modelling of Chapter 3 to explore the impact of both coolant channel design and inlet velocity on key outputs such as coolant coverage, velocity along the cutting edge, and tool temperature.
- Chapter 5 focuses on the analysis of coolant velocity in the chip formation region along the cutting edge in a milling application. A new tool design is developed and modelled which achieves an improved upwards coolant flow along the cutting edge compared to a standard tool geometry.
- Chapter 6 begins the work with cryogenic coolants, with a review of their use in machining operations, followed by a discussion of the physical properties of CO_2 and an examination of the literature modelling CO_2 releases from high pressure.
- Chapter 7 contains experimental results for CO_2 cooling in a purpose designed and built heat transfer test rig.
- Chapter 8 presents a validated CFD conjugate heat transfer model for cooling with CO_2 jets. Results also include a pilot study where the model is used to simulate cooling of a milling tool during machining.
- Chapter 9 concludes the thesis with a summary of the findings, and suggestions of further work.

Chapter 2

An introduction to machining processes and the application of coolants

Contents

2.1 Machining of metals

Machining is one of the most widely used manufacturing techniques today. In the machining process a cutting tool is used to remove material from a less resistant workpiece material and in the process the tool is subjected to high stresses and thermo-mechanical loads (Aggarwal et al., 2008). Some key machining definitions are provided below, and illustrated in figure 2.1:

- **Rake face** is the part of the tool surface over which the chip, formed in the cutting process, slides,
- **Flank face** is the part of the tool surface over which the machined surface, produced on the workpiece, passes,
- **Cutting edge** is a theoretical line of intersection of the rake and the flank surfaces of the tool,
- **Workpiece** is the material which is being machined,
- **Chip/swarf** is the material removed from the workpiece during a machining process.

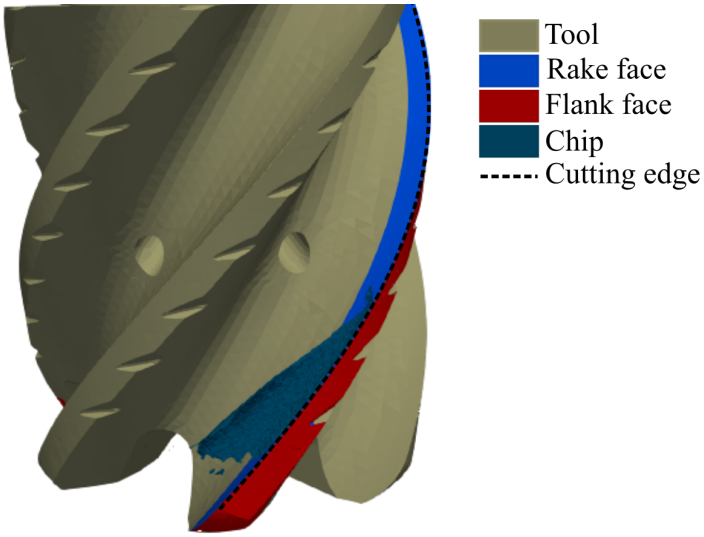

Figure 2.1: Milling tool with features around the cutting edge highlighted. The geometry shown is a result of a machining simulation for the end milling of titanium, with the chip formation modelled using Advant Edge software and provided by Sandvik Coromant.

There are many types of machining operation, including drilling, turning and milling, among others. Milling is one of the most versatile machining operations. Similar in appearance to drilling tools, milling tools have sharp cutting edges which extend up the length of the tool, as seen in figure 2.1, meaning there are more degrees of freedom in milling than most operations as the tool can traditionally cut into the workpiece from above or from the side and at a range of angles (Grzesik, 2008b).

The high mechanical loads and nature of the machining process means that there is extensive deformation near to the cutting edge. A schematic of a single shear plane model for a typical cutting operation is shown in Figure 2.2 and we can see there are three major deformation areas in the cutting process, with the primary zone located where the chip-workpiece interface experiences high shear forces and elasto-plastic deformation (Shokrani et al., 2012b). In the secondary zone, which is found between the chip and the rake face, the chip slides along this rake face resulting in high frictional forces and away from the chip there can also be found a tertiary deformation zone between the workpiece and cutting tool flank face as they slide past each other creating large frictional forces.

It can be seen in Figure 2.2 that there is heat generated at all three deformation zones near the cutting edge. In fact, a large proportion of energy used in machining processes is transformed into heat at the cutting zone (Huang & Yang, 2016) and this was defined by Shaw & Cookson (2005) as one of the main issues that affects machinability.

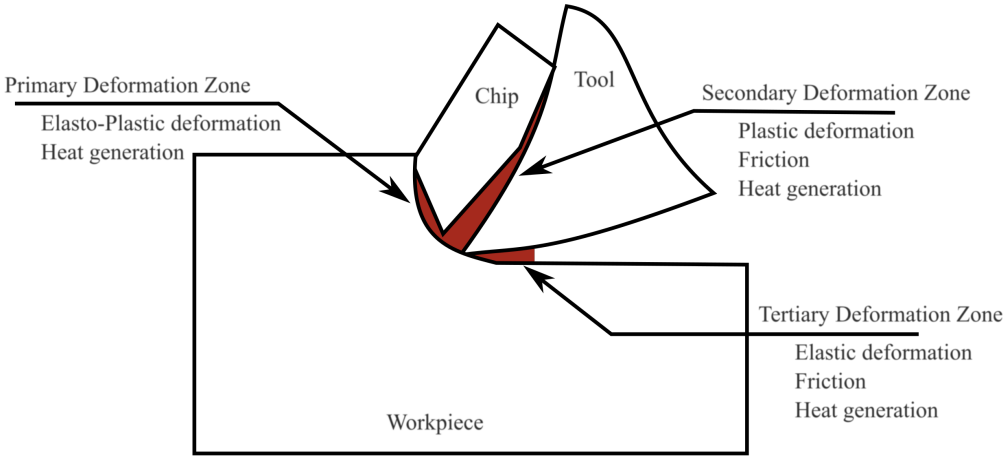

Figure 2.2: A diagram of the three main deformation regions in a typical cutting operation. Based on illustration of single shear model presented by Abukhshim et al. (2006).

Excess heat generation, along with high cutting forces and several other factors affecting machining processes are often exacerbated when machining Hard-To-Cut (HTC) materials (Ezugwu et al., 2003). There has been an increased demand in the last century for these HTC materials which are mostly advanced engineering materials with elevated strength and high heat-resistance (Klocke et al., 2012). Materials with these enhanced properties are often used in applications such as aerospace and turbine components with two widely used HTC materials being titanium and nickel based alloys which have high toughness, wear resistance, yield strength, corrosion resistance and high-temperature strength and hardness.

Another frequently encountered property of these HTC materials is a low thermal conductivity. This feature coupled with the high strength and toughness of HTC materials can result in especially high temperatures in the cutting zone as there are increased cutting forces required to machine the parts and limitations on how much heat can be dissipated through the workpiece or chips due to low conductivity (Klocke et al., 2012).

High temperatures in the cutting zone can cause significant problems in the machined product since large amounts of heat generated in the workpiece at deformation regions leads to very high local temperatures which reduces the dimensional accuracy, can alter the microstructure of the material, and induce residual stress and microcracks which can affect the fatigue life of the component (Richardson et al. (2006a), Shokrani et al. (2012b)).

Further to the impacts on the life of the machined component there are significantly shorter tool life-spans when cutting HTC materials, leading the machining of these advanced engineering materials to be often associated with high costs and low

productivity as cutting parameters such as speed and feed rate often have to be limited in order to machine economically (Komanduri & Hou, 2001). The potential of high cutting temperatures to negatively impact on cutting-tool life has long been recognised. Taylor (1906) developed the empirical relationship,

$$V(TL)^n = C, \tag{2.1}$$

between cutting speed (and therefore cutting temperatures) and tool life which is still widely used today, with cutting speed V, tool life TL, and constants, n, C which depend on the workpiece-tool pairing.

There has been considerable work carried out with an emphasis on both investigating experimentally and mathematically modelling the cutting temperatures in machining processes in order to understand better the temperature distributions and the influence of various cutting parameters on these temperatures. Up until the middle of the 20th century much of the experimental cutting temperature data was obtained using either thermocouples to measure tool/workpiece temperatures at various locations (Shore, 1924) or calorimetric methods (Schmidt, 1949). Thermocouples are still commonly used in more recent experimental studies (O'Sullivan & Cotterell (2001), O'Sullivan & Cotterell (2002)) however the method has limitations, one of which is that it is difficult to measure temperatures very close to workpiece or tool surfaces where extreme temperature variations are found since there are limitations in placement of the thermocouples themselves. In addition to this, it must be taken into account that the drilling of a hole into workpiece or tool materials for thermocouple embedding is an intrusive procedure and the method will likely affect the heat transport and cause significant distortions in the measurements (Kato & Fujii (1997), Attia et al. (2002)). Another, less intrusive, method is to use infrared photography (Tyler & Schmitz, 2014). This technique benefits from fast responses, no adverse effects on temperatures and materials, no physical contact which limits thermal damage to equipment, and allowing measurements on objects which are difficult to access (Abukhshim et al., 2006). As with much experimental observation near to the cutting edge, however, the obstruction of the chip can make it difficult to monitor the region along the cutting edge, where the chip formation region coincides with one of the highest temperature regions. There are advantages and disadvantages to the use of all measurement techniques used in machining cases, with the best approach usually depending on individual, specific requirements of the data collection.

As computational power has increased, Finite Element Method (FEM) based models have become more widespread and are now commonly used to predict cutting temperatures and forces along with other machining outputs in computational modelling of cutting operations. These models can be applied to better understand the underlying physical processes and identify causes of wear or tool failure. Özel & Altan

(2000) simulated flat end milling using commercially available software DEFORM-2D and obtained reasonable agreement with experimental results. Very high tool temperatures of over 1000°C were predicted on the rake face, at the primary cutting edge, which Özel & Altan concluded was a key factor in the crater wear development found here. Yang et al. (2014) studied tool temperatures in the milling of Ti-6Al-4V and the findings that the tool temperatures were highest on the rake face for low cutting speeds was consistent with the experimental data in the literature. Finite Difference based models have also been successfully used to predict machining temperatures (Ulutan et al., 2009).

Often the aim within much of the cutting temperature modelling work is to adequately describe the complex loads acting on the cutting edge so that this information can be applied and then suitable conditions can be chosen for each tool/workpiece combination to maintain acceptable cutting temperatures (Klocke et al., 2012). Having control over cutting temperatures in machining can be very beneficial as we can theoretically increase machinability up to a maximum according to the first law of metal cutting (Makarow's Law):

For each combination of tool and workpiece materials there is a cutting temperature, referred to as the optimum cutting temperature, at which the combination of minimum tool wear, minimum stabilised cutting force and highest quality of the machined surface is achieved. This temperature is invariant to the way it has been achieved.

Based on this first law, Astakhov (2006) showed that increasing the temperature up to optimal cutting temperature (where the highest ratio of cutting tool hardness over workpiece hardness is achieved) improved machinability and continuing to increase temperature past this point led to poor machining conditions. Most commonly the naturally occurring temperatures in machining are above this optimal cutting temperature and applying coolants is the most popular technique to decrease temperatures toward optimum.

2.2 A review of coolant application in industrial milling and other machining settings

Coolants, or cutting fluids as they are often referred to in a machining context, have been used for decades and their potential for enhancing efficiency in cutting processes has been recognised since the early 20th century. They are used for a variety of reasons, they can increase the machinability of the workpiece by lubricating the tool-chip-workpiece interface and reducing friction as well as removing heat generated at the cut-

ting zone and helping to evacuate the chips from the working environment (Shokrani et al., 2012b).

Currently, most machining in commercial settings is carried out with the use of large quantities of coolant. The most commonly used coolants, however, are not environmentally friendly and often not economical to use due to the regulation for disposal of the hazardous fluid. There is, therefore, substantial industrial interest in more targeted, advanced applications of coolant to reduce usage, and in the identification and development of alternative, cleaner coolants (Richardson et al., 2006a).

There are several types of coolant and a variety of application methods to choose from. Water is a commonly used coolant. It is cheap and readily available, however it has a minimal lubrication effect and can in fact wash away separately applied lubricants and therefore increase tool wear. It can also be problematic to use water near ferrous materials if they form part of the tool as it can cause corrosion which can be expensive to repair. More often water miscible cutting fluids are used with a soluble oil dispersed in the water aided by emulsifiers (Grzesik, 2008a). This addition of soluble oils increases the cutting fluid lubrication effect and prevents corrosion of the ferrous materials (Shokrani et al., 2012b). Oil based cutting fluids are an alternative (Baradie, 1996). Made up primarily of mineral oils, they excel at reducing friction and therefore friction induced heat at the cutting edge however can only be used in a lower temperature range as at high temperatures they can smoke and make mist (Shokrani et al., 2012b). Coolants may also be applied in various ways, either in large quantities externally, though internal tool channels, or using a Minimum Quantity of Lubrication (MQL) spray of particles.

The effect of cutting fluids, and their application methods, on machining processes has been researched across a broad range of machining applications, as a result of their popularity in metal cutting operations. The studies help to identify the benefits and limitations of the application of cutting fluids as well as improving understanding of which machining operations can be most enhanced by their use.

Machining experimental studies can be expensive and time consuming and often any conclusions drawn from testing are specific to the particular workpiece-tool pairing and the cutting conditions used (Astakhov, 2006). Abele & Fröhlich (2008) suggested there is a set of several machining parameters which all must be considered together and modified to achieve a good removal rate for each machining setup. Despite these difficulties, however, over time a vast bulk of knowledge and experience has been accumulated through experimental testing for various tools and processes (Akhtar et al., 2014), (Sarikaya et al., 2021). These tests continue now as new methods, coolants and workpiece materials are developed and are often the most efficient way to determine viability of new concepts in a machining context.

Even in some of the earliest key literature on machining there is evidence of cooling being applied successfully in experimental tests. As early as 1883, Frederick Winslow Taylor published experiments showing the direction of a constant stream of water to the cutting edge allowed significant increases in cutting speed. When 'On the Art of Cutting Metals' was published by Taylor (1906) later on, it contained results of 50,000 machining tests and his design for a circulating coolant system was already being introduced in other workshops (McCoy, 2017).

Since the work of Taylor, coolants have been developed significantly so that a broader range of fluids can be used today. A thorough review of this development has been carried out by McCoy (2017). Since one of the key objectives when using a cutting fluid is to reduce the cutting temperatures, it is important to understand their thermal capabilities. Sales et al. (2002) carried out a series of non-machining tests involving the preheating of a test piece and then cooling with some appropriate coolants to produce cooling curves, see Figure 2.3.

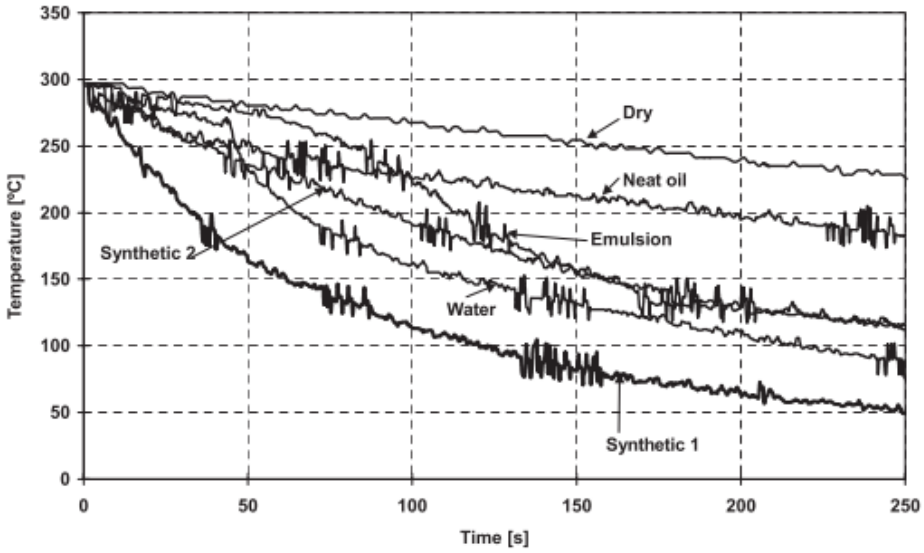

Figure 2.3: Temperature reductions through time for a standard workpiece material cooled using five widely used coolant fluids, with a coolant free 'dry' cooldown included. Republished from (Sales et al., 2002) with permission of Emerald Publishing Limited.

It can be seen that water and the synthetic coolants were the most effective in the tests. However when Sales et al. tested the same coolants in a series of machining tests using thermocouples to monitor the tool-chip interface temperatures it was found that the water and synthetic-1 coolant actually exhibited some of the highest temperatures at the interface. This was attributed to a lack of natural material softening which can happen as some workpiece materials achieve a high enough temperature so that their material properties have changed and their hardness is reduced, making the workpiece easier to cut. If the water or synthetics applied cooled the workpiece so efficiently that this temperature was never reached and the workpiece remained at a

high hardness then this could be an explanation for the results. It is likely that other factors are playing a role too, such as the lubrication provided by the coolants to the cutting process. Any coolant providing a significant lubrication effect could showcase lower cutting temperatures in these tests by virtue of having reduced the cutting forces.

It is important to choose cutting fluid carefully, considering both the lubrication and heat removal properties required for each tool-workpiece pairing. Often a trade off will be needed since lubrication and heat transfer cannot necessarily be optimised simultaneously when choosing a suitable coolant. This is illustrated in Figure 2.4, which shows water with a very high cooling capability but a very poor lubrication capability, and alternative categories of coolants such as emulsions and mineral oils with increased lubrication properties but reduced thermal benefits.

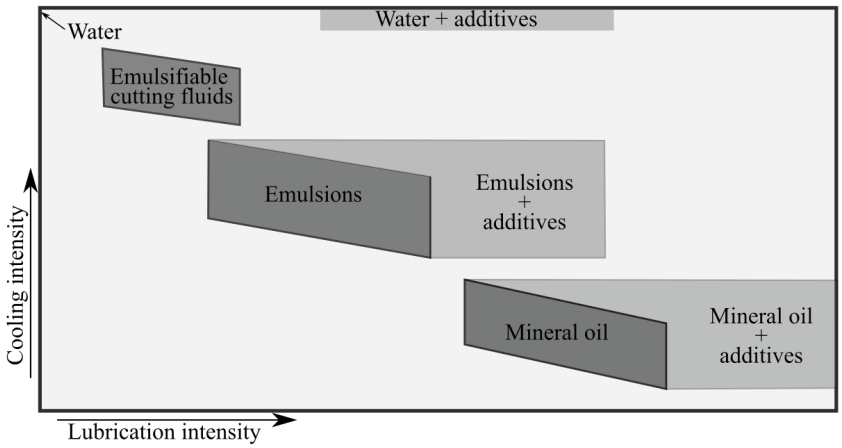

Figure 2.4: Cooling and lubrication capabilities for common coolants. Based on the illustration found in (Grzesik, 2008a).

The machining operation of primary interest in this thesis is milling, which as previously discussed is a versatile and useful machining process. It can be however a more complex process than other single point processes such as drilling or turning, due to its intermittent cutting whereby the cutting edge is not constantly engaged with the workpiece but rather continuously engages then disengages as the tool rotates (Cui et al., 2017). The use of conventional flood coolants in milling operations has had varying results across workpiece-tool pairings and a range of cutting parameters. Gu et al. (1998) suggested special tests were needed to evaluate whether the use of coolant was appropriate since it is not always the case that coolant will enhance the tool life. The following review of a selection of the available literature highlights the variability of coolant performances.

Mixed results have been seen for milling of steel in particular. Both Ozcelik et al. (2011) and Da Silva et al. (2011) found application of flood coolant was only beneficial in the milling of steel at lower cutting speeds and smaller feed rates during

their experimental investigations. In the tests of Ozcelik et al., which are plotted in figure 2.5, only at the lowest cutting speed tested (100m/min) did the coolant test finish successfully — while the dry cases finished all tests without reaching critical wear levels the wet case failed the trials at relatively low cutting speeds (150m/min). At the lowest cutting speed the improvements when using the wet coolant over dry are clear: The wear is significantly reduced. These low cutting speeds and feeds however are not ideal for high productivity as it limits the material removal rate significantly.

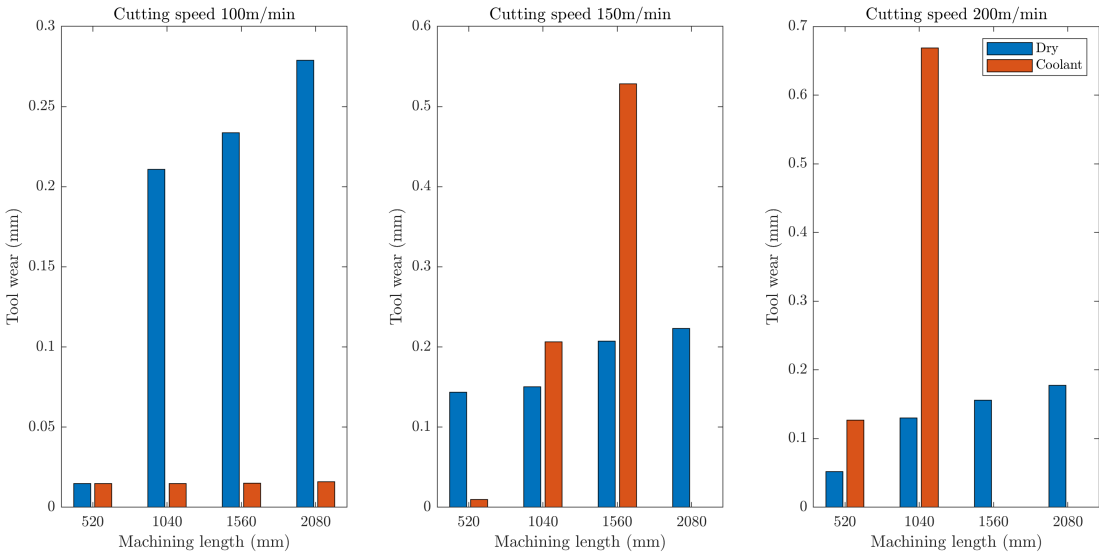

Figure 2.5: A plot of the experimental data of Ozcelik et al. (2011), comparing tool wear for dry and wet machining cases over a range of cutting speeds.

When comparing MQL, flood, reduced flow rate and dry conditions during the milling of medium carbon steel, Da Silva et al. (2011) found that performance again was heavily impacted by cutting conditions. Material removed before tool failure recorded by Da Silva et al. (2011) is shown in Figure 2.6 and highlights the variability in the best coolant method with variations in cutting conditions. For a cutting speed of 200m/min and a feed rate of 0.14mm/rev, flood cooling was the best condition for high material removal, however it was the worst performing for an increased feed rate and cutting speed of 0.22mm/rev and 260m/min respectively. Both the dry and reduced flow rate conditions perform to a reasonable level across all tests in this study. This appears to be consistent with the work of Ozcelik et al. (2011) and suggests strong attention must be paid to cutting conditions.

Tool life and material removal limits are not the only parameters that need to be considered when identifying the best cooling strategy. Coolant condition can have a significant effect on the surface roughness or finish of the workpiece that is being produced and sometimes this can take precedence. Thepsonthi et al. (2009) compared dry, flood and an externally applied high pressure pulsed jet cooling condition for

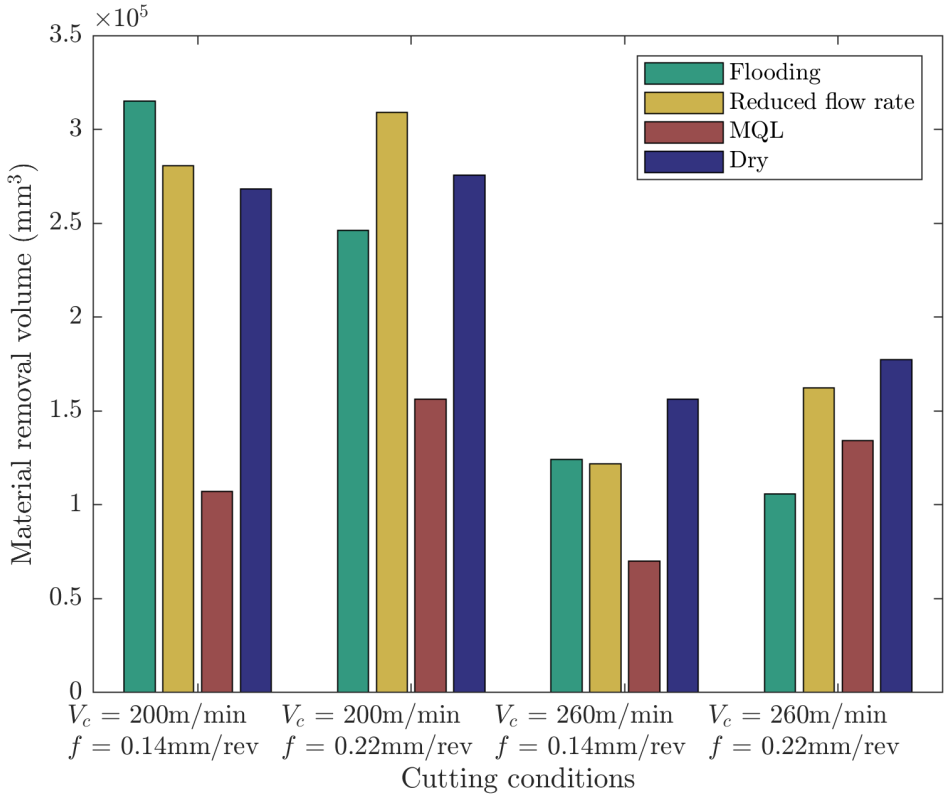

Figure 2.6: Plot of the experimental data of Da Silva et al. (2011) for material removed before failure for various cutting conditions and cooling techniques.

the slot milling of hardened tool steel. Over the range of cutting speeds tested (125-175m/min) the coolant approaches outperformed the dry conditions in achieving a lower surface roughness on the finished part. The flood conditions did however also show the highest flank wear, which was the failure mode in these cases, across all cutting speeds here. Initially in the machining tests, the flood and dry conditions showed significantly more flank wear than in the pulsed jet coolant condition but at later times, this flank wear increased more slowly in the flood and dry cases than in the pulsed jet case so that ultimately the failure times were all very similar (approx 90 minutes). Thepsonthi et al. analysed chip colouration as part of the experiments and interestingly the chips indicated that the flood coolant tests had resulted in the lowest cutting temperatures of the three conditions by a significant margin. Flank wear is generally caused by the abrasive action of the flank face over the machined surface of the workpiece and is not usually attributed to thermal causes, so despite the effective thermal management of the cutting edge observed by introducing the flood coolant, it was not expected that this flank wear would be dramatically reduced as a result. Lubrication effects are more beneficial in managing flank wear as they reduce the frictional forces between the tool and workpiece/chip. One possible explanation for the good results produced by the high pressure pulsed jets is that although the coolant is the same as in the flood

condition, the high pressure application likely allowed it to pentrate further into the cutting zone and act more effectively than in the low pressure flood case.

In a similar study by Kim et al. (2001), the tool wear and thermal characteristics during high speed ball-end milling of hardened steel were compared for dry milling, wet milling (conventional flood coolant used) and compressed cold air. As can be seen in figure 2.7, the tool wear for the wet condition was similar to other scenarios for a certain amount of machining but rose to the cut off level of wear in less cutting length than the other cooling methods — indicating that the dry and compressed air coolants would allow for a longer tool life in this case. Kim also used thermocouples to record temperatures near the cutting zone and it can be seen that the wet cooling conditions maintain the lowest cutting temperatures, though the compressed air conditions still remain significantly lower than the dry condition.

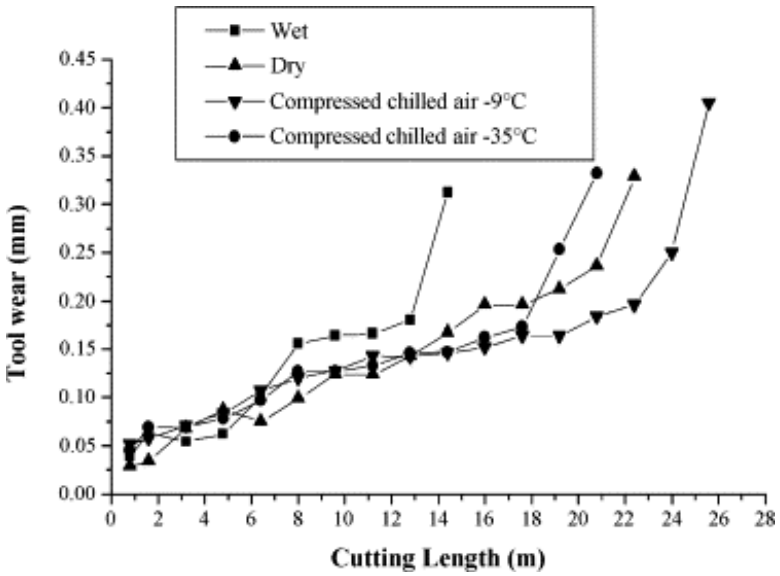

Figure 2.7: Tool wear development with increased cutting edge for various cooling methods (Kim et al., 2001). Reprinted from Journal of Materials Processing Technology, Vol 113, Kim S., Lee C., Lee D., Kim J., Jung Y., Evaluation of the thermal characteristics in high-speed ball-end milling, Pages No. 406, Copyright (2001), with permission from Elsevier.

Cutting Environment	Temperature °C
Dry	790
Conventional coolant	350
Compressed chilled air (-9°C)	540
Compressed chilled air (-35°C)	450

Table 2.1: Maximum cutting temperatures for various cooling methods (Kim et al., 2001).

Kim concluded that the significant temperature variations experienced cyclically in the wet milling case caused tool failing thermal fatigue. The tool is cooled

exceptionally well by the coolant, however it still experiences high thermal loads whilst the cutting edge is engaged, so that it cycles between extreme hot and cooler temperatures with a greater temperature range than is expected with coolants which do not cool the region as effectively. It can also be seen that the colder air condition results in the second fastest tool failure (Table 2.1), again possibly as a result of the greater temperature differences.

A similar set of results, in which lower cutting temperatures coincided with reductions in tool lives, were observed when using coolants by Vieira et al. (2001) for the face milling of AISI 8640 steel. A range of cutting speeds (100 – 220m/min, moderate to high) were tested and it was found that dry cutting resulted in a longer tool life than any of the industrial cutting fluids tested. The reduction in cutting temperatures when applying coolant was found to be most pronounced at lower cutting speeds and over cutting speeds of around 160m/min the difference was minimal. A variety of wear types can be exhibited when milling steel, including chipping on the edges due to thermal cracks, notch wear and built up edges. Vieira et al. noted that the major failure mode in these machining tests was comb cracking. This wear is typical in milling of steels and can be attributed to the high thermal loads as well as mechanical stresses. Applying coolants in these conditions is rarely advised as they exacerbate the problem by inducing strong thermal shock, which seems to explain the tool life results in this work.

Flood cooling has been applied with more definitive success to the milling of superalloys and HTC materials. Comparing flood, dry and MQL conditions in the end milling of Inconel718, Park et al. (2015a) found that flood cooling resulted in the longest tool life and lowest flank wear of the three conditions. Liu et al. (2018) reported similar findings with flood conditions, managing to extend tool life by over 75% and reduce flank wear considerably for milling Inconel718.

Titanium alloys can also be traditionally quite difficult to machine. Su et al. (2006) concluded that flood coolant was unsuitable for high speed end milling of Ti-6Al-4V, a widely used titanium alloy in the aerospace and automotive industries. It was observed to cause massive thermal shock problems and although the cooling was effective, the rapid thermal cycling caused thermal cracks to form and propagate. Under flood cooling these thermal cracks grew much quicker than in other conditions observed and lead to excessive chipping and finally fracture of the cutting tool.

In cases where flood cooling has limited benefits, the Minimum Quantity Lubrication (MQL) method, applying only small amounts of coolants in droplet form dispersed in an air jet is often tested as an alternative. Sun et al. (2006) varied several machining parameters including the cutting speed, feed rate and depth of cut whilst comparing MQL, flood and dry cooling conditions in the milling of the same titanium

alloy Ti-6Al-4V. It was shown by Sun et al. that across all cutting speeds, feed rates and depth of cuts tested the MQL coolant method performed significantly better than both the dry and flood conditions and gave the longest tool life, highest material removal and the smallest cutting force. As part of this work it was also highlighted that at the higher cutting speeds there was very little benefit of using the flood coolant compared to dry conditions, although a moderate improvement was still noticeable at the lowest cutting speed tested (40m/min). It was suggested by Sun et al. that a more efficient use of the coolant is to localise it to tool faces with well controlled, focused jets.

High pressure coolant jets are sometimes used when there is vaporisation of regular flood coolant before it can reach the cutting edge. The high pressure jets are able to penetrate into the tool-chip interface and reduce the temperature gradients there as well as improve chip breakability in difficult-to-cut materials. These high pressure jets can either be applied externally or through the tool itself. Reznikov & Zhivoglyadov (1989) used 2D modelling to investigate the thermal impact of including a coolant hole in the tool and observed a reduction in temperature of over 100 degrees. This process, called flushing at the time, was tested with a variety of cutting operations and found to reduce flank wear and improve tool life (Wertheim et al. (1992), Mazurkiewicz et al. (1989))

Kovacevic et al. (1995) studied the use of high pressure water jets as coolants in milling using two application methods. The jet was injected into the tool-chip interface in one instance using the flushing method through the tool rake face from an internal tool channel and in the other via an external nozzle. Kovacevic's results showed a significant reduction in cutting forces and surface roughness as well as an increased tool life for through tool high pressure cooling as opposed to flood cooling. Due to the success of early tests and modelling investigations, through tool cooling is now widely used in industry.

The design and application of effective through tool cooling for some HTC materials is now a research area of significant interest. Oezkaya et al. (2016) investigated the influence of both coolant supply pressure and coolant channel diameter for through tool cooling of drilling with Inconel718 Nickel alloy and found that pressure had a significant impact not only on the longest achievable tool path before failure but also on the surface integrity of workpiece, both of which improved as pressure was increased for the ranges tested. Where Sun et al. (2006), Su et al. (2006) found that applying flood coolant in the milling of Ti-6Al-4V titanium alloy reduced the tool life compared to dry conditions, through tool coolant is generally successfully used in many modern machining settings and frequently recommended by machining companies for milling of titanium alloys. Bermingham et al. (2014) compared through tool to flood cooling

of Ti-6Al-4V for end milling and found that when applying through tool coolant it was possible to increase cutting parameters while maintaining the same tool life, enabling a higher level of productivity. By increasing these cutting parameters Bermingham et al. achieved up to a 30% reduction in machining time and after carrying out initial cost analysis on the process they calculated a 19% cost saving was possible when applying the coolant through tool.

As with flood coolant, through tool coolant may not always be beneficial. Rahman et al. (2000) varied cutting speeds, depth of cut and feed rate while milling steel with un-coated inserts using high pressure through tool coolant. For each of the cutting parameters tested, there existed a point where one coolant method became more useful than the other, highlighting the variability still present in which coolant application is preferable. Senthil Kumar et al. (2002) tested steel of various hardness levels in end milling experiments with through tool coolant applied and found that it greatly reduced flank wear and increased tool life but only for steel within a certain hardness range.

As discussed here, the incorporation of active cooling through the use of cutting fluids in machining process can offer many benefits including an extended tool life and increased quality in the manufactured part. The application must be well considered however since it is evident that the benefits are not universally observed across the broad range of machining parameters and workpiece-tool pairings that make up many operations needed in the manufacturing industry today. The excessive use of coolants also gives rise to environmental and safety concerns due to the hazards associated with disposal and working in close proximity to them.
The effective use of reduced quantities of coolant through more advanced application methods such as through tool cooling or MQL is of high interest. New methods which can aid in the explanation of coolant variabilites would be very valuable to reduce the need for extensive, expensive tests such as those reviewed here, which are needed for each tool-workpiece pairing and across a broad range of cutting conditions.

2.3 Computational studies of coolant flow in machining operations

One technique used to investigate coolants in machining is the application of computational modelling. When coolants are applied, they are intended to provide lubrication and reduce both the tool and workpiece cutting temperatures. Although some of the resulting effects of coolants can be observed though experiments, such as changes in tool life, workpiece surface roughness and cutting forces, it is more difficult to get a direct picture of the distribution of the coolant and the temperatures. Direct measuring

using thermocouples poses challenges due to the hostile environment and there is limited success with infra red imaging because often the chip is in the direct line of sight to the cutting edge. Calculations can be applied but many approaches lose their validity when the workpiece is being continuously cooled so modelling using computational fluid dynamics (CFD) can be an alternative method which allows a clearer picture of the underlying effects of adding coolants to machining processes (Chowdhury et al., 2014). The application of using CFD in machining has been a challenging problem within the industry. The complex geometries coupled with the need for carefully implemented boundary conditions make the modelling challenging (Oezkaya et al., 2016).There is also a heavy level of interaction and interdependence between many of the solid mechanics and fluid mechanics aspects of the machining processes which are very difficult to couple (Catherine et al., 2018).

One of the key areas in research within machining with CFD is the flow field of the coolant. Using experimental techniques it is very hard to observe where the coolant reaches in the cutting region since the area is so visually obstructed, so computational techniques can provide great insight here. The geometries are often challenging to mesh and include in these machining applications and often the tool is considered but the workpiece is neglected since it adds another layer of complexity to the simulation.

Najiha et al. (2012) modelled externally applied jet flow onto a milling operation with a four-teeth milling bit. The simulations indicated that flow and lubrication were not evenly distributed along the tool and that the cutting fluid had not completely penetrated to the cutting edge. This work was further developed (Najiha & Rahman, 2014) to include three equally spaced external jets which the author found enabled a much improved coolant coverage on the tool. The simulations however did not include the workpiece which is often what prevents fluid getting to the cutting edge in machining operations (Fallenstein & Aurich, 2014), and it is possible that the flow field and coolant distribution could be significantly altered were this workpiece introduced as is the case in real life processes. A more recent study by Catherine et al. (2018) also used CFD to analyse the effect of external coolant nozzles on the coolant distribution onto the tool. Comparing the use of one and two coolant nozzles Catherine et al. found that the coolant was significantly better distributed near to the cutting edge which experiences the highest thermo-mechanical loads in the two nozzle experiment. The workpiece and chip however, which commonly cause the biggest obstruction in supplying coolant to the cutting edge were also not included here and would likely have a significant impact on the coolant flow in the tool's vicinity.

MQL flow is also of interest in machining. Comparing the flow for emulsion and MQL coolants applied externally, López de Lacalle et al. (2006) used Pamflow software to investigate the flow fields around milling tools under both coolant conditions using a simplified single phase fluid model. The primary difference between the

simulations is the velocity the coolant is applied at, the conventional emulsion coolant has relatively low speeds under 10m/s at the inlet whereas the MQL which includes pressurised air has velocities over 100m/s. This difference in velocity causes major variations in the flow fields observed. In each simulation the rotation of the milling bit is included which is an important factor in externally applied coolants. López de Lacalle et al. found the rotation of the tool caused a rotational flow field around the tool periphery to develop, caused by the tool's movement. This flow pattern impacted on the coolant jet path in the emulsion coolant simulations and prohibited the coolant from effectively reaching the cutting edge. With the high speed jet used in the MQL case on the other hand, the coolant could effectively cover the majority of the tool face, highlighting its benefits here. The assumption made here of single phase flow simplifies the problem and makes the simulations more manageable in this setting, and it is likely to be valid for the MQL simulations which comprise heavily of air. For the emulsion coolant simulations, however, where the coolant jet is predominately water, the fluid properties should be taken into account and it is unrealistic that the flow of air around the tool generated by the tool's movement would be sufficient to prohibit a water jet breaching it to reach the tool. The single phase assumption is widely adopted when considering the flow field in machining cases seen here but the important inclusion of tool rotation here could highlight the limits of its applicability.

Zou et al. (2013) investigated MQL simulations also and introduced a cryogenic element by varying the carrier air flow temperature. Through tool coolant was simulated and a variety of internal channels considered, from single direct and double direct channels to double helical channels. Temperature and velocity were monitored along the tool axis path as the coolant left the tool. Reducing the temperature of the coolant initially led to reduced temperatures along the path and an increased flow velocity at the inlet resulted in increased velocity along the path, as would be expected. Rotational velocity of the tool was also investigated and found to have only negligible impact on the outputs considered.

More complex physical features were incorporated into MQL milling modelling by Zhu et al. (2018) who used COMSOL multiphysics to investigate the 2 phase behaviour of MQL. The flow field was investigated as well as the oil droplets present within MQL spray. Particle trajectories and spray impingement modelling was included as part of a study into the optimal nozzle to tool distance for external MQL applications in milling. When the nozzle was very close to the tool it was found that there was rebounding of the droplets although many of these droplets did become re-entrained in the flow and still adhered to the tool surface if the air flow was high enough. For too large nozzle spacing there was not sufficient kinetic energy and the droplets were predominantly re-directed away from the tool with the carrier fluid due to the high rotational forces applied. The study here shows the potential for CFD simulations to

allow better understanding of the processes in fluids within a machining context and can indicate better machining practices to be tested. Although the model is difficult to validate, as many are in machining, optimal nozzle distances predicted by the model were tested in a series of milling operations and the lowest surface roughness and cutting forces were observed in the optimal regions, which indicates an important practical level of validation of the model.

Evdokimov et al. (2015) proposed a method for calculating thermal fields in machining operations by combining ANSYS CFX modelling for the cutting fluid and air modelling and ANSYS Explicit Dynamic modelling for the calculations of cutting parameters such as the contact length between tool and chip. Heat flux boundary conditions were calculated according to the work of Resnikov (1986),(1963) and were applied to the boundary between the chip and tool, which was predicted using the Explicit Dynamic module in ANSYS. There were problems arising when importing the complex milling tool geometry into ANSYS geometry so the authors suggested a simplification of the surfaces although acknowledging that impacts on the quality of the results. There was good agreement found for the maximum tool temperatures dependent on feed rate between the results of Evdokimov et al. (2015) and experimental results in the literature, however the details of the modelling assumptions made and the equations to be solved are not present, either for the multiphase air-water fluid domain or the solid-fluid conjugate heat transfer between the tool and fluid. As a result, although Evdokimov et al. suggests this combination of modelling approaches could be applicable to any cutting operation there would likely be difficulty in implicating the same model and replicating the results. As such, the good level of agreement between experiments and simulation predictions should only provide limited confidence in this approach pending further modelling details. Tool temperature modelling was carried out by Perri et al. (2016) in the software Fluent. A 3D model which included the milling tool and externally applied coolant was used to compare the effects of coolant flow rate on tool temperature. An increased flow rate resulted in decreased tool temperature in all of a series of tests which also varied coolant temperature. The working fluid was air in the tests and so a single phase model assumption was made. Validation of the model was carried out using thermocouples in the tool and temperature profiles and values match well between experiments and simulations.

The research area of CFD in a machining context is relatively new and ongoing. The primary interest for this work will be in milling operations, where variability is higher and there has been less CFD modelling focus in the literature. The works available relating to milling show the potential of applying CFD in this discipline. There has been significant work on CFD simulations for drilling operations to determine both distribution, flow fields, and heat transfer with conventional coolants. The equivalent work for milling is limited though much of the modelling process and the

methodology would be very similar and some of the drilling findings are still relevant to other machining operations. The following research on drilling operations is included for completeness of modelling methodologies.

Fallenstein & Aurich (2014) conducted a study on the thermal conditions in cemented carbide drills when applying coolant which is driven down high pressure internal channels. Computer Aided Design (CAD) models with varying coolant channel exit position were used to identify the optimum tool geometry for reducing tool temperatures near the cutting edge. Both the radial and circumferential position were varied as seen in Figure 2.8. Fallenstein and Aurich applied a constant temperature boundary

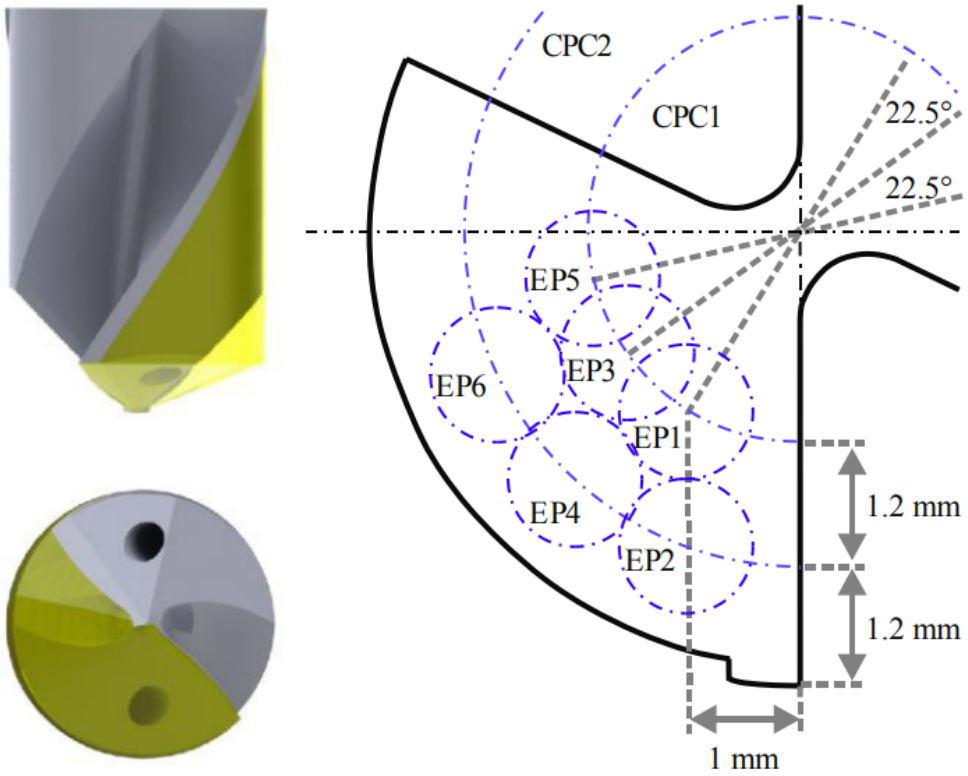

Figure 2.8: Coolant channel exit positions(EP1-6) tested by Fallenstein & Aurich (2014) for a twist drilling CFD study. Exit positions were varied over three angles and two centre point circles (CPC). Reprinted from Procedia CIRP, Vol 14, Fallenstein F., Aurich J. C., "CFD based investigation on internal cooling of twist drills, Pages No. 293, Copyright (2014), with permission from Elsevier.

on the effective rake face where the tool-chip interface would be located by linearly interpolating between nine set points. This temperature field is usually described by a heat flux boundary condition from the chip through to the tool rake face but this could not be applied here due to the active cooling (Agapiou & Stephenson, 1994) so it was set to remain constant due to constant regeneration of chip boundary in real operations. The effect of both the coolant channel position and the coolant flow rate were found to be significant on the temperature profiles and the heat transfer. For all

channel positions a reduced flow rate led to reduced heat transfer rates, though the impact of flow rate was much more pronounced when the coolant channel position was located further from the cutting edge compared to near the cutting edge.

Johns et al. (2018) also simulated coolant flow from internal channels in drilling when the exit position was varied. Instead of investigating the heat transfer, a two phase Volume of Fluid (VoF) model was implemented to study the distribution of the coolant and the wetting of the tool. A machining FEM model was used to calculate the formation of chip and workpiece in a drilling operation. This geometry was then used by the authors in a Finite Volume Method (FVM) model in OpenFOAM where the multiphase VoF method was used to track the interface between the coolant and surrounding air in order to establish the wetting of the tool. This analysis allowed insight into the regions of the tool that benefit from coolant wetting and increased lubrication. The ability to predict coolant coverage in this way allows for improved tool designs which can then target coolant at the correct regions, something that would have been difficult to do with any accuracy experimentally due to the challenges in monitoring flow features in such a hostile, visually obstructed environment. The numerical model was combined with response surface methodology to analyse the effect of channel positioning on wetting of the tool. The meta model results indicated that no design either fully flooded the domain or lubricated the entire tool so that there are areas of the tool which are not supplied with coolant.

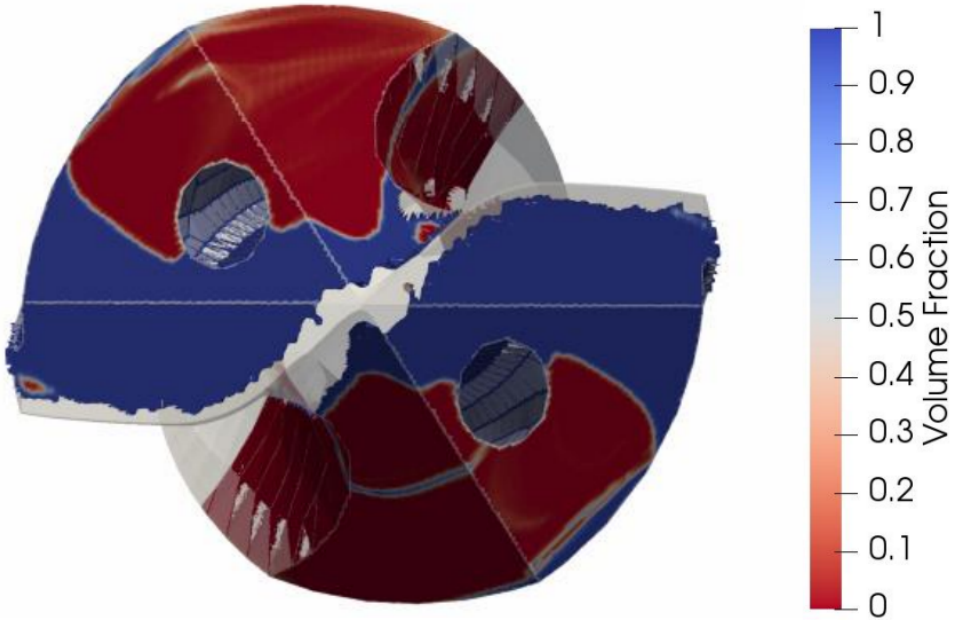

Figure 2.9: Distribution of coolant in drilling simulation with volume fraction of coolant between 0 and 1 (Johns et al., 2018). Reproduced under creative commons license CC-BY 3.0.

Dead zones where there is either no coolant distributed or where the flow is very slow in single phase models were also observed by Oezkaya et al. (2016) who mod-

elled the coolant distribution when internal channel diameter and pressure of coolant were varied. Even at the highest pressures Oezkaya found that the areas near the cutting edge only see slower velocities so again there were areas of the tool geometry which were not being cooled or lubricated.

For internal channel cooling the geometry of the channel can be a key parameter for improving chip evacuation, heat transfer or coolant supply to specific regions (Johns et al., 2018). Kao et al. (2017) investigated the flow structure for triangular coolant channels as well as the more common circular channels in a study on MQL drilling using both experimental and CFD techniques. The authors found that there was a significant variation in the flow structure depending on geometry, though the observed effects were quite specific to the MQL fine oil mist structure, it could indicate that this parameter should be considered in further optimisation studies for conventional coolant through tool channels. In gun drilling the practice of adopting alternative geometries was shown to be beneficial in a study by Woon et al. (2016) which highlighted the kidney bean configuration to be the best in terms of preventing loss in hydraulic pressures over the rake face.

2.4 Chapter conclusions

In this chapter, key features of machining processes have been introduced, and the importance of effectively managing tool temperatures has been discussed. Various cooling methodologies for machining practises have been presented and some key experimental literature around the use of oil-water emulsion coolant over a range of application techniques, cutting conditions and tool-workpiece pairings has been highlighted. In review of the findings from coolant application experimental studies in the literature, it was clear that the majority of work presented results on machining output such as cutting forces, and surface roughness of the final workpiece product. While essential to the overall machining process, these results struggle to inform how well the coolant is targeting key areas along the tool.

To address this and explore coolant behaviour in more detail, CFD models have been applied to machining studies. Advanced CFD modelling including multiphase interface tracking methods, full geometrical complexities with tools, workpieces and chips, and detailed temperature modelling have been shown to be successfully applied to drilling operations. The review of the literature has highlighted a gap in the application of these methods to milling operations. There is also the potential to incorporate the advanced modelling methods listed into one study — for example the multiphase fluid dynamics and the multi-region conjugate heat transfer.

Chapter 3

CFD modelling of coolant flows in milling processes

Contents

3.1 Introduction

Conventional oil-water emulsion coolants remain the industry standard today when actively managing temperatures during machining operations. They are widely used and well established across the sector. The literature review highlighted many studies

showcasing the benefits of applying coolant in various machining processes and there is a wealth of experimental data and industrial expertise on when coolants are effective. Predominantly, the experience and knowledge of coolant application comes from the observation of secondary effects in machining cases (Kui et al., 2021). These secondary effects can include a change in tool wear extent or type, or an impact on the workpiece surface finish (Sankar & Choudhury, 2015). Direct observations of coolant application are difficult due to the hostile machining environment so the fundamental flow behaviours such as wetting and cooling capabilities are not well established in most processes.

Modelling of coolants within the cutting process using computational fluid dynamics (CFD) gives insight into the coolant behaviour and can explain some of the secondary effect observations. Modelling of drilling processes (Johns et al., 2018), (Fallenstein & Aurich, 2014) has shown effective application of CFD to machining and highlighted the potential for tool design exploration.

In this chapter, CFD is used to investigate coolant distribution and flow fields for a milling process. Both the tool and workpiece geometries are included which is a development on current work in the published milling literature. In a novel contribution, models to account for both the multiphase coolant-air flow and conjugate heat transfer will be considered together using OpenFOAM software. These will be applied to milling applications for the first time to extend on previous work for drilling and other machining applications.

3.2 CFD machining case configuration

3.2.1 Milling process geometries

Simulations of the milling process have been carried out using geometries provided by Sandvik Coromant and unless explicitly stated, all tool geometries refer to the CoroMill Plura solid carbide end mill for High Feed Side milling. The tool, used in a range of milling operations, has six flutes and coolant is delivered to each cutting edge via a central coolant channel and six smaller channels directing the coolant to each cutting edge through the flutes as seen in Figure 3.1.

Most machining coolant simulations in the literature with a milling focus investigate unobstructed free flow from the tool coolant channels with no workpiece geometry involved. In this work, both the workpiece and tool geometries are included to create a more representative simulation for an engaged tool cutting edge (Fig 3.2).

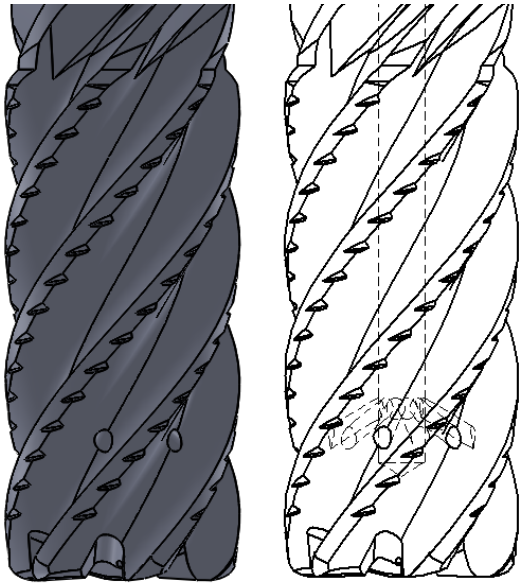

Figure 3.1: Sandvik CoroMill Plura solid carbide end mill geometry (*left*) with internal coolant channels illustrated (*right*).

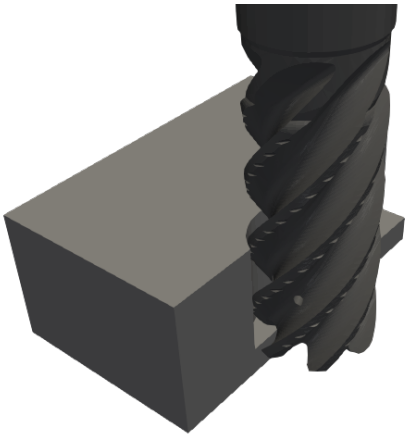

Figure 3.2: Tool and workpiece aligned in a milling process

The workpiece is in contact with the cutting edge during the milling process and it has a clear impact on the coolant flow since it lies directly in the path of the coolant jet. It is therefore deemed important to include when evaluating the tool wetting and distribution of the coolant. Additionally, during the cutting process chips are generated as the tool removes material from the workpiece. Along with the workpiece, these chips can also affect coolant delivery by obstructing coolant accessing the cutting geometry. It is possible to include an accurate representation of these chips in the CFD simulation geometries. Johns et al. (2018) combined FE solid mechanics simulations of a drilling process with CFD modelling to include accurate chip geometries along the cutting edge where they are generated. The chips in the study by Johns et al. were generated using ThirdWave Systems AdvantEdge software in a model which rotated

the tool through three rotations and simulated the cutting process. The same FE modelling of the machining process for a milling operation was carried out by Sandvik and provided with the tool geometries for analysis here. It can be difficult, however, to obtain good mesh quality since the chips formed in the simulation process are often very thin with complex rough surfaces, as small shavings of the workpiece material are removed. Along with the steady production of larger chips, very small fragments are also produced in the cutting. In single region studies, including only the coolant and air filled fluid domain, it is possible to obtain higher quality meshes whilst including chips in the geometry, however in this work, the focus is on multi-region simulations which allow investigation of the conjugate heat transfer. Exploratory simulations have been run for this work using the FE milling output geometries provided by Sandvik with the chips included, static in time as a simplification. The chips were found to reduce the mesh quality too much and they were therefore neglected from all remaining simulations and results in this work. In the multi-region cases to be studied in this work, all non-fluid regions in the geometry are meshed and retained instead of being neglected, as is the case in single region fluid domain cases. These solid regions include the very small chips created in the machining process. The smallest of these chip regions can be comprised of only a couple of mesh elements even after the refinement process and seemed to cause instability in the solution of the energy equation for the multi-region solver. Higher levels of mesh refinement were tested in an attempt to resolve this, however with increased refinement, increased numbers of small solid chip pieces were identified in the automated meshing process. Ultimately, there were hundreds of these small regions to consider and their inclusion increased the complexity and instability of the numerics without providing much benefit. The geometry of the chip and its contribution to the problem is also dynamic, which poses more modelling challenges. In further work it could be beneficial to consider the chip more thoroughly and separate the components so that some chip regions with significant impact including the large chip formation seen on the cutting edge is included and all other chip regions can be discarded.

During the milling process not all of the tool cutting edges are engaged at the same time — it is an intermittent cutting process. The primary aim of these simulations is to investigate the coolant flow at the engaged (actively cutting) tool edge. A static tool and workpiece configuration is used in these simulations since the inclusion of a rotation of the tool would significantly increase computational cost and scope of the work. The simulations are targeted on the fully engaged contact of the tool and workpiece, where the tool temperatures and coolant are of the most interest. The geometry is clipped to a small zone in this vicinity to enable a targeted investigation into the region of interest. The CFD model is configured to capture the flow leaving one of the radial coolant channels and interacting with the cutting edge and workpiece in the cutting zone, with the region of interest used as the fluid domain shown in Figure 3.3

where the fluid domain is highlighted in white in the context of the machining geometries. To summarise, in this chapter we are modelling the tool in an engaged state, and including both the tool and workpiece geometries, with chip features neglected.

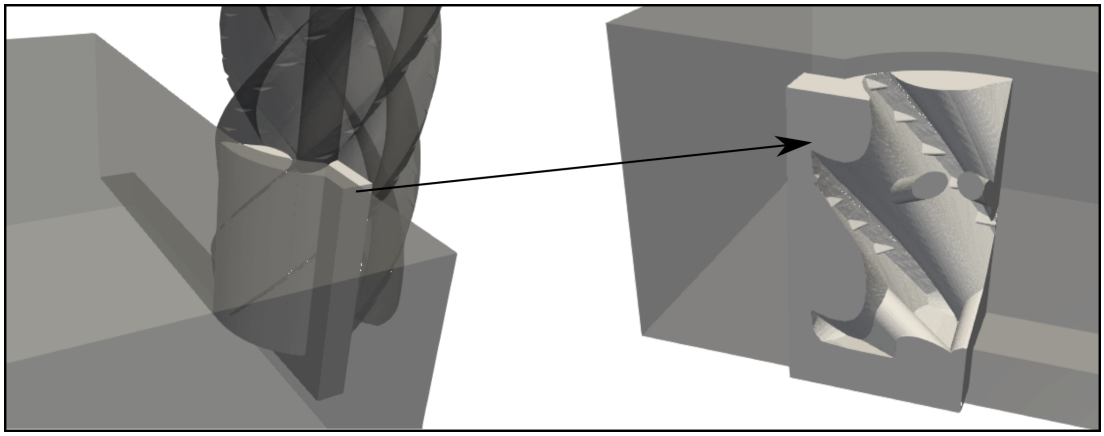

Figure 3.3: Fluid domain viewed through workpiece perspective (*left*), and tool perspective (*right*), with the fluid domain shown in both and marked with an arrow.

3.2.2 Limitations of a static model

Although this modelling work will proceed with static tool and workpiece configuration, it still needs to be recognised that the rotational behaviour of the tool has an impact on any modelling. An example engagement of the tool through a rotation is shown in Figure 3.4. Schematics at the top show the coolant channel position along with the outline and positions of the top and base of the flute, further around the tool, in greyed out regions. The edge which tapers off more and leads the rotation is the flank edge at the top of the flute, and the following edge at the back of the grey region is the rake edge, which meets the tool more abruptly. Only one flute's top and bottom are shown in the schematic, as well as the direction of that flute's coolant channel. In the 3D models accompanying them, this is the flute indicated by a white star.

The figure begins with the base of the flute already partly engaged, as the flank region is engaged here, but the rake is not. As the tool turns, the base of the rake edge and flank of the same leading cutting edge also becomes engaged in the second image. After further rotation, the coolant begins to impinge on the workpiece and supply coolant along the cutting edge wherever it is also engaged. As the tool continues to turn, the region of engagement of the edge rotates around. The base of the tool becomes disengaged. These points can be seen for the flank in the fourth image and the rake in the fifth. Continuing further through the rotation, a point will be reached, as seen in the final image of Figure 3.4, when the coolant application will also no longer impact on the workpiece but be jetted into the surroundings instead.

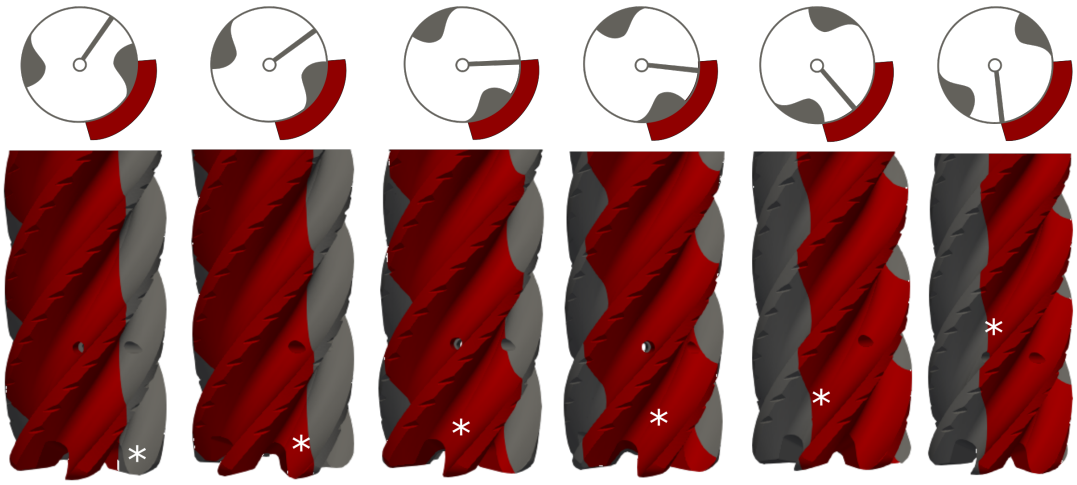

Figure 3.4: Engaged region of the tool shown in red as it rotates through a cut. As the tool is turned through a rotation, a white star marker is used to identify one flute of interest. Schematic of a simplified 2D impression which rotates clockwise along with the full 3D geometry is included above the 3D model, with the coolant channel, and the base and top of the cutting region flute shown in grey. The figure begins with the base of the flute partly engaged on the left, and ends as the tool is rotated to the point where the coolant channel no longer impinges on the workpiece, on the right.

From that point onward, there is no new coolant provided up to the rest of the rake edge which can be still engaged and cutting, especially if the axial engagement, a_p is high. For the work in this study, the modelling has been carried out with the tool and workpiece geometries rotationally positioned so that the cutting edge is as engaged in the coolant application region and is kept consistent between models. A study of average coolant coverage on the engaged section of the cutting edge has been carried out using rotations of the tool geometry about its central axis to determine the impact. The results are presented in Figure 3.5, where there is shown to be a short range of ≈20° where a consistent high coolant application is seen. As the tool is rotated out of this region the coolant distributed along the rake edge reduces and once the tool rotates out of the -40° - 50° range no coolant is applied successfully to the cutting edge. This 90° range makes up a quarter of the tool's rotation, and highlights the very transient nature of the coolant application in milling processes.

The coolant coverage and heat transfer through a full transient rotation would be of significant interest in any further work, although here it is considered out of scope. A rotational CFD model could incorporate this feature, but the modelling would have increased computational expense.

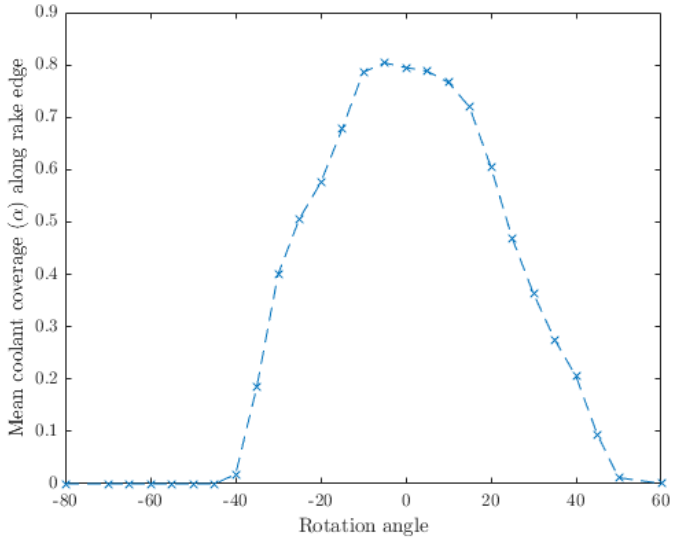

Figure 3.5: Mean coolant coverage results along the rake face in the cutting region are plotted for a series of modelling results with the tool rotated to varying degrees. The 0° point is the standard configuration, with the angle of rotion taken as positive in the clockwise direction.

3.2.3 Meshing

To apply CFD to this problem, good quality meshes need to be generated in all regions of interest in order to successfully solve the discretised governing equations (Fabritius & Tabor, 2016). In this study `snappyHexMesh` has been chosen to mesh both the fluid and solid domains. This is done by firstly creating an underlying mesh over the desired region made up of regular hexahedral mesh elements using the OpenFOAM tool `blockMesh` and then transforming this mesh so that the domain volume conforms to the geometry extracted from the CAD file using the `snappyHexMesh` tool. The `snappyHexMesh` tool first refines the background hexahedral mesh in any cells which see an intersection with the CAD files for the tool and workpiece so that there is considerable refinement near all the boundaries (Fig 3.6).

The meshing tool proceeds by splitting the domain up, taking the CAD surface files as boundaries between each region. Regions intended for use in the CFD model are returned whilst the mesh elements in regions not intended for use are discarded. Once unnecessary elements are removed, the elements near the boundary are then transformed to reflect the surface of the CAD files provided. Those mesh points near the surfaces are attracted towards them in a 'snapping step' which creates a conforming mesh.

For simulations focusing only on the coolant flow, the fluid elements are retained, however for conjugate heat transfer simulations multiple regions are required — the fluid, workpiece and tool mesh regions. Individual meshes for each region are created

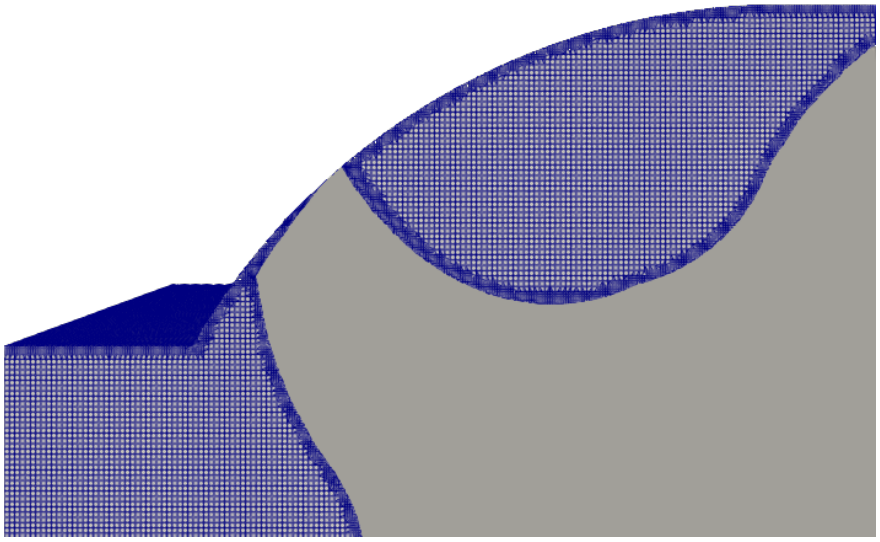

Figure 3.6: Mesh refinement of tool region at tool and workpiece interfaces.

from the `snappyHexMesh` output using the `splitMesh` utility which separates the main mesh along the internal boundaries and saves all regions as distinct meshes. The meshes created in this chapter contain approximately 14.5 million cells, which was determined suitable in a mesh sensitivity study presented later in section 3.8.3.

3.3 Combining Conjugate Heat Transfer and Two Phase Flow

The numerical modelling used for the machining simulations comprises of two separate models with a one-way coupling between. The first model, referred to as the multiphase fluid model, is used to investigate the coolant distribution and flow field. This two-phase fluid model uses a VoF method to track the coolant-air interface throughout the simulation, following the method of Johns et al. (2018). The second model, referred to as the conjugate heat transfer model, is used to solve the energy equation across the tool, workpiece and fluid region containing the coolant and air as solved in the first multiphase model. The one-way coupling means that the multiphase fluid model runs independently of the conjugate heat transfer model, however the conjugate heat transfer model is dependent on the multiphase fluid model.

Both models are implemented in OpenFOAM, an open-source C++ toolbox utilising the FVM to solve partial differential equations, particularly those relating to fluid dynamics. Advantages of the OpenFOAM software include the accessibility of the

source code which allows for user development and modification along with the wide range of features available and the large, active user community (Rojas-Sola et al., 2016). The code structure of the multiphase and conjugate heat transfer libraries in OpenFOAM are significantly different and do not allow for easy integration into one combined solver hence the breakdown of the simulations into two separated models here. This approach limits the solution to a one-way coupling between energy and flow which could be unsuitable in some applications where the flow has compressibility effects causing temperature changes or where buoyancy has a significant impact.

Since both phases in the multiphase model here (the coolant and surrounding air) are assumed to be incompressible (Ma < 0.3) the need for a two-way coupling between the models due to thermal effects of expansion and density changes is removed. Buoyancy is also predicted to have negligible impact due to the very low Richardson number,

$$\mathrm{Ri} = \frac{g\beta(T_{\mathrm{hot}} - T_{\mathrm{ref}})L}{U^2} \approx 4 \times 10^{-05} << 0.1, \tag{3.1}$$

which in thermal convection problems relates the importance of natural convection relative to forced convection, for gravity, g, thermal expansion coefficient, β, temperatures T_{hot} and T_{ref} for the hot wall and reference temperature, characteristic length, L and characteristic velocity, U. This very low Richardson number indicates that forced convection is dominant over natural convection in this case. Taking into account these assumptions, the coupling between energy and flow is reduced to one-way and the modelling approach taken here to separate the solution process is valid.

3.3.1 Multiphase Fluid Model

Applying through-tool coolant flow in milling provides high pressure, locally focused, coolant jets which has advantages over flood application in many machining settings. With this method however there is a need to better understand the coolant flow and distribution to ensure that it is focused in the most beneficial area. A multiphase model capable of accurately simulating the two phases present, the coolant and surrounding air, and tracking the interface between them is needed. In these simulations the coolant simulated is a water-oil emulsion with the oil making up a small volume fraction, $\approx 5\%$, of the coolant and having properties similar to those of water. As such the coolant is modelled as water.

Following the multiphase modelling method of Johns et al. (2018), a Volume of Fluid (VoF) free surface modelling technique, first developed by Hirt & Nichols (1981) and implemented in OpenFOAM by Weller et al. (1998), is used to track the interface between the two phases. The volume fraction, α, of coolant, referred to herein as water,

is traced through each element in the mesh, with elements comprising entirely of air having phase fraction $\alpha = 0$ and those of only water, $\alpha = 1$. For cells containing part of the fluid interface, a value between 0 and 1 is assigned $0 < \alpha < 1$.

Fluid properties such as density, ρ, and viscosity, μ, are calculated in each cell as a combination of the two phases representative properties using a weighted average:

$$\rho = \alpha\rho_{\mathrm{w}} + (1 - \alpha)\rho_{\mathrm{a}}, \tag{3.2}$$

$$\mu = \alpha\mu_{\mathrm{w}} + (1 - \alpha)\mu_{\mathrm{a}}. \tag{3.3}$$

Subscripts w and a refer to the water and air components respectively.

The VoF fluid method must combine the interface tracking with the solution of a single set of Navier Stokes equations,

$$\frac{\partial u_j}{\partial x_j} = 0, \tag{3.4}$$

$$\frac{\partial(\rho u_i)}{\partial t} + \frac{\partial}{\partial x_j}(\rho u_j u_i) = -\frac{\partial p}{\partial x_i} + \frac{\partial \tau_{ij}}{\partial x_j} + \rho g_i + f_{\gamma i}, \tag{3.5}$$

describing both fluids in the mixture where u represents velocity, g_i the gravitational acceleration, p the pressure, τ_{ij} the viscous stresses and surface tension $f_{\gamma i}$.

Accounted for as a body force in the momentum equation (3.5), the surface tension at the coolant interface with the surrounding air generates an additional pressure gradient (Navascues, 1979). This is evaluated using the continuum surface force (CSF) model proposed by Brackbill et al. (1992) in equation (3.6) for surface tension, γ, normal vector of the interface, $\hat{\mathbf{n}}$, the interface delta function, δ_s and the mean curvature of the interface, κ, defined in equation 3.7:

$$f_\gamma = \gamma\kappa\hat{\mathbf{n}}\delta_s, \tag{3.6}$$

$$\kappa = \nabla \cdot \left(\frac{\nabla\alpha}{|\nabla\alpha|}\right). \tag{3.7}$$

An additional transport equation (3.8) is solved for the phase fraction in the VoF method,

$$\frac{\partial \alpha}{\partial t} + \frac{\partial}{\partial x_i}(\alpha u_i) = 0. \tag{3.8}$$

This is required to conserve the various components of the multiphase fluid mixture (OpenFOAM, 2018).

A modification is made to the conventional transport equation above in the implementation in OpenFOAM (Deshpande et al., 2012). In order to sharpen the interface and manage the numerical diffusion an additional compression velocity term, u_c is added,

$$\frac{\partial \alpha}{\partial t} + \frac{\partial}{\partial x_i}(\alpha u_i) + \frac{\partial}{\partial x_i}((u_c)_i \alpha(1-\alpha)) = 0 \tag{3.9}$$

The compression term only acts in the vicinity of the interface since it is combined with an $(\alpha(1-\alpha))$ term (Rusche, 2003). Compression velocity factor, u_c, is defined here as

$$u_c = C_a \left| \frac{\phi}{S_f} \right| \hat{\mathbf{n}}, \tag{3.10}$$

for $\phi = u_f \cdot S_f$ where u_f is the velocity vector at face f, S_f the cell face area vector, C_a is an adjustable compression coefficient and $\hat{\mathbf{n}}$ again the interface unit normal. This governing set of equations for the VoF model is implemented in OpenFOAM as the `interFoam` solver. The solver has been widely employed and validated across a range of multiphase fluid applications (Deshpande et al., 2012).

3.3.2 Conjugate Heat Transfer Model

Heat transfer across a combination of fluid and solid components is commonly referred to as conjugate heat transfer. One of the main causes of tool wear in machining can be high temperatures along the cutting edge. The effect of coolant on these temperatures is a key point of interest in simulations since it is so difficult to monitor experimentally due to the adverse conditions with high temperatures and mechanical loads. Only by conducting conjugate heat transfer studies and including both the fluid and solid key components such as the tool, workpiece and coolant, can a study of the heat transfer in this application be carried out.

As described in section 3.3, the heat transfer and multiphase solutions are separated here and limited to a one-way coupling, so that only the energy equation is solved in the conjugate heat transfer modelling. The solution from the multiphase model is applied to the case to give a realistic coolant distribution and flow field — it effectively acts as a frozen flow field base that the energy equation can be solved on top of.

In this frozen flow fluid region, the energy equation is solved using a one fluid method. In order to account for the thermal properties of both fluids present, relevant fields such as thermal conductivity, λ, and density, ρ, are constructed using the properties of both components, appropriately weighted in each cell. This is done by reading in the volume fraction field, α, from the VoF solution which provides the water volume fraction in each cell, and then using it to create a weighted average of

the required fluid thermal properties:

$$\rho = \alpha\rho_{\mathrm{w}} + (1-\alpha)\rho_{\mathrm{a}}, \tag{3.11}$$

$$\lambda = \alpha\lambda_{\mathrm{w}} + (1-\alpha)\lambda_{\mathrm{a}}. \tag{3.12}$$

The conjugate heat transfer solver available in OpenFOAM, `chtMultiRegionFoam`, solves the following energy and temperature equations in fluid and solid domains respectively:

$$\rho\frac{DE}{Dt} = \rho\frac{De}{Dt} + \rho\frac{DK}{Dt} = \nabla(\sigma\cdot u) - \nabla\cdot q + \mathbf{F}\cdot u + r, \tag{3.13}$$

$$\frac{\partial T}{\partial t} = \frac{\lambda}{\rho C_p}\nabla^2 T. \tag{3.14}$$

The fluid energy equation implemented is often in terms of total energy, E, or internal energy, e and kinetic energy, K where $E = e + K$ and comprises of both thermodynamic and mechanical components. Terms include, q, the heat flux vector, r, the heat source, $\mathbf{F}$, the body forces and the stress tensor, $\sigma = (\tau - p\mathbf{I})$, made up of the thermodynamic pressure, p and the viscous stress tensor τ. The heat transfer in the solid is modelled using a somewhat simpler Laplacian equation, with parameters including the thermal conductivity, λ, density, ρ, and specific heat capacity, C_p.

Regions are usually coupled using a `compressible::turbulentTemperatureRadCoupledMixed` boundary condition which solves to match temperature and heat fluxes across each boundary.

To solve the thermal field over the multiphase fluid region, a temperature equation is implemented in the fluid region in place of the full energy equation. For the sake of completeness a short section here illustrates the transition from the energy equation previously implemented to a simplified temperature advection-diffusion equation.

Considering the kinetic energy per unit mass, $K = \frac{1}{2}u^2$, the material derivative is given as

$$\rho\frac{DK}{Dt} = u\rho\frac{Du}{Dt} = u(\frac{\partial\rho u}{\partial t} + \nabla\cdot(\rho uu)). \tag{3.15}$$

Substituting in the relation $\frac{\partial\rho u}{\partial t} + \nabla\cdot(\rho uu) = -\nabla p + \nabla\cdot\tau + \mathbf{F}$ from the momentum equation 3.5 here gives

$$\rho\frac{DK}{Dt} = -u\cdot\nabla p + u\nabla\cdot\tau + u\cdot\mathbf{F}. \tag{3.16}$$

Further substituting this equation for $\rho\frac{DK}{Dt}$ back into the energy equation eliminates

most of the mechanical terms when the stress tensor $\sigma = (\tau - p\mathbf{I})$ is expanded as follows.

$$\rho\frac{De}{Dt} - u\cdot\nabla p + u\nabla\cdot\tau + u\cdot\mathbf{F} = -\nabla\cdot q + r + \nabla\cdot(\tau\cdot u) - \nabla\cdot(up) + u\cdot\mathbf{F} \tag{3.17}$$

$$\rho\frac{De}{Dt} = \nabla\cdot(\tau\cdot u) - u\nabla\cdot\tau + u\cdot\nabla p - \nabla\cdot(up) - \nabla\cdot q + r \tag{3.18}$$

$$\rho\frac{De}{Dt} = \tau\nabla u - p\nabla\cdot u - \nabla\cdot q + r \tag{3.19}$$

Following the method of Bird (2002), the internal energy is now given in terms of enthalpy, h, using the relationship $e = h - p/\rho$ to leave

$$\rho\frac{Dh}{Dt} = \tau\nabla u + \frac{Dp}{Dt} - \nabla\cdot q + r \tag{3.20}$$

This equation is combined with the following relation for enthalpy in an element of moving flow (Bird (2002) Eq 9.8-7)

$$\rho\frac{Dh}{Dt} = \rho c_p\frac{DT}{Dt} + \left[1 + \left(\frac{\partial \ln\rho}{\partial \ln T}\right)_p\right]\frac{Dp}{Dt} \tag{3.21}$$

Equating these we can get the energy conservation equation in terms of temperature as opposed to total energy or enthalpy:

$$\rho c_p\frac{DT}{Dt} = \tau\nabla u - \nabla\cdot q + r\left(\frac{\partial \ln\rho}{\partial \ln T}\right)_p\frac{Dp}{Dt} \tag{3.22}$$

This is required due to the fact the specific heat capacity, c_p, is used to construct the enthalpy or energy variables and this process is now non-trivial since the fluid domain contains both air and water, each with its own value of C_p. Using temperature in place of enthalpy or total energy is perfectly acceptable within the context we are interested in since the fluids are incompressible and there will be no shock waves or similar features which have been found to require use of either enthalphy or internal energy in place of temperature as the solution variable. Under the assumption of incompressible flow, which results in ($\partial \ln\rho$ / $\partial \ln T = 0$), negligible viscous dissipation and the absence of a heat source, the thermal equation reduces to

$$\rho C_p\frac{DT}{Dt} = -\nabla\cdot q \tag{3.23}$$

Now using Fourier's law $q = -\lambda\nabla T$ with the thermal conductivity λ and assuming this is constant,

$$\frac{D\rho T}{Dt} = \frac{\partial \rho T}{\partial t} + \rho u\cdot\nabla T = \frac{\lambda}{C_p}\nabla^2 T \tag{3.24}$$

There are certain limitations accepted when applying this simplified thermal

model. Due to the sharp interface between the two phases in the VoF fluid results there will be discontinuities in the thermal properties across the domain. Near to the interface of the component fluids there are expected to be limitations in the accuracies of solvers of this type, as has been noted with other software using a similar approach (Fluent User Guide). In addition, certain features of thermal flow, such as buoyancy effects, are no longer modelled due to the reduction from a two-way to one-way coupled system, which, while not foreseen to be an issue here due to very low Richardson numbers, could be desirable in other applications. Other terms, such as source terms, which have been neglected from the fluid equation here for simplicity could be re-incorporated with reasonable ease and may be considered in any further work, if found to be suitable for machining cases. What has been provided by this solver is the capability in OpenFOAM to investigate conjugate heat transfer in applications where the fluid flow is a multifluid problem in itself.

3.4 Turbulence Modelling

The coolant is applied at high pressures to generate the high flow rates needed to cool the tool effectively. As such, we are predominantly working with fully turbulent flow in the simulations in this work. This is confirmed by considering the ratio of inertial to viscous forces, commonly referred to as the Reynolds number, $\mathrm{Re} = \frac{\rho u L}{\mu}$, which is often used to indicate laminar or turbulent flow. The transition region between the laminar and turbulent regimes is identified using a critical Reynolds number which can depend on the geometry. For a straight pipe channel flow, $\mathrm{Re}_{\mathrm{crit}} \approx 2000$ (Versteeg et al., 2007) and in the milling process setting the central coolant channel Reynolds number lies in the range $50000 < \mathrm{Re} < 80000$ which means the flow is fully turbulent.

Though difficult to formally define, turbulence can be very significant in determining flow features and has a large impact on mixing and heat transfer among other things (Tennekes & Wyngaard, 1972). Under turbulent conditions, flow fluctuations on various length scales are present. The Navier-Stokes equations (3.4, 3.5) are capable of resolving across these varying length scales using Direct Numerical Simulation (DNS) methods but this approach can be very computationally expensive since extremely fine mesh resolution is required to resolve the smallest length scales.

Turbulence modelling is often introduced across CFD applications to eliminate the need for resolving all length scales where this is infeasible. Large Eddy Simulation (LES) models resolve the large scale turbulence structures (large eddies) directly and only use modelling approaches for the small scale (sub-grid-scale) turbulent motion (Zhiyin, 2015). LES methods retain much of the accuracy of DNS techniques since the length scales for variables such as turbulent energy are captured by resolving the

larger structures, but they also benefit from computational cost and mesh density requirements by modelling over the smallest scales. Another widely employed approach is to use the Reynolds-Averaged Navier-Stokes (RANS) equations which model across all turbulent length scales. There are many RANS models available to suit various applications since no one turbulence model has thus far been found to suit all cases, however all boast a significantly reduced computational cost compared to fully resolved DNS solutions. For a more in-depth study of turbulence modelling the reader is directed to Spalart (2000). For the purpose of this work the computational cost of LES and DNS approaches are considered too high and RANS modelling is utilised. An overview of the RANS equations and three popular models, the $k-\epsilon$, $k-\omega$ and $k-\omega$SST models are outlined below along with a discussion of near-wall treatments.

3.4.1 RANS modelling

Fundamentally, RANS modelling operates on the process of splitting each fluid flow component into two parts, a mean value and a fluctuation,

$$u_i = \overline{u_i} + u_i', \tag{3.25}$$

where $\overline{u_i}$ is the mean value over a period of time t and u_i' is the fluctuating part. Substituting the Eq (3.25) into the full Navier-Stokes equations (3.4), (3.5), gives

$$\frac{\partial}{\partial x_i}\left(\overline{u_i} + u_i'\right) = 0, \tag{3.26}$$

$$\rho\left(\frac{\partial}{\partial t}\left(\overline{u_i} + u_i'\right) + \left(\overline{u_j} + u_j'\right)\frac{\partial\left(\overline{u_i} + u_i'\right)}{\partial x_j}\right) = \frac{\partial\left(\overline{p} + p'\right)}{\partial x_i} + \nu\left(\frac{\partial^2\left(\overline{u_i} + u_i'\right)}{\partial x_j \partial x_j}\right) + \rho\left(\overline{f_i} + f_i'\right). \tag{3.27}$$

These equations are then time averaged. The fluctuation components average to zero over time so that for example $\overline{u_i'} = 0$. With this and other minor manipulations the equations can be written as

$$\frac{\partial \overline{u_i}}{\partial x_i} = 0, \tag{3.28}$$

$$\rho\left(\frac{\partial \overline{u_i}}{\partial t} + \overline{u_j}\frac{\partial \overline{u_i}}{\partial x_j}\right) = \frac{\partial \overline{p}}{\partial x_i} + \nu\left(\frac{\partial^2 \overline{u_i}}{\partial x_j \partial x_j}\right) + \rho\overline{f_i} - \rho\frac{\partial \overline{u_i' u_j'}}{\partial x_j}. \tag{3.29}$$

The final term in the RANS momentum equation, (3.29), $\rho\overline{u_i' u_j'}$ is known as the Reynolds stress term and creates a closure problem which different models attempt to close by defining in terms of known variables.

Boussinesq (1877) was one of the first to approach the closure problem when he proposed the relation

$$\rho\overline{u_i' u_j'} = \frac{2}{3}k\rho\delta_{ij} - \nu_t\left(\frac{\partial\overline{u_i}}{\partial x_j} + \frac{\partial\overline{u_j}}{\partial x_i}\right), \tag{3.30}$$

where k is the turbulent kinetic energy and ν_t is the turbulent eddy viscosity. Equation (3.30) can then be used in the equation (3.29) to replace the Reynolds stress tensor. The governing equations for the system now include an additional two variables however and these need to be solved for or approximated. Many models have been proposed which introduce additional equations for the new turbulence variables, such as the $k-\epsilon$ and $k-\omega$ models.

$k-\epsilon$ Model

One of the most popular and widely used two-equation turbulence model is the $k-\epsilon$ model (Launder & Spalding, 1983). It is well established and has been extensively tested across a breadth of CFD applications (Leschziner & Launder, 1993). Two transport equations are needed, one for the turbulent kinetic energy, k:

$$\frac{\partial k}{\partial t} + \frac{\partial k\overline{u_j}}{\partial x_j} = \frac{1}{\rho}\frac{\partial}{\partial x_j}\left(\frac{\nu_t}{\sigma_k}\frac{\partial k}{\partial x_j}\right) + \frac{\nu_t}{\rho}\left(\frac{\partial\overline{u_i}}{\partial x_j} + \frac{\partial\overline{u_j}}{\partial x_i}\right)\frac{\partial\overline{u_i}}{\partial x_j} - \epsilon, \tag{3.31}$$

and another for the turbulent dissipation rate, ϵ:

$$\frac{\partial \epsilon}{\partial t} + \frac{\partial \epsilon\overline{u_j}}{\partial x_j} = \frac{1}{\rho}\frac{\partial}{\partial x_j}\left(\frac{\nu_t}{\sigma_\epsilon}\frac{\partial \epsilon}{\partial x_j}\right) + \frac{C_1\nu_t}{\rho}\frac{\epsilon}{k}\left(\frac{\partial\overline{u_i}}{\partial x_j} + \frac{\partial\overline{u_j}}{\partial x_i}\right)\frac{\partial\overline{u_i}}{\partial x_j} - C_2\frac{\epsilon^2}{k}, \tag{3.32}$$

In the model the eddy viscosity, ν_t is defined from k and ϵ,

$$\nu_t = C_\mu\frac{k^2}{\epsilon}, \tag{3.33}$$

where C_μ is a dimensionless constant. The five constants for the model, $C_\mu, C_1, C_2, \sigma_k, \sigma_\epsilon$ are usually provided as standard values in any CFD software and calculated from comprehensive data fitting of a range of turbulent experimental cases (Bardina et al., 1997). Although the $k-\epsilon$ model is generally very robust, it can struggle to predict flow for certain applications such as wall bounded flows (Mansour et al., 2012).

$k-\omega$ Model

Alternatively to the $k-\epsilon$ model family, a range of $k-\omega$ models have been developed and are also widely used.Proposed by Wilcox (1988), the $k-\omega$ model utilises the turbulence

frequency, ω,

$$\omega = \frac{\epsilon}{k} \tag{3.34}$$

as the second variable of interest alongside k. The turbulent viscosity is instead now defined as

$$\mu_t = \rho \frac{k}{\omega}. \tag{3.35}$$

One main advantage of the $k-\omega$ model is its improved performance near to the wall compared to other models such as the $k-\epsilon$ (Yusof et al., 2020). The following two equations are solved for k and ω,

$$\frac{\partial \rho k}{\partial t} + \frac{\partial \rho k \overline{u_j}}{\partial x_j} = \rho \tau_{ij} \frac{\partial u_i}{\partial x_j} - \beta^* \rho \omega k + \frac{\partial}{\partial x_j}\left[\left(\mu + \sigma_k \frac{\rho k}{\omega}\right)\frac{\partial k}{\partial x_j}\right], \tag{3.36}$$

$$\frac{\partial \rho \omega}{\partial t} + \frac{\partial \rho \omega \overline{u_j}}{\partial x_j} = \frac{\gamma \omega \rho}{k} \tau_{ij} \frac{\partial u_i}{\partial x_j} - \beta \rho \omega^2 + \frac{\partial}{\partial x_j}\left[\left(\mu + \sigma_\omega \frac{\rho k}{\omega}\right)\frac{\partial \omega}{\partial x_j}\right] + \frac{\rho \sigma_d}{\omega}\frac{\partial k}{\partial x_j}\frac{\partial \omega}{\partial x_j}. \tag{3.37}$$

The turbulent kinetic energy is set to zero and turbulence frequency tends to infinity as the wall is approached. In these cases a large value can be applied near to the wall at the closest mesh point (Wilcox, 1988). The sensitivity to this set value has been shown to be reasonably low in the extensive use of this model (Versteeg et al., 2007).

It is away from the wall, under free-stream conditions that the $k-\omega$ model has exhibited limitations. In this region both the turbulent kinetic energy and frequency tend to zero which is problematic when calculating turbulent viscosity μ_t. An assumed free-stream value is taken for ω instead, limiting the accuracy in these regions (Menter, 2012).

$k-\omega$ SST Model

Proposed by Menter (1994), there is a popular modified shear stress transport (SST) formulation of the $k-\omega$ turbulence model. It combines the favourable features of both the $k-\omega$ and $k-\epsilon$ models. The $k-\omega$ model is employed near to the wall in the inner parts of the boundary layer throughout the viscous sub-layer and incorporates the $k-\omega$ accuracy of near-wall regions. The SST model switches to a $k-\epsilon$ behaviour in the free-stream regions which allows it to avoid the sensitivity of the $k-\omega$ model to the free-steam turbulence properties. The turbulence model is solved for:

$$\frac{\partial \rho k}{\partial t} + \frac{\partial \rho k \overline{u_j}}{\partial x_j} = \tau_{ij} \frac{\partial u_i}{\partial x_j} - \beta^* \rho \omega k + \frac{\partial}{\partial x_j}\left[\left(\mu + \sigma_k \mu_t\right)\frac{\partial k}{\partial x_j}\right], \tag{3.38}$$

$$\frac{\partial \rho \omega}{\partial t} + \frac{\partial \rho \omega \overline{u_j}}{\partial x_j} = \frac{\gamma}{\nu_t} \tau_{ij} \frac{\partial u_i}{\partial x_j} - \beta \rho \omega^2 + \frac{\partial}{\partial x_j}\left[\left(\mu + \sigma_\omega \mu_t\right)\frac{\partial \omega}{\partial x_j}\right] + 2(1-F_1)\frac{\rho \sigma_{\omega 2}}{\omega}\frac{\partial k}{\partial x_j}\frac{\partial \omega}{\partial x_j} \tag{3.39}$$

$$\mu_t = \frac{\rho a_1 k}{max(a_1\omega, \Omega F_2)} \tag{3.40}$$

Here F_1 and F_2 are the blending functions which determine where the model operates as either $k-\epsilon$ ($F_1 = F_2 = 0$) away from the boundary or as $k-\omega$ ($F_1 = F_2 = 1$) near to the boundary. The nature of the blending functions helps to handle the numerical instabilities that can arise when switching between the models and their differing calculations of properties such as the turbulence eddy viscosity. In the CFD modelling of machining cases in this work, the $k-\omega$ SST RANS turbulence model is used due to its success in modelling near-wall turbulence features which are key in heat transfer applications (Menter & Esch, 2001).

3.5 Boundary conditions

Alongside a relevant geometry, good quality mesh and representative governing equations, carefully selected boundary conditions are required to set up the CFD models. The fluid model domain is shown in Figure 3.7. The view is through where the tool would be placed, with the workpiece behind the domain from this perspective. The domain is shown with tool and workpiece geometry in figure 3.3 for improved visualisation.

The domain is defined with an inlet boundary located within the coolant channel in the tool geometry, a wall boundary along both the tool and workpiece surfaces which correspond to the boundaries between the solid and fluid region meshes, and several regions which comprise the outlets of the model where the coolant and air flow out. The OpenFOAM boundary conditions applied at these boundaries are summarised in Table (3.1).

	Inlet	Outlet	Fluid-Tool/Workpiece
U	60 ms^{-1}	`inletOutlet`	`noSlip`
p	`zeroGradient`	1 atm	`zeroGradient`
α	1	`zeroGradient`	`zeroGradient`
k	5.4 Jkg^{-1}	`inletOutlet`	`wallFunction`
ω	700 s^{-1}	`zeroGradient`	`wallFunction`

Table 3.1: Boundary conditions applied to the CFD model of milling for parameters in the multi-phase fluid model.

The 60m/s velocity boundary condition applied at the inlet is of fixed value type and directed suitably along the coolant channel. The α variable representing the phase fraction of coolant is set to 1 at the inlet to model a 100% coolant volume fraction incoming flow into the domain that is initially filled with only air (α=0). The

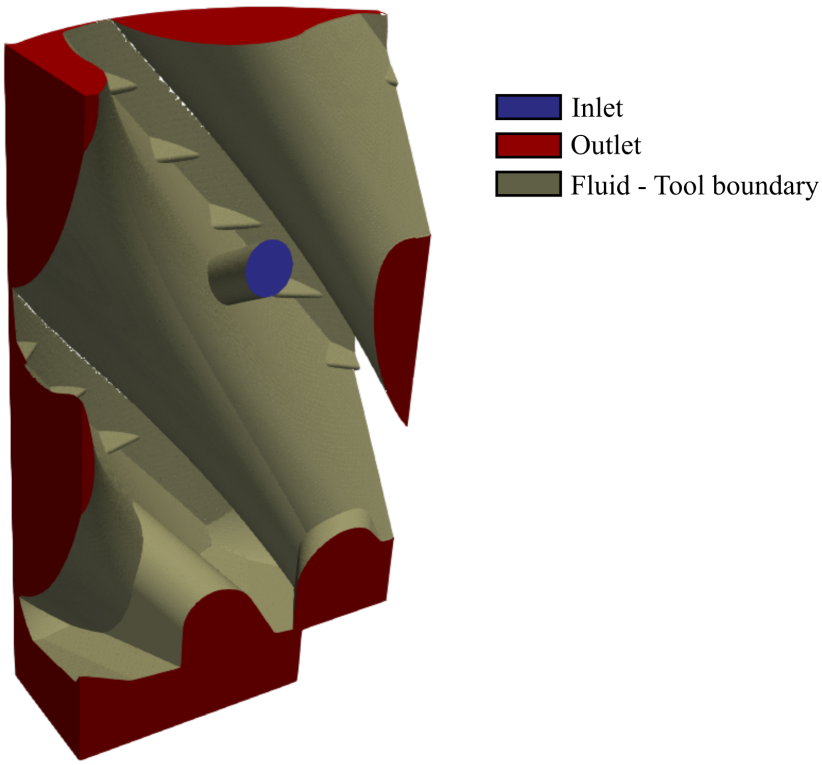

Figure 3.7: Fluid model domain, labelled with boundary regions, without tool or workpiece geometry since they obstruct the region boundaries.

`zeroGradient` Neumann condition with no flux added or removed at the boundary is applied in several places, including for pressure at the inlet, and is simply an extrapolation onto the boundary from the nearest cell so that no specific value is imposed, values are effectively inherited from calculated simulation output. Initial values for k and ω have been estimated at the inlet using the general relationships in equations (3.41 - 3.44) with turbulence intensity, I, over turbulent length scale, L.

$$I = 0.16Re^{-\frac{1}{8}} \tag{3.41}$$

$$k = 1.5(uI)^2 \tag{3.42}$$

$$\epsilon = C_{\mu}^{\frac{3}{4}} k^{\frac{3}{2}} L^{-1} \tag{3.43}$$

$$\omega = k^{\frac{1}{2}} L^{-1} \tag{3.44}$$

The `noSlip` boundary condition used along walls describes a fixed zero velocity condition. As the tool rotates, these walls actually move relative to the tool at a fixed speed depending on the spindle speed of the machining operation. For the current tool geometry with a diameter of 16 mm, and a cutting speed, v_c, of 90m/min this results in

a speed of 1.5 m/s of the workpiece surface, which has been neglected due it being small in comparison with the large coolant application velocity of 60 m/s. If a significantly higher cutting speed or smaller tool geometry were used then it would be beneficial to include this as a fixed velocity boundary representative of the cutting parameters used. The `inletOutlet` condition applied at the outlets stipulates a `zeroGradient` boundary condition for all outward flow however constrains any inflow back into the domain, with the condition transforming into a `fixedValue` of 0m/s in the case of inflow here. A constant atmospheric pressure condition is applied at the outlet. Along the tool and workpiece walls there are wall functions applied for the k and ω boundaries and the blending option has been implemented which smoothly blends the wall modelling between the viscous sub-layer and log layer above depending on $y+$ value. This allows for a transition from applying wall functions at larger values of $y+$, to resolving the turbulence for lower values, since a variation was observed here due to the two phases present with varying flow properties and the complexity of the near wall refinement in the mesh.

Thermal boundary conditions are introduced into the conjugate heat transfer simulations, where the boundaries between regions are coupled to match the temperatures and heat flux across all solids and fluids of interest. All domain edge solid boundaries and the fluid outlets are given `zeroGradient` conditions and the coolant inlet temperature is taken as 293K.

The high machining temperatures are incorporated into the CFD model by setting a small region of the cutting tool, at the cutting edge, to a fixed high temperature of 773K, which is an estimate for a cutting temperature of milling titanium alloys, though this is very variable over cutting conditions (Kikuchi, 2009).

3.6 CFD Methodology Summary

To summarise the approach for the CFD methodology here when modelling the coolant flow and heat transfer in machining, the key stages are shown in a flow chart in Figure 3.8.

The CAD geometries for both tool and workpiece are used to construct realistic and accurate machining fluid and solid domain regions and meshes. Once all meshes have been generated and separated, the fluid mesh is used to run a multiphase VoF model to track the liquid - air interface as the coolant is applied from the tool's internal channels towards the cutting edge where the tool and workpiece meet. This simulation is run in a transient configuration for a real time duration of 0.001 seconds. This time is long enough for the coolant flow to reach the required region and stabilise. The simulated flow in the fluid region is not truly steady state as it includes elements of

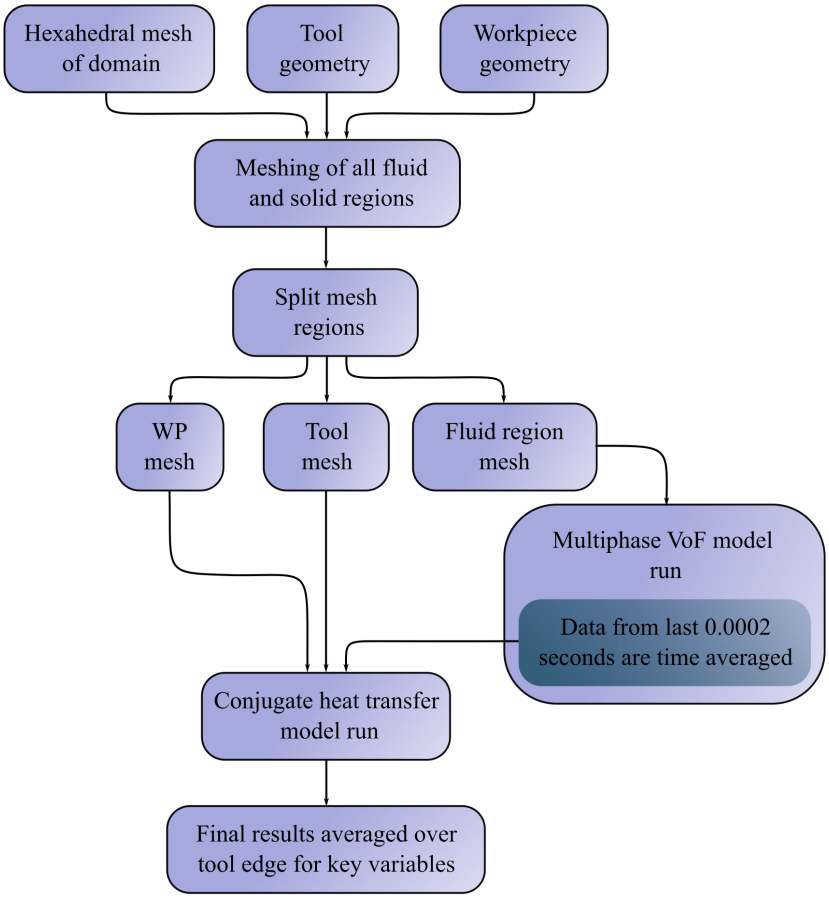

Figure 3.8: Flow chart for CFD methodology.

splashing and transient features. In a realistic application, the cutting edge would also not be engaged throughout the full rotation either. In order to assess the heat transfer under average conditions while the cutting edge is fully engaged, the flow fields are time averaged over the last 0.0002 seconds of the simulation results to create a time averaged data set for the fluid domain. Averaging over this length of time was determined to give a representative mean value of the developed flow field, including the region which experiences the regular, consistent supply of coolant, and that which can be covered with occasional splashing coverage. The results of this time averaged flow field are then substituted into the conjugate heat transfer model as a fixed flow field, with the multi region thermal model subsequently solved for all fluid and solid regions.

The conjugate heat transfer model is run to a steady state convergence, with the recording of temperatures in the tool from probe data and monitoring of the CFD solution residuals used to manage the process. Results from the heat transfer model are then post-processed to extract the results of key variables along the cutting edge which is the critical region for machining.

3.7 Machining model CFD results

3.7.1 Observations of coolant flow behaviours and effects

Observing the coolant distribution along tool and workpiece surfaces is incredibly difficult in real machining settings due to the difficulty in gathering visual experimental data of the high temperature, highly loaded cutting region and inherently obstructing machining parts. A key output of these simulations is to be able to visually inspect the coolant behaviours and distribution. The results in the fluid domain cover both the coolant and air phases. By filtering these results to show only cells with a value of α greater than 0.5 we can obtain a good visualisation of the interface between the phases and the coolant distribution onto the workpiece from the tool channels.
The nature of the application and geometry being used in these simulations means that any visualisation of the area of interest along the cutting zone is highly obstructed by both the tool and workpiece in the simulations as well as in the experiments, as can be seen in Figure 3.9. Although the tool and workpiece obstruct the view somewhat they are often needed to provide some context to the results and coolant flow. In Figure 3.9, the view is directed along the cutting edge as it engages with the workpiece. The coolant jet can then be seen impacting on the workpiece surface, very close to the tool edge. Following this impact, coolant can be seen to spread across both tool and workpiece surfaces and creates some splashing effect as the small amounts of coolant become separated from the bulk flow.

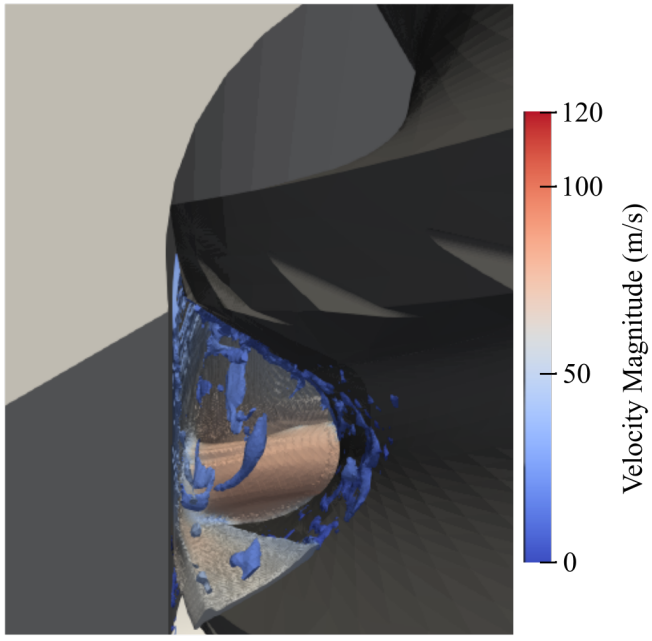

Figure 3.9: Results of the fluid region multiphase model showing the coolant impinging jet along cutting zone. Simulation results have been filtered to show only mesh elements containing $> 50\%$ coolant to allow visualisation of the coolant distribution.

For a simplified view of the coolant behaviour, a 2D slice is presented in Figure 3.10 which gives a clearer visualisation of the domain while still including the tool and workpiece geometries for context. The velocity of the coolant is plotted as a contour, so that the structure of the jet can be seen and a clear stagnation region is observed as it impinges on the workpiece. The machining case here is very 3D in nature so although these thin cross sections of results can be useful to attain an initial understanding of the flow, they can be misleading if used to investigate details such as impingement proximity to the cutting edge.

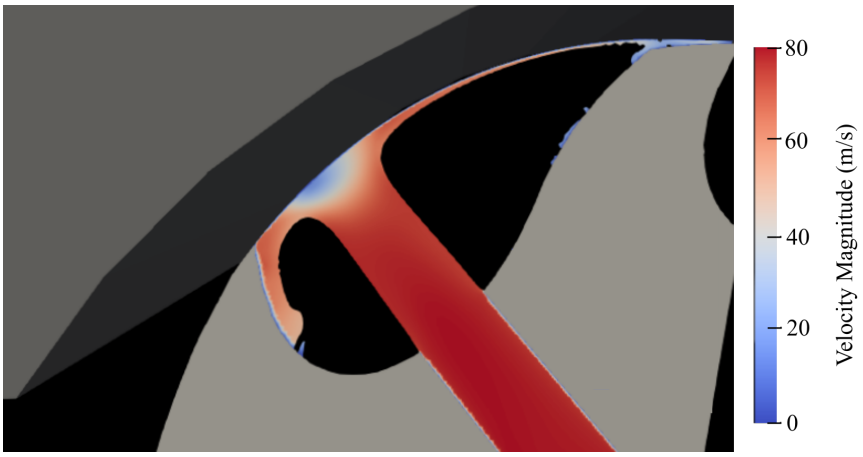

Figure 3.10: Coolant velocity magnitude results shown in 2D as a slice angled to match the coolant jet trajectory. Tool and workpiece geometries are included for context, with all surroundings in black.

3D images of the domain, viewed through either the tool or workpiece positions, provide the most insight into the coolant distribution. Figure 3.11, with the tool geometry not shown, allows a clear view of the fluid domain. The coolant impacts the workpiece, just above the cutting edge, closer than Figure 3.10 would have indicated, emphasising the importance of considering the results in 3D. The coolant coverage across the length of the lower cutting edge can be observed. The coolant can also be seen to reach and well cover the cutting zone above the impingement.
The Sandvik end milling tool used in the modelling work includes a cooling booster feature along the flank face of the tool in the form of small flow grooves which can be seen in the geometry (Figure 3.1) and from closer up in Figure 3.9. Here, in Figure 3.11, the flow can be seen to cover the surfaces of these coolant grooves at the higher cutting edge above the coolant application. Designed to increase the removal of heat from the cutting edge, these coolant grooves significantly increase maximum contact surface area for the coolant to encounter at the cutting edge.

The flow around a cooling booster groove is inspected using glyph vectors, coloured and sized according to flow rate in the vicinity of a groove in Figure 3.12. This view, from the workpiece position and with the tool geometry included for context shows that the flow has aligned with the direction of the groove and is flowing generally

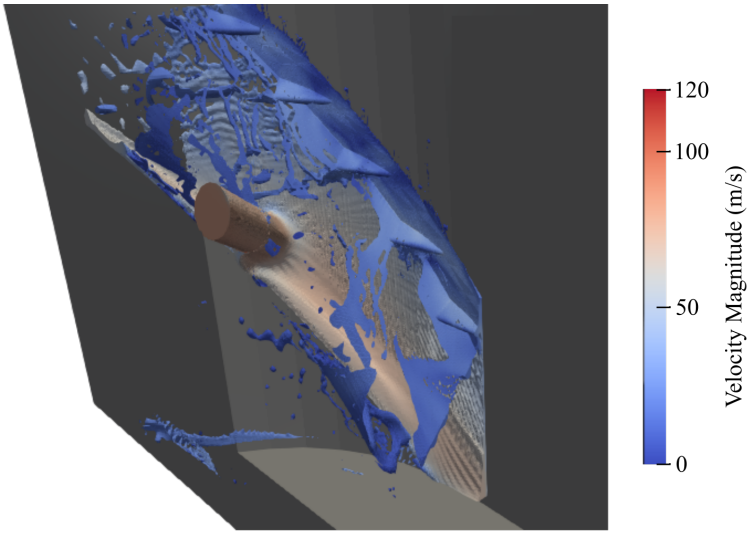

Figure 3.11: Coolant coverage in the fluid domain, shown by filtering CFD results to display elements with $\alpha > 0.5$, and coloured according to velocity. Tool geometry is omitted for improved visualisation here.

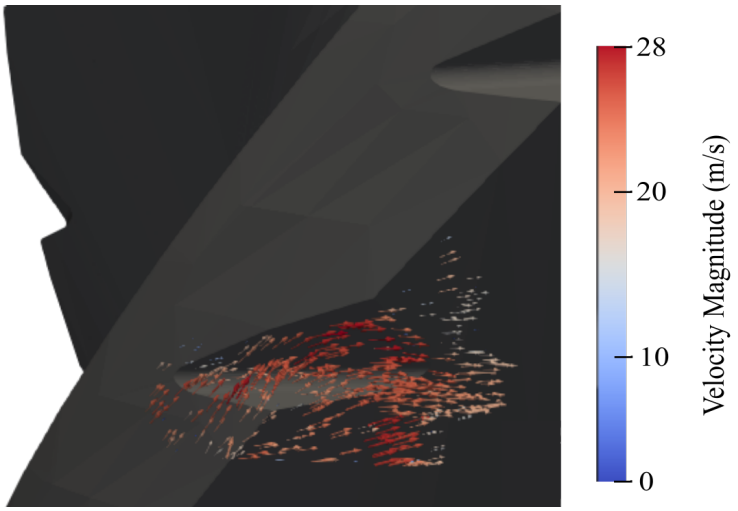

Figure 3.12: Glyph vectors showing flow near to cooling booster features of the tool geometry. Vectors are coloured and scaled according to the velocity magnitude.

down the groove away from the cutting edge. This is due to the fast flowing impinging jet forcing coolant flow across the workpiece surface and upwards to the higher cutting edge where it encounters a region of high pressure and the flow is redirected back along the tool surface and through the cooling grooves. The results show a moderate flow rate of over 20m/s is observed through the groove and these speeds along with the high surface area and good wetting in the region could help explain the effectiveness of these grooves in improved temperature management found when employed in high feed milling situations.

Other features of the coolant application and flow include a stagnation region,

observed where the jet impinges on the workpiece. Figure 3.13 (a) which captures the coolant velocity just above the workpiece surface shows the region clearly, just above the lower cutting edge and extending down to make contact with the cutting edge. A similar view with glyph vectors applied in Figure 3.13 (b) shows the region of low flow magnitude and also the higher magnitude flow around it. The highest speed flow is directed straight down the cutting edge, which is beneficial for cooling in the region, likely due to the vertical angle of the impinging jet and coolant channel which provides significant downward momentum to the coolant as it is applied.

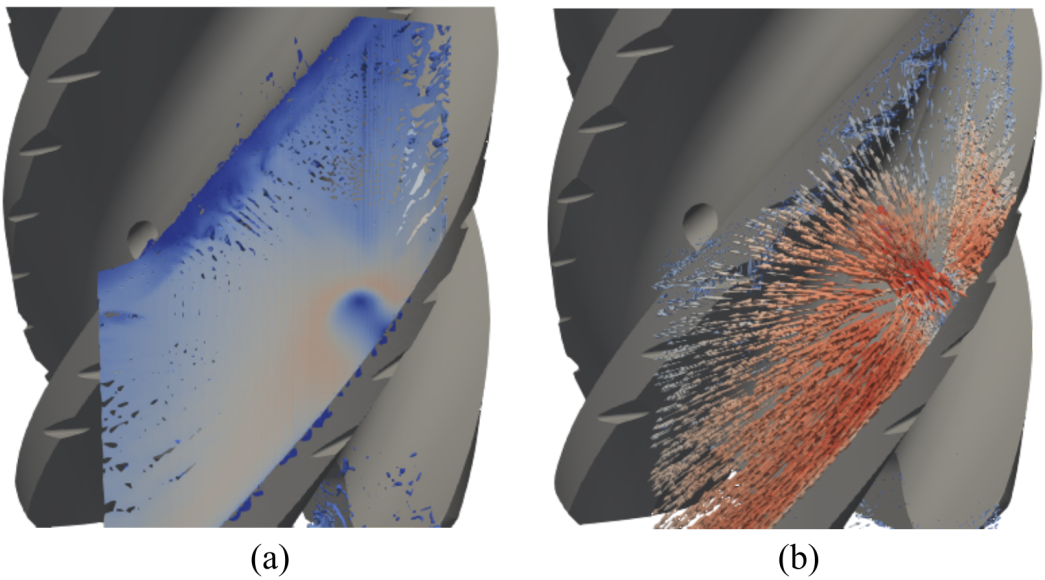

Figure 3.13: Impingement and stagnation region seen from workpiece perspective (a) Velocity field in the coolant (b) Glyph vectors, coloured according to velocity magnitude.

Tool temperatures from the final steady state results show effective cooling of the tool region near to the cutting edge. Contour temperature lines along the tool have been applied. Figure 3.14 (a) and (b) present the results with a focus on the rake and flank sides of the cutting edge respectively. The area where the coolant has been applied between the two cutting edges investigated shows much improved cooling to those regions not cooled. Across both cases the maximum temperatures is still very high due to the fixed temperature hot boundary condition. The effective cooling of the rake face near to the lower cutting edge then indicates a very steep temperature gradient in this region with the contour lines close together.

3.7.2 Quantitative output along the tool cutting edge

In addition to the visual inspection and interpretation of the simulation, results need to be quantified to gain more information and enable comparisons between different

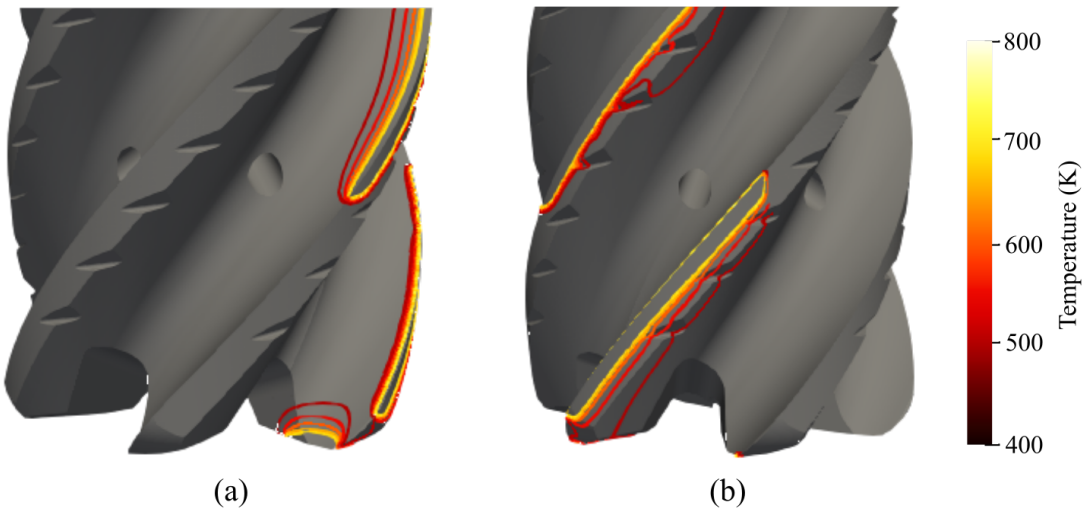

Figure 3.14: Tool temperature contours for two views, focusing on (a) rake face and (b) flank face. The two edges surround the flute which is modelled with coolant application, and the temperatures are reduced on the rake and flank in this flute.

geometries and cutting parameters. The results of primary interest are the wetting of the tool near to the cutting edge, the velocity of the coolant in the chip forming region and the temperatures of the tool. These aspects have been chosen since the wetting analysis can provide insight into how well the coolant is being distributed and lubricating the area near to the cutting edge, the velocity of coolant in this region is used to predict the successful removal of chips from the area and the temperatures in the tool can help to understand the levels of thermal wear experienced and predict the formation of chips.

Post processing and analysis of results is needed in areas near to the cutting zone. To enable easy extraction of the relevant cells, the rake face has been isolated on the tool geometry and is used in conjunction with the workpiece to identify the mesh elements required. Mesh elements within 0.1 mm of the cutting edge are sampled to record the fluid velocity, U, and wetting, α, values which are then averaged over the area. For tool temperatures a similar process is used to extract cells inside the tool region within 3mm of the workpiece. The numerical results from the standard tool model are included in Table 3.2. This output supports the observations made, based on visualisation output, that the coolant coverage is already excellent along the cutting edge, with an average coolant volume fraction of 97.8%.

Output	Result
Wetting, α	97.8%
Vertical coolant speed, u_z	-12.7 m/s
Tool temperature, T	626.9K

Table 3.2: Quantitative results output for key variables along the cutting edge.

3.8 Model validation

Part of the motivation for developing CFD techniques for machining processes is due to the difficulty in carrying out experiments in the hostile environment near to the cutting region, where the extreme temperatures and forces are at their peak. This difficulty extends to validation of the CFD work due to the absence of extensive experimental data.

The VoF fluid solver `interFoam` has been extensively validated for a range of applications (Deshpande et al., 2012) for both inertia and surface tension dominated flows. A further qualitative validation was carried out by Johns et al. (2018) for a twist-drilling machining application in particular, which remains relevant for this work since the Reynolds numbers of the coolant flow of between 40,000 and 80,000 are the same in drilling as the milling work studied here. Using a specialised polymer coating on a drilling tool, Johns et al. was able to compare the wetting results for experimental and numerical tests and observed that the regions with predicted high levels of wetting in the simulations corresponded well to the regions where the polymer had been washed away in the experiments.

Validating the temperatures predicted in the tool is difficult so the model and implementation has been validated through other methods. Firstly the implementation of the new conjugate heat transfer solver, `chtInterFoam`, was tested to verify that it reads in correct thermophysical properties for either water or air depending on indicator function α. Channel flow cases with a single fluid present (water/air) were modelled by applying either $\alpha = 1, 0$ throughout the domain in the new solver. These results exhibited a near exact match when compared to the already available conjugate heat transfer solver in OpenFOAM, `chtMultiRegionFoam`, which is suitable for single phase flow applications, providing confidence in the implementation and numerical solution.

To further validate the model, the full solution approach incorporating both the multiphase and conjugate heat transfer components has been bench-marked against a commercial solver, ANSYS Fluent, for a simplified cooling jet case. Further to this, the `chtInterFoam` solver has been compared to experimental cooling data in another case with simplified geometries from the literature. At the full complexity of the machining case a mesh independence study has been carried out to ensure independence of the machining simulation outputs from grid sizings.

3.8.1 Benchmarking with alternative software

There are several benefits in comparing simulation results between various software. Comparing a new solver against well established and widely used code allows confid-

ence in the implementation and model used. Benchmarking open-source codes such as OpenFOAM against commercial software can also be important when deciding which tool to use.

When comparing between the two softwares here the primary focus is on the temperature predictions across the domain. Other elements such as the multiphase and turbulence modelling approaches have been investigated in other work and have been widely reviewed and evaluated in the literature Deshpande (2014), Jasak (2009), Singh et al. (2020). A simplified test case of a water jet impinging onto a heated plate is used to compare the two softwares. The 2D geometry used, shown in Figure 3.15, includes both a solid and fluid region. Although this test case is highly simplified when compared to the full machining case setup it has much in common in terms of the underlying physics and is primarily used to verify the model implementation here. Although the geometries are complex when working with machining tools, at the most fundamental level we are applying an impinging water jet onto a heated surface. The model has therefore been benchmarked here to verify these fundamental aspects.

The solid component is taken to be aluminium and is heated from below with a fixed temperature boundary condition of 270K. The fluid region is initially filled with air and an inlet boundary defined at the top of the domain on the left introduces a high speed (20m/s) water jet at a fixed temperature of 250K.

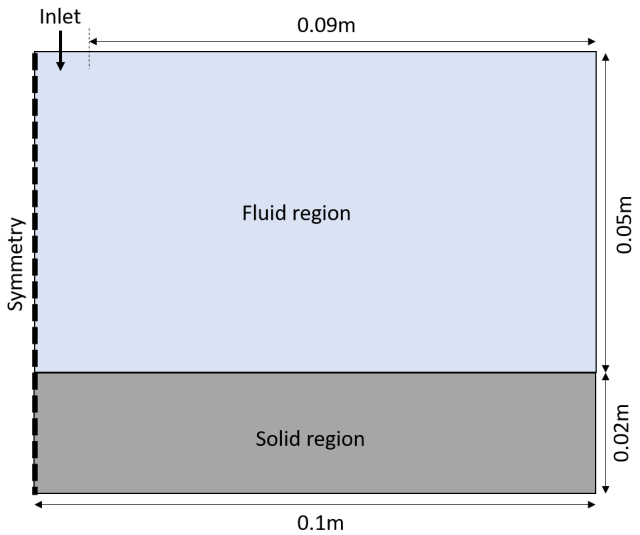

Figure 3.15: Multi-region geometry for a simplified benchmarking test case. A solid and fluid rectangular region are created.

A symmetry plane at the centre of the jet is used to reduce the computational complexity of the simulation. Outlet boundary conditions on the right hand side allow the out flow of fluid (both water and air) and manage the properties of any inflow along

the boundary. Any flow back into the domain via either the top boundary or outlet on the right hand side enters the domain with ambient temperature to match the initial conditions at 260K.

To maintain consistency in mesh quality and refinement between both softwares being compared, the same mesh is used in both. Generated in ANSYS mesher, a mesh of 55250 elements is used with refinement near to both the fluid-solid region boundary and the symmetry boundary where much of the higher speed liquid flow is expected.

In OpenFOAM the solution process is applied in two stages, for firstly the multi-phase fluid model and secondly the multi-region conjugate heat transfer model, as described in previous sections 3.3.1 and 3.3.2. In Fluent, these physical models are coupled. This creates a small difference in the modelling, since buoyancy will now be incorporated into the Fluent simulation as a result of including the gravity which is necessary for the multiphase VoF component. Other differences can be expected in the modelling and numerics between the two solvers. Where possible, similar finite volume schemes and solvers have been selected but it is difficult to completely eliminate differences. The flow in these test cases is highly turbulent and the $k-\omega$ SST model has been applied. This may also cause minor differences to arise in the cases since in Fluent any near wall treatment is applied internally and automatically depending on simulation conditions whereas in OpenFOAM each boundary condition must be set explicitly to determine this approach to the modelling at the walls.

To compare results from the two softwares a series of temperature profiles are sampled vertically along the domain from the fixed temperature heated wall at the base of the solid up to the atmospheric condition at the top. One of these profiles, shown in figure 3.16, shows the well matched profiles along the height of the domain given by both softwares. Each has a temperature of 270K at $H = 0$ on the heated wall. The temperature then shows a smooth, steep decrease across the solid region down to the lower temperature at the wall where solid and fluid regions meet. Here Fluent predicts a slightly higher wall temperature of 252.8K whereas OpenFOAM gives a lower prediction of 251.6K. The discrepancy at the fluid-solid boundary could be due to the small differences in near-wall turbulence discussed previously or in different implementations of heat transfer between multiple regions in conjugate heat transfer simulations, however, as the difference is only small, there is still reasonable agreement between the OpenFOAM and Fluent simulations.

Increasing the height along the temperature profile, the temperature decreases rapidly to 250K in both cases as we move through the water flow over the solid plate. The bulk of the water flow is at 250K which is the same as the inlet value, with only small increases near to the wall and air interfaces. In the fluid region there is very good

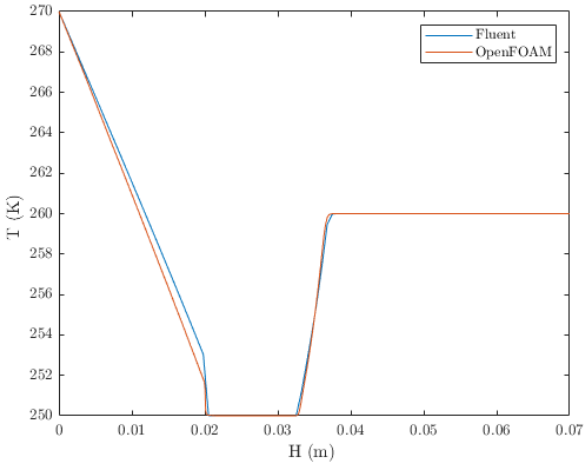

Figure 3.16: Temperature profiles from Fluent and OpenFOAM benchmarking simulations over the height, H, of the multi-region geometry, at x=0.02m from jet centre line.

agreement between Fluent and OpenFOAM, across both the water flow, ambient air and the interface between. The profile shows a gradual increase in temperature just above the air-water interface which is found along this profile at $H = 0.032$m. In this region the air near to the jet flow has been slightly cooled. Moving further up through the domain, the temperature reaches the ambient condition of 260K and remains there throughout the rest of the profile.

A collection of these samples taken across the domain show high levels of consistency and a good similarity in the results. These are shown in Figure 3.17 where they are overlaid onto the test case geometry with the resulting water-air interface, as recorded in Fluent for context. The temperature results have been normalised to scale well into the diagram using the inlet temperature T_{in}=250K.

The comparison between OpenFOAM and Fluent shows very good agreement on temperature throughout the fluid region of the simulations. This was the particular region of interest in this benchmark case, as the model being tested introduced the multiphase aspect into the fluid region in OpenFOAM. Observing the excellent match across both the water and air, as well as over the interface, provides great confidence in applying this model further to the machining applications.

3.8.2 Validation of the model against experimental data

The model has also been validated against experimental results. Validating the `chtInterFoam` solver against a machining case is relatively difficult due to the complexity of the geometries and the difficulty in obtaining relevant experimental data. A reasonable alternative is to identify experiments for simpler systems which retain many of the physical

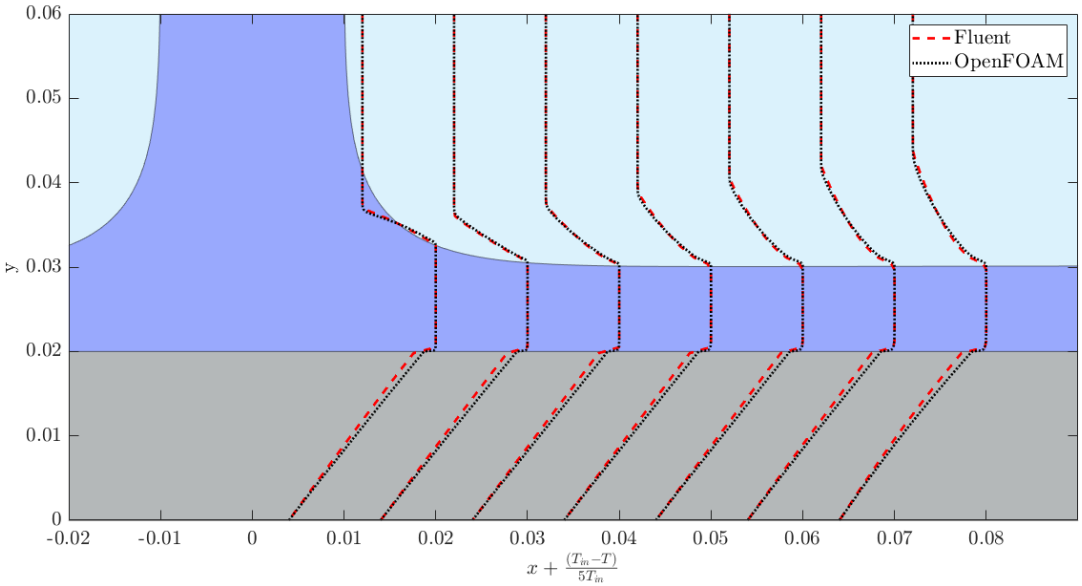

Figure 3.17: Fluent and OpenFOAM benchmarking simulations temperature profiles across the domain, scaled with inlet temperature T_{in} and distance from the jet centreline, x, to put results in visual context.

characteristics. The case of cooling using impinging jets was identified as a good representation of the machining coolant process when comparing with alternative software. The `chtInterFoam` solver is here tested using experimental data from the literature (Dou et al., 2014) for an impinging water jet onto a metal block with embedded thermocouples. The metal block is initially heated up to a temperature of 1200K before being cooled by the impinging water jet in a transient process.

A geometry is set up to replicate that used by Dou et al. (2014). The configuration is very similar to the previous test case (Fig 3.15) and is comprised of two blocks, a solid region and fluid region with a symmetry plane at the centre line of the jet to reduce computational expense. In the previous case, a planar 2D approach was taken when comparing between the softwares. In this case, an axisymmetric approach is used instead to better represent the circular impinging jet. In OpenFOAM a wedge boundary condition designed for these axisymmetric cases is used with the axis taken as the centre line of the jet. An inlet boundary is defined at the top of the domain with the neighbouring boundaries in the fluid domain used as atmospheric boundaries. At the inlet, the water volume fraction α is set to 1 since the incoming flow is pure water, whereas the surrounding domain is initialised with only air present, $\alpha = 0$. The inlet is given a velocity boundary condition of 18.4m/s while the outlet conditions are provided with a `zeroGradient` boundary condition, allowing fluid to both leave and enter the domain as required. Surrounding air will be entrained into the jet as it develops and so it is important that fluid be allowed to enter through the top boundary and

leave with the jet as it flows along the plate and out of the domain to best represent the most natural flow structures. The boundary between the solid and fluid regions is coupled using a `compressible::turbulentTemperatureRadCoupledMixed` boundary condition, which is used in OpenFOAM to couple the temperatures and heat fluxes across two regions for conjugate heat transfer simulations.

Visualisations of the flow in Figures 3.18 (a) and (b) show the high speed, highly turbulent water jet impinging onto the hot plate. In both figures there is a clear stagnation region as the jet impinges, a feature which was also observed in the full machining cases and one which can have a significant impact on heat transfer.

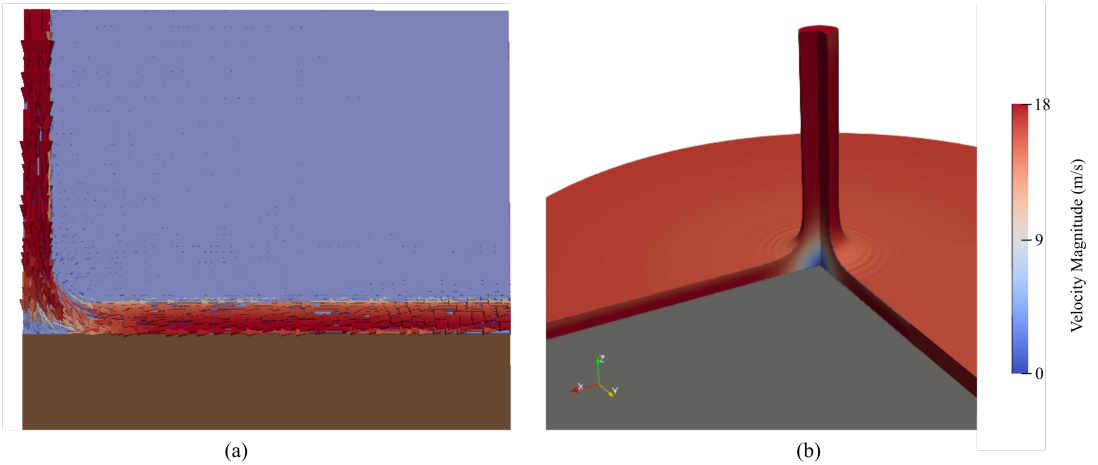

Figure 3.18: Underlying flow for impinging jet in Dou et al. (2014) validation case, shown for the simulation domain (a), and extended to a 3D representation of the axisymmetric case (b).

The fluid flow of the jet is in the turbulent regime with a Reynolds number of 4.1×10^5. Several RANS turbulence models were tested here including the $k-\epsilon$, $k-\epsilon$ Realisable and $k-\omega$SST. Initially the $k-\epsilon$ Realisable model was chosen due to its suitability for turbulent jets and efficiency however when this model was utilised here to predict the coolant flow, the conjugate heat transfer simulations that followed predicted the test block was cooling much faster in the OpenFOAM simulations than in the experimental results of Dou et al. (2014), as seen in Figure 3.19.

It has been reported in the literature (Singh & Doom, 2017) that the $k-\epsilon$ turbulence models can over-predict the turbulent energy in the stagnation region for impinging jets which has in turn led to predictions of increased heat transfer and would explain the faster than expected cooling of the test block initially observed here. To rectify this, other turbulence models were tested, with the $k-\omega$SST model performing best and showing very good agreement with experimental results (Fig 3.19).

In the experimental study, Dou et al. (2014) monitored temperature across

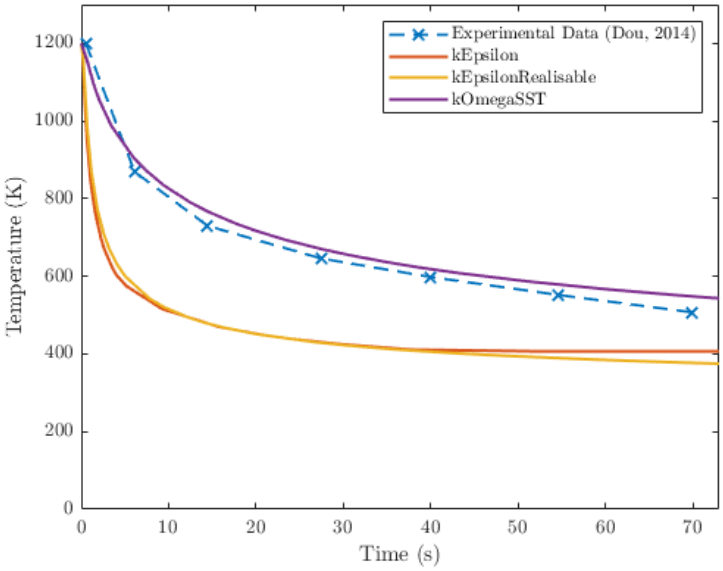

Figure 3.19: Comparing cooling curves using various turbulence models to experimental results from the literature Dou et al. (2014).

multiple points in the solid test block and the locations of the probes are shown in Figure 3.20.

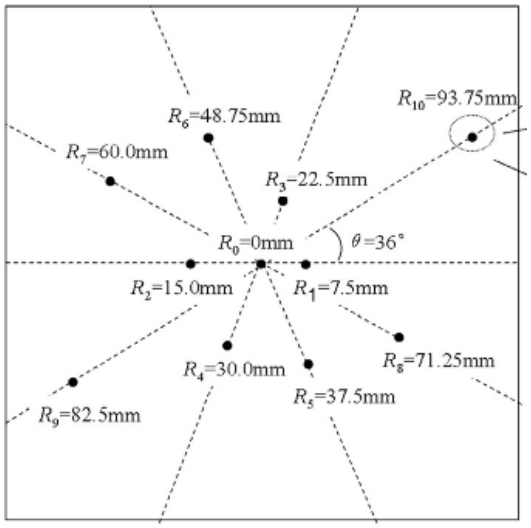

Figure 3.20: Thermocouple locations used by Dou et al. (2014), with radial distances to the centre of the test block labelled. Reprinted from Applied Thermal Engineering, Vol 62, Dou R., Wen Z., Zhou G., Liu X., Feng X., Experimental study on heat-transfer characteristics of circular water jet impinging on high-temperature stainless steel plate, Pages No. 738, Copyright (2014), with permission from Elsevier.

One notable difference found between the experimental results from the literature and the CFD cases in this study was that the probes showed a very uniform cooling down across the width of the block when using the $k-\omega$SST and other turbu-

lence models which has led to only small differences across test sites in the simulations with the cooling curves for probes 1 and 6 only exhibiting $\approx 1^oC$ difference. For the corresponding thermocouples in the experiment there were variations observed across the block, as can be seen in Figure 3.21.

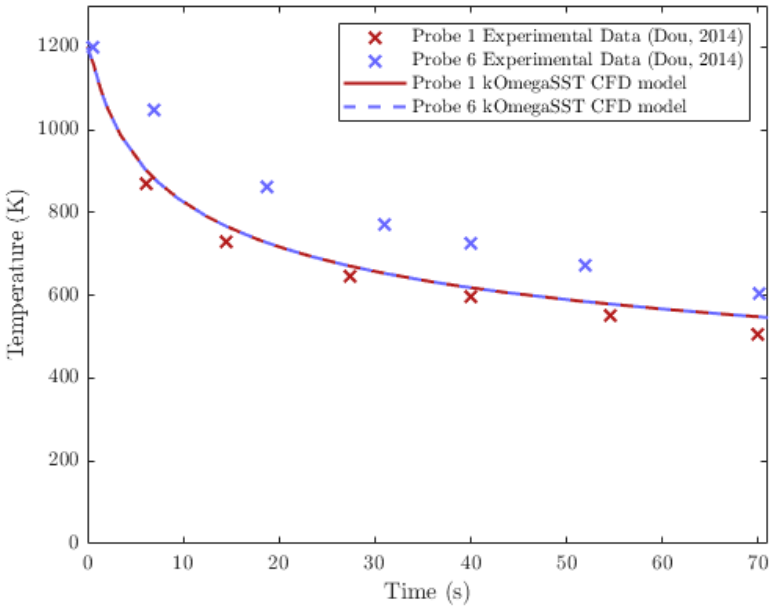

Figure 3.21: Comparison of CFD model results and experimental data (Dou et al., 2014) for probes in locations one and six.

The cooling curves experimental data did not necessarily follow a trend that would be expected such as a reduced cooling rate as distance from the jet centre increased. Thermocouples in positions 1,3 and 4 gave very similar readings to each other across the experiment of Dou and these values were well predicted by the $k-\omega$SST model here. There was less agreement between the CFD and experimental data for thermocouples in positions 0,2,5 and 6. Table 3.3 with Figure 3.20 shows the average error at t=40 for these values predicted compared to experimental results and there does not look to be an obvious pattern or trend in the error locations. One possible explanation for this is that there are perhaps some 3D effects not being captured properly by the 2D OpenFOAM geometry used here or that there was some feature in the experiments that affected only certain thermocouples. In fact, thermocouples 7, 8 and 9 were removed from experimental results by Dou et al. due to them breaking. Based on the good correspondance with a selection of thermocouples places over the block, reasonable agreement has been managed for the `chtInterFoam` solver.

The turbulence model used for the machining simulations is the $k-\omega$SST since this proved superior for validating the temperature fields and heat fluxes for impinging jet style simulations in this validation case.

probe	R0	R1	R2	R3	R4	R5	R6
% error	28	0.5	25	0.8	0.8	22	15

Table 3.3: Errors for each probe location for simulation compared to experiments.

3.8.3 Mesh sensitivity study

At the full scale machining simulation level, a mesh sensitivity study has been carried out to ensure independence of the simulation output from parameters such as cell sizings and number of cells. Carrying out this study also allows for progression with the lowest reasonable number of cells for any large scale geometry exploration requiring many simulations. The computational cost can be greatly reduced by managing mesh element numbers effectively which is highly desirable, especially in industrial applications where a quick turn around for CFD simulations is of great importance.

For this study, two key outputs of the machining simulations are investigated: the wetting of the tool edge in the fluid domain, and the temperature of the tool near to the cutting edge. These parameters, described previously in section 3.7.2 are compared for a series of meshes of varying levels of refinement. The meshes have been refined as underlying block meshes at the beginning of the automated process. The further surface refinement is scaled accordingly with this as part of the meshing process. Final meshes for the domain range here from just under 500,000 cells to 17.5 million elements.

The results for wetting near to the tool edge, shown on the left in Figure 3.22, indicate no strong dependence on grid sizing for most of the wetting results here. Since this is a fluid volume fraction integrated over an area and a very large scale feature this is reasonable. Only small variations are seen across most of the meshes tested in this study - with a 1.2% difference between all results.

Tool temperature had a more obvious dependence on the grid sizing up to a point, as seen on the right in Figure 3.22. Where the results for wetting appear very consistent across the meshes used, the tool temperature exhibits a convergence like behaviour, with very coarse meshing showcasing low tool temperatures which are increased as the number of mesh elements is increased. The heat transfer is highly dependent on small flow features near to the tool and workpiece walls as these have a key impact on turbulent heat transfer. To conclude the study, the mesh sizing of 14.5 million cells is taken as suitable to progress with for further work investigating geometries. The mesh refinements chosen are highlighted on the Figure with a red marker. Increasing the number of elements to 16.5 million results in a temperature change of less than 1 degree from the chosen mesh density.

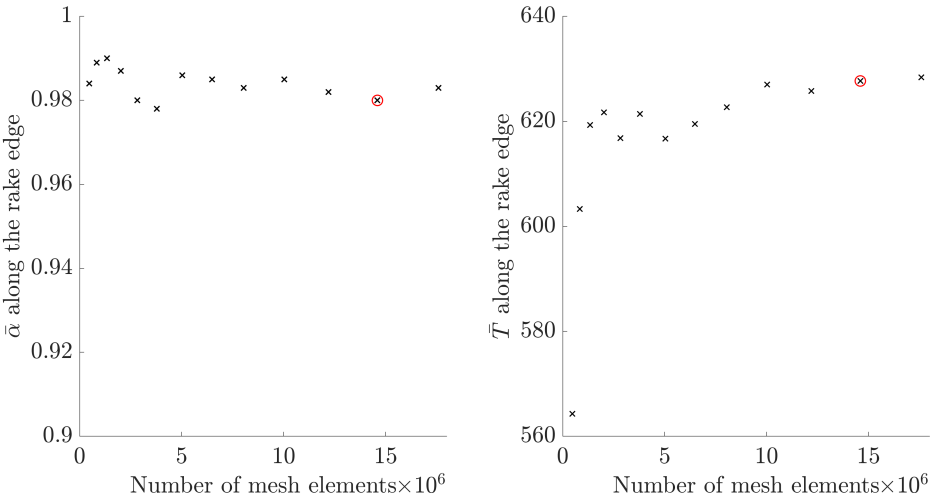

Figure 3.22: Left: Wetting results for mesh sensitivity study. Right: Tool temperature results for mesh sensitivity study.

3.9 Conclusions of the chapter

A new solver, `chtInterFoam`, has been implemented in OpenFOAM which combines a multiphase capability into the standard conjugate heat transfer solver available. The solver can be used to combine the a multiphase volume of fluid method with a multi-region heat transfer simulation using a one-way coupling method.

This model has been used to investigate the coolant flow and temperature profiles in a milling machining case. The visual output provides great insight into the behaviours of coolants in machining which are very difficult to observe in practice due to the obstruction of the cutting environment by the tool, workpiece and chip geometries. The coverage of the coolant and interaction with various features on the cutting tool has not been previously identified and the visual results presented here can be used by tool designers to better observe the coolant flow behaviour and inform any tool design improvements. The coolant flow spreading out over the workpiece was shown to interact and cover both the rake edge and flank edge, indicating that the current tool design provides lubrication to both regions. The combination of the visualisations presented and the quantitative results extracted at the rake cutting edge confirm that this Sandvik tool model has excellent coolant coverage at the cutting edge where the lubrication is most required. The impact location of the jet can be identified in the simulation results and could be of interest in further work on chip formation and breaking and local thermal wear.

The OpenFOAM model implementation has been compared to an equivalent physical configuration in the commercial CFD software ANSYS Fluent for a simplified impinging jet case, which incorporates many of the physical features seen in machining,

and has successfully been benchmarked against this code. Further validation has been carried out using experimental results for an impinging water jet from the literature to assess the suitability of the model in these applications. Although there was more variation in temperature across the test block observed in the experimental data from Dou et al. (2014) than was predicted by the CFD model a very good agreement was seen between the new model and the experiments in several thermocouple locations and we can now move forward with the validated model for further investigations of machining configurations.

In further work, the modelling of the coolant distribution and heat transfer could be extended to include the rotation of the tool for this intermittent cutting operation. A short study presented here on the importance of the rotational position of the tool provided valuable insight into the impacts of rotation and showed this would be very important to include if looking at the intermittent features of milling in more detail. It was shown that the cutting edge receives no coolant during the rotation while the impingement region of the cutting edge is not actively cutting.

The new solver will next be used to test a variety of new tool designs for milling applications to find an optimised tool design.

Chapter 4

Coolant Channel Analysis

Contents

4.1 Introduction

In chapter 3, modelling of coolant flow for a standard milling tool was introduced. In this chapter, the model is applied to investigate optimal tool designs using surrogate modelling and optimisation techniques. Firstly, the surrogate modelling and optimisation approaches are introduced; this describes the generation of a Design of Experiment (DOE) sample plan, the use of radial basis functions to interpolate response surfaces over the design space and different validation methods for these models. Next, variables of interest are identified from both a tool design and machining parameter space and their potential impacts are discussed. Finally, two DOE cases are explored and analysed to identify potential new, optimal designs for the key objectives of maximised coolant distribution and minimised tool temperatures.

4.2 Theory

When working towards designing an improved process or product — such as a new machining tool — the entire design space would ideally be considered and evaluated to observe which design could provide the best outputs.
In reality, it is rarely feasible to test the outputs over the full design space. There are usually some limitations which prevent this practice — these are often time and money related. In an experimental setting, testing for a new tool design could mean prototyping the tool for each design of interest and then testing for the desired results. This practice is very time consuming and labour and resource intensive, as well as expensive. Using a CFD approach, there is still an element of manual interaction time costs since each geometry needs to be generated, but the main limitation is computational resources. Each simulation in this case can take around 1,200-2,000 CPU hours to complete which limits the number of CFD simulations which can be run.

Given the limitations here which prohibit the investigation of the whole design space, a measured approach must be taken. A manageable, fixed number of data points can be sampled and this information and output is then interpreted to build up a clear picture of the whole design space.

4.2.1 Creating Design of Experiments (DoE) points - latin hypercube

To get the most information about the design space from a set number of points, a good sampling plan is needed. Techniques used for selecting the best data points to test are often referred to as experimental design, or design of experiments (DOE) techniques. There are many DOE techniques available, suiting various needs and with different levels of complexity (Cavazzuti, 2013). Here the latin-hypercube method is used. For this method, the design space is divided up in to N^n blocks or subgrids for the number of sample points needed, N, and the number of design variables, n. These blocks grid the entire design space and along each orthogonal axis, blocks are chosen so that only one sub volume is used, as can be seen in an example (Fig ??). A random sample is chosen from each selected block to carry out the experiment or simulation.

When identifying the subgrid regions to use in the LH, technically, a selection of only diagonal subgrids would meet requirements of one selection per row/column. However, it is clear that the majority of the design space would remain unexplored in this configuration due to the high correlation of the subgrid choices. In addition to fulfilling the minimum requirement of achieving only one selection per row/column, usually a space-filling algorithm is employed to ensure the selected subgrids are spread out in the domain and reduce correlations.

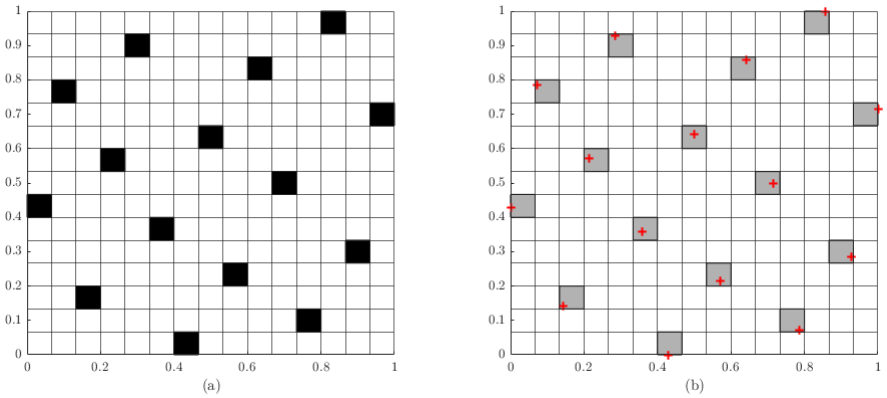

[Latin hypercube subgrid and sample points schematic](a) Latin hypercube subgrids for $N = 15, n = 2$, (b) Sample points within the latin hypercube subgrids.

These methods are often evaluated using a 'space-filling' metric which considers the distances, d, between all pairs of points in the sample plan (Johnson et al., 1990).
Here the Morris-Mitchell condition (Morris & Mitchell, 1995) is used which maximises the distance between all points, calculated using a p-norm(p=1 is rectangular distance, p=2 is euclidean norm),

$$d(x^{(i1)}, x^{(i2)}) = \left(\sum_{j=1}^{k} |x_j^{(i1)} - x_j^{(i2)}|^p \right)^{1/p} \tag{4.1}$$

A detailed explanation of the theory and example of an implementation of the method in MATLAB can be found in Forrester et al. (2008)

Metamodel theory

After the sample points for the DOE have been finalised, the CFD simulations are run with the finalised input parameters. Results from these simulations are processed to extract key outputs we would look to optimise or improve. The results for the output variables are used to approximate these key variables across the design space. The response surface, characterised by a variable y is an unknown function of the design variable parameters. At each DOE sample point, the value of the response surface is known from the CFD output and fixed at this value, and in the spaces between, a surface is interpolated from the data.
To build the metamodel using the CFD output data, a Radial Basis Function (RBF) approximation to the surface, $\hat{f}$, is needed:

$$\hat{f}(x) = w'\phi = \sum_{i=1}^{n_c} w_i \phi(||x - c^{(i)}||), \tag{4.2}$$

where x is the position in the design space, w is a vector of weighting values and ϕ is the n_c vectors containing the values of the actual basis functions, evaluated at the euclidean distances between the prediction site x and the centres $c^{(i)}$ of the basis function (Forrester et al., 2008).

There are many basis functions that could be used:

- linear: $\phi(r) = r$
- cubic: $\phi(r) = r^3$
- Gaussian: $\phi(r) = e^{-r^2/2\beta^2}$
- multiquadratic: $\phi(r) = (r^2 + \beta^2)^{1/2}$
- inverse multiquadratic: $\phi(r) = (r^2 + \beta^2)^{-1/2}$

with the linear and cubic functions being examples of fixed bases and the further three including the β variable being parametric basis functions.
The vector of weights, w, is calculated from an interpolation condition,

$$\Phi w = y, \tag{4.3}$$

$$\hat{f}(x_j) = \sum_{i=1}^{n_c} w_i \phi(||x_j - c^{(i)}||) = y_j, j = 1, 2, ..n. \tag{4.4}$$

The results $y = [y^{(1)}, y^{(2)}, ...y^{(n)}]'$ on the surface are known at the n sample points, $x = [x^{(1)}, x^{(2)}, ...x^{(n)}]'$. Φ is the Gram matrix, $\Phi_{i,j} = \phi(||x^i = x^j||)$ for $i, j = 1, ..., n$. This creates a response surface, which coincides with the DOE dataset at sample sites but creates an interpolated surface over the remaining domain. The models which are parametric in approach and include a tuning parameter, σ, can be tailored to provide better responses through further analysis and validation.

4.2.2 Validations of models

To ensure the response surface is predicting the results accurately across the design space, it will be subjected to cross-validation.
A collection of the CFD data points are held back from the data set while the response surface is constructed and then the surface is evaluated by considering the disparity between its predictions and true values at those withheld data points.

The error for the surface can be defined using several approaches:

– Root Mean Squared Error

$$RMSE = \sqrt{\frac{1}{n}\sum_{i=1}^{n}(\hat{f}_i - f_i)^2}, \tag{4.5}$$

– Relative Average Absolute Error

$$RAAE = \frac{\sum_{i=1}^{n}|\hat{f}_i - f_i|}{n\sigma_{sd}}, \tag{4.6}$$

– Relative Maximum Absolute Error

$$RMAE = \frac{\max\{|\hat{f}_1 - f_1|, |\hat{f}_2 - f_2|, ..., |\hat{f}_n - f_n|\}}{\sigma_{sd}}, \tag{4.7}$$

with σ_{sd} here being the standard deviation of observations. As the values of RMSE, RAAE and RMAE tend to 0 it signifies the improvement of the model. Through cross validation methods the parameters can be tuned and improved, with the goal being to reduce the RMSE or other error quantifier. There are several validation methods which can be used. Two used here are detailed below:

Leave-One-Out

Leave-One-Out cross validation is an example of an exhaustive validation method. In turn, each of the DOE sample data points is held back and the remaining become the training set and are used to construct the response surface. Error is then evaluated by comparing the 'left out' data point CFD result to the prediction by the generated surface.

k-Fold

K-fold validation on the other hand is an example of an in-exhaustive method. A random subset of k points are held out, with the $N - k$ remaining being used as the training data to build the response surface. Errors are calculated at each of the k validation points and an optimisation algorithm can be used to iteratively reduce the error.

An optimal tuning parameter is found here using a golden search algorithm together with cross-validation methods and error calculations. Iterating through values of σ while validating and assessing errors mean the final results surface predicts the response as well as possible with the data that is available.

Once the response surfaces are created they can be analysed over the design space and used to investigate the response of key parameters over the design space

and highlight any scope for improved or optimised designs. Running CFD simulations can be expensive and time consuming and in this application, if calculating new input parameters during the optimisation algorithm iterations and then running simulations at these points, the computational time and cost would be too high. The meta-model created here means that the design space can be explored in an optimisation algorithm with output from the response surface presumed to well-predict CFD results across the design space. With these predictions used instead from the response surface, optimisation techniques become much more practical to use to identify the local and global maxima and minima.

4.3 Design space

Within machining and, more specifically here, milling, there are lots of potential variables to consider when looking to make improvements to the cutting process. Some of these variables are related to the tool design and coolant channel configuration and some are related to the running conditions.

4.3.1 Variables for consideration

The variables and parameters which fully define a tool design are extensive and complex. These can include things like the number of flutes on the tool, and the angle of the cutting edge. The majority of these variables are fine tuned to individual cutting applications and have been through an extensive design processes. During this targeted study with a focus on coolant application, tool design parameters which link to the design of cutting edges and would affect the cutting mechanism or process extensively have not been considered. Even if significant improvements were observed here for coolant objective outputs, the designs would have to be further considered from a solid mechanics perspective. In further work, if a combined model which combined analysis of the structural integrity and cutting process with the coolant application were used these would be good variables for consideration, but it is beyond the scope of the work in this case.

Modifications made to the design of the coolant channels do not have a heavy influence on the cutting process itself and yet have the most significant impact on coolant management, making them ideal candidates for exploration. Machining condition parameters also have the potential to have large impacts on the coolant application results here and exploring a parametric study with these conditions can also be considered. A collection of some potential design variables for internal coolant channels can be seen in Figure 4.1.

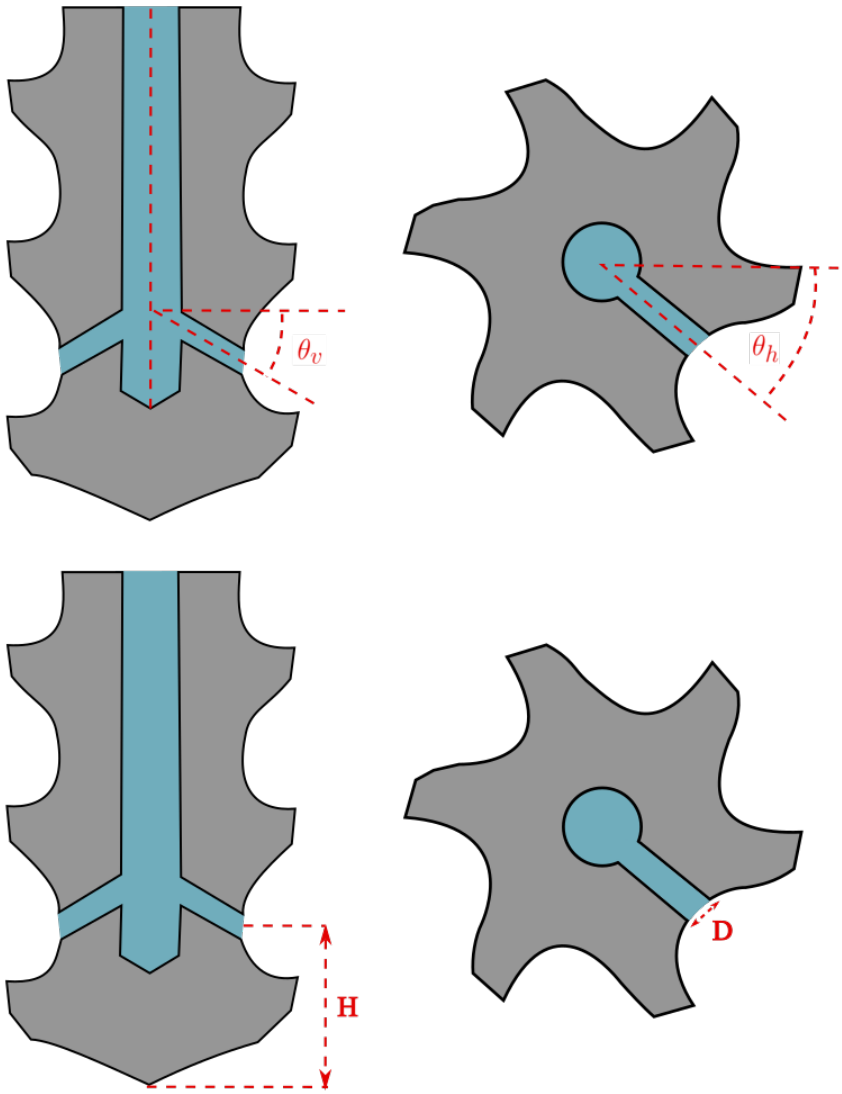

Figure 4.1: Schematic of potential parameters for design space exploration. Vertical and horizontal coolant channel angle are shown at the top, with coolant channel exit height, H, shown on the bottom left, and coolant channel diameter, D, on the bottom right.

Targeting coolant application well with internal coolant channels is one of the primary objectives in thermal management of machining. Three variables that dictate the direction and impingement site of the coolant jet are the horizontal and vertical channel angles, θ_h, θ_v, and the coolant channel exit height, H. Managing these variables, there is complete control of application of the coolant within feasible limits. As well as dictating the impinging jet location, the channel angles also affect the coolant flow velocity as it enters the cutting zone. This influence on the coolant direction could dictate whether the bulk of flow is directed upwards or downwards along the cutting edge for example, which would have great importance to chip evacuation in some cases. A steep vertical angle typically results in the bulk of coolant flowing downwards of

the jet impact point and wetting the tool/workpiece below this point as opposed to a straight horizontal channel which causes the coolant to flow into the domain much more evenly. The angle of impingement has also been found to affect local heat transfer coefficients in flat plate tests (Attalla & Salem, 2014) so this is of interest in machining too.

The tool design variables listed above have the advantage of being applicable to a range of operations. Once prototyped and tested, new tool designs could still be investigated further with a focus on machining conditions for different applications. It is important to have designs which operate well under a range of conditions and considering the machining condition parameters alongside the tool design parameters can highlight some of the limitations of even some of the best tool designs across a range of operating conditions.

Although there are several ways to control the impingement centre of the coolant jet by modifying tool design as mentioned here, there are only small changes that can be made to the distance, L, between the coolant jet exit from the tool to impingement on the workpiece. This could be somewhat important when considering the local heat transfer on the tool and workpiece surfaces. One of the characteristic parameters for heat transfer in impinging jets is the ratio of distance between channel exit, L, and channel diameter, D. For most milling cases using standard channel diameters the characteristic impinging jet parameter is around $L/D \approx 2$. This value is smaller than is generally optimal for impinging jet coolant (Baughn & Shimizu, 1989). The coolant channel diameter can be varied to some extent, however reducing the channel sizes significantly also greatly increases the pressure drop over the system, and therefore increases the pumping power needed to deliver coolant at similar flow rate magnitudes.

Changes to coolant flow rate would have the potential to have significant impacts on the cooling capability, not only due to the introduction of higher convection and turbulence, but the capacity to shift the location of high heat transfer points (Sagot et al., 2008). In addition to coolant flow rate, the machining condition parameters of interest could be the tool engagement, both axially and radially. These settings are often changed to achieve different results in machining and have a significant impact on the levels of thermo-mechanical load experienced by the tool. They are important to consider from a coolant perspective, as it would be beneficial to have the coolant targeted at a suitable region along the cutting edge, and if the axial engagement was very small for example, then coolant would ideally be directed at that small region near to the tool tip. In large radially engaged settings, a longer stretch of the cutting face is engaged at any one time, and a good distribution of the coolant over the larger area might be more beneficial.

Here a combination of both tool design and machining condition factors are investigated, with two DOE studies undertaken, each with two design variables used. One takes both a machining condition parameter and a tool design parameter to investigate, and the second explores two tool design parameters together.

4.4 Optimisation Study I: Coolant flow rate and horizontal coolant channel angle

4.4.1 DOE setup

The first optimisation study investigates the coolant speed, U, and horizontal channel angle, θ_h as the two design variables considered. This combination will provide insight into both a tool design parameter and machining condition parameter and the case can be used to determine the relative impact of each.
The full range of horizontal channel angles used is $12.5^o \leq \theta_h \leq 45^o$ and a standard vertical angle, θ_v of 30° is taken. A small horizontal angle aims the coolant at the cutting edge and results in a larger distance between the channel exit and the impingement surface of the workpiece. At the minimum angle, the coolant jet should impinge with the centre slightly above the cutting edge. This minimum horizontal angle is limited by the process used to create the channels — when the coolant channel intersects the cutting edge of the tool then the design becomes non-feasible since these coolant channels are machined into the tool externally and adding the channel would damage the cutting edge in the event of an intersection. Figure 4.2 shows this minimum horizontal angle, as the view is directed along the coolant channel axis. Any further direction towards the cutting edge and it is clear that the cutting edge itself would be compromised by an overlap.

For the maximum angle value of 45^o the coolant channel exits the tool through the flank edge which follows the cutting edge. This angle value is also on the limit of feasible geometries, since a further increase would see the channel path interfering with the tool surface in the flute above. Exiting the tool at the flank edge means much of the coolant is expected to cover this edge and generally leads to a much smaller distance before the coolant jet impinges on the workpiece surface.

Coolant speeds ranging from 30-80 m/s are used for the simulations. A sample size of 25 points is used across the design space, located according to the optimised latin hypercube shown in Figure 4.3. This N=25 value is chosen for this study based on the balancing of successful capturing of the output variables response against computational limitations, as it is not mandated when using an optimised Latin hypercube sampling

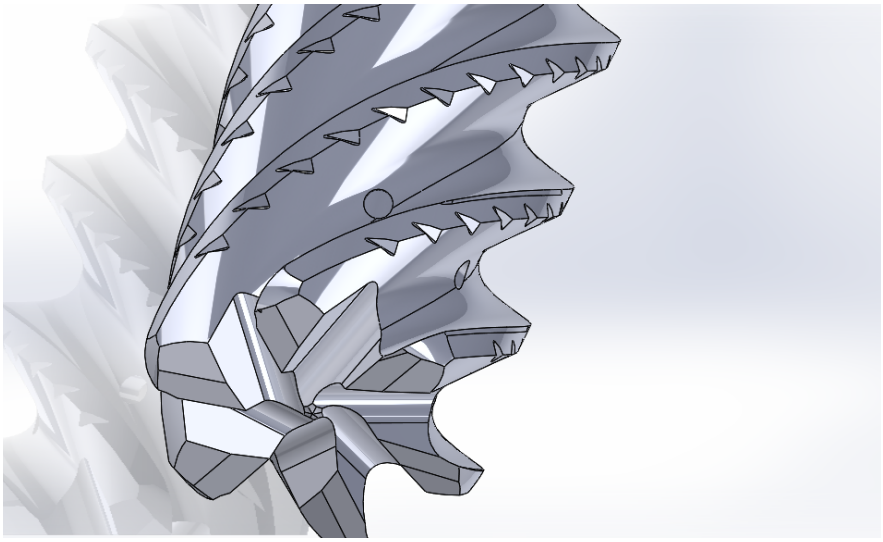

Figure 4.2: View down coolant channel axis at maximum value of horizontal angle.

approach. In this study of the design space, 25 samples were deemed to represent the behaviour across the design space well, with Leave-One-Out cross validation of the response surface fitting resulting in a Root Mean Squared Error (RMSE) of 0.043, 0.08, 0.169 for wetting, vertical coolant speed and tool temperatures respectively. The tool temperature has a higher RMSE than wetting and coolant speed. If possible, more sample points would have been used in the regions of low horizontal angle, where there is more variation in the response of the tool temperature results in order to reduce this value, however this was not possible due to computational cost and time. In further work an adaptive methodology whereby further sample points could have been added into the regions of high variability would be an improvement and more efficient use of computational resources.

For each of the 25 sample points a new tool geometry design is created in Solidworks. The geometries are each automatically meshed following the process described in section 3.2.3 using surface 'standard triangle language' (STL) files from the tool geometries and the same `snappyHexMesh` script. Refinement process and background base meshes are consistent between all cases.
Simulations are each run on 40 cores on the University of Leeds ARC clusters to a final time of 0.001 seconds. Data between 0.0008-0.001 is then extracted and time-averaged using python scripts to offset any unsteadiness in the simulations.

The required variables are post processed to calculate average values for the solid and fluid regions of interest, following the process described in section 3.7.2.

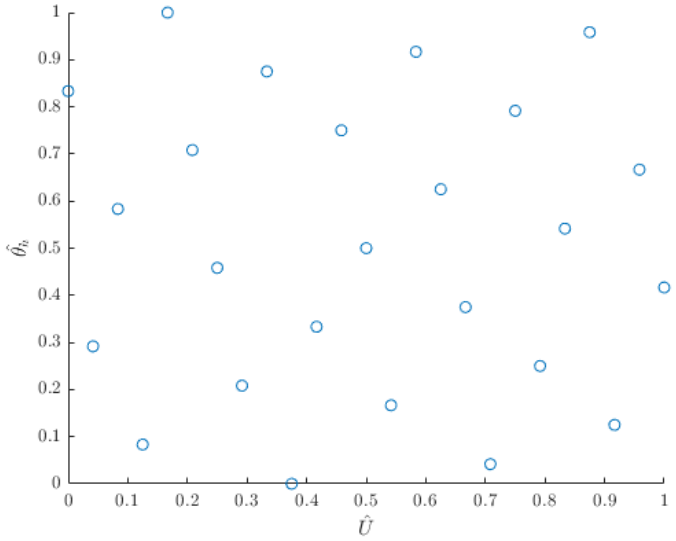

Figure 4.3: Sample points generated using an optimised Latin hypercube method on a 2D unit square for a DOE study with two design variables, coolant inlet speed and horizontal coolant channel angle.

4.4.2 Results

Radial basis functions have been used to create response surfaces for each output variable in the DoE case. Each response surface has been fitted using an inverse multiquadratic radial basis function and an optimised tuning parameter and validated using a leave-One-Out cross validation. The β tuning parameters are provided with each set of results and have been optimised using a golden search algorithm, with the results included in Figure 4.4

Figures 4.5-4.7 show the response surfaces for wetting, vertical coolant flow in the chip formation zone, and tool temperatures, with the red points representing the CFD simulation output at the DoE sample points. Across each response surface a yellow point also shows an optimised value on the surface where each variable has either been maximised or minimised according to the desired outcome.

The results for wetting % in Figure 4.5 show horizontal channel angle has a clear impact on the coolant distribution, with the low angles which direct towards the cutting edge exhibiting the highest coolant flooding here. This would be the expected outcome and is intuitive given the directing of the coolant, though even as the channels are directed instead towards the rake face, where wetting is the lowest, the values are still over 40% coverage. This is significantly lower than the $> 85\%$ maximum but would likely still be vastly improved on a dry machining case. The coolant speed appears to have very little impact on wetting % across these ranges compared to the channel angle.

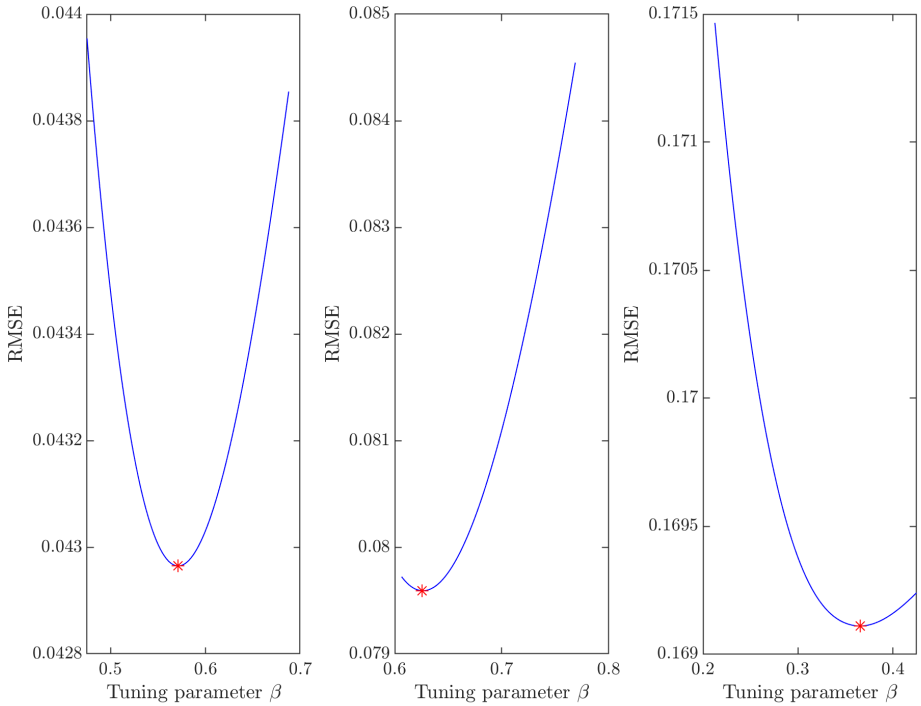

Figure 4.4: Tuning parameter optimisation results from a golden search approach for (*left to right*) wetting, vertical coolant speed, and tool temperature. The β tuning parameter is plotted against RMSE.

For the vertical speed results, U_z, shown in Figure 4.6 all the results are negative. This is likely due to the standard vertical coolant channel angle used across these simulations which is 30°. All flow entering the domain and impinging on the tool is directed downwards as a result of this and a generally downward flow as a result is expected. A positive flow would be beneficial to evacuate chips upwards in a full-slot milling case, however minimising the magnitude of downward flow can also be beneficial as there are cases where there be multiple priorities to consider which do not allow for an upward flow configuration.

Aiming the coolant flow at the flank face with a high θ_h value means a larger proportion of the coolant is directed upwards once interacting with the cutting edge.

Increasing the coolant flow entering the domain makes this effect more pronounced and we can see a more significant increase in magnitude when increasing the channel angle at the highest speed of 80m/s ($u_i = 1$) compared to the lowest. Low speeds generally show a smaller magnitude of U_z across the results, since a lower coolant speed applied results in a smaller magnitude flow across the domain in general.

Where wetting results showed a strong dependence on the θ_h parameter, and

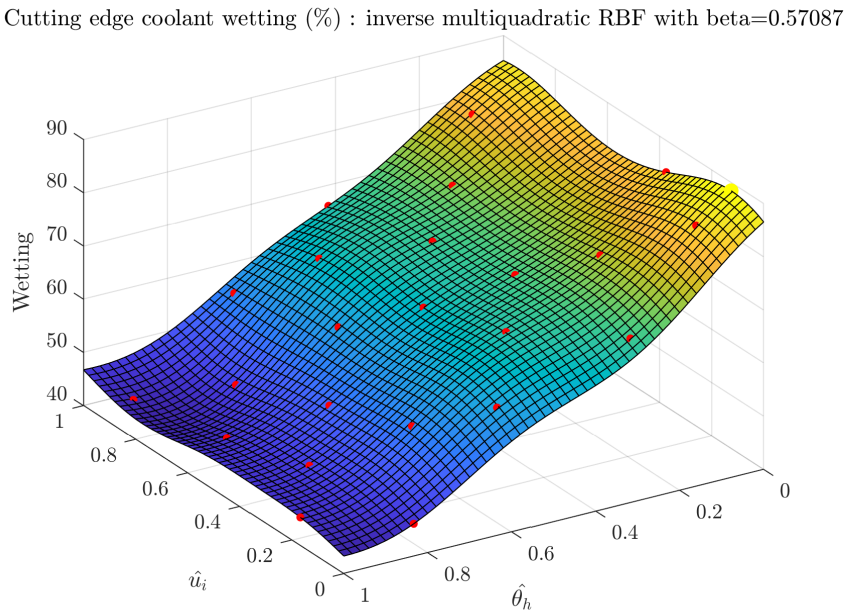

Figure 4.5: Response surface fitted using an inverse multi-quadratic radial basis function for coolant coverage, α, along the rake face for DoE study of the coolant inlet speed, u_i, and horizontal channel angle, θ_h parameters.

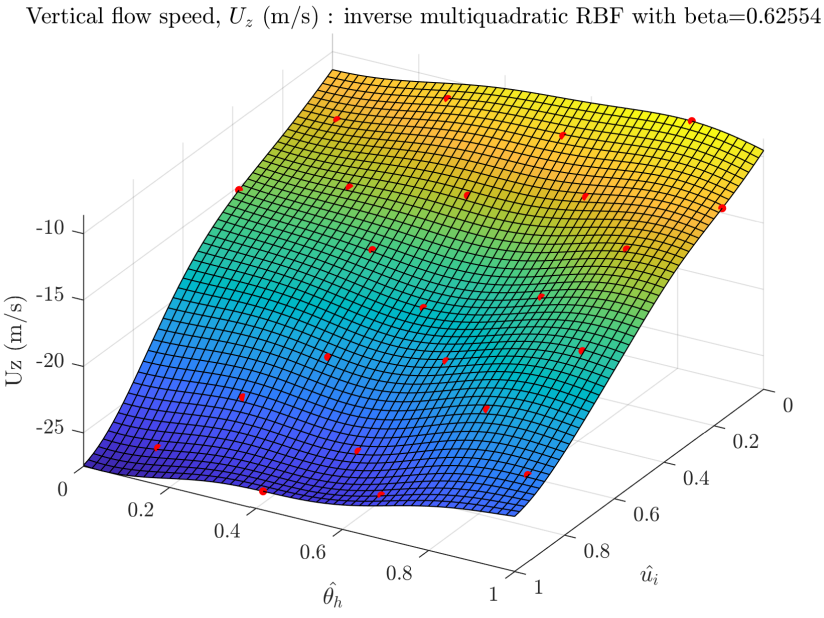

Figure 4.6: Response surface fitted using an inverse multi-quadratic radial basis function for vertical coolant flow, u_z, along the rake face for DoE study of the coolant inlet speed, u_i, and horizontal channel angle, θ_h parameters.

the vertical coolant velocity results depended on both θ_h and u_i, the response surface for tool temperatures (Fig 4.7) show greater dependence on u_i across the design space. Generally, as the coolant inlet speed is increased, the tool temperature is decreased.

There is a small region of exception to this across the domain where $\hat{\theta_h}$ is at its minimum value of 0 and there is low coolant inlet speeds. Here the tool temperature remains high, with similar values to those around the maximum of 620K seen for the lowest coolant flow supplies. The tool designs with this minimal angle direct flow more successfully along the cutting edge instead of over the whole tool surface, which can reduce the cooling capacity in these simulations. This feature is further discussed in the results of 4.5, where it is more prominent and critical to the results analysis.

We would expect a good correlation between low temperatures and high wetting as the coolant is applied to decrease tool temperatures. Instead of a similar profile however, the tool temperature is shown to be much more dependent on coolant speed than the level of coverage on the cutting edge in this instance. This emphasises the importance of the consideration of both machining conditions and tool design parameters in tandem since a change in conditions could drastically change outputs across the case. Tools need to be robustly designed to perform well across a range of conditions instead of at the absolute best in a very narrow and unsustainable set of ideal conditions.

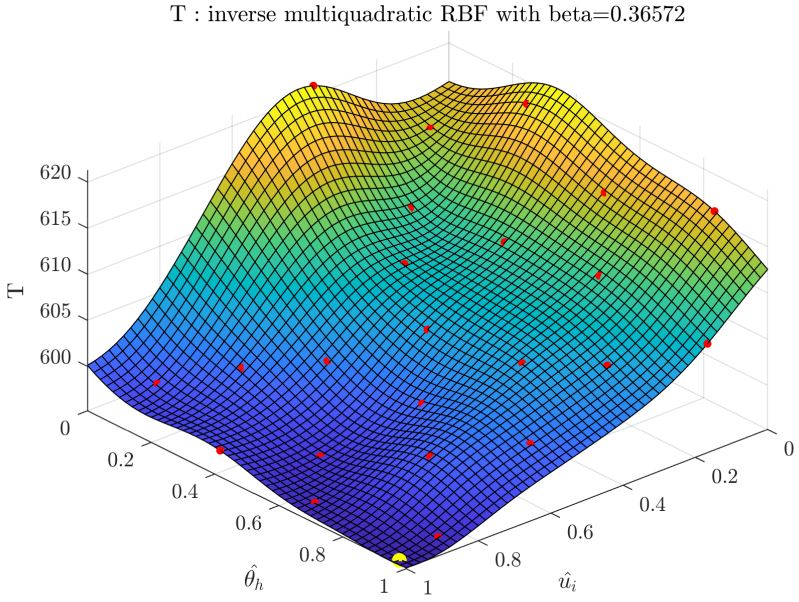

Figure 4.7: Response surface fitted using an inverse multi-quadratic radial basis function for tool temperature, T, along the rake face for DoE study of the coolant inlet speed, u_i, and horizontal channel angle, θ_h parameters.

It can also be observed from Figure 4.7 that fairly small temperature ranges are observed across the design space. This is due to a fixed high temperature boundary condition being applied between the workpiece and tool. In reality, the high temperatures generated here would be dependent on friction and a range of machining conditions. High levels of coolant coverage near to this boundary introduce a good covering of lubrication which is one of the main benefits of applying the coolant. This

is turn would reduce the actual temperatures generated here and if this were taken into account, the results would likely be more closely corresponding to the wetting surface. Using the meta-models created for the response of the key variables wetting, vertical coolant speed and tool temperature, tool designs can be optimised to maximise or minimise any of these results. Single objective optimisation to maximise coolant coverage and minimise vertical coolant speed and tool temperatures are presented in Table 4.1.

Variable	Optimised output	$\hat{u_i}$	$\hat{\theta_h}$
α	88%	0.13	0.0
u_z	-8.65 ms^{-1}	0.0	0.83
T	595.2K	0.98	0.96

Table 4.1: Single objective optimisation results, maximising α, minimising u_z and tool temperature T, with optimised tool designs variables $\hat{\theta_h}$ and $\hat{u_i}$.

The investigations into the design space here have allowed the comparison of the impacts of a tool design variable, $\hat{\theta_h}$, and a coolant supply condition variable, $\hat{u_i}$. It was noted that both impacted on the simulation output parameters to different extents, with the coolant channel design having a more significant impact on the coolant distribution along the cutting edge and the coolant supply inlet speed having a more significant impact on the tool temperatures.

4.5 Optimisation Study II: Vertical and horizontal coolant channel angles

4.5.1 DoE setup

The second design exploration case considered takes two tool design parameters as the design variables used. This combination allows much more versatility in the direction and location of coolant jet impingement. The full vertical channel angle range of 0-45° is taken as the fixed range. A vertical channel angle, θ_v, of 0° means the coolant channel lies in the horizontal plane. Having the flute coolant channels directed upwards from the horizontal would cause an unnecessary pressure drop and predominantly the desired cooling region is below the coolant point anyway so there is little to be gained from increasing above the horizontal plane.

Minimum and maximum horizontal angle are again dictated by what it is possible to machine. If the angle becomes too large the cutting of the coolant channel interferes with the following cutting edge, and if it is too small, with the preceding flank face. In the first optimisation study at a fixed vertical angle this range was fixed and easier to explore. When the vertical angle is varied in tandem, there are more

complicated limitations on horizontal angle.

At the smallest vertical angle of 0°, there is room for a wider range and so we vary horizontal angle between 12.5° and 55°, whereas at a 45° vertical angle that range is limited to 19° - 37° to maintain feasible tool designs. A DoE is generated across a regular unit square design space, as shown in Figure 4.8 (a), and then scaled dependent on vertical angle as indicated in Figure 4.8 (b).
The response has been more complex in this second design space exploration and an increased number of sample points, 80, are generated, with geometries created and meshed for each new tool design. Ideally, further sample points would be added in the region of the smaller horizontal channel angle, since this is a high change region.

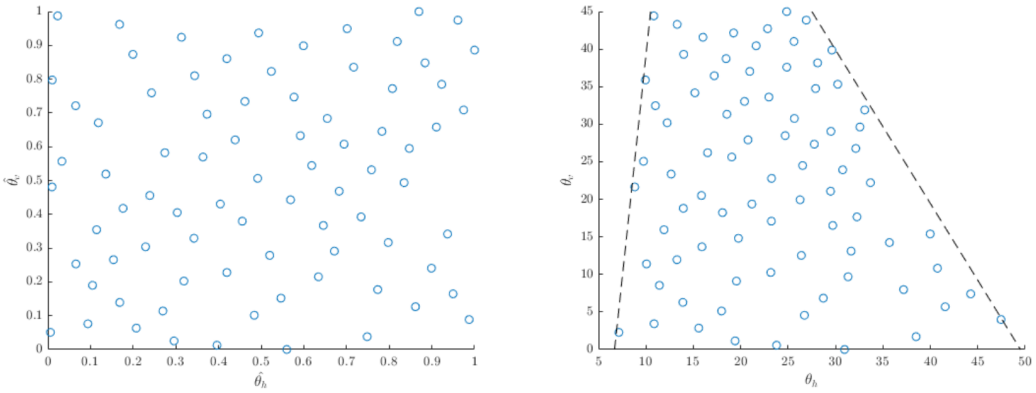

Figure 4.8: Sample points generated using an optimised Latin hypercube method on a 2D unit square for a DOE study with two design variables, the vertical and horizontal coolant channel angle.

Examples of the extreme geometries which would represent the corner points in the design space can be seen in Figure 4.9. The extra range which is attained for the small vertical angles is clear here, with the geometry (a) cooling channel exiting the tool right through the flank edge and the geometry (c) coolant channel with the larger vertical angle exiting the tool in the flute instead. Comparing the geometries (b) and (d) with maximum horizontal angles, the geometry (b) cooling channel exits the tool much deeper into the flute than the geometry (d) cooling channel.

4.5.2 Results

In general the results from the second DOE case here exhibit less clear trends in the behaviours across the design space. Particularly in regards to the tool temperatures and vertical component of the coolant velocity near to the cutting edge. Increasing the number of tool design parameters used as design variables from one to two between

Figure 4.9: Extreme geometries (a) $\theta_v = 0, \theta_h = 12.5$ (b) $\theta_v = 0, \theta_h = 55$ (c) $\theta_v = 45, \theta_h = 19$ (d) $\theta_v = 45, \theta_h = 37$.

these cases has exhibited a clear increase in complexity of the response across key outputs. In other cases where more design variables could be considered to try to fully parametrise the coolant channel design by also including, for example, coolant channel vertical position, a significantly higher number of data points would be required to capture the details of the response surface. At 20 sample points for two variables there appear to be limitations still and global maxima and minima observed could be non-physical and due to over fitting.
Response surfaces for the second design space exploration are presented in figure 4.10 for wetting, vertical coolant speed and tool temperature. In each of the response surfaces, there is a region with a clear isolated peak/trough at around $\theta_h = 37°$, $\theta_v = 35°$. This is clear on the plots as an outlying high region in the vertical speed and tool temperature response surfaces, and a low region in the wetting.

This region is small and there is no obvious geometrical reason for the variable behaviour compared to other tool designs within close proximity in the design space. There is confidence that the results correspond to a real feature of the flow in this region of the design space, since although there is one tool design in the space which predominantly creates the extreme peak values shown, a neighbouring tool design has results which lie nearly half way up the steep slope near the extreme points and out of the range of all remaining points in the design space. Further examination of these CFD results show a very limited consistent coolant coverage for the two results in question. Visualisations of the coolant coverage are shown in Figure 4.11 from multiple angles and the coverage on the workpiece is not the solid red which corresponds to consistent high levels of coolant, as was seen in Chapter 3. Instead there appears to be a significant

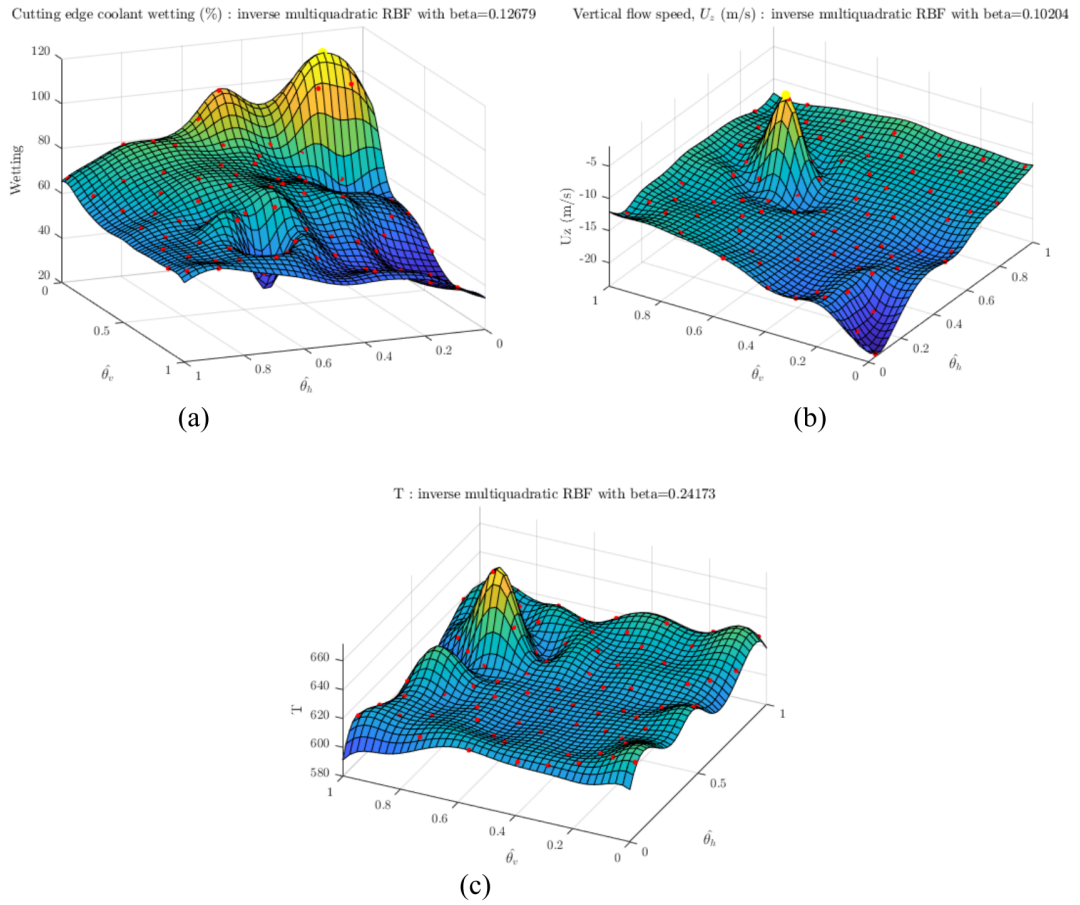

Figure 4.10: RBF response surfaces fitted using an inverse multi-quadratic radial basis function for (a) wetting of the cutting edge (%), (b) Vertical speed, u_z, (c) Tool temperature, T.

amount of splashing flow in the flute and a good coverage on the flank edge above the flute being modelled. There is no obvious reason why these tool designs would create a higher amount of splashing, as the impingement point is not especially close to a complex region of the tool-workpiece cutting interaction or any other particular feature. From this set of results it is found that any design which exhibits this excessive splashing flow is to be avoided if possible, since it has contributed to a low coolant coverage and a very high tool temperature. The response surface fitted to the DOE results is also impacted by the inclusion of these outlying values in the domain, with the surface nearby over-fitted with local peaks and troughs to compensate for the values. To progress the analysis of the rest of the domain, the splashing points in the isolated region are omitted from further analysis, in order to analyse the domain under more regular conditions.

The same set of results, with response surfaces refitted while witholding the two tool designs which showcased outlying splashing features are presented and discussed below. Each response surface has been fitted using an inverse multi-quadratic

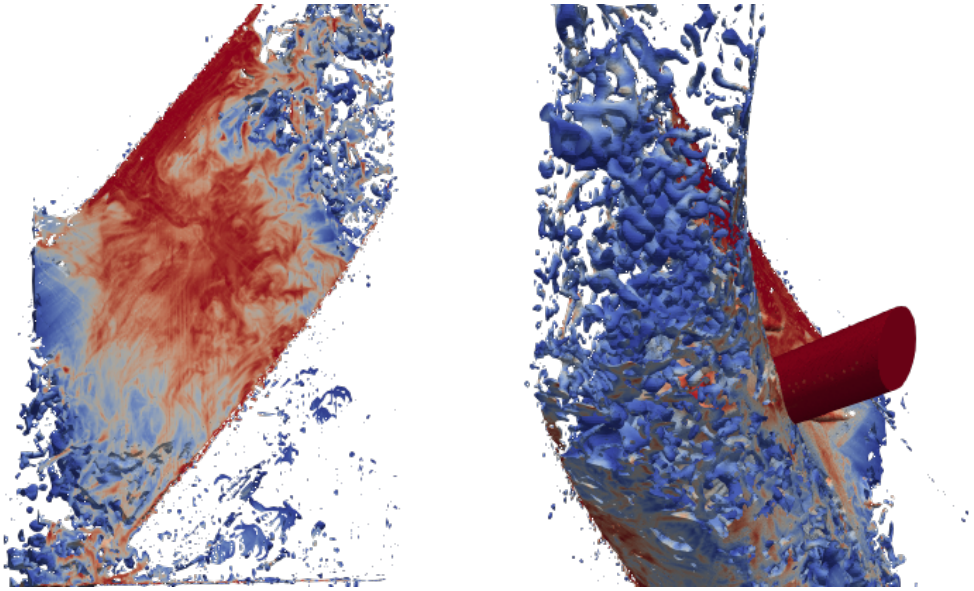

Figure 4.11: Visualisation of tool design with $\hat{\theta_h} = 0.61, \hat{\theta_v} = 0.69$. The fluid flow presented is at the end time of 0.001s in the simulation, but is coloured with the time averaged results for coolant coverage. The fluid domain is filtered to show only coolant filled regions with $\alpha > 0.5$ and significant amounts of splashing flow can be seen in the tool flute.

radial basis function and an optimised tuning parameter. The β tuning parameters are provided with each set of results and have been optimised using a golden search algorithm, with the results included in Figure 4.12

With the splash generating tool designs removed, the results for coolant coverage are shown in Figure 4.13 with a mostly smooth response. Neither of the two angles are seen to dominate the design space, with both clearly having an impact. There is excellent wetting at the lowest values for $\hat{\theta_h}$ and $\hat{\theta_v}$, where the coolant is directed at the cutting edge with a low vertical angle. Generally, reducing the vertical angle appears to increase the coolant coverage across the domain, although interestingly, this is far more pronounced when directing the coolant at the cutting edge with low $\hat{\theta_h}$ values. At high values of $\hat{\theta_h}$, the vertical channel angle, $\hat{\theta_v}$, has very little impact since the coolant is impacted further away on the workpiece surface and spreads out evenly, which generates a generally good coolant coverage up the rake face on the cutting edge. Reducing the $\hat{\theta_h}$ values from a maximum of 1 to ≈ 0.5 increases the wetting on the rake across the full range of $\hat{\theta_v}$ angles, as the coolant is directed more towards the cutting edge. After the $\hat{\theta_h}$ is decreased below ≈ 0.5 however, the wetting starts to depend strongly on the $\hat{\theta_v}$ parameter. At the lowest value of $\hat{\theta_h}$, when the coolant is directed directly towards the cutting edge, a small $\hat{\theta_v}$ angle creates a well spread out coolant application and shows the highest wetting, however at the minimum $\hat{\theta_v}$ the coolant distribution is reduced to $\approx 40\%$. This coverage is a reduction compared to the $\approx 60\%$ values achieved for high $\hat{\theta_h}$ values, with the coolant now directed steeply down towards the

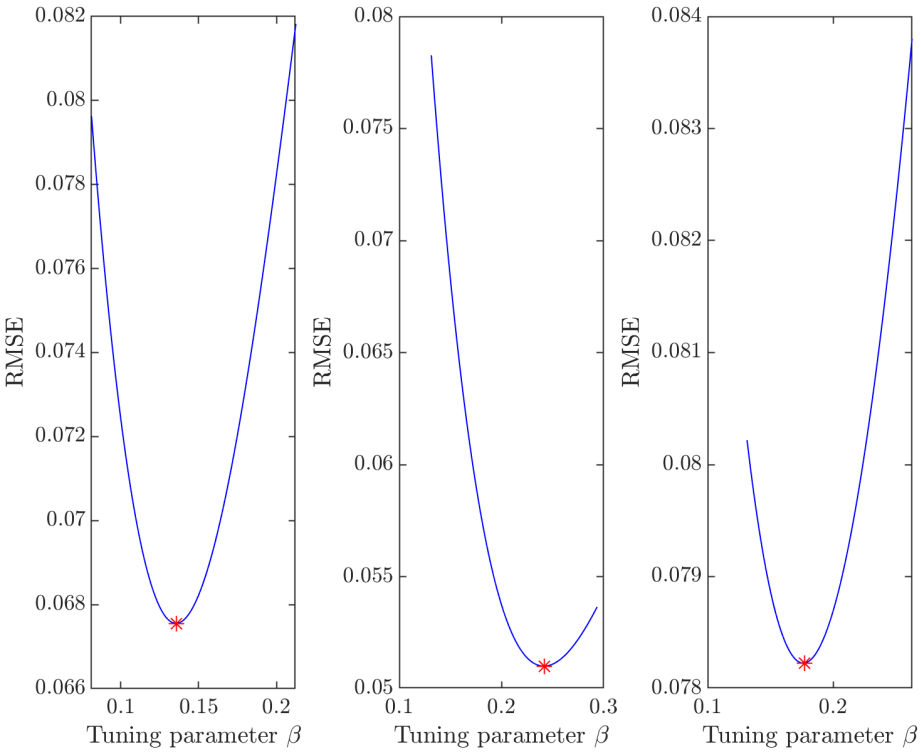

Figure 4.12: Tuning parameter optimisation results from a golden search approach for (*left to right*) wetting, vertical coolant speed, and tool temperature. The β tuning parameter is plotted against RMSE.

base of the cutting edge, and much of the coolant then flowing to the base of the tool, with less flow travelling up the cutting edge to provide the even coverage needed for a high average α result.

The response surface results for the vertical velocity along the cutting edge rake face is presented in Figure 4.14. Once again all vertical speeds recorded are negative, with the coolant directed downwards on average. A large part of the domain results in a flow of around -15m/s along the cutting edge, while the corner of the design space with the lowest $\hat{\theta_h}$ and $\hat{\theta_v}$ values have a significantly higher magnitude of downwards flow, closer to -25m/s. This coincides with the tool design region where high wetting was observed in Figure 4.13. At this point, coolant impacts at the highest point in the domain and is directed at the cutting edge, so almost all flow then travels down the rake edge, causing the high magnitudes seen here.

It was hoped that including small vertical angles in the range would allow the opportunity for some more significantly reduced downward flow over the cutting edge, and although this has been successful to some extent it has been offset by the fact that decreasing the vertical angle has actually raised the point of impingement

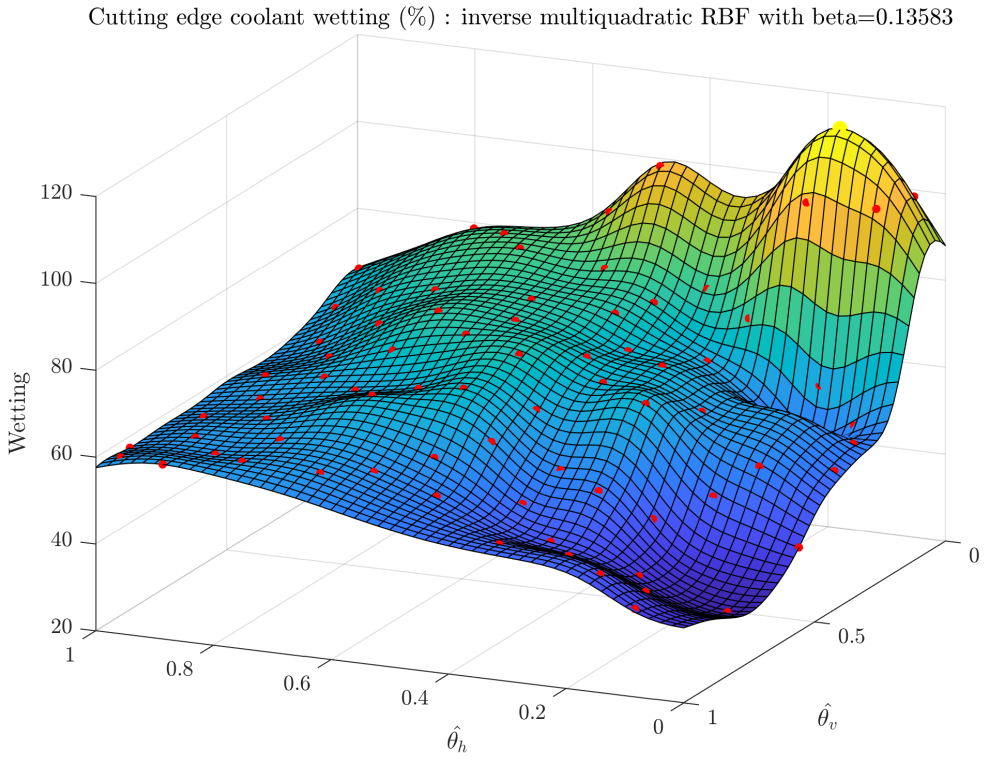

Figure 4.13: Response surface fitted using an inverse multi-quadratic radial basis function for coolant coverage, α, along the rake face for DoE study of the horizontal and vertical channel angles parameters, θ_h and θ_v.

on the workpiece in the domain. As the site of impingement moves upwards in the domain, naturally more of the coolant flow spreading out from the site is directed downwards along the cutting edge since most of the region of interest is now below this site. To fully explore this further with a targeted investigation of U_z, the vertical height of the coolant channel would also be a variable of paramount importance. A small vertical angle coupled with a lower vertical exit/ impingement point would seem a strong candidate.

Results for the tool temperature are more difficult to interpret in this DOE with two channel angle parameters taken as the design variables compared to the previous study in section 4.4. The response surface shown in Figure 4.15 shows greater variability than observed in the previous case, and a higher RMSE was seen in Figure 4.12 for the validation and optimisation of the tuning parameters for the radial basis function fitting. The number of sample points was increased from 25 to 80 between the first and second optimisation studies conducted in this chapter in an attempt to capture the tool temperature response, however even more sample points would be ideally used if the increased computation cost could be allowed, since this is a complex variable response across the design space.

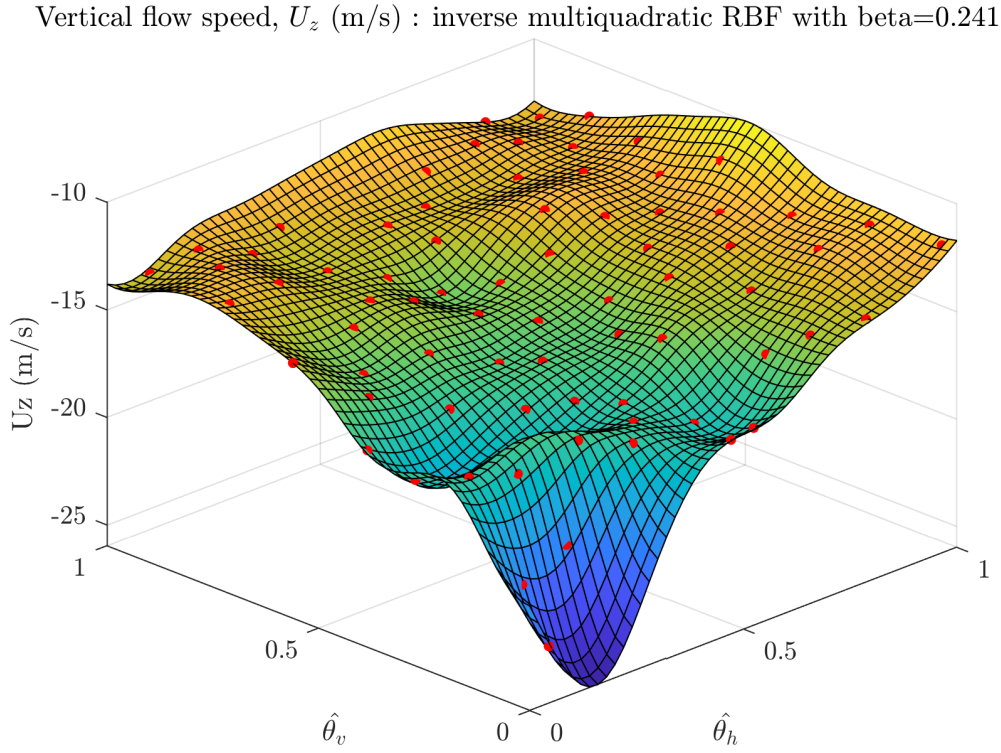

Figure 4.14: Response surface fitted using an inverse multi-quadratic radial basis function for vertical coolant speed, u_z, along the rake face for DoE study of the horizontal and vertical channel angles parameters, θ_h and θ_v.

The surface shows a region of low temperatures near to the middle of the design space, with tool temperatures rising as the horizontal angle, $\hat{\theta_h}$, becomes close to either the maximum or minimum points at the edges of the design space. The tool temperature also rises as the vertical channel angle, $\hat{\theta_v}$, is reduced to its minimum value of 0, for a level horizontal channel where the maximum temperatures of just over 630K are observed. Low tool temperatures were expected to correlate to regions of high wetting for these studies, however these CFD results and response surfaces show very little correlation between the two results outputs. In fact, the region of highest tool temperature occurs in the low $\hat{\theta_h}$ and $\hat{\theta_v}$ corner which resulted in the maximum coolant coverage for the rake edge. To investigate this counter intuitive relationship, two tool designs are selected and presented from different view points below in Figure 4.16. Marked on the response surfaces in (a), a high wetting, high temperature model is highlighted with a black ring and shown in (b), while a moderate wetting, low temperature model is highlighted with a white ring and shown with detailed views in (c). The spread of coolant along the workpiece surface is good for both models, as shown on the left hand of (b) and (c) where the tool is included for visual context. To the right of this, two views of each model are included showing the coolant coverage on the tool surface in the flute, from different angles. The central images showing

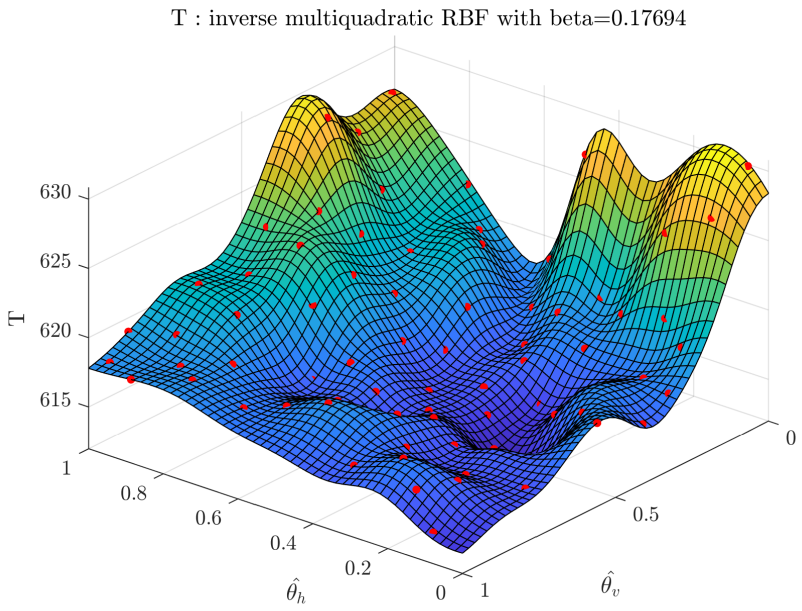

Figure 4.15: Response surface fitted using an inverse multi-quadratic radial basis function for tool temperature, T, along the rake face for DoE study of the horizontal and vertical channel angles parameters, θ_h and θ_v.

the coolant coverage over the tool surface show much better coverage for the model at the bottom, shown in (c), which had reduced temperatures compared to the model above it (b). The third visualisation, on the right hand side, for the two models shows that (b) has a much thicker and more concentrated layer of coolant application along the cutting edge than the model (c) below it, which shows good coverage but in a thinner layer. This is the reflection of the wetting results in (a) and are due to the coolant being well targeted towards the cutting edge for this model shown in (b), so that the coolant travels along the cutting edge in larger quantity and with high speed. From this analysis, the tool temperature looks to be more dependent on a good coolant coverage over a broader area of the tool, rather than a concentration near to the high temperature tool tip. A larger contact region between the tool and coolant enhances the heat transfer in these cases and makes the tool designs which spread the coolant more evenly appear to be the best option for thermal management.

The closer dependence of tool temperature on coolant coverage over the entire tool surface is confirmed by considering the correlation of results for each variable. There is a very low correlation of 0.08 between the tool temperature and coolant coverage of the cutting edge, whereas a correlation of -0.60 is found for tool temperature and wetting of the whole tool surface in the flute. It should be noted however, that although there is not a clear link between the tool temperature's response and the wetting results at the cutting edge in this work, this is not likely to be realistic. The good application of lubricating coolant to the cutting edge would significantly reduce

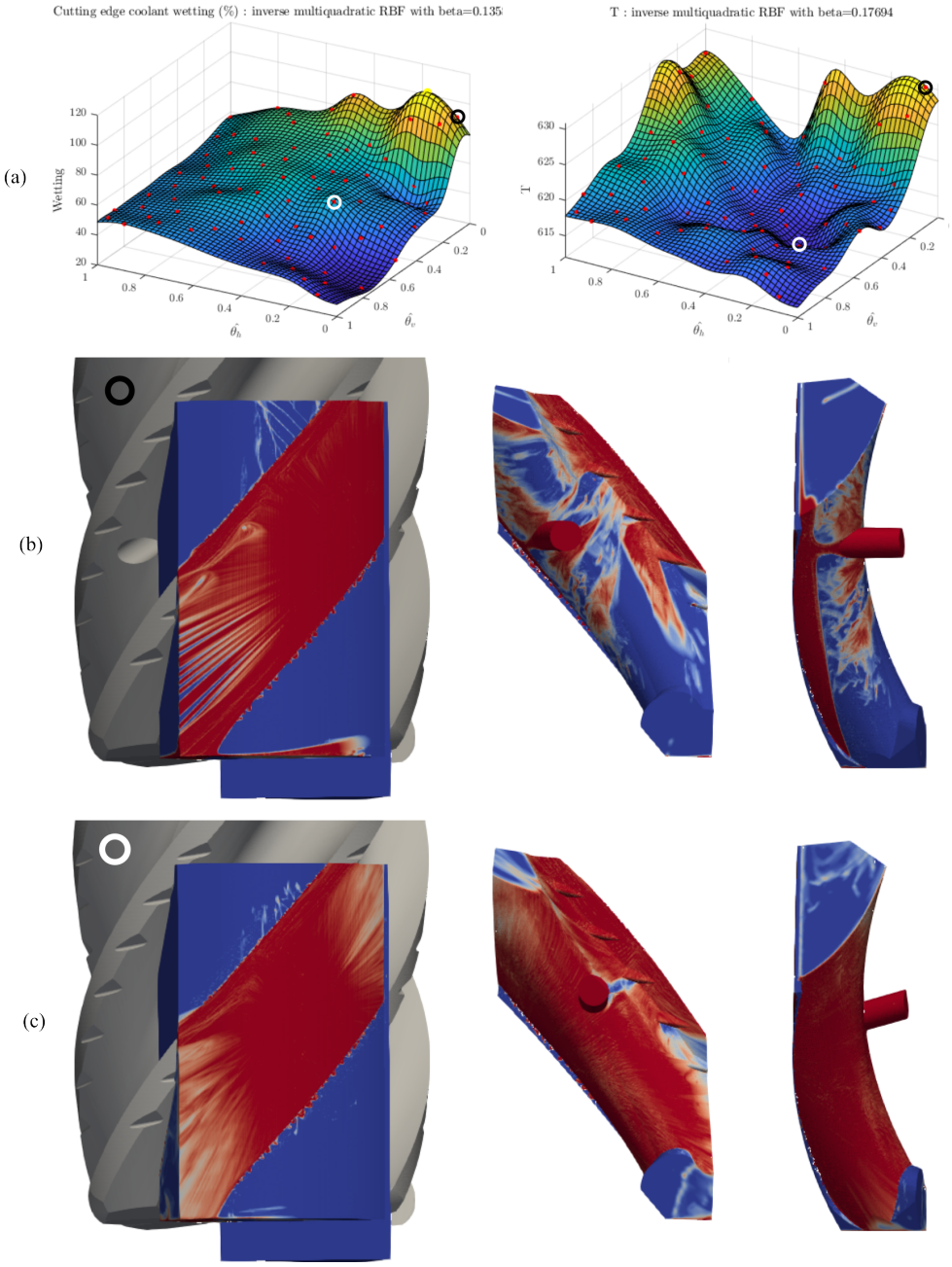

Figure 4.16: Two models to consider in more detail are highlighted on the wetting and tool temperature response surfaces in part (a), with a black ring for a high wetting, high temperature tool design, and a white ring for a moderate wetting, low temperature tool design. There CFD models are presented from three viewing angles in (b) and (c) respectively. Visualisations in (b) and (c) show the fluid domain coloured according to wetting, with red regions having high coolant coverage and blue having none. The left hand side view shows the flute as though through the workpiece, the middle shows the view as from the centre axis of the tool, and the right hand side view shows the cutting edge side of the flute more clearly.

friction and any associated heat generation at these cutting edges. To develop this

work further, a realistic factor which accounts for successful lubrication of this interface could be incorporated when setting up thermal boundary conditions and tool tip temperatures in the conjugate heat transfer model.

Using the meta-models created for the response of the key variables wetting, vertical coolant speed and tool temperature, tool designs can be optimised to maximise or minimise any of these results. Results of single objective optimisations to maximise coolant coverage and minimise vertical coolant speed and tool temperatures are presented in Table 4.2.

Variable	Optimised output	$\hat{\theta_h}$	$\hat{\theta_v}$
α	$> 100\%$	0.16	0.04
u_z	-10.26 ms^{-1}	1.0	0.49
T	612.0K	0.25	0.52

Table 4.2: Single objective optimisation results, maximising α, minimising u_z and tool temperature T, with optimised tool designs variables $\hat{\theta_h}$ and $\hat{\theta_v}$.

The optimal tool designs do not coincide for the results presented. Since the tool design cannot be optimal for each output simultaneously, a trade off is required and a series of optimal tool designs is found using a multi-objective optimisation. The results of a multi-objective optimisation minimising tool temperature and maximising wetting (minimising $(1 - \alpha)$) are shown as a Pareto front in Figure 4.17.

The maximum wetting of 100% corresponds to an optimal design with tool temperature of 624K, while the minimum temperature of 612K accompanies a wetting of just over 50%.

4.6 Conclusions

In this chapter, two design space exploration studies have been carried out considering both a machining coolant supply parameter and tool design parameters. The first considered one coolant supply parameter and one tool design parameter, and the second considered two tool design parameters. Across these studies, CFD simulation output has been generated at sample points over the design space and meta-models have been created using radial basis function methods.

Over both studies, results for coolant coverage, vertical coolant velocity and tool temperature on the rake face of the cutting edge were analysed. The first study investigated a design space with two design variables, $\hat{u_i}$ and $\hat{\theta_h}$ and found that the coolant inlet velocity, $\hat{u_i}$, had a significant impact on the tool temperatures and vertical coolant velocity along the cutting edge, with higher inlet speeds resulting in lower tool temperatures and higher magnitude downwards coolant flow. On the wetting, the inlet

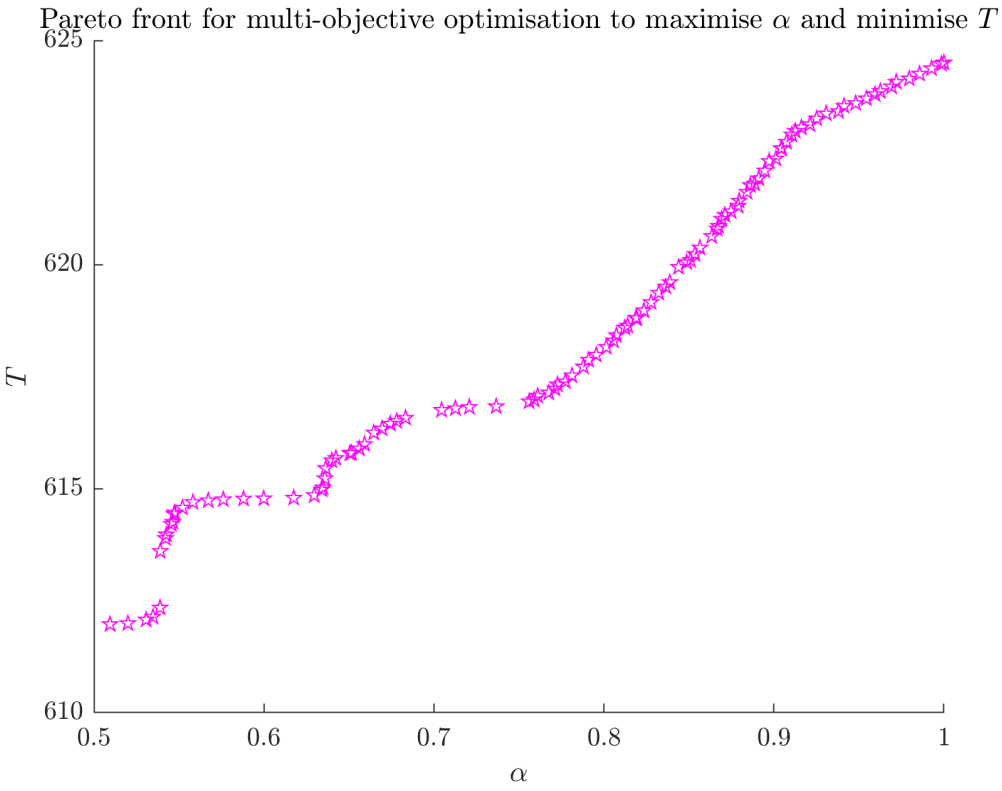

Figure 4.17: Pareto front results for a multi-objective optimisation which maximises the tool wetting along the cutting edge rake face, and minimises tool temperature for a design space varying θ_h and θ_v.

velocity had only minimal impact, however the horizontal coolant channel angle, $\hat{\theta_h}$, significantly altered the wetting, with small values of $\hat{\theta_h}$ directing the coolant as far as possible towards the cutting edge resulting in the highest levels of wetting.

The results of a second study which considered both the vertical, $\hat{\theta_v}$, and horizontal, $\hat{\theta_h}$, coolant channel angles as the two design variables showed increased variability in the results across the design space for all the response surfaces analysed for coolant coverage, vertical coolant velocity and tool temperature. Instead of a clear dependence on one of the parameters, the response surfaces show dependence on both design variables across the domain for each output variable. The highest levels of wetting were found for small values of $\hat{\theta_h}$ and $\hat{\theta_v}$ when the coolant is directed at the cutting edge, however for large values of $\hat{\theta_h}$ the variation with $\hat{\theta_v}$ was significantly reduced compared to the steeper decrease in wetting as $\hat{\theta_v}$ increases at very low $\hat{\theta_h}$.

Tool temperatures in this second analysis were very variable over the domain, and in any further work or later optimisation studies, it would be beneficial to target the work on a smaller design space and increase the number of sample points to fully capture the response surface accurately. Across these results, the tool temperature generally

was decreasing as $\hat{\theta_h}$ decreases, which corresponds to the increase in wetting and is intuitively expected. There was however a region of high tool temperatures at the corner of the design space with minimum $\hat{\theta_h}$ and $\hat{\theta_v}$ which resulted in the maximum coolant coverage. Explored in more detail, it was found that the tool temperatures actually correspond more closely to the overall tool surface wetting, instead of the small region near to the cutting zone, and in this corner of the design space the spread of the coolant was significantly reduced as it was focused along the cutting edge. This change in behaviour of the coolant flow in milling operations has not previously been observed or noted but could be critical in tool design and performance. Another unexpected feature that was identified in the coolant channel design space exploration results was a region of tool design which created an extremely inconsistent flow with significant amounts of splashing. The results of simulations in this small region of the design space, at around $\hat{\theta_h}$=0.65 and $\hat{\theta_v}$=0.8, were shown to have low wetting, and high tool temperatures, making this very undesirable in most applications. No immediate explanation for where this splashing development is obvious, and it is possible that the Reynolds number could impact where the splashing flow develops. In further work, the presence of this type of coolant flow should be experimentally verified where possible, and further sample points in the vicinity could be added to better understand the effect. The location of the splashing flow could vary in the design space with Reynolds number or other coolant supply parameters which would also need to be taken into account as tool designers look to avoid this region in the future.

The results presented for the design space exploration in this chapter can provide information to tool designers. One can use these results to drive forward suggestions for improvements depending on the application and the requirements of the coolant.

One area for development of the model used in this work could include an incorporation of a correlation between the coolant coverage at the rake face, and the fixed temperature boundary condition at the cutting edge which represents the heat generated in the cutting process. In reality, the application of coolant here reduces frictional forces and heat generation significantly , but this is not captured in the model here and further work on the tribological effects of the coolant application would be required to accurately implement an appropriate correlation.

Chapter 5

Tool optimisation in full slot milling applications

Contents

5.1 Introduction

In Chapter 4, two surrogate model studies investigating the design space for face milling processes were studied, with over eighty new internal coolant channel designs simulated. One finding from these parametric studies was that the vertical component of coolant flow along the cutting edge was a negative, downwards flow in all cases. The coolant flow speed magnitude could be reduced compared to the original standard geometry model but the average flow remained downwards. In many milling applications this would not necessarily have a negative impact, but there are cases which rely on an upwards flow to evacuate chips in an effective way (De Lacalle et al., 2001). Full slot milling is one such application. Examples of full slot milling with various tools are shown in Figure 5.1, with the solid carbide end milling tools modelled in this thesis being observed on the far side.

While face and side milling applications which have previously been considered in chapters 3 and 4 have only a moderate overlap between tool and workpiece (the radial

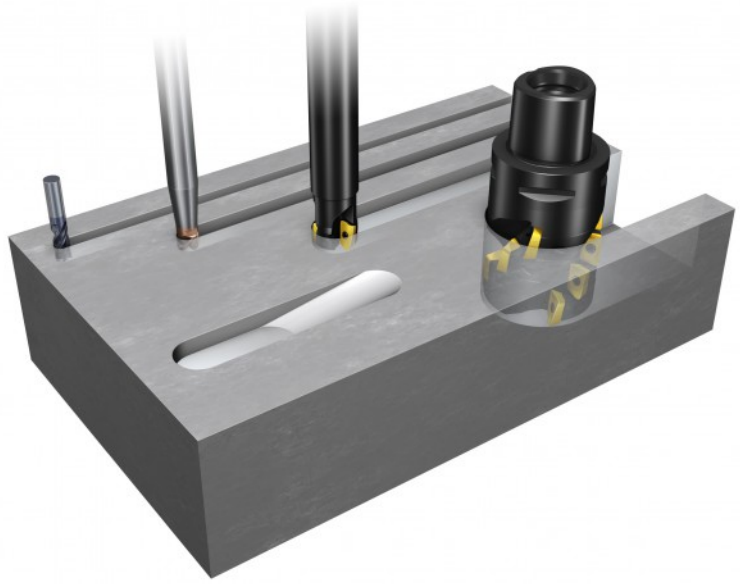

Figure 5.1: Full slot milling examples with various Sandvik cutting tools (Sandvik Coromant website, accessed July 12th 2022).

engagement, a_e), full slot milling involves a complete engagement as the tool is used to machine horizontally into the workpiece, instead of removing material along one side. The clear increase in radial engagement is highlighted in Figure 5.2.

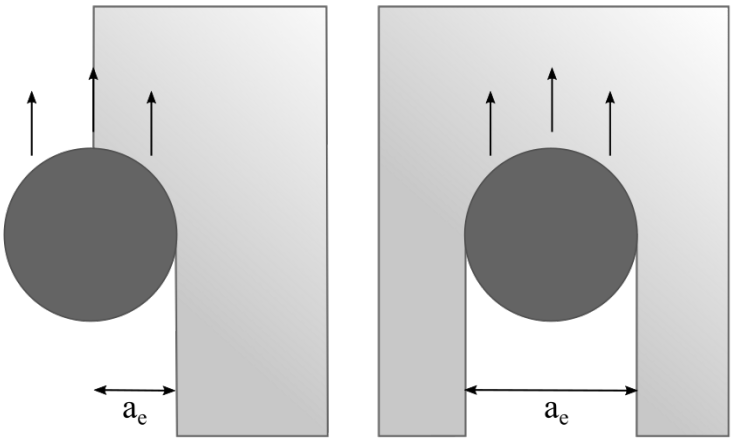

Figure 5.2: Schematic showing different extents of radial engagement, a_e, for a side milling configuration (left) and a full slot operation (right).

Having the tool fully engaged can make full slot milling a demanding operation due to an increased contact length between tool and workpiece, which leads to significantly higher thermo-mechanical loads (Adesta et al., 2018). These increased loads can be managed to various extents depending on the workpiece material. In most materials, decreasing the cutting speeds and feeds can reduce the temperatures and forces respectively on the cutting edge and the high temperatures observed (Sun et al. (2009) Daymi et al. (2009)). Reducing the depth of the slot (axial engagement a_p) can

also offset the increased width of cut by in turn reducing the depth of cut, and has been seen to reduce cutting forces (Lai, 2000).

Another common difficulty of full slot operations can be the problem of chip evacuation. In face milling there is an adequate amount of open space near to the cutting zone in which chips are usually evacuated to naturally, due to the coolant assisting the evacuation and the natural momentum gained through being cut away. In the full slot cases the cutting region is much more contained (Fig 5.2) and the chips aren't always easily removed from this zone (Patil et al., 2014), as can be seen in Figure 5.3. These chips that remain too near to the cutting zone can cause problems such as chip

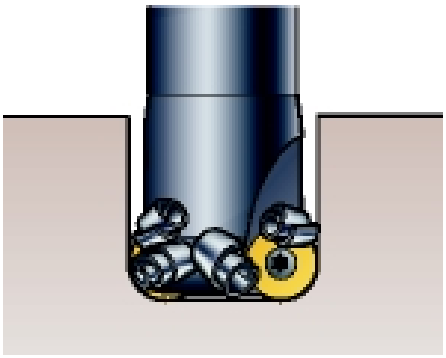

Figure 5.3: Chip jamming and re-cutting illustration for a milling tool with inserts shown for a slot operation (Sandvik Coromant website, accessed July 12th 2022).

jamming or the re-cutting of chips. Problems with chip management can cause damage to the tool and reduce the surface finish quality on the workpiece. Whilst the chips remain in the cutting zone, they also keep large amounts of thermal energy trapped with them (Pabst et al., 2010), meaning the potential for increased thermal wear can be introduced.

Usually chip management with coolant can direct the chips down along the cutting edge and they are removed as the tool turns and the cutting edge in question is disengaged. In the deep slots which can be created here, evacuating the chips downwards is not always so beneficial as they are likely to interfere with the tool base and become trapped. If they are instead evacuated upwards they could leave the cutting zone in any direction. A strong upwards flow along the bulk of the cutting edge would be needed for this to be successful. The previous findings of chapter 4 gathered data for the average flow down the edge and found all of these to be directed downwards. A deeper understanding of the flow is needed before further modifications can be added to the tool.

In this Chapter, the Coromill Sandvik standard milling tool geometry used in

Chapter 3 is simulated in a full slot milling process, with an appropriate new workpiece geometry and the flow near to the cutting edge is analysed. The results for coolant flow in chapter 4 were provided as averaged values over the entire cutting edge region. In reality there could be smaller regions of both upwards and downwards flow and the locations of these could prove critical to chip evacuation. Using these new CFD results for full slot milling and a deeper investigations into coolant flow along the cutting edge, along with the results of the DOE study carried out in Chapter 4, a new tool design is conceived to promote upwards flow and aid chip evacuation for full slot milling. Initial testing of this design is conducted, with a study of the internal channel flow using a single phase model. Once a suitable design is identified, this geometry is tested using the full external flow model described in chapter 3. The new design is compared to the standard geometry using the deeper analysis of the cutting edge flow and the improvements have been quantified.

5.2 Variations in coolant flow near to the cutting edge for a full slot milling case

5.2.1 CFD Case set up

Full slot milling is chosen as the focus of the more detailed study of coolant flow along the cutting edges of the tool, since chip evacuation problems are common in this application. Since the machining application has been changed to a full slot configuration, the setup of the CFD case needs to be updated from the approach presented in chapters 3 and 4. New geometries are needed to simulate the coolant flow. The standard tool geometry remains consistent, with the Sandvik Coromill Plura cooling booster being used again, however the workpiece geometry has been substituted with an appropriate full slot configuration. The two parts are shown together in Figure 5.4.

In previous case setups (chapters 3 and 4), a smaller fluid model domain covering one flute near to the base of the cutting edge was all that was simulated since the axial engagement of the tool was so much lower and the length of the cutting region on the tool was less in the face milling cases.

It can be seen from Figure 5.4 that for the full slot geometries used now, approximately half of the tool's cutting edges are engaged at any given point in rotation. This region of the cutting edge is highlighted in Figure 5.5 for both face and slot milling and it can be seen that the full slot milling cutting region (right) is significantly larger than the face milling cutting region (left). We are interested in a larger horizontal and vertical region in these full slot cases, so a new domain size has been chosen to reflect this. Similarly to the case set up in chapters 3 and 4, one tool flute is the focus of

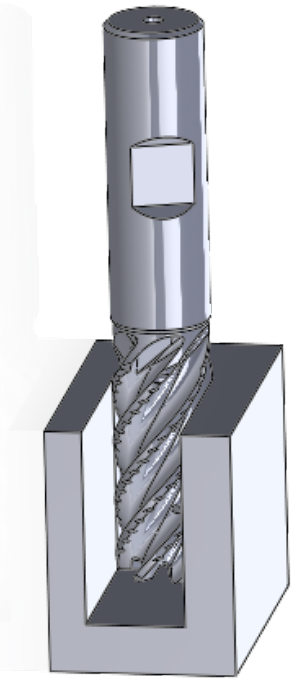

Figure 5.4: CAD geometries used for a full slot milling application. A CoroMill Plura solid carbide end mill by Sandvik, and the workpiece with a machining slot, cut in at a axial depth of 32mm.

Figure 5.5: Engaged cutting edges of the tool for side milling operations (left) with lower radial engagements, and full slot milling (right) with total radial engagement.

the simulations, however, this single flute now extends across a larger radius of the tool, as can be seen in Figure 5.6. As a result, the domain has been extended both in terms of height and reach around the tool as it is preferable to include as much of the simulated flute as possible. Due to the high axial engagement chosen here it is not

possible to have an entire flute fully engaged with both flank and rake edges contacting the workpiece over the full height but a good configuration should still have each predominantly engaged and the domain needs to capture this. The highlighted flute shown in Figure 5.6, for example, has both rake and flank edge mostly in the engaged light grey section but there is a region of disengaged flank at the base of the tool and a region of disengaged rake at the top.

Figure 5.6: Views of the engaged region of a single flute (blue) from both sides of the tool. Dark grey colouring shows the disengaged regions of the tool, with light grey showing the engaged regions. The blue coloured single flute spans the height of the tool and can not be seen in entirety from a single perspective.

In this study, the primary focus is on the coolant flow field along the tool. In order to save time and resources therefore, a single region simulation is run in these cases, instead of the full multi-region conjugate heat transfer approach used in previous chapters. This single region simulation method requires a significantly smaller mesh since the tool and workpiece regions do not need to be meshed — but also means a lower level of refinement is needed across the fluid region since mesh independence is observed at coarser refinement levels for these larger scale behaviours than was required for the heat transfer aspect in Chapter 3. This reduction in both meshing requirements and simulation time is beneficial since the domain sizing has been extended significantly. Once meshed, the fluid model applied is the same as described in section 3.3.1. The OpenFOAM volume of fluid solver `interFoam` is used to solve the Navier-Stokes

equations and an additional advection equation to track the coolant-air interface and coolant volume fraction. The coolant enters an air filled machining domain via one of the tools internal coolant channels, with a velocity of 50m/s and impinges onto the workpiece surface and tool edge. The tool and workpiece surfaces act as walls in the simulations with no-slip boundary conditions. Outlets at the edge of the domain at the top and bottom of the flute allow the coolant to flow out of the domain after its application. A full list of boundary conditions can be found in chapter 3, table 3.1. Once the flow has become fully developed, the results are time averaged for the entire region to calculate mean velocity in each mesh element.

The averaged results for the two cutting regions along the flank and rake edges of the tool are then extracted by taking cells within a distance of 0.3mm from both the cutting edge and the workpiece to obtain the mesh regions of high interest. Time averaged velocity fields for the extracted mesh regions can then be processed to spatially average the data and provide results for wetting of the cutting edge dependent on the vertical height along the tool edges.

5.2.2 Visualisation of the coolant flow field

As well as the more detailed quantitative results along the cutting edge, visualisations of the flow are again informative for broader behaviours in this full slot application. In Figure 5.7, the development of flow for these full slot simulations is observed. This view of the coolant coverage of the fully engaged portion of the tool faces is seen through the workpiece perspective as it impinges on this surface, with the red regions showing the coolant and the blue regions having only air present. Beginning at time t=0.0001 seconds, the jet impinging on the workpiece can be seen in Figure 5.7 (a). The coolant jet then spreads out radially across the tool flute being simulated to the top and bottom edges of the flute, which are the rake and flank respectively (b-f). Observing the development of the flow is useful to inform the beginning of the time averaging period, which in this case has been taken to start at time = 0.00065 seconds (Figure 5.7 g) and shows that the simulations reach a level of steady behaviour with the flow in the regions of interest having a broadly similar appearance after this point. The coolant coverage appears very good below the impingement point and covers most of the flute and both edges for the lowest parts of the tool. The rake face which lies at the base of the flute in these visuals, also shows coolant flowing up the length of the tool edge, though the quantity is reduced compared to below the impinging point. There is also a reduced application of coolant above this point on the flank edge (at the top of the flute); for a large region at the top of the flank edge there appears to be very little coolant reaching the space at all, and even the coverage that does find the middle region of the flank appears to be less consistent and more splashy in nature,

with the wetted red regions sporadic and spread over the edge instead of covering a large region, as was seen on the rake face.

The impingement point in the new full slot case is relatively low in the domain now that the domain and cutting edge are extended to greater vertical heights. This means that a lot more of the cutting edge being used lies above the coolant application point and is likely to see more positive vertical flow than was found previously in chapter 3.

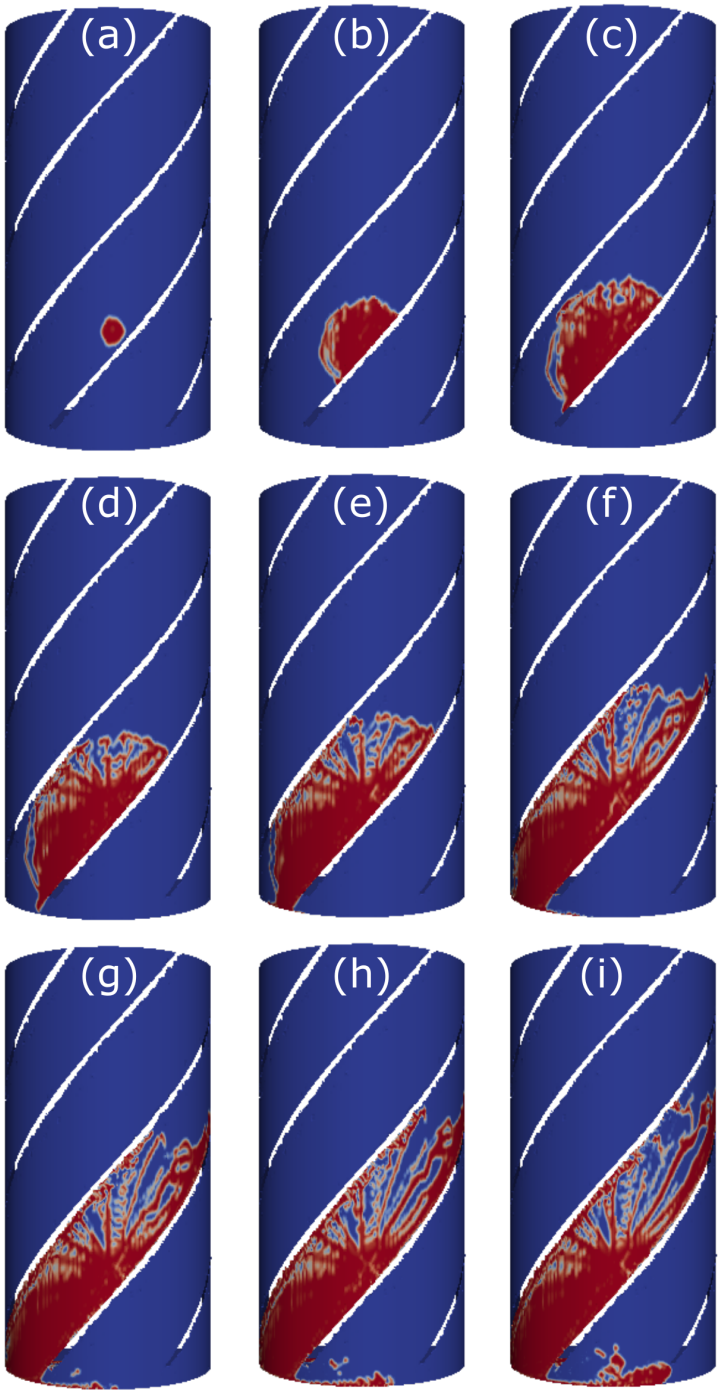

Figure 5.7: Wetting of workpiece surface with the development of the flow field.

The magnitude of the coolant velocity near to the workpiece surface is shown in Figure 5.8. The key features are the same as seen in the face milling case in chapter 3, with a clear stagnation region where the jet impinges and high speed flow surrounding this region. The flow speeds below the stagnation point are higher than those seen above the same point, which is likely caused by the direction of the coolant jet as it is applied — with a high vertical angle and a natural downwards momentum due to the coolant channel design. There is a high speed flow of between 40-60m/s over much of the workpiece region below the impingement point, but the region above shows the flow slowing down as it travels up the rake edge. The same region on the flank edge above also shows significantly slowed flow.

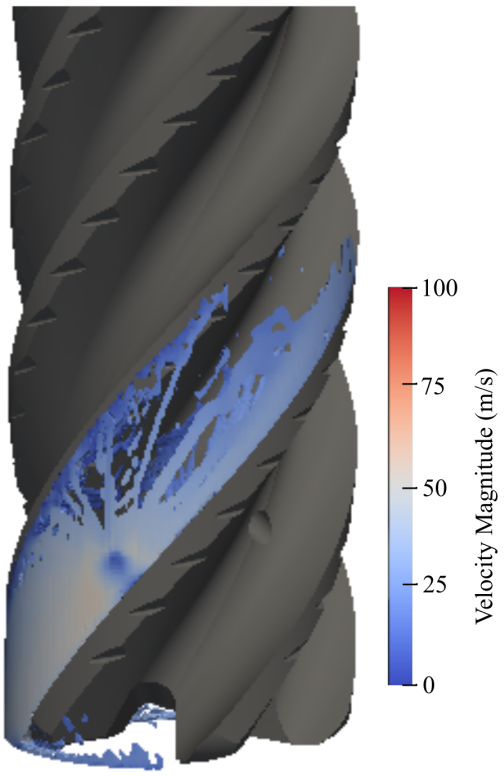

Figure 5.8: Contour plot of velocity magnitude (m/s) for coolant flow applied at 50m/s from the coolant channel inlet for a full slot milling application. Results are filtered using a volume fraction ($\alpha > 0.5$) to show only the mesh elements containing high quantities of coolant.

The better coolant coverage and higher flow speeds below the jet impinging point suggests the bulk of coolant is applied to the lower section of the tool which is confirmed by analysing the volumetric flow radially around the coolant jet. A sample is taken along the axis of the coolant jet at a small radius and split in two to determine the upwards and downwards flow out from the jet site. The sample location is highlighted in Figure 5.9 with the sample over the red dashed surface presumed to flow down the tool and the sample over the blue dashed line presumed to flow up.

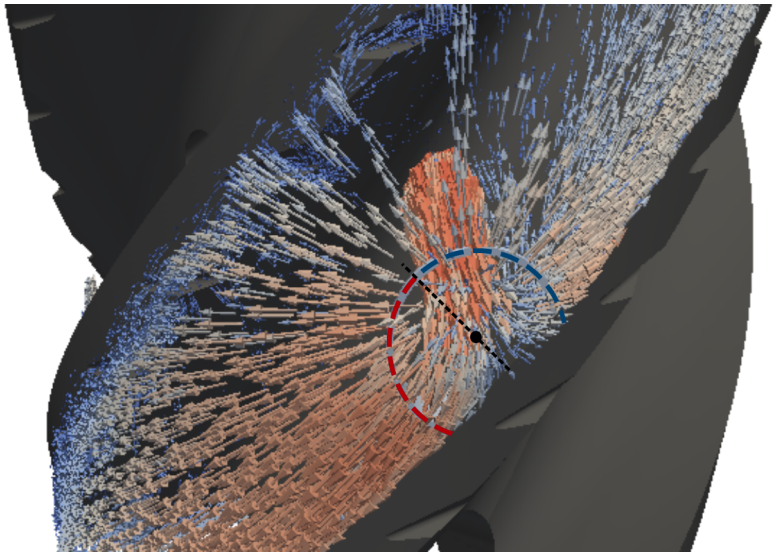

Figure 5.9: Coolant flow is sampled over through a sample slice at a fixed radius. The sample region for coolant flow direction is taken over a fixed radius of 1mm from the centre of the impingement (shown with a black dot in the figure). The sample has been divided into flow directed up the tool (through the blue dashed sample line) and flow directed down the tool (through the red dashed sample line). The sample region is shown here with glyph vectors representing the coolant velocity for context.

Direction	Velocity magnitude average (m/s)	Volumetric flow of coolant (m^3/s)	Percentage of coolant
Upwards	49.75	10.00×10^{-4}	21.8%
Downwards	59.82	3.58×10^{-3}	78.2%

Table 5.1: Flow directed upwards and downwards from coolant jet impingement.

The results are filtered to only consider the region of the sample surface which contains coolant since this is the element interested in and any high speed air flow in the vicinity could skew the results. Results, shown in table 5.1, make clear the disparity, with over 78% of the coolant directed downwards from the impingement site. This directing of the coolant somewhat offsets the benefit of having such a low down application site on the flute which was expected to generate upwards flow due to the extended space above.

5.2.3 Numerical results along the cutting edges of the tool

Numerical results have been collected along both the rake and flank edges and the variation with height has been monitored. The data has been averaged in 50 bands which split the velocity data over vertical height intervals. The results for this standard tool geometry for coolant coverage and velocity are shown in Figures 5.10 and 5.13 respectively for a fully engaged cutting edge. Firstly the results for wetting/flooding

of coolant are considered (Fig 5.10). The time averaged results are given by the solid red line and the standard deviation over the time period used for averaging has been shaded on to indicate the variation over the domain during the chosen sampling period.

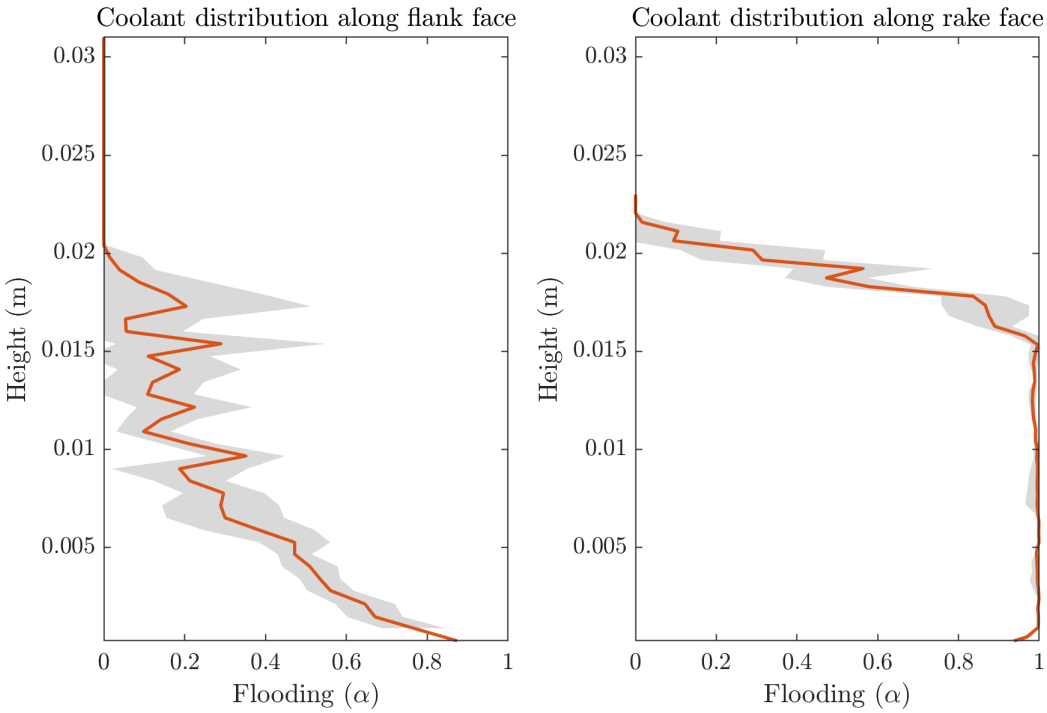

Figure 5.10: Average profiles for coolant volume fraction over the length of tool cutting edges (left: flank face, right: rake face). Time averaged results are plotted as mean value in red and one standard deviation over the time period is shaded on either side of the mean values in grey.

As expected from visual inspection, the coolant coverage is very good at the base of the tool for both edges with the flooding/volume fraction values averaging close to one. The volume fraction of coolant stay very high at a near maximum value of 1 along the majority of the engaged rake face. About half way up the coverage begins to decrease sharply. The rake edge starts to disengage the workpiece earlier than the flank side and the full contact reduces from a height of roughly 0.019m. This likely is having a large impact but the flow is reducing before this point and the reduction in flooding starts lower down in the domain than this point and it could be seen in the visual examination that flow appeared to be reducing in quantity and speed as it spread up the cutting edge. Across the whole engaged rake edge however, a coolant flooding percentage of over 30% is seen, which still indicates a quantity of coolant is reaching the entire region and hasn't shown any length of the tool edge receiving no coolant at all.

Although the coolant distribution along the rake edge decreases quite quickly from the maximum value of one to minimal coverage as the position along the height of the tool is increased in figure 5.10b, there is actually a layer of coolant covering the cutting

edge surface the whole way up the edge to the point of disengaging. The quantity and therefore flooding percentage in this thin sample instead decreases so a thinner layer of coolant is seen as one moves up the tool. This behaviour is clearly shown in Figure 5.11 where the layer of coolant applied reduces significantly near to the top of the tool edge.

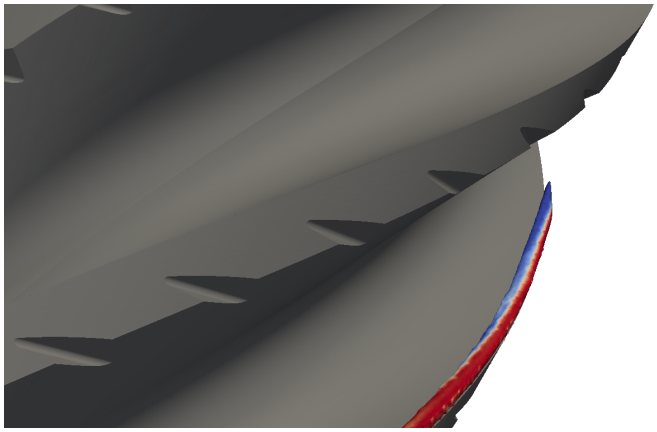

Figure 5.11: Flooding near to the top of the rake face in the sample region. The base of the sample region shown here has a high volume fraction in red, but the proportion of blue colouring in the sample increases as one moved up the height of the tool. The coolant region becomes a thinner layer but remains located along the edge.

This smaller layer of coolant would still most likely be enough to provide the important layer of lubrication to the cutting edge and reduce friction here along the whole length but the reduction in the quantity could have other impacts. A reduced amount of flow is less capable of providing the strong carrier for chip evacuation which is beneficial in full slot and it could have further impacts on the heat transfer near to the cutting edge. In addition to the layer thinning as it progresses up the tool, it is arriving at the top of the tool having already travelled over the hot cutting edge surface which could limit its potential for transferring heat away at these higher regions. The isothermal simulations carried out here cannot address the possibilities and a full study including the multi-region conjugate heat transfer model would be needed to fully establish this behaviour.

Figure 5.10 shows that the coolant distribution along the flank edge is more variable. The mean value shows sharp fluctuations across the length of the tool and the standard deviation shaded in grey is larger than the rake face observations. Visual inspection of the flank edge showed a much less consistent wetting in Figure 5.7, but upon further inspection, much of the coverage remains roughly steady as the time steps advanced, leading to these sharply defined regions of high and low flooding on the flank. The features can be matched between the graph and visualisation results, as seen in Figure 5.12.

Figure 5.12 shows the simulation results scaled according to the graph y-axis

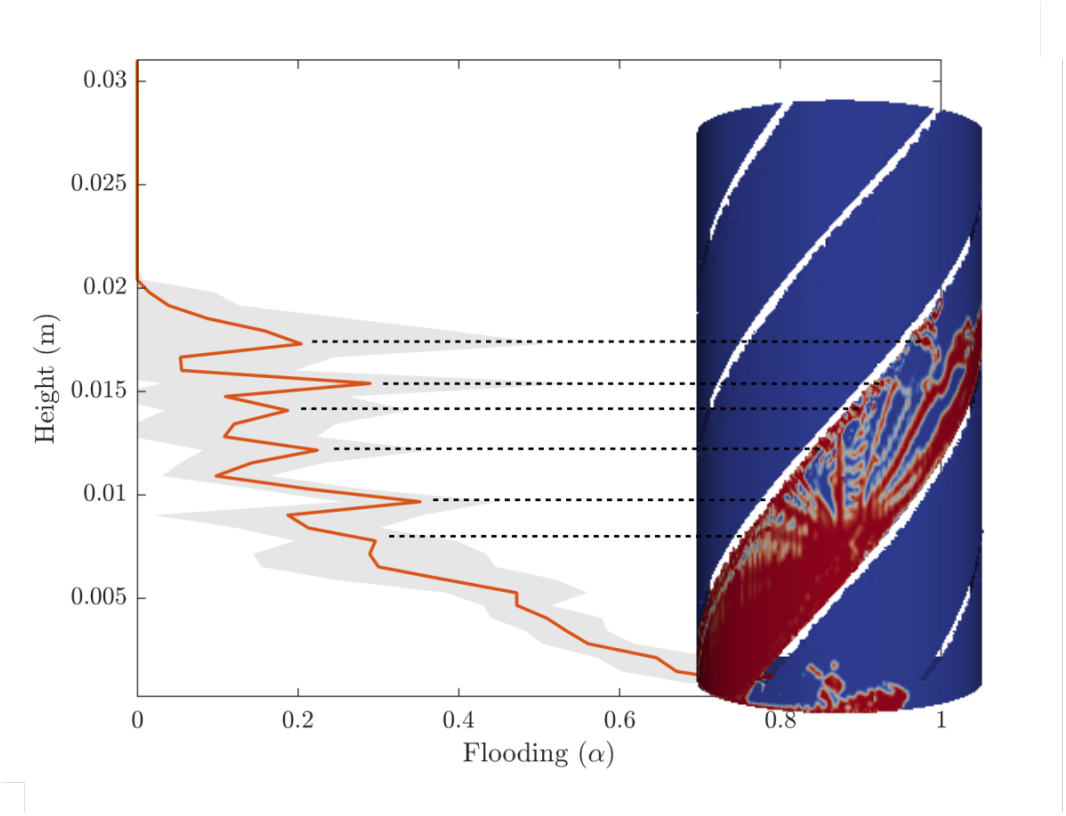

Figure 5.12: Feature mapping of coolant on the flank edge. The spikes in volume fraction flooding (Fig 5.10) in the numerical results match to the regions of consistent coolant application in red in the visualisation.

and the spikes correspond to the region with streams of coolant interacting with the flank edge in the visualisation, with the generally larger spikes seen as the background coolant reduces as one moves up the edge. Nearly a third of the edge sees no coolant at all (the top third) and low supply ($< 50\%$) is seen for most of the flank. Again, this would provide an element of lubrication to the edge but that is less useful on the flank as it was on the rake edge since the flank follows the actual cutting edge instead of preceding it.

The results for the vertical component of the velocity along both edges is shown in Figure 5.13. Flow along the flank edge shows a relatively low speed for most of the tool edge and this is negative for the bottom third of the tool edge, which coincides with where all the high wetting was seen in Figure 5.10, and suggests the bulk of coolant applied to the flank edge has a downwards vertical component. There is a region of positive vertical flow in the middle third of the tool edge where a lot of the splashing and inconsistent wetting was seen. Much of this region however shows a very high standard deviation, suggesting the flow is less steady here which is perhaps expected in this area of high splashing.

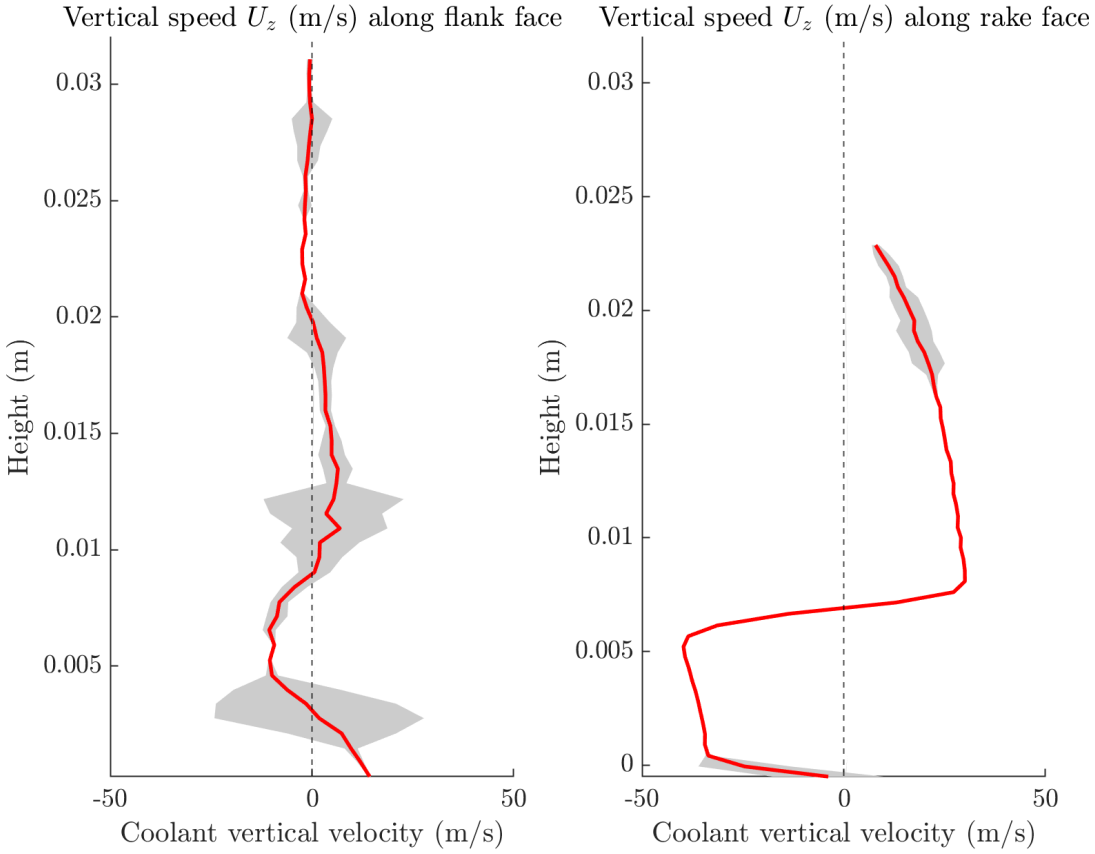

Figure 5.13: Average profiles for coolant vertical flow over the length of tool cutting edges. Time averaged results are plotted as mean value in red and one standard deviation over the time period is shaded on either side of the mean values.

The magnitudes for the flow on the rake face are generally higher values, with a maximum upwards flow of 26.8m/s and maximum downwards flow of 38.7m/s. The largest magnitude values are observed on either side of the impingement location with a smooth acute change between the two extremes seen around ≈ 0.007m. Moving away from the impingement site, the magnitudes of both the upwards and downwards flow decreases, either to the base of the tool or disengagement with the workpiece. Since the point of impingement is low here and the axial engagement is so high, the majority of the edge actually sees good upwards flow, which is beneficial for the chip evacuation. The flow is also very consistent, with only negligible standard deviation over the fully engaged region of the tool. We know however that the actual volumetric flow of the coolant shows a heavy downwards directional bias which was highlighted in the Figure 5.10 for the rake edge.

Even though the standard tool geometry shows improved vertical flow in the full slot application compared to face milling - there were still design potentials high-

lighted in the Design of Experiments study in Chapter 4 which showed improvements could be made. Previous results showed a reduction in the vertical angle of the coolant channel and a reduction in coolant speed both reduced the average magnitude of the downwards coolant flow. A new tool design could enhance the upwards flow further and potentially deliver it in higher volumes up the rake or flank faces.

5.3 New tool designs

There were several important parameters which were not explored in the previous design space studies in Chapter 4. Two important variables for vertical coolant flow were expected to be the vertical channel angle, θ_v and the channel exit height, H. Although the vertical angle was chosen as a variable for study in the second DOE case in Chapter 4, there were only small improvements which could be achieved even when reducing the channel angle to 0 degrees. The problem in these low angle cases was that, although the coolant was directed more evenly across the tool/workpiece impingement surface than in cases with a large vertical angle, the impingement site itself was higher in the domain. If the site of impingement could be lowered while maintaining this small vertical angle then there is a good potential for considerably increased upward directed flow. Channel height exit, H, was raised as another variable of interest when the design space was analysed and reducing it here would achieve the desired shift in coolant application site. The channel exit height could be reduced to a very small value in theory. This would lower the site of impingement to be down towards the tip of the tool, however this is not usually desired for solid end-mill tools such as this. In practise, as these tools are used and wear down, they can often be reconditioned so that the end is reshaped and sharpened to promote a much longer tool life (Kumar et al., 2015). Having coolant channels very near to the tip limits this practise as they would interfere with the new tool shape once it had been cut down.

A new tool design will be tested here, combining the small vertical angles where the best vertical speed, U_z results were observed previously, with a parameter study on the channel exit height. The height, H, will be tested over 4 values between 5 - 20 mm. This is seen in context in Figure 5.14 on the left where the tip of the tool at height 0mm is marked as (f), the axial engagement, and therefore the top of the workpiece, is marked (a) at 32mm, and the letters (b) through (e) mark the new channel heights to be tested at 20,15,10 and 5mm.

To further introduce more coolant near to the base of the tool a new design concept is also introduced. In drilling tools, through-tool coolant exits the tool near to the tip and this results in a largely upwards flow and greatly assists chip evacuations.

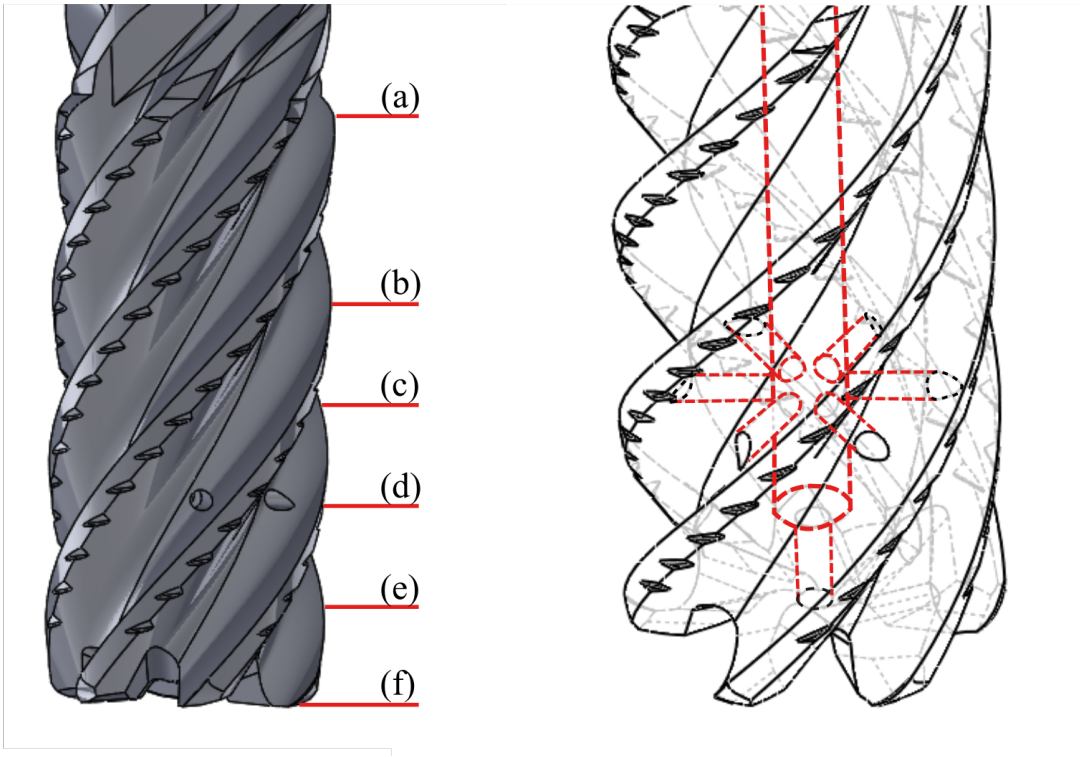

Figure 5.14: CAD geometry and drawing of channel heights and new axial channel features
Left: New tool design with vertical coolant channel angle, θ_v equal to 0 degrees. Additional height markers (a),(f) show maximum axial engagement and tool tip heights respectively. Markers (b)-(e) show the points at which the coolant channel exit height will be 20,15,10 and 5mm from the tool tip.
Right: Internal coolant channel configurations shown in red with a new axial channel accompanying the six radial channels.

Although milling tools profit more from the radial coolant channels in each flute which are used here, a new axial coolant channel will complement these in a trial design to investigate the effect of the contributions. Along with the six radial coolant channels, an axial channel is added as seen in Figure 5.14 on the right.

5.4 Internal channel analysis

The addition of an axial coolant channel to the geometry is a concept that needs to be investigated at a simplified level initially. The quantity of coolant which will be directed through axial or radial channels and the changes in pressure drop over the system need to be assessed to identify suitable designs. A small internal channel flow parameter space is investigated using a DoE with the axial and radial channel diameters taken as the two design variables. The axial channel diameter is varied between 0.5 to 1.5mm

and the six radial channel diameters are varied between 0.75mm to 1.5mm. They are usually fixed at 1.29mm for the standard tool geometry. 20 sample points are generated over this design space, using an optimised latin hypercube method. For a full methodology of the DOE process, please refer back to chapter 4. A 'blank' tool template is used as a foundation for the geometries. This simplifies the external features of the tool and provides clear features for the channels, as seen in Figure 5.15.

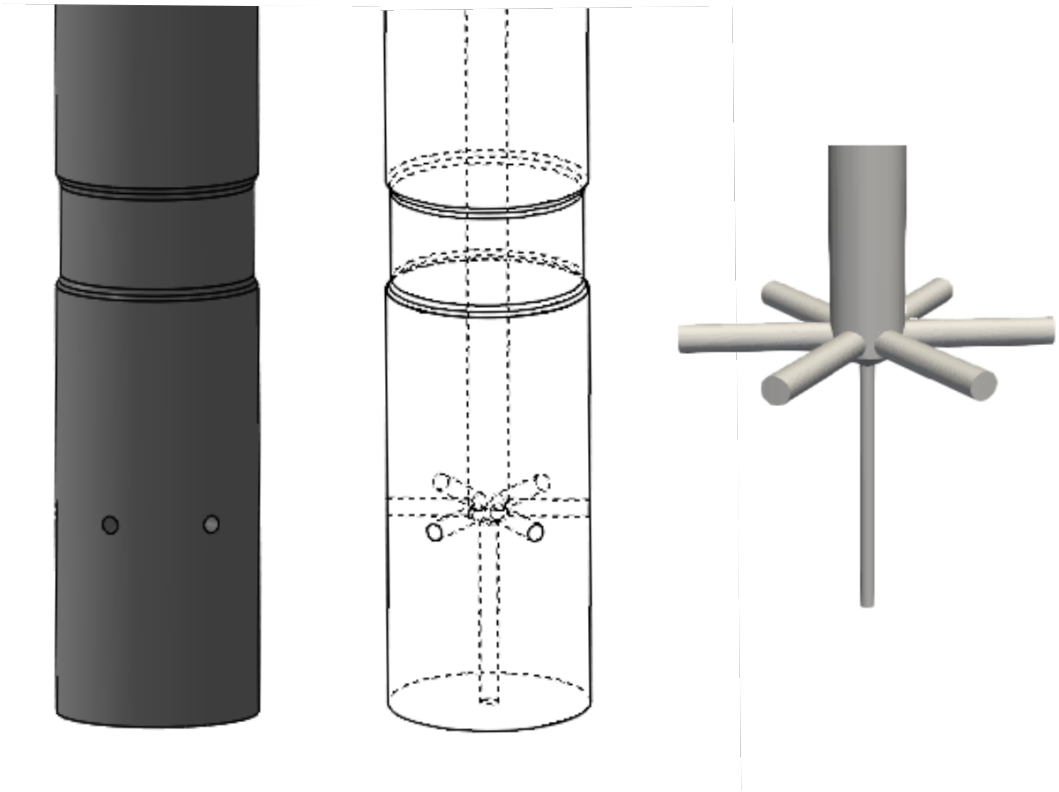

Figure 5.15: Blank tool geometries with the outer cutting features to the tool simplified to a smooth cylinder are used for the internal channel simulations.
Left: Full tool geometry example. *Middle*: Interior of blank tool geometry. *Right*: Domain used for internal channel simulations which includes all internal channels.

It is expected that the tool channels will be flooded with coolant and so a single phase model is used here. The OpenFOAM solver `simpleFoam` is used for a steady state, turbulent simulation with the $k-\epsilon$ turbulence model used. The geometry is once again automatically meshed using the `snappyHexMesh` tool, with only the fluid region retained. Once the simulations have converged, results are extracted on slices of the domain at the end of each of the channels. Coolant speed is extracted from both the axial and radial channels in each simulation and the pressure relative to the zero pressure channel outlets is recorded at the inlet. From this data, and using the dimensions of the coolant channels in each case, volumetric flow rates have been calculated, along with the proportion of the coolant flow which will be applied through

the new axial channel.

This case setup and simulation has been carried out at each of the twenty sample points in the design space, with the design variables of both coolant channel diameters varied. Radial basis functions have been used to create a metamodel from the extracted simulation results following the methodology outlined in section 4.2. A multiquadratic function has been used to fit the response surfaces and they have been validated using a k-fold cross validation approach with 3 points left out in each case and a golden search algorithm applied to tune the β parameter in each case. The RMSE variation with β as it is optimised is shown for each case in figure 5.16.

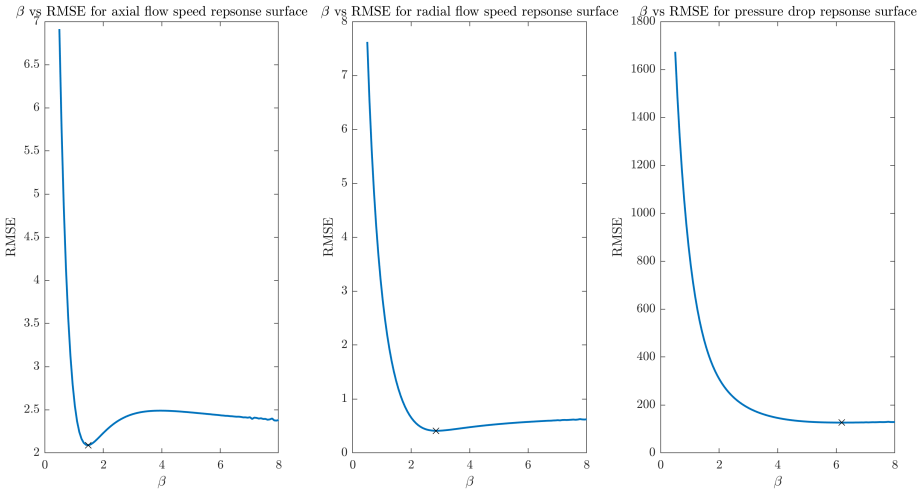

Figure 5.16: Plot of tuning parameter β against RMSE for the axial flow speed, radial flow speed and system pressure drop during golden search algorithm optimisation. Optimal minima for each β value are marked with crosses.

Response surfaces for the coolant speeds and pressure drop can be found in Figures 5.17, 5.18 and 5.22.

The results for the coolant channel exit speeds in both channel types are shown in Figures 5.17 and 5.18. In both sets of results, the ranges over the design space for coolant speed were observed to be roughly the same ($\approx 40 - 130$ m/s). The radial channel diameter seems to be the dominant variable; The smaller the radial channel diameter, the higher the flow rate for both axial and radial outlets. For the axial channels this will be due to higher volumes of coolant exiting in this direction due to the increased pressure and constriction of other channels. For the radial channel results, the effect can be explained due to the fact that a smaller channel diameter increases the flow speed and so increases in pressure drives higher speeds and is enough to offset the decreasing volumetric flow rates.

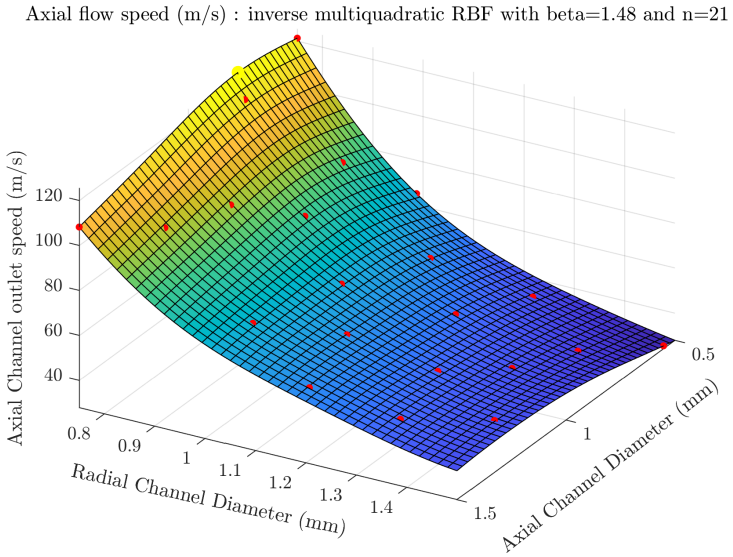

Figure 5.17: Response surface fitted using an inverse multi-quadratic radial basis function for axial coolant channel exit speed for DoE study of the axial and radial channel diameter parameters.

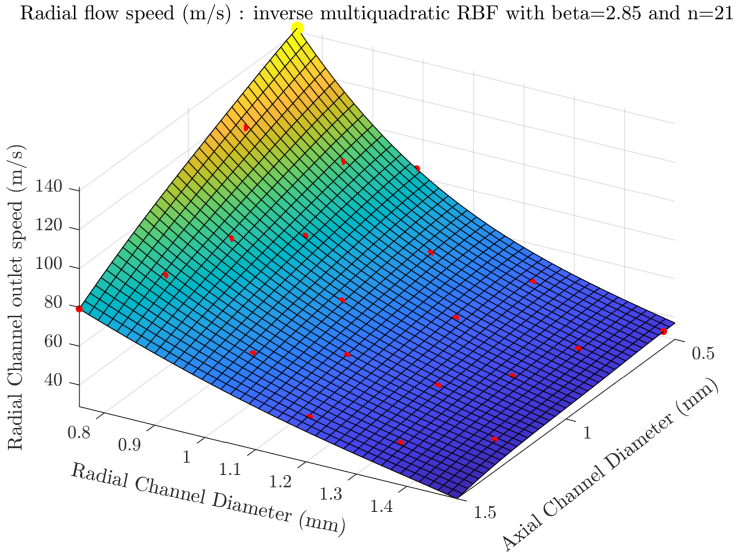

Figure 5.18: Response surface fitted using an inverse multi-quadratic radial basis function for radial coolant channel exit speed for DoE study of the axial and radial channel diameter parameters.

The effect of increasing the axial diameter is to reduce the coolant speed in the radial channels across all radial diameters. Axial channel speed on the other hand increases with axial diameter at large radial diameters, but at small radial diameters, it decreases with increasing axial channel diameter. At some point across this transition, the increased flow rate is beginning to have a larger impact than the increased pressure.

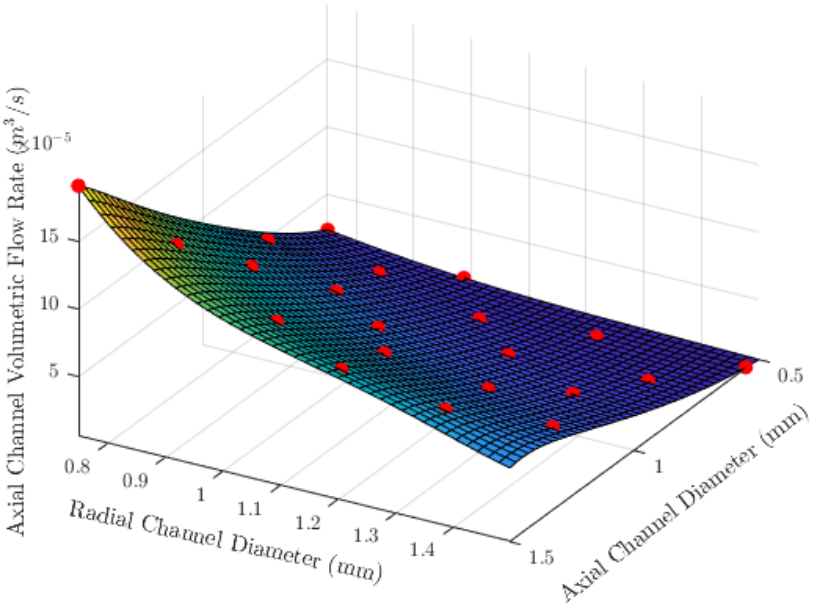

Figure 5.19: Axial coolant channel volumetric flow rate calculated from the response surface for axial coolant channel velocity (Fig 5.17).

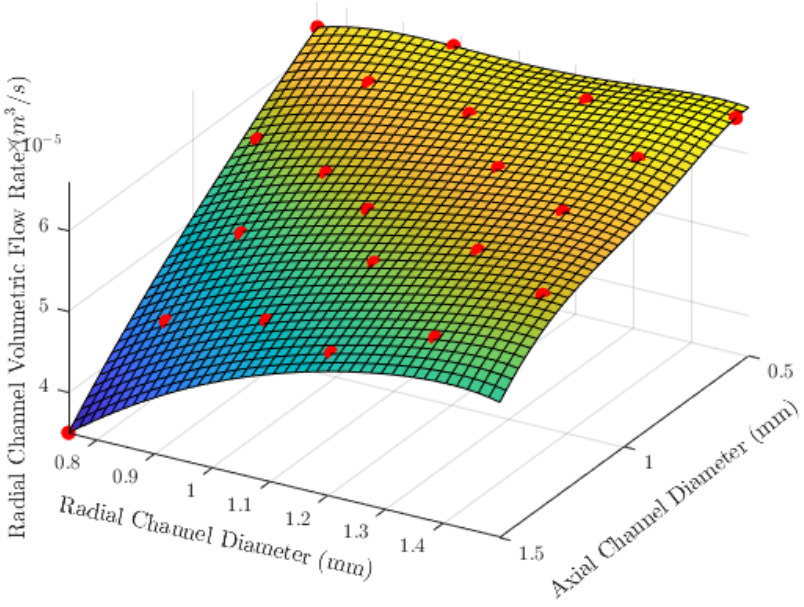

Figure 5.20: Radial coolant channel volumetric flow rate calculated from the response surface for radial coolant channel velocity (Fig 5.18).

Results for volumetric flow rate are given in Figures 5.19, 5.20. The highest volumetric flow rates for each channel are found near the design space corner where that channel diameter is largest, and the other is smallest, which is an intuitive result as it maximises flow through these channels. For the axial results this is much clearer,

but for the radial results in Fig 5.20 there are high volumetric flow rates along most of the region with low axial channel diameters - not just in the corner where the radial diameter is highest. These low axial channel diameters force the large bulk of the coolant to flow through the six radial channels and so, although we saw in the response surface for radial channel speed that there was a significant change in flow speed, the actual volume of coolant is only minimally affected.

The percentage of coolant from the central supply channel to the new axial coolant channel is given in Figure 5.21. The surface shows the same trends as that of the volumetric flow rate surface for axial flow. The percentage remains under 50% throughout the design space, which is expected since there are six radial channels and only a single axial channel, so even attaining a 50% coolant flow here is high compared to the 8% which would be resultant in each of the radial channels. The axial diameter has a large impact on this flow percentage; Where the axial diameter is low the percentage is under 10% and a higher diameter is needed on this channel to ensure a substantial amount of coolant exits through the new channel. It is as of yet unknown what % of coolant is needed to change the external flow dynamics for a full external model test similar to those carried out in Chapter 3 and achieve the desired goal of increasing the upwards flow along the cutting edge.

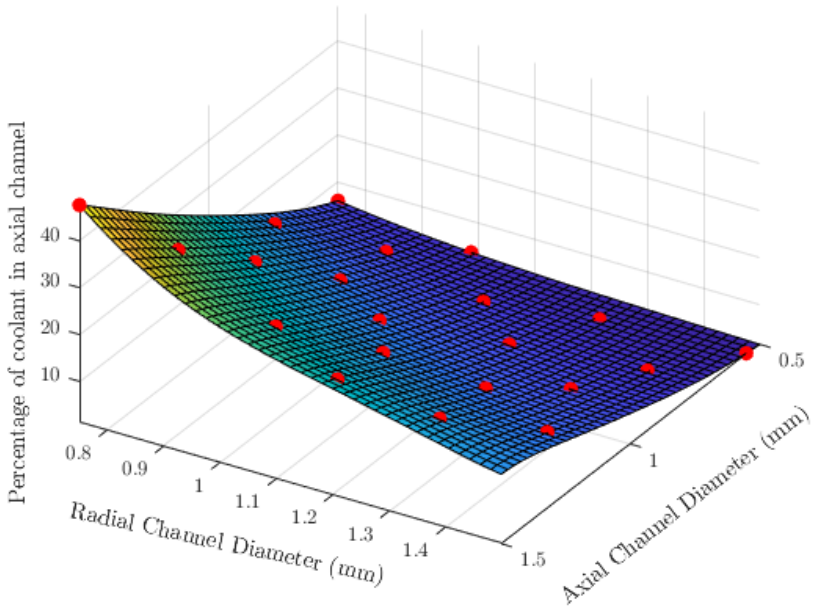

Figure 5.21: Response surface calculated for the percentage of coolant flowing through axial coolant channel compared to the total supplied through the main inlet channel for DoE study of the axial and radial channel diameter parameters.

Finally, the pressure drop over the internal channel design space has been studied in Figure 5.22. The design space corner with both channel diameters at their smallest is the location of the largest pressure drop, which was to be expected. There

is a steep increase in the pressure drop near to this point, with many solutions in the near vicinity offering significant reductions. There is a reduction of almost 75% in the pressure drop as axial channel diameter is increased from minimum to maximum value — even while retaining the minimum diameter option for the radial channel.

An internal channel simulation with a standard model was carried out in order to get some context for the pressure drop and flow rates seen here. The pressure drop in the standard case was 1713 Pa, which is lower than most of the values seen in the new channel designs. Even though an additional channel has been added with an extra outlet for the coolant, the channel diameters are extended to a range smaller than the standard tool geometry uses which has caused this increased pressure drop. If there were significant improvements to be made, a small increase in the pressure drop and hence power needed to pump the coolant could be considered, but this could not extend to the highest pressure drop seen here of over 19,000 (an increase of an order of magnitude).

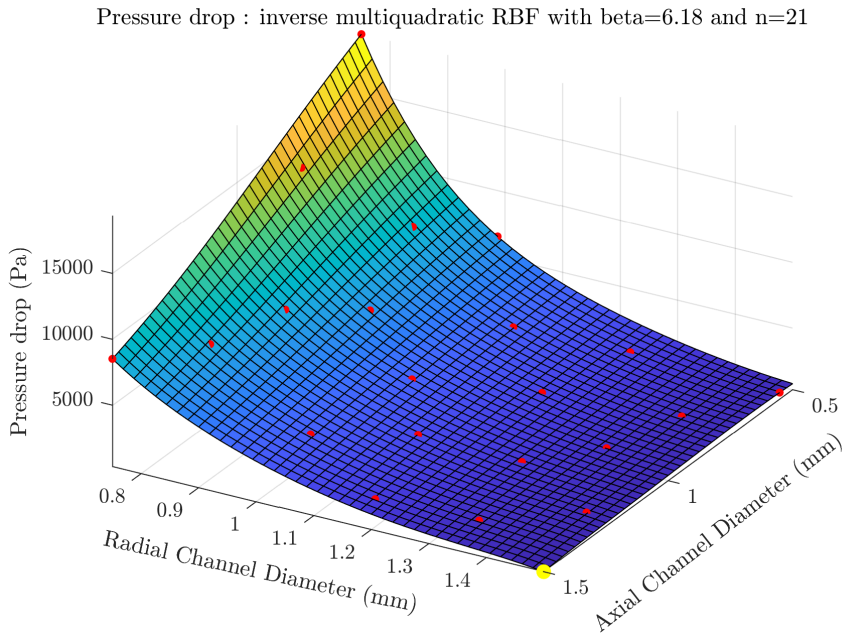

Figure 5.22: Response surface calculated for the pressure drop over the internal coolant channels system for DoE study of the axial and radial channel diameter parameters.

When developing the new tool design and including the axial coolant channel, a large proportion of coolant may need to exit through the new channel to have a significant impact. Some of these high axial flow percentage tool designs, however, have been seen to coincide with significant pressure drop increases as the radial channel diameter decreasing is the largest contributing factor. As well as each of the individual results set being searched for an optimum solution in single objective optimisation studies, here a multi-objective optimisation is carried out to minimise both pressure drop and the percentage of coolant through the radial coolant channels (therefore maxim-

ising percentage flow through the axial channel). A multi-objective genetic algorithm implemented in MATLAB has been utilised to identify a series of optimal points in the design space.

This allows the selection of tool design where an appropriate trade off can be made. A selection of optimal Pareto points is found throughout the design space which provide points for which any improvement for one of the objective functions would mean a compromise in the additional objective function. The pareto front of optimal points can be seen in Figure 5.23. The pressure drops were limited in this results set to 3000, in order to maintain feasible designs. This limits the radial flow percentage to a minimum of over 70% and as a result, means a maximum axial percentage of under 30%.

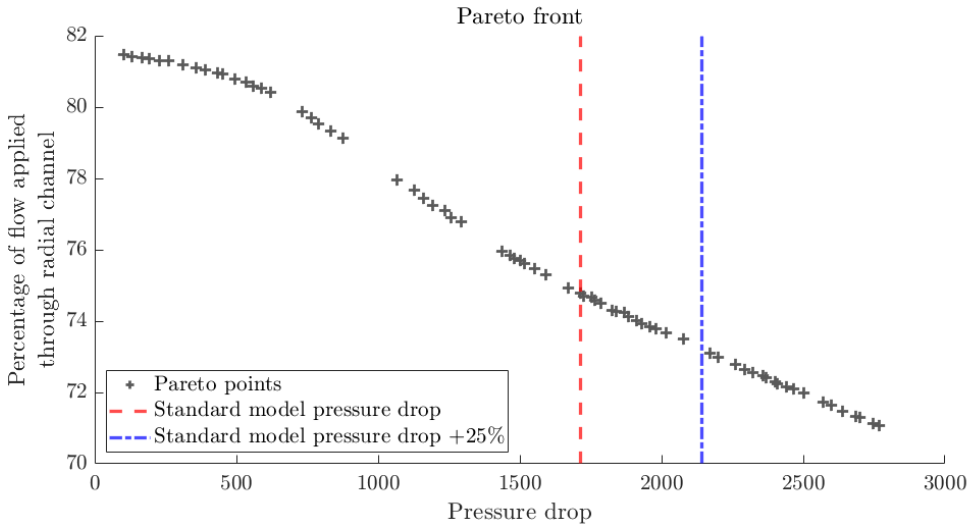

Figure 5.23: Plot of optimal results in a Pareto front for design space varying axial and radial channel diameters for multi-objective optimisation to minimise pressure drop and maximise coolant percentage through the new axial channel.

To provide some context for the pressure drop of the current system, the pressure drop observed in the original milling tool geometry before any modification has been overlain in red, with an increase of 25% of this shown in blue. Here we can see that if an optimal point were chosen to comply with current pressure drop and system power requirements, a minimum radial percentage of 74.92% is predicted. Increasing the pressure drop allowed over the system by 25% provides 73.28% of coolant flow through the radial channels. For the significant increase in power this would need, less than a 2% difference is seen in the flow through each set of channels. For this exploratory study, a new tool design is chosen that operates with the same pressure drop as the standard tool geometry in order to compare the results of the simulations with similar pumping power requirements. This configuration has an axial channel diameter of 1.5mm and a radial channel diameter of 1.17 mm. This tool design will be modified to also vary the heights to the four heights selected previously and shown in

Figure 5.14.

5.5 External flow models

We use the optimised design from the previous section and apply the axial and radial channels at the proposed diameters. Multiple geometries with these configurations are generated, varying the channel exit height H. In all geometries generated, the vertical angle, θ_v, is kept at zero, and the horizontal angle, θ_h, is chosen as close to the cutting edge as possible without impacting its shape, to maximise the coolant distribution here.

Previously, it was discussed that capturing a fully-engaged flute, for a given tool position, is a challenging prospect. In the standard geometry case in section 4.2, a rotational (horizontal) position was chosen which gave a full engagement at the base of the tool for both the rake and flank faces, however, this limited the engagement at the top of the tool. To effectively compare geometries, we would like to keep the configuration as consistent as possible. If the tool maintained a fixed rotational orientation between simulations and the same flute were considered in each, there would be simulations which featured coolant jet impingement near to the edges of the domain which would not provide a full picture of the local flow field. To mitigate this the tool orientation is varied so that for all geometries, the angular position of the tool has been chosen to direct the coolant to the most engaged section of a flute, as seen in Figure 5.24. As a result of this setup however, not all the tools experience the same engagement over the rake and flank edges but the local area around the impingement site should remain comparable and deductions about the behaviour at the base and top of each flute may be needed to some extent.

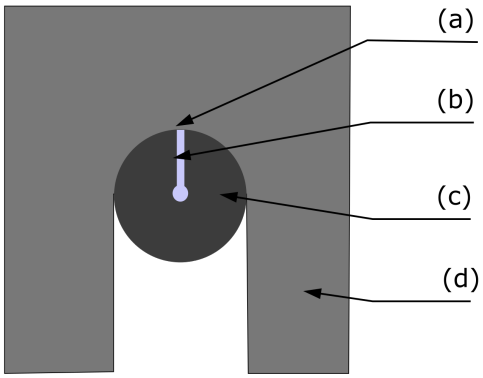

Figure 5.24: Full slot schematic showing the coolant channel (b) orientation directed towards the centre of the engaged region (a) of the tool (c) and workpiece (d) shown as simplified here.

The simulations are set up with a single computational region, the fluid region, as was described in the full slot milling modelling with the standard tool geometries in section 3.2.3. Two separate patches are created in the mesh for each of the inlets and velocities of 46 and 56 m/s are directed along the radial and axial inlets respectively. This is compared to the 50 which was applied for the standard geometry case at the radial inlet and shows that for the radial channels in the new design, there is a clear reduction in volumetric flow rate observed since both the flow speed and radial diameter has been reduced.

5.5.1 Analysis of the coolant flow from the new axial channel

An initial simulation is run applying coolant through only the new axial coolant channel to determine the flow this produces without interference from the additional radial channels. The results, presented in Figure 5.25, showcase the flow as seen from the base of the tool, as though looking up through the workpiece surface. The shape of the fluid domain is seen as curved and then straight which follows the shape of the workpiece which confines the tool and fluid. The domain extends past the region of engagement slightly and along the cut slot to provide more insight and fully include the axial channel flow, which exits the tool tip from the central axis. As seen in Figure 5.25 on the left, the flow impinges on the workpiece underneath the tool and spreads across this surface evenly. As it spreads out from the tool centre point, the even flow is disrupted by the six contact zones with the tool at the tips of each flute. This is seen in both the images in Figure 5.25 as it separates the flow at these points and creates regions with no coolant present (areas seen in blue). Apart from this disruption to the flow, the coolant covers the base of the slot in the workpiece until it reaches the the edges of the domain. At this point, the coolant either flows out of the domain along the workpiece surface (seen at the bottom of figure 5.25) or reaches the sides of the slot and is redirected upwards along the workpiece (the top and side boundaries of 5.25)

Figure 5.26 shows the flow up the sides of the workpiece, using a threshold filter to select only areas of the domain which are occupied by coolant and coloured to represent the velocity within these regions. Again, the view is technically as though looking through the surface of the workpiece, which is not shown due to the obstructive nature of its placement. Here we can see the coolant flow from the axial channel once it has flowed over the base of the workpiece. Once the coolant reaches the side walls of the workpiece region it is forced to change direction and flows upwards over this surface until it interacts with the tool cutting edge and then appears to be diverted to flow upwards along this surface instead to provide a well flooded region along the base of the flank edge.

The curve of the tool means that the contact zones at the base almost com-

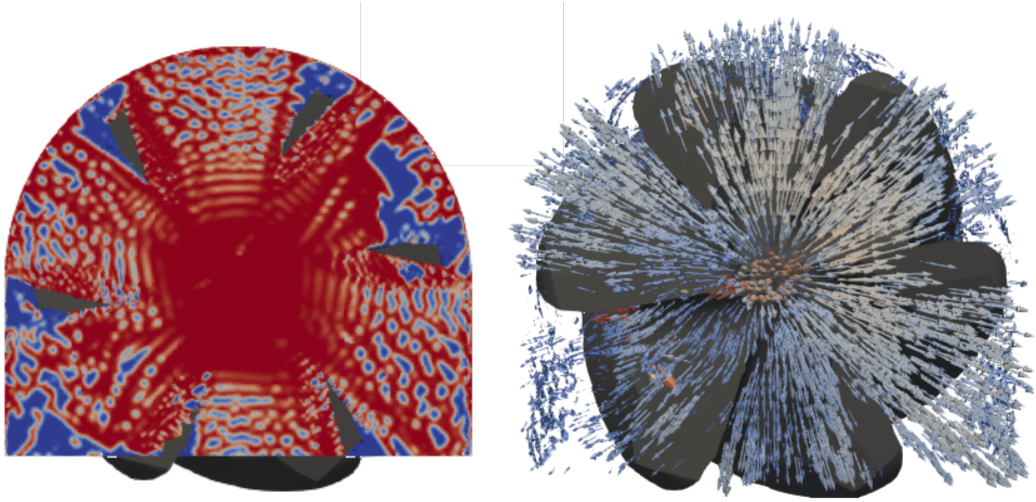

Figure 5.25: Axial channel coolant flow shown by looking up at the tool base from the workpiece perspective. Coolant coverage (left) is represented as volume fraction with red regions showing the presence of coolant and blue showing the surrounding air. Flow speeds in the coolant region are shown using glyph vectors for the same view on the right.

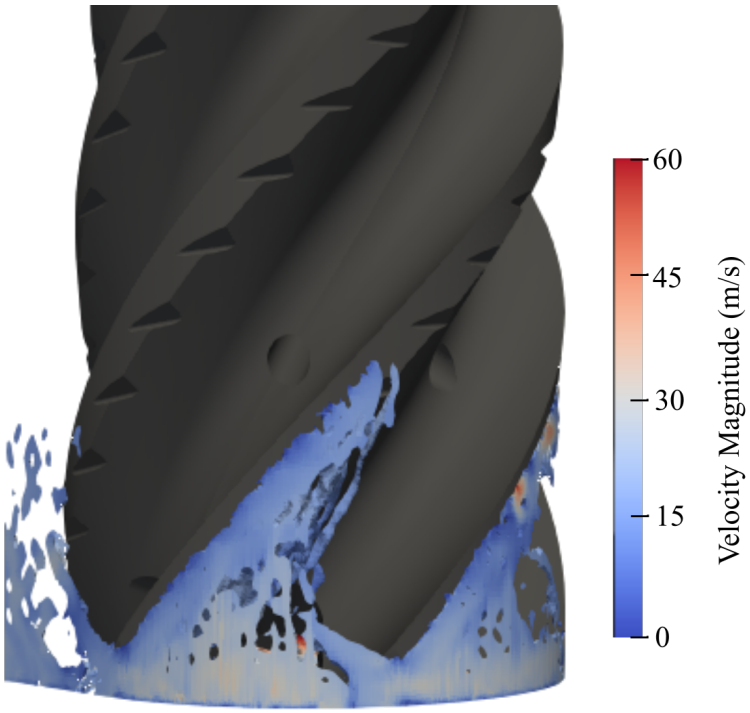

Figure 5.26: Visualisation of the coolant flow up the tool flutes resulting from the supply via the axial coolant channel, shown here using a threshold filter so that only the mesh elements with high proportions of coolant are visualised.

pletely restrict any of the new axial flow from reaching the rake face. This was the primary region of interest for an introduction of new upwards flow in order to combat the strong downwards flow usually seen here and to remove chips from the region. As

a result this may limit the success of this new design feature. There could likely be modifications made to the tool in order to combat this behaviour. Some small deformation of the back of the cutting edge on the flank side could redirect the upwards flow along the rake edge instead or the axial coolant flow could be modified at the base of the tool. This could mean increased complexity of applying it through six individual channels at the tool base instead of through a central one or modifying the base of the tool to better direct the coolant towards the rake face from underneath the tool. Most of these modifications would require some addition or change to a part of the tool in contact with the workpiece — since most of the flow observed is dictated by flow along the workpiece. This would effectively either change or introduce a new cutting zone which is outside of the scope of this work but has potential for future work which incorporates the machining mechanics more comprehensively to ensure the cutting design is not compromised.

The coolant flow from the new channel does introduce a good flow along the tool base however where we could potentially get chip re-cutting usually. This could prove to still have a positive impact if any chip which reaches the base of the tool is then carried outwards towards the workpiece and up along the rake face until the tool has rotated sufficiently to remove the chip from the tool zone. Keeping the chip in the vicinity means that a lot of heat from the cutting process would also remain nearby however and evacuating the chips low down in the domain into the previously cut slot region may become problematic if another pass is made to deepen the slot at a higher axial engagement. If chips littered the region then they may obstruct the tool as it begins to cut again. It is difficult to assess the overall contribution of the axial flow in this chip evacuation without the inclusion of actual chip geometries in the simulation.

5.5.2 Results for new design full external flow models

After studying the axial flow independently, the complete new designs are now considered. The four new tool design geometries have been simulated and the data time averaged over the same period as described for the standard tool geometry full slot milling case in section 5.2. The results are also post processed in the same manner, with the data taken along the length of the tool to provide a clear idea of the behaviour throughout the regions of high interest.

Figure 5.27 displays the coolant coverage for each of the new designs, with the red regions seeing full coolant coverage and the blue regions containing only the surrounding air. The view looks through the workpiece surface, which is not displayed due to its obstruction of the results. The results look directly onto the centre of the cut slot region and the impingement point of the coolant jet.

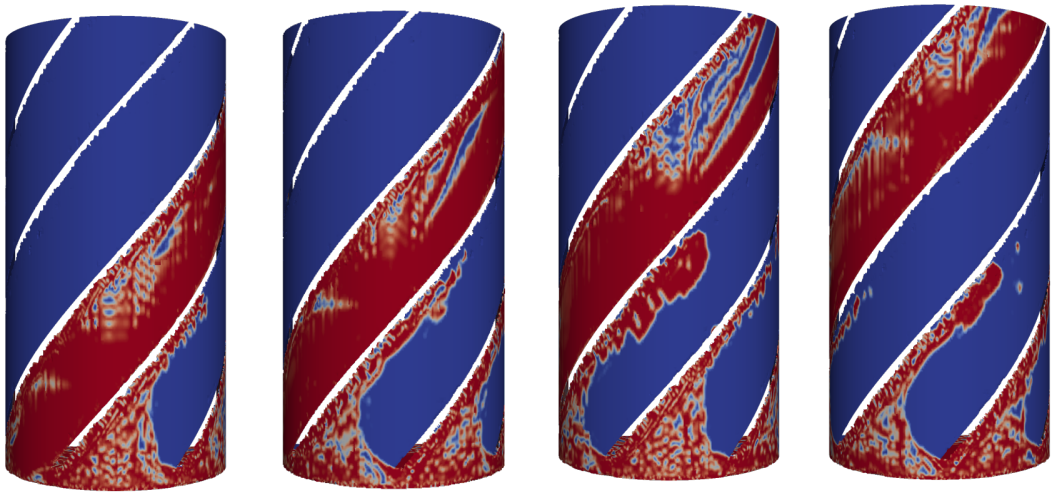

Figure 5.27: Coolant distribution for four new tool designs. Left to right, channel exit height, H, 5mm, 10mm, 15mm, 20mm. Red regions show high coolant distribution with volume fraction, $\alpha = 1$, blue shows air filled regions with volume fraction,$\alpha = 0$.

Considering the coolant coverage on all the designs, they appear very similar in broad behaviours, with a good coolant covering on the length of the rake edge for the sections in sight and a reasonable spread of coolant through the flank face in addition. This is a marked change when compared to the standard tool geometry simulation results which showed large areas of the flank edge received no coolant. This improvement is likely due to the minimal vertical angle of the coolant channel which is now zero. Instead of directing the coolant heavily down the rake edge, the coolant appears to spread much more evenly.

The axial flow contributions to other flutes also appear somewhat different, though this in itself should not be affected by the changing of radial channel height,H. The introduction of the radial flow, however, through only the single channel used in these simulations has potentially caused a bias in the flow at the base of the tool, since it is impacted on by the flow from the used flute, though in reality it would experience the same impact from all engaged flutes and any differences observed here are not believed to be truly physical in a situation where all flutes are in use. The interaction between radially and axially provided coolant flows could be greater for the smaller values of H, since the application sites proximity is increased.

Results for the velocity over a filtered threshold of the domain are shown in Figure 5.28. The velocities also show the same profile across all channel heights used. The high speed flow seen around the stagnation points on these models however is evenly spread around the point instead of being greater in the region underneath the impingement only, as was seen for the standard geometry with a higher vertical channel angle. Here the flow speed is even instead, and again the distribution of flow

from the coolant application appears much more even in these new designs. The high speed regions clearly move up the height of the tool with the impingement points as the channel exit heights increase.

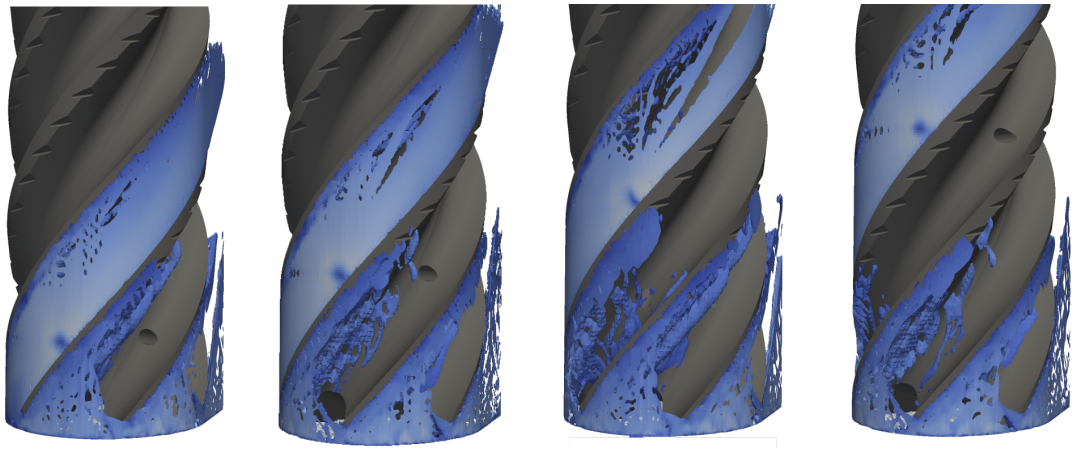

Figure 5.28: Coolant velocity magnitude for four new tool designs. Left to right, channel exit height, 5mm, 10mm, 15mm, 20mm.

For the standard geometry simulations the results for flooding volume fraction and vertical velocity were analysed over the lengths of each tool edge in the flute being modelled here. In Figure 5.29 the same values for the new models have been plotted alongside the standard tool results. The primary objective of the new designs was to promote upwards flow along an increased portion of the cutting edge to aid in chip evacuation. This is most important on the rake edge since this is where the chips are formed. The vertical velocity results on both edges are seen in Figure 5.29.

The rake edge on the right shows a very similar profile across all the new designs. They feature both a region of positive and negative vertical flow, which transitions across the impingement point coincident with their exit heights. The geometries show very similar maximum positive U_z values of between 25 and 30 m/s, which would be expected since the coolant flow rate at the inlet of each radial channel was the same. Interestingly, the values observed for the U_z above the impingement point for the new tool designs also lie in the same range as that observed for the standard geometry case, which is also included in the graphs. The higher magnitude flow rate applied through the radial channels in the standard geometry simulation was expected to provide higher velocity values in all directions around the impingement point, however the lower flow rates used for the new designs have still managed to match the maximum U_z above this point. In addition, all the new geometries also showed a decrease in maximum magnitude for the negative vertical flow below the impingement site, reducing the magnitude from nearly 40m/s to just over 25m/s. There is also a difference in the velocity flow at the base of the tool for the new geometry with channel height H=5mm. This geometry is the only truly comparable geometry at the tool base since it is only

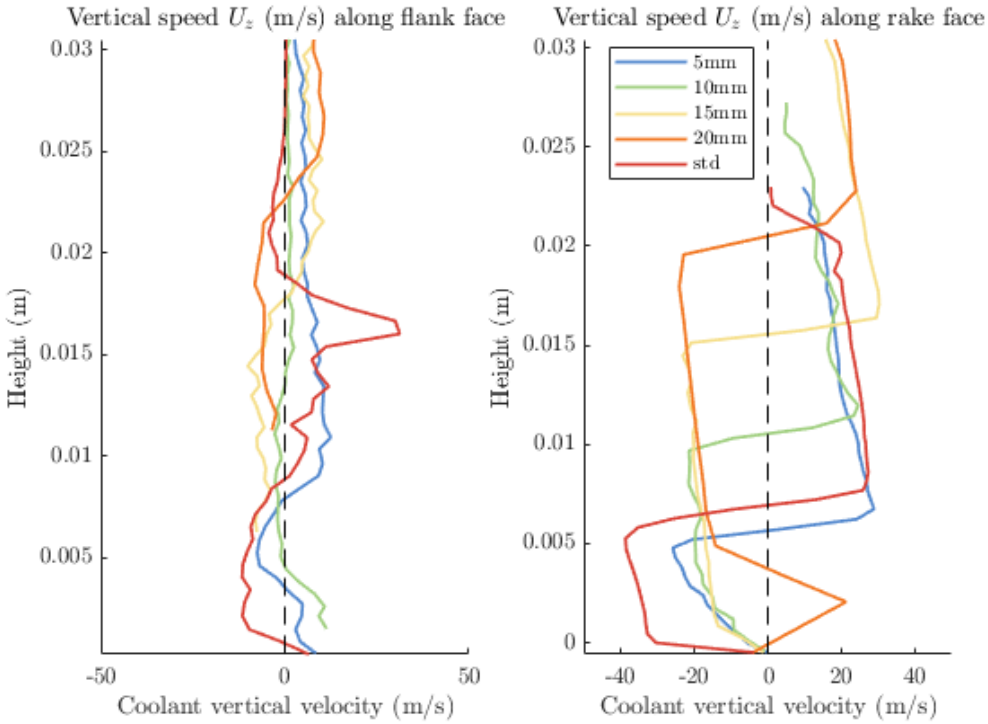

Figure 5.29: Plot of time-averaged vertical velocity against height along both the flank (left) and rake (right) edges of the tool. New designs with radial outlets at 5,10,15,20mm are included alongside the standard geometry results.

these two which see both flank and rake fully engaged at the base. Where the standard geometry results show a slow decrease in magnitude in the downwards flow under the impingement point, the new design with H=5mm decreased in magnitude again quite quickly to head more directly towards 0m/s at the base. The other models H=10,15mm in green and yellow respectively also show a smoother decrease towards zero at the base of the tool where the rake edge does still remain engaged for these models. This reduction in magnitude here could be a result of the axial flow provided by the new coolant channel. It was not expected to impact heavily on flow on the rake face but if it were to have an effect, this would be most significant near the base.

The new tool design with the H=5mm configuration seems to outperform the standard tool in terms of the vertical velocity along the rake. Not only in the impingement region movement to further down the tool, which results in a larger section experiencing upwards flow, but the region of downward flow sees a significant reduction in magnitude. The other models with channel exit heights of H=10, 15 and 20mm do not provide clear improvements on the upwards flow objective immediately, however they could still prove to be the best option going forward with full slot milling operations.

The models of 5mm and the standard case in red and blue have impingement centres very low in the domain. As a result of this configuration, less of the top of their flute's rake and flank edges remain engaged. It can be seen that the lines for vertical velocity end at around 0.025m in the figure, which is the height that the sample ends and the tool edge disengages. This is not the same height as the axial engagement however and the exit of this flute is not at the top of the workpiece but to the rear of the tool as the flute turns around the tool centre. Although the engagement of the tool ends here, the results seem to indicate no reason why the rake edge would not continue to see upwards flow at the same steady decreasing magnitude up to the top of the tool if it were engaged. It could be possible therefore that these low impacting models like the H=5mm configuration could see even more of the tool experiencing upwards flow than is shown here.

On the other hand, however, it should be noted that there are potential downsides to the low impact point which appears, at least on the surface, to be very successful here. The current orientation shows the flute exiting to the rear of the tool, as was mentioned. What this potentially means is that, although so much of the tool sees a good upwards flow along its cutting edge and may remove all chips successfully with this flow, they are not necessarily removed from the path of the tool permanently. If the chips exit the flute with the coolant as part of this stream out to the rear of the tool where the slot has been cut, they are not truly effectively removed from the area since if they are then trapped in the slot and fall to the base they could still obstruct the tool on the next pass. As such, an alternative geometry may be preferable so that it is mostly ejecting chips through a fully engaged flute at the top of the cutting zone. The models H=15,20mm have fully engaged rake faces and a good magnitude of upwards flow along them at the exit point. These models would likely provide a better, more permanent evacuation of the chips at the current orientation. At all chosen heights of channel exit height, H, there are always time periods which will see the flute exiting behind the tool instead of over the workpiece, but this is reduced as the channel height exit point increases in height.

The impact of rotational position on coolant distribution on the tool surface was discussed in section 3.2.2, and it was pointed out that the impact is especially significant in milling cases with a high axial engagement, as is seen in these full slot simulations. It was highlighted in a schematic (Figure 3.4) that for a deep axial engagement, there is a considerable portion of the cutting edge yet to complete its engagement before the coolant supply to the flute ends — the top of the rake for example has not even begun to engage the workpiece yet. If the axial engagement is very high and the coolant impact point is low, therefore, there is actually only a small window of coolant delivery to the cutting edge for most of the cutting window. Much more of the tool edge sees at least some wetting over the cut if the coolant is located closer the the

middle of the tool height, as opposed to very close to the base.

These contributing factors ultimately mean there are pros and cons of choosing an outlet height at any point on the tool flute. Placing the channel outlet very close to the tip has been shown to provide the greatest proportion of the tool with upwards flow to aid chip evacuation. Setting the channel outlet towards the middle of the tool will theoretically spread the coolant best through time as the tool rotates and still provides a significant amount of upwards flow along the tool edge, which does not reduce as significantly as in the lowest positioned options. Placing the channel exit towards the top theoretically may evacuate the chips more effectively as they leave the tool zone, however very few chips would make it to the point of evacuation since the bulk of the cutting edge sees only downwards flow and hence the majority of the chips would be carried downwards along the tool edge and could cause chip jamming.

As well as fluid velocity along the rake edge, Figure 5.29 also shows the flow along the flank edge. In general the flow shows smaller magnitudes and greater variability, which was the case along the flank in the standard model too due to the slightly more unsteady and splashy distribution of coolant to this edge. Once again, the H=5mm new tool design shows increased upwards flow along the tool edge compared to the standard model, which mostly encounters downwards directed flow.

This study with the four new tool designs has found an improved tool design for the initial objective of increasing the amount of upwards flow along the rake edge. The new design with the configuration of channel exit height, H=5mm provided a greater proportion of the tool with upwards flow and decreased the magnitude of the downwards flow where it was found. The benefits of other models tested were also hypothesised to have potentially greater benefits than either the standard model or new improved design in a more realistic machining setting with variable levels of engagement as the tool rotates, however this would require a fully rotating time variable model to be developed.

5.6 Conclusions

In this chapter, the standard cooling booster design has been investigated in a full slot milling application, which has a high axial engagement. The behaviour of the coolant flow and coverage along the rake and flank edges of the tool has also been examined in more detail. Full slot milling has not previously been assessed using CFD modelling and the results presented in this chapter show the development of the coolant jet as it reaches and interacts with both the rake and flank cutting edges. The standard tool geometry was found to direct most of its coolant to the small region beneath

the low down impingement point. An analysis of the spread of flow showed that over 78% of the coolant supplied to the cutting edge flowed downwards after impinging on the workpiece surface, which looked to be at least partly driven by the high vertical angle of the standard model. Despite this, the transition from face milling to full slot application showed an improvement in the overall upwards flow as the coolant coverage and vertical flow remained reasonably high across the long portion of the edge above the coolant application. The high percentage of downwards flow helps explain and support the findings in Chapter 4 which observed only negative vertical velocity components on the cutting edge across the design space.

Results tracking the vertical coolant velocity component and wetting along both the rake and flank edges were extracted to provide more detail in this study, compared to the averages along the whole region used in Chapter 3. These results highlighted the dramatic change in coolant velocity direction across the impingement point, below which lies the largest negative vertical magnitude and above which lies the largest positive vertical magnitude.

Observing the findings and combining these with the results from the DoE study investigating coolant channel angles in Chapter 4, a new tool design was trialled, which minimised the vertical angle of the coolant channel and added an additional coolant channel, exiting at the base of the tool, with the hope of introducing some upwards flow to the region at the base of the tool which rarely experiences a strong upwards flow. The size of the axial channel relative to the radial channels was optimised to maximise the percentage of coolant flow through the new axial channel while minimising the pressure drop. Internal channel single phase CFD modelling for a range of sample points in a design of experiments was used to create a response surface and perform a multi-objective optimisation.

Four versions of the new tool design were tested, each with the radial channels having different channel exit point heights. Improvements in vertical velocity along the rake face were observed with this new tool design, with all new designs showing a significantly reduced downwards velocity magnitude compared to the standard tool model. For the lowest channel exit height of 5mm, the height of the impingement point was also lower than the standard model, resulting in an improvement for upwards coolant flow along the majority of the tool cutting edge and an attractive candidate tool for further analysis and development. The implications of other outcomes of changing channel exit height were also discussed in detail and are recommended for further consideration using an extended version of the current model which extends the static case to consider the variability of the tool's rotational position through time.

Chapter 6

A review of liquid carbon dioxide as a potential coolant for industrial machining processes

Contents

Conventional emulsion coolants are a well established and accepted cooling approach in a range of machining tasks (Zheng Yang et al., 2022), however, in recent years there has been a growing need to find alternatives to oil and water-miscible coolants. The costs associated with using conventional cutting fluids accounts for approximately 16% of total manufacturing costs (Byrne & Scholta, 1993). A large chunk of these associated costs can be attributed to the disposal of the coolants after use, which can be up to twice as much as the price of the coolants in the USA and four times as much in Europe (Hong et al., 1999). There are also significant environmental and health concerns associated with conventional coolants. They often contain chemical additives which are hazardous substances to both work with and dispose of, and they can be difficult to clean off of finished manufactured products.

Gas or vapour phase fluids can be used as alternative coolants and are thought of as a more environmentally friendly alternative. Carbon dioxide, nitrogen and helium are among the most widely used gas based coolants, although they often need to be chilled or compressed to enhance their ability to remove heat from the cutting zone since gases in general have poor thermal conductivity and cooling capability (Shokrani et al., 2012b).

Gases can also be liquefied and are often then referred to as cryogenic coolants. Liquid nitrogen and liquid carbon dioxide in particular have exhibited enhanced cooling behaviours and are being extensively tested in this form (Shokrani et al., 2012b). Their low temperatures can generate high temperature gradients to increase heat transfer away from the cutting edge (Jawahir et al., 2016).

In Chapters 3 and 4, modelling work of conventional coolant was presented and used to predict and support improved coolant channel designs. Ultimately, similar work would ideally be carried out for liquid CO_2 coolants in machining, however more groundwork is required to build up the knowledge of the cooling and tribological processes involved when using CO_2. In the following chapters, both experimental and modelling methods will be extended to build towards the improved understanding of liquid CO_2 as a coolant in machining.

In this chapter, the use of cryogenic coolants in machining is discussed, with a focus on the properties and use of liquid CO_2. The physical properties which enhance heat transfer when using CO_2 coolant are reviewed, followed by the machining results available in the literature where CO_2 has been applied in cutting operations and compared to alternative coolants. To support further studies in this work, a review of the process of a CO_2 release from high pressure is then presented, with both experimental and numerical work available in the literature. A fundamental understanding of this release process is required to better understand the variability of success in machining applications and build towards the development of a model which can be used to predict the heat transfer when using cryogenic CO_2 coolant.

6.1 An introduction to cryogenic coolants

In general, when cryogenic cooling has been implemented on an uninterrupted cutting process such as turning, there have been several positive effects including increased tool life and reduced surface roughness (Shokrani et al. (2016), Ravi & Kumar (2012), Ravi & Kumar (2011)). In contrast to this, the effect of cryogenic cooling on interrupted or intermittent operations such as milling is less well understood (Tyler & Schmitz, 2014). Intermittent machining operations can already be prone to large temperature variations and the addition of a significantly colder cutting fluid has the potential to increase thermal cracks and fatigue so it is less commonly investigated and applied (Yildiz & Nalbant, 2008). There has, however, been research showing that implementation of a cryogenic cooling system can boast significant improvements over dry and conventional cooling in milling processes (Yildiz & Nalbant, 2008), and a deeper understanding of the processes involved could lead to improved machining and reduced cutting temperatures

across milling operations.

Liquid nitrogen (LN2) is perhaps the most commonly researched cryogenic coolant in machining. It offers significant cooling capacity due to very low temperatures (the boiling point at 1 atm is -195.8 °C), and also possesses lubrication properties that are desirable in coolants (Hong, 2006). In a range of published work, it can be seen that LN2 cooling has the potential to reduce cutting temperatures, improve surface finish and increase tool life relative to both dry and wet machining conditions dependent on the cutting parameters and workpiece (Ravi & Kumar (2011), Shokrani et al. (2012a), Su et al. (2006), Nalbant & Yildiz (2011), Islam et al. (2017)).

Although LN2 is the most popular choice for cryogenic cooling there are several disadvantages in using it. Consumption of LN2 can be high which increases the overall cost of machining (Kalyan Kumar & Choudhury, 2008), it also pre-cools the workpiece due to extreme low temperatures which can have adverse affects on the cutting forces as the workpiece hardens (Hong & Ding, 2001). Another significant limitation of the LN2 coolant is the difficulty in supplying it to the cutting site. All connections and piping supplying liquid nitrogen have to be thermally insulated and specifically engineered (Shah et al., 2020). It has to be supplied externally in the vast majority of situations since the practicalities of running the coolant through tool are challenging due to the insulation difficulties (Park et al. (2015b) Sivaiah & Chakradhar (2018)).

Another coolant commonly referred to as cryogenic is compressed or chilled air. Although not technically cryogenic since it has often not been cooled or pressured enough to achieve liquid form, chilled compressed air has been successfully applied in several tests. Compressed air is already used in cooling methods as it makes up the carrier fluid in MQL coolants most of the time. Cooled air is perhaps the cleanest and most environmentally friendly coolant among cryogenics (Su et al., 2011).

Reducing the temperature or the air component in MQL operations can have significant benefits from a cooling perspective in machining. The milling of titanium alloy Ti-6Al-4V using a cooled air MQL approach was researched by An et al. (2006), with the small particles of coolant carried by a high pressure jet of cold air at -20°C. Implementing this system greatly reduced both the temperature in the cutting zone and the flank wear found on the tool. The effect of the carrier air temperature was investigated using CFD modelling by Chowdhury et al. (2014) who decreased the MQL mist temperature from the usual 25°C to -50°C and saw a reduction in the modelled tool interface temperature from over 550°C to around 480°C. In a similar study Yuan et al. (2010) varied MQL mist temperatures between -15 and -45°C and found evidence of reduced wear compared to tests using room temperature MQL coolant, dry conditions or flood conditions. Although initially the vast majority of research into cryogenic machining focused on LN2 (Shokrani et al., 2013) there has since been significant work

carried out with cryogenic CO_2.

In the following section, several key physical properties of CO_2 which increase its capability as a coolant are discussed, before a review of the use of CO_2 in machining is presented.

6.2 Physical properties of cryogenic Carbon Dioxide

Carbon dioxide, CO_2, is a compound of carbon and oxygen which is most commonly found in gaseous state and is part of the make up of our atmosphere. There are several physical properties of CO_2 which make it an interesting candidate for cooling applications. Originally studied by Joseph Black in the 18th century, it was often called by other names such as fixed air or carbonic acid gas until the term dioxide came into use in the late 1860's (West, 2014). It was first liquefied by Humpry Davy and Michael Faraday under applied pressure and then observed in solid form by Thilorier soon after as a product found when liquid form CO_2 is released from the pressurised state (Roller & Thilorier, 1952).

Many gases can be liquefied under high pressures, low temperatures, or often a combination of both, but once released back into atmospheric conditions they will return to their natural gaseous state. The phase change processes involved in releases of liquid CO_2 from high pressure containers to (eventually) gaseous CO_2 at atmospheric pressure conditions are of particular interest due to the location of the triple point (Pursell, 2012).

A triple point is defined as the temperature and pressure combination where all three phases (solid, liquid, gas) of a substance can exist simultaneously in thermodynamic equilibrium. As can be seen in the phase diagram of CO_2 shown in Figure 6.1, the triple point is located at a pressure of 5.1 bar ($\approx$ 0.52 MPa) and a temperature of -56.7°C. This means that liquid carbon dioxide cannot exist at atmospheric pressure and so a release from high pressure causes a phase transition process from a liquid state, followed by a saturated two-phase liquid/vapour mixture to a solid/vapour mixture at atmospheric pressure where the solid phase sublimates to eventually give CO_2 gas in single phase as it absorbs heat from the surroundings (Pursell, 2012).

The presence of sublimating solid CO_2 particles in the coolant jet after expansion has the potential to offer additional cooling benefits. By taking in additional thermal energy from the jet and absorbing it as latent heat of sublimation, the coolant jet will retain its cold temperature for longer before starting to exhibit an increase in temperature once the solid CO_2 has all sublimated.

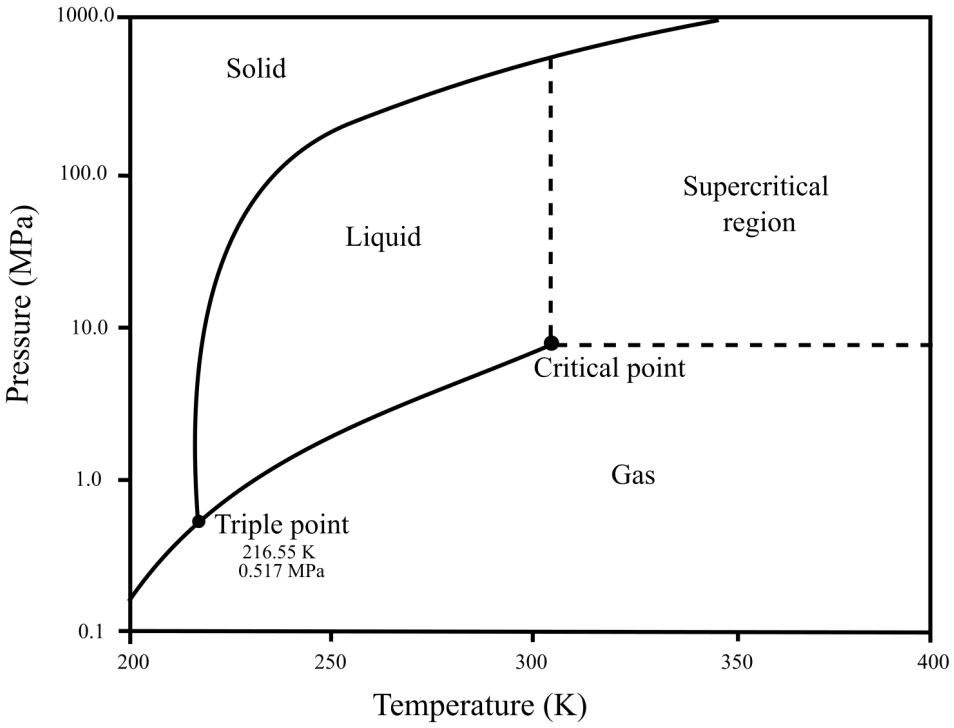

Figure 6.1: CO_2 phase diagram for solid, liquid, gas and supercritical phases with the triple and critical points. (Adapted from Witkowski et al. (2014))

A CO_2 expansion process is often assumed to be an isenthalpic process (Mazzoldi, 2009) with constant enthalphy, h. In the isenthalpic expansion of CO_2 across nozzles, temperature and volume changes accompany the pressure drop observed. The limiting ratio of the temperature change, ΔT, to the pressure change, ΔP, is given below in equation 6.1 with μ_{JT} known as the Joule-Thomson coefficient.

$$\mu_{JT} = \left(\frac{\Delta T}{\Delta P}\right)_h \tag{6.1}$$

Measured extensively by Roebuck et al. (1925), carbon dioxide has a particularly high Joule Thompson coefficient compared to other common gases, meaning that as it experiences the pressure drop from the high pressure reservoir it will have a greater corresponding change in temperature, a factor which may be beneficial in the cryogenic cooling applications in machining. As well as a high Joule-Thomson coefficient and a triple point located above atmospheric pressure, several other factors make CO_2 an attractive option for a machining coolant. As highly compressed CO_2 is released to atmospheric conditions and is allowed to depressurise, it also expands and can form a wider diameter cooling jet than is seen in single phase conventional coolant applications. This has the potential to cool regions on the cutting tools which were previously difficult to target. CO_2 is also significantly cleaner to work with than conventional

coolant. Applied in liquid form, the final waste product is gas phase CO_2 which can be vented to the atmosphere. This process can be made more environmentally friendly if recycled CO_2 is sourced.

6.3 Machining studies with CO_2 cooling

In this section, a review of machining studies applying CO_2 coolant will be presented. The available literature covers a range of cutting parameters and machining operations, as well as the application of CO_2 via both external and through tool methods. The range of studies and their collective results are discussed to assess the variable success in industrial applications of CO_2 as a coolant. The results will be shown to be sensitive to a range of machining variables, including cutting parameters, workpiece material, and coolant application method.

As with most cryogenic coolants, the available literature has predominantly been focused on turning operations especially for metals and 'hard to cut' materials (Fig 6.2).

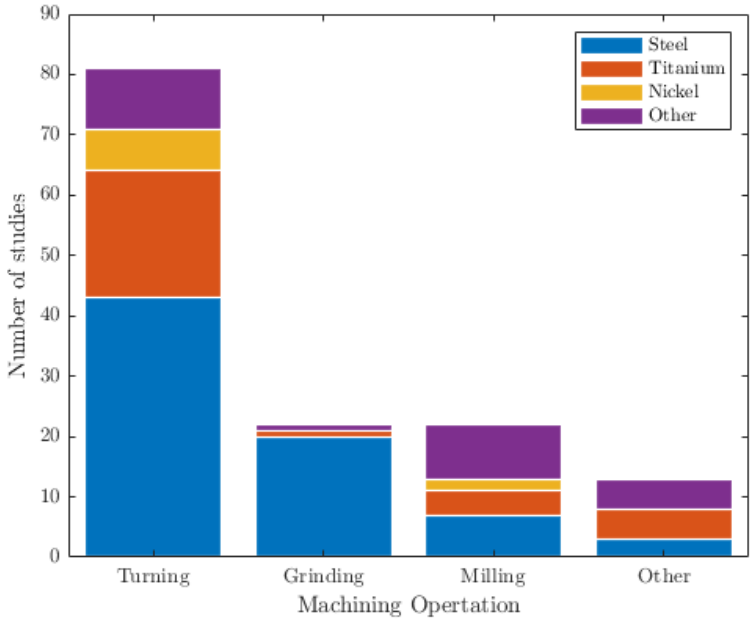

Figure 6.2: Number of studies available in the literature for cryogenic machining research (Shokrani et al., 2013), plotted according to machining operation.

Jerold & Kumar (2012) investigated the effect of using CO_2 as a cutting fluid on cutting temperatures, tool wear, cutting forces and surface finish in a turning of steel machining operation. The application of CO_2 gas reduced the cutting temperatures significantly compared to cases with dry and conventional cooling, and less flank and

crater wear was observed on the tool. Similarly, in the turning of titanium, Biermann et al. (2015) found that using CO_2 as a cryogenic coolant increases the tool life when turning the alloy Ti-6Al-4V. However, the same did not apply in that study for the turning of another higher strength titanium alloy, Ti-6Al-2Sn-4Zr-6Mo, which required a combination of CO_2 and MQL to increase tool life, highlighting the variability of machinability of workpieces. Machai & Biermann (2011) used CO_2 'snow cooling' when carrying out turning operations on another high strength titanium alloy, Ti-10V-2Fe-3Al and found that when supplied close to the cutting edge, the CO_2 could decrease the tool wear development compared to emulsion cooling conditions, however the CO_2 stream was still found to be unable to effectively penetrate the tool-chip interface and reduce contact and friction between the tool and chip.

Over the last decade there has been a significant interest in applying CO_2 to milling operations as promising tests have encouraged enthusiasm within the industry. A study carried out by Nimel Sworna Ross & Manimaran (2019) found that CO_2 outperformed MQL, dry and wet cutting conditions in the milling of a difficult-to-machine Nickel-Cromium alloy. CO_2 was the best coolant tested in terms of cutting forces, cutting temperatures, minimal tool wear and a reduced surface roughness. The reduction in cutting temperatures was particularly notable as seen in Figure 6.3. The

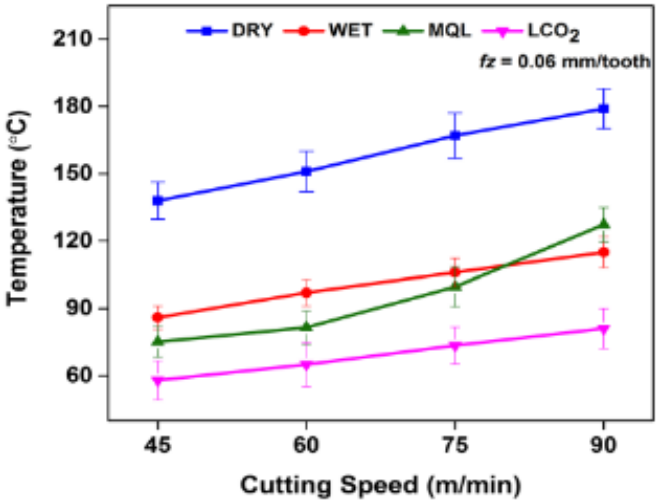

Figure 6.3: Cutting temperatures for dry, wet, MQL and liquid CO_2 cooling conditions (Nimel Sworna Ross & Manimaran, 2019). Reproduced with permission from Springer Nature

application of CO_2 by Nimel Sworna Ross & Manimaran was through an external nozzle directed towards the cutting zone, an application technique already seen to be commonly used for conventional coolants and MQL. CO_2 can also be successfully targeted at the cutting zone through internal channels in the cutting tool. Cordes et al. (2014) investigated the milling of high strength stainless steel using a specially adapted tool with internal channels allowing coolant flow of cryogenic CO_2 and compressed air

simultaneously. Comparing tool life between dry and cryogenic conditions, Cordes et al. observed a 63% lower flank wear in the cryogenic case compared to dry under the same cutting conditions. Investigating the potential for increased productivity, Cordes et al. found cutting conditions could be increased in the cryogenic case from 320m/min to 400m/min and 0.4mm feed rate to 0.55mm feed rate and still maintain the same level of tool wear as in the dry conditions - resulting in a 72% increase in material removal rate.

As was the case with conventional coolants, significant research has been carried out with a focus on titanium alloy Ti-6Al-4V due to its low machinability and high demand. Nimel Sworna Ross & Ganesh (2019) tested liquid CO_2 as a cryogenic coolant in the milling of Ti-6Al-4V. Employing an external application method, with a nozzle 20mm away from the cutting zone, it was found that the cutting temperatures and surface roughness were considerably reduced compared to wet conditions.

Considering the productivity benefits when milling Ti-6Al-4V with liquid CO_2 coolant, Sadik et al. (2016) found a significant increase in tool life compared to conventional emulsion coolant. Sadik et al. used CO_2 for through tool cooling and tested 3 nozzles of different diameter while comparing flank wear and notch wear on the tool. Tool wear was examined throughout the test for all nozzles in both the conventional and cryogenic coolant experiments. Initially, the tool wear progresses at a similar rate for both coolants however the notch wear, which is the failure mode for these cases, is delayed to much later machining times in the cryogenic cases and for the case using nozzle A (that with largest diameter and thus highest CO_2 flow rate), the tool life in the cryogenic experiment was 350% longer than that of the conventional experiment. Interestingly, the cracks that often form due to extreme thermal cycling when milling titanium alloys propagated differently in the cryogenic and conventional cases here. Sadik et al. found that instead of the propagation in the usual direction which causes chipping of the cutting edge, the cracks instead propagated laterally, delaying the tool failure. The application of CO_2 coolant did not reduce all types of tool wear however, in fact the non-limiting flank wear observed at the end of tool life was slightly higher in the cryogenic case compared to the conventional. Flow rates were also varied for the milling operations with findings suggesting that the flow rate does have an influence and that higher flow rates lead to a longer tool life, though the effect was more pronounced in the cryogenic case than in the conventional coolant case.

Pittalà (2018) carried out a similar end milling study comparing conventional coolant to cryogenic CO_2 coolant for a milling operation on Ti-6Al-4V. Instead of the indexable endmill tools used in the study by Sadik et al., solid end mills were used with a central internal CO_2 supply and 5 radial channels supplying coolant to each flute. Both the diameters of these channels, and their positioning were varied between two locations as can be seen in figure 6.4 with configuration 'A' in the middle of the

flute and the configuration 'B' channel directed towards the cutting edge. Both flank wear and notch wear were examined with the dominant being the flank wear. The configuration A gave reduced tool wear results compared to B, which is likely due to better cooling of the flank side of the tool (Pittalà, 2018) and whilst channel exit dimension had little impact on the wear for configuration B, there was a significant reduction in wear for the larger radial hole compared to the smaller in configuration A, which is possibly attributable to increased flow rate of CO_2 in this case. For the cutting parameters used in this case there was no dramatic difference in tool wear between the cases using CO_2 and those using conventional coolant. In the configuration B, for a cutting speed of 130m/min and feed rate of 0.14mm/tooth, the CO_2 case showed less tool wear than the conventional however as the feed rate was reduced to 0.088mm/tooth and configuration A was used, there was a slightly reduced tool wear for conventional coolant compared to CO_2, though in both of these examples the difference was within the range of experimental error. Therefore, although there was no dramatic increase or decrease in tool life as was seen by Sadik et al. (2016) and Tyler & Schmitz (2014), CO_2 has been shown to be a viable alternative to conventional coolant for this milling operation and performance may be further improved with tailoring of tool and nozzle design.

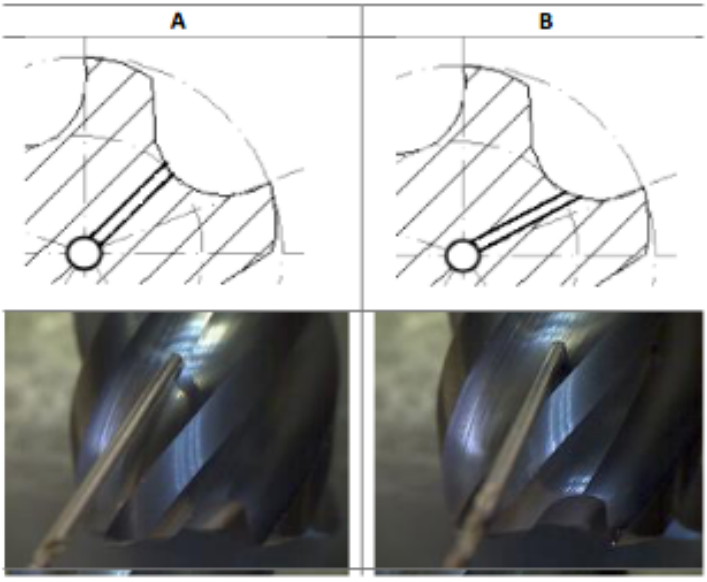

Figure 6.4: Channel exit positions for CO_2 cryogenic milling trials by Pittalà (2018) Reproduced under creative commons license CC BY-NC-ND 4.0

Investigations into cutting and tool temperatures have also extended to modelling for cryogenic coolants. Augspurger et al. (2019) modelled cutting temperatures for a variety of coolants including MQL and CO_2, applied internally through the spindle in seperate channels. Validated using thermocouples embedded in the tool, the model showed reduced temperatures at the tool tip with CO_2 compared to MQL cooling.

Not all tests with CO_2 have indicated an improvement in tool life over alternative coolants however. Although it has shown great potential compared to dry conditions (Sadik et al., 2016) several studies indicate that there are limitations in using CO_2 compared to MQL. Tapoglou et al. (2017) compared dry, flood, through tool emulsion, through tool CO_2, MQL and a combination of CO_2 and MQL in the shoulder milling of Ti-6Al-4V. In contrast to the study by Sadik et al., the findings of Tapoglou et al. suggested that the emulsion coolant performed better in the milling of this titanium alloy than CO_2 when they assessed tool wear. Between the two cases, the cutting parameters are a clear difference in otherwise similar work. Where Sadik et al. used lower cutting parameters, with a cutting speed of 80m/min and a feed per tooth of 0.15mm, Tapoglou et al. used a 100m/min cutting speed and a feed per tooth of 0.45mm, indicating that as seen with conventional coolants, there may be regions within the cutting parameter space where certain cooling/lubrication methods may outperform others and careful consideration should be paid in each case. It was seen in the study by Pittalà that the optimal channels for conventional coolants are not necessarily the most effective channels for CO_2 application and it could be possible here that tailoring the tool geometry may increase the range of cutting parameter ranges where an improvement using CO_2 would be possible.

Although the conventional coolant performed best in the studies of Tapoglou et al. (2017), the performance of CO_2 could be improved by combining it with MQL. Combining the cooling and lubricating properties of these two methods resulted in a better tool life than when using either method independently in the first trials conducted. The improvement of the CO_2 and MQL combination relative to the MQL stand alone coolant was also found to be dependent on cutting conditions. As cutting speed increased the improvement in tool life allowed by combining MQL and CO_2 was reduced and at the highest cutting speeds in the 5 insert tests there was only a nominal difference observed and in fact the MQL showed the higher tool life.

CO_2 is a decidedly more complex cutting fluid than the conventional oil or water based options due to the rapid phase changes and behaviour as it depressurises in the cutting zone. The fundamental physics involved are not typically investigated in this setting and usually only machining parameters are of interest in the studies undertaken. Pušavec et al. (2019) investigated the underlying heat transfer capabilities of CO_2 in a non-machining set of experiments, comparing it to LN2 and conventional coolant. The coolants were applied through a nozzle directed towards a heater with a thermocouple included. Such fundamental work can give great insight into the heat transfer capabilities and is incredibly useful to help interpret machining results when they are somewhat varied as has been seen with the milling of Ti-6Al-4V for example. Pušavec et al. tested two nozzle orientations, one with a perpendicular angle to the heater and one at a 60°. Comparing the cooling capabilities at 60° showed relatively

similar performances between the three coolants, though the cryogenic CO_2 and LN2 slightly outperformed the emulsion when the heater was at a lower temperature.

Although similar performances were observed for the angled nozzle across the coolants tested there was a clear increased cooling capacity observed for the emulsion coolant in the perpendicular nozzle case, and the disparity greatly increased as heater temperature increased. Overall, the fundamental study carried out by Pušavec et al. indicated a reduction in cooling capacity when using the cryogenic coolants compared to conventional options. Although the cryogenic coolants can provide enhanced heat transfer by increasing the thermal gradient in the region due to their low temperatures, they are still predominantly comprised of the gas phase in the heat transfer region and so can transfer less heat away than their liquid conventional counterparts. Such research is very valuable in interpreting the findings in machining tests and giving insight into some of the complex cryogenic behaviours. A more fundamental study of CO_2 cooling was also carried out by Gross et al. (2019) who monitored CO_2 coolant jet temperatures as they developed from the outlets of an application nozzle. The temperatures, measured with a mimumum just under -70°C were observed to be not strongly dependent on CO_2 mass flow rate or channel diameter, although the distance from the release point/nozzle that remained cold did depend on these factors. They observed, as a result, that the best CO_2 cooling in machining would be found when decreasing the distance between nozzle and cutting region.

Further to the non-machining tests, Pušavec et al. (2019) also conducted a series of milling tests using Ti-6Al-4V. Applying the same three coolants though internal tool channels and monitoring the cutting temperatures it was found that emulsion enabled the lowest temperatures, followed by CO_2 and finally LN2. These machining test findings correspond well to the fundamental heat transfer experiments conducted in the same work, but potentially differ with some of the surrounding literature. Although no direct comparisons can be made due to the variations in specific cutting conditions it is interesting to look at the work alongside that of Nimel Sworna Ross & Ganesh (2019) who also considered the cutting temperatures for milling of Ti-6Al-4V but instead noticed a significant decrease in temperatures when milling with CO_2 compared to wet conditions. One key difference to note is that where Pušavec et al. applied coolant through tool, Nimel Sworna Ross & Ganesh used an external application which could explain the disparity. It is also highly likely that the performances of coolants as stand alone and relative to each other are dependent on cutting conditions applied. Success in reducing cutting temperatures with coolants should also be treated with caution since tool temperatures that cycle rapidly as can be observed when using coolant in intermittent cutting operations have the potential to significantly reduce tool life instead of improving it. As suggested by Pušavec et al., tool life experiments are needed along with cutting temperature monitoring to obtain a fuller picture of the

effects of these coolants.

Throughout much of the literature researching coolants in milling operations, one of the standout features is the variability of the results. Coolant performance depends on workpiece material, tool composition and properties, cutting parameters and coolant flow parameters among others.

Fernández et al. (2019) tested through tool CO_2 coolant in the milling of inconel 718, Gamma Ti-Al and Steel with varying success. In the inconel case, an equally short tool life was observed for both the emulsion and CO_2 tests and considerable cracks were observed. In contrast, the titanium alloy workpiece tests resulted in a 100% longer tool life when using CO_2 compared to emulsion. An even greater increase in machining time of 175% was seen in the steel tests. Interestingly, although the tests show a clear variation in tool life increases it can be seen that for none of the workpieces considered here has the CO_2 coolant reduced the tool life compared to conventional.

Tyler & Schmitz (2014) applied coolants externally into the cutting zone of a milling operation of Hastelloy X, a nickel-chromium superalloy. The cooling methods compared were MQL and a CO_2 spray which was a mixture of a compressed air jet and a jet comprised of gaseous and solid CO_2 (dry ice particles) which is formed when CO_2 expands from compressed liquid form back to atmospheric pressure. The tool life of CO_2 cutting experiments was considerably lower than those achieved using MQL for the low speed tests (the change in tool life was approximately 90% for the lowest cutting speed). Only at the highest speed tested did the CO_2 spray give a longer tool life than the MQL spray. To investigate the difference in tool life further, Tyler examined the tools under a microscope and found that the failure mode was different for the CO_2 case compared to the MQL case. For the MQL cooled case, the tool life was ended when the flank wear reached a maximum allowable limit but for the CO_2 case there a chipping of the cutting edge which then caused a catastrophic failure of the tool soon after. Thermal analysis was carried out by Tyler to compare temperatures of the cutting process and it was found that maximum cutting zone temperatures were similar for both cooling strategies though the minimum observed temperature in the CO_2 case was -4°C compared to 14°C in the MQL case. Tyler also observed that the CO_2 does cool the cutting edges outside of the cut but cannot penetrate to the cutting zone itself where temperatures are highest. This improved cooling of the edges on the cutting edge periphery however, increases the effect of the thermal cycling for intermittent cutting temperatures and likely causes thermal fatigue.

Jebaraj et al. (2019) investigated multiple workpieces under both cryogenic and conventional coolant conditions. Externally applying LN2 and CO_2 while end milling Al6082-T6 alloy (Jebaraj & Pradeep Kumar, 2019) it was found that wet conditions reduced the cutting forces the most, closely followed by CO_2, and LN2 showed

higher forces. A reduced surface roughness in the workpiece was also observed for wet coolant here. The cryogenic coolants reduced the cutting temperatures, with LN2 resulting in the lowest temperatures. Investigating slot milling of 55NiCrMoV7 die steel (Jebaraj et al., 2020) cutting temperatures were also found to be significantly reduced when using the cryogenic coolants, especially at higher feed rates. At the highest feed rate of 0.04mm/rev there was a reduction from roughly 190°C degrees to 90°C when using CO_2 coolant compared to emulsion. Although the reduction in temperatures shows a similar trend between these two workpieces investigated, the results for surface roughness and cutting forces show opposite trends, with the cryogenics instead performing best in reducing both surface roughness and cutting forces for this workpiece instead of the conventional, as seen in Al6082-T6. A third workpiece material, SKT4 steel, was later considered by Jebaraj et al. (2021). Again, cutting temperatures were significantly reduced for CO_2 cooling compared to wet cooling, with a decrease of between 3 - 51%. For this steel, an analysis of the tool wear was included in the study and when using the cryogenic CO_2 coolant in place of conventional, it eliminated the tool edge chipping and reduced the cutting wear which had been observed under wet conditions.

Also exploring the effect of various parameters, Iqbal et al. (2020) kept the workpiece consistent in a parametric study, using Ti-6Al-4V in all tests and varied other key parameters. The first parameter varied was cutting fluid, LN2 was compared to throttled CO_2 flow and MQL. Also varied was the cutter's helix angle, the milling orientation and the cutting speed. Iqbal et al. concluded from the results presented in this work that the MQL coolant was more favourable than the two cryogenic options in all outputs considered including tool wear and surface finish. The results published by Iqbal et al. were extensive and showed the effects of all parameters considered in some detail. Although the MQL coolant appeared to achieve the best results for reduced flank wear across the design space in general, the results are interesting and over all the parameters tested, the trends and best performances vary with coolant type significantly. Extracted results, shown in Figure 6.5, at a cutting speed of 100m/min the lowest value for tool wear found in the tests was 0.05mm flank wear, seen in the MQL down milling test with a 32 degree cutter angle, the the MQL up milling test with a 42 degree cutter angle and in the LN2 down milling test with a 42 degree cutter angle.

At the same cutting speed however, CO_2 showed a 0.06mm flank wear in the down milling test with a 42 degree cutter angle, showing that it still has potential as an alternative coolant. Given that the MQL coolant has performed particularly well here it could indicate that lubrication is required for successful milling on Ti-6Al-4V. Previous tests comparing emulsion have mostly shown an improved performance for the CO_2 coolant. It could be, however, that MQL may still be the preferred method for milling

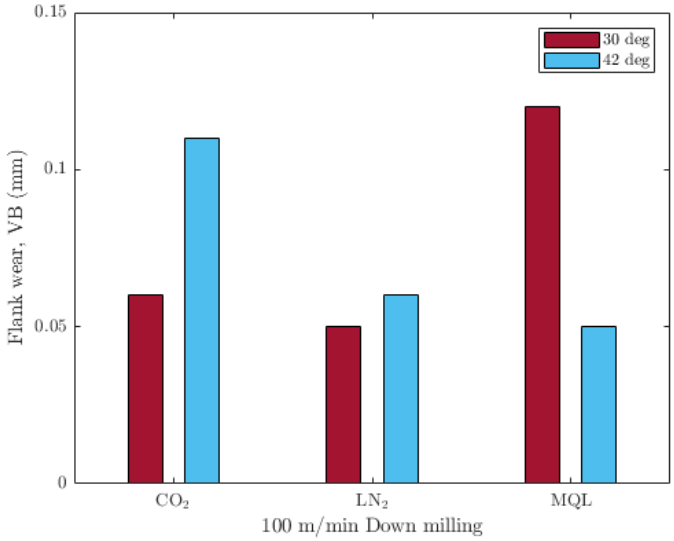

Figure 6.5: Flank wear for machining tests by Iqbal et al. (2020)

this alloy under certain cutting conditions. Introducing more lubrication could combine the benefits of this with the cooling capabilities of the CO_2 and LN2 cryogenic coolants to provide yet more effective coolants. The heavy dependence on many parameters is again highlighted in this study by Iqbal et al.. In the 100m/min down milling case in particular, it can be seen that between the three coolants tested here, there are three very different responses to cutter angle on the tool. In the MQL case using the 42 degree angle more than doubles the tool wear compared to the 30 degree case, whereas in the CO_2 tests the opposite effect is seen and the 42 degree angle shows a significant reduction in flank wear compared to the 30 degree case. The LN2 coolant in these tests on the other hand show very little dependence on cutter angle under these cutting conditions. Comparing these cases directly shows clearly that a certain configuration or set of cutting conditions that have provided good results with one coolant by no means guarantee good results with a different coolant, although good results have still be possible. It highlights again the point raised by Pittalà (2018) that coolant application methods developed to optimise performance from conventional coolants may be different to those which will result in a good performance from cryogenic coolants and attention should be paid to develop new methods or tool geometries to investigate optimal configurations for cryogenic coolants also.

In a further study investigating the milling of Ti-6Al-4V with a sustainability focus, Iqbal et al. (2021) assessed tool wear, productivity and the consumption of fluid and power to compare the sustainability of different coolants. The externally applied, choked CO_2 flow was found to be the most sustainable option in these tests when drawing on both economical and environmental factors. The most sustainable conditions identified were at the highest cutting speed and CO_2 mass flow rate, however

the flow rates considered in this work only reached a maximum of 0.6kg/min which is significantly lower than that seen elsewhere (Up to 10kg/min Pittalà (2018)). The findings cannot necessarily be assumed to be valid under such different conditions, as tool wear may not decrease as much as fluid costs increase, for example.

The emphasis on increasing sustainability is usually the primary reason for the investigation and adoptation of alternative coolant methods. Another study assessing the sustainability of CO_2 use in milling by Jamil et al. (2021) calculated carbon emissions in a variety of cooling approaches. Interestingly, the carbon emissions are actually lower in CO_2 cooled machining than in dry, MQL and liquid nitrogen aided machining. Further to being the most sustainable choice, Jamil et al. also found that the tool wear and temperatures were lowest for the CO_2 coolant in Ti-6Al-4V milling.

Considerable work has been carried out by Pereira et al. (2015, 2016, 2017b, 2017a) in investigating possible developments of coolant applications for CO_2. Initial investigations into both converging and converging-diverging nozzles employed computational fluid dynamics (CFD) and experiments to investigate the coolant jet speeds and spreading. These initial tests indicated that although greater jet velocity is generated when using a converging-diverging nozzle it also produced a more dispersed jet and so a converging nozzle was chosen for the machining tests as it was deemed more important to concentrate the coolant on the cutting edge.

Later machining tests milling inconel 718 (2015) applied coolant externally through the developed nozzle and observed that CO_2 coolant application improved tool life compared to dry conditions. Tool life was reduced, however, to 68% of that seen in wet conditions. CO_2 combined with MQL was also tested in these experiments and although the tool life of wet conditions could still not be matched, the tool life times were much closer with the CO_2MQL combination showing a 93.5% tool life compared to wet. Applying the coolant instead through tool Pereira et al. (2017b) compared internal CO_2MQL to several other coolants again and found that although conventional coolant still enhanced tool life the most, the CO_2MQL approach outperformed the standard MQL and were more environmentally friendly. The external vs internal applications of CO_2MQL were also compared here, with the internal application better managing tool life. This was attributed by the authors to the cooling being targeted at the tool and not the workpiece so hardening of the workpiece material could be avoided.

Halim et al. (2019) also investigated the cryogenic milling of inconel 718 and utilised a modified system to adapt the cooling to crygogenic CO_2. The coolant used was combination of liquid and gas CO_2 along with compressed air, combined in a cooling system designed to control the phase changes in the system by regulating the pressure. The coolant was applied externally through a nozzle 40mm away from the cutting zone and results showed a 70% increase in tool life compared to dry conditions, which agrees

with the findings of Pereira et al. (2015) who also observed significant improvements for CO_2 over dry using this workpiece material.

CO_2 has also been investigated as a coolant in machining in its supercritical form. CO_2 becomes a supercritical fluid when it is heated and pressurised beyond 304.13 K and 7.3773 MPa respectively and in this state embodies some physical properties from both the gaseous and liquid phases.

Supercritical CO_2 has been tested for potential as an alternative to near-dry (MQL) conditions and dry conditions for the milling of Ultra-high-strength-steel (UHSS) by Mulyana et al. (2017). Supercritical CO_2 was tested as a coolant both with and without the addition of lubricant and in both forms performed well compared to dry and MQL machining conditions with regard to reduction of cutting temperatures and prolonging tool life. The addition of lubricant improved the CO_2 as a coolant by reducing cutting forces and cutting temperatures. It made the most marked difference in extending tool life however, there was a much more significant improvement in tool life for the CO_2 plus lubricant coolant than the for the CO_2 alone compared to the MQL, as can be seen in figure 6.6.

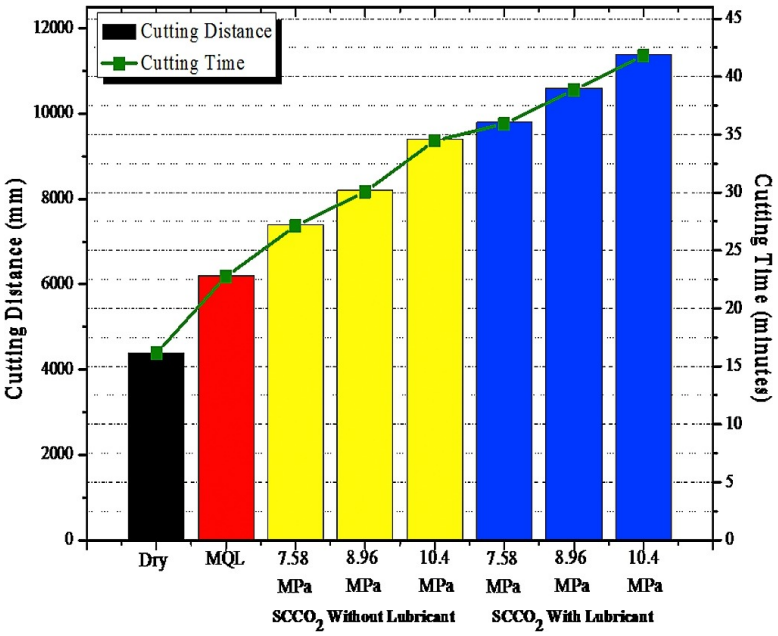

Figure 6.6: Cutting distance and time before tool failure for set cutting conditions under various cooling strategies (Mulyana et al., 2017) Reprinted from Journal of Cleaner Production, Vol 164, Mulyana T., Rahim E. A., Md Yahaya S. N, The influence of cryogenic supercritical carbon dioxide cooling on tool wear during machining high thermal conductivity steel , Pages No. 950-962, Copyright (2017), with permission from Elsevier

Wika et al. (2019) investigated milling of steel using $scCO_2$ with MQL dissolved into it and applied the coolant through tool. The tool life improvement compared

to flood was considerable, the maximum increase of 324% was achieved at the lowest cutting parameters of 0.5mm/tooth feed rate and a cutting speed of 215m/min.

Cai et al. (2020) tested scCO_2 alone and compared it to the results for two scCO_2 MQL combinations as well as dry conditions in the peripheral milling of Ti-6Al-4V. The externally applied coolants all reduced the cutting temperatures compared to dry conditions, although they were most reduced when the MQL was incorporated into the CO_2.

To summarise, clear potential has been found in the application of CO_2 as a coolant in milling operations over the last few decades. As observed in milling with conventional coolants, the response of machining outputs such as surface roughness and tool wear can be somewhat unpredictable when adding coolants and a fundamental understanding of the physics involved would allow better informed decision making in the tool design and machining processes for both types of coolants. Extensive experiments have provided a wealth of information on the benefits and drawbacks of applying coolants in a wide range of situations but there are alternative methods of investigation available including simulations and modelling.

In the use of conventional coolants, the properties of the coolants are reasonably well understood and usually close to those of water. CFD models are often employed to investigate further the causes of discrepancy between coolant behaviour across various cutting conditions. There is however a limited understanding of the behaviour of CO_2 as a coolant as it undergoes phase changes and expansions to cool the tool and workpiece. The physical processes involved in the CO_2 multiphase flow need to be better understood so that the variability in its performance as a coolant can be explained and tools can be developed to best exploit its cooling capabilities. These knowledge gaps in the machining industry, along with the sheer complexity of the two or three phase flow, make it more difficult to model CO_2 coolant processes. Research into more fundamental aspects of CO_2 flow and heat transfer could significantly advance the efforts to switch to this more sustainable cooling method. In the following section, a brief overview of the physical behaviours of carbon dioxide during releases from high pressure systems is presented. These high pressure releases cover the application of CO_2 in most machining coolant applications, where the CO_2 is supplied from high pressure cylinders through a series of tubing or internal tool channels to the cutting edge.

6.4 Carbon Dioxide Release from High Pressure

The depressurisation of CO_2 from a dense phase state to atmospheric pressure is a complex process and experimental observations can provide great insight into the phenomena occurring in the near-field expansion.

There are three stages in the release of CO_2 from a high pressure reservoir to atmospheric conditions, the first stage involving the flow between the reservoir and orifice, which may be along pipes or channels, the second being the rapid expansion downstream of the orifice and the third a slower expansion due to the entrainment of air. The process is illustrated in the schematic in Figure 6.7.

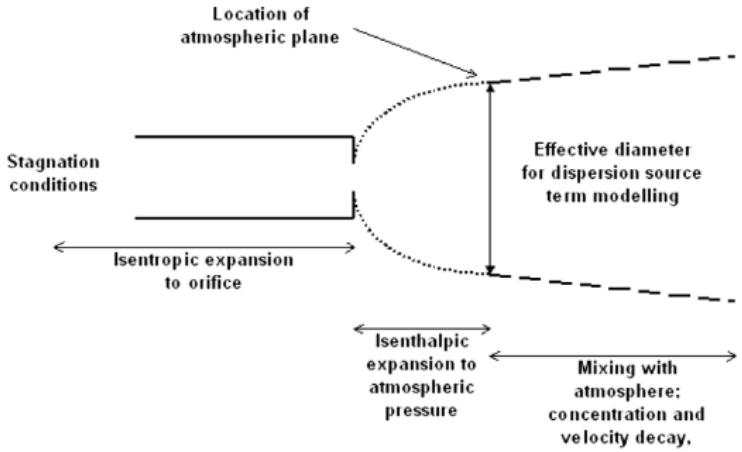

Figure 6.7: Three stages of depressurisation of CO_2 from high pressure reservoir to atmospheric plane (Pursell, 2012). Contains public sector information licensed under the Open Government Licence v3.0.

6.4.1 Experimental studies of CO_2 depressurisation features

There has been significant interest in the release process within the Carbon Capture and Storage (CCS) industry due to the need to quantify all the hazard consequences associated with any CO_2 pipeline failure (Webber, 2011). The UK Health and Safety Executive (HSE) has funded the development of an experimental facility at the Health and Safety Laboratory (HSL) and an experimental rig was used by Pursell (2012) there to study a high pressure release. Pursell (2012) carried out an experiment focusing on the release of CO_2 from a vessel using two sizes of nozzle and reservoirs of either saturated liquid CO_2 or saturated vapour CO_2. Measurements of the fast, near-field expansion stage, which is assumed to be isentropic, included the recording of temperature and pressure at both the vessel and nozzle. Measured values for the flow rate at the nozzle were compared to those calculated based on the initial conditions under the assumption of isentropic flow. This allowed a calculation of the quantity of gaseous

CO_2 for two different cases tested, cases with a reservoir tank full of saturated vapour CO_2, and cases with saturated liquid CO_2 in the vessel. It was found that between the vessel and orifice there was a condensation of 10-11% of the gaseous CO_2 to liquid for the saturated vapour case and a vaporisation of 14-16% of the liquid CO_2 from the saturated liquid CO_2 case depending on nozzle size. In addition, calculated ideal flow rates and flow rates measured at the orifice are used by Pursell to calculate a discharge coefficient for each case. The lowest discharge coefficient was calculated to be 0.63 in the case using the larger 4mm diameter nozzle and a vessel of saturated liquid CO_2 as the feed phase and the highest calculated discharge coefficient was for saturated vapour feed phase and a nozzle diameter of 2mm. When comparing discharge coefficient for a consistent nozzle diameter the saturated liquid cases had lower values in both cases. It could also be seen that for both feed phases the discharge coefficient decreased as the nozzle sizes increased. Coefficients were compared by Pursell to the values experimentally determined by Richardson et al. (2006b) and fell in the same range.

Pursell also made calculations of the mass fraction of solid CO_2 at the atmospheric plane using a pressure-enthalpy diagram, in all cases under the assumption of adiabatic expansion between orifice conditions and atmospheric pressure. The short distances and time-scales involved as well as the higher than ambient pressures are used by Pursell to justify this assumption. Solid contents were calculated to be 3 and 34% for the vapour and liquid feed phase cases respectively which is a significant difference.

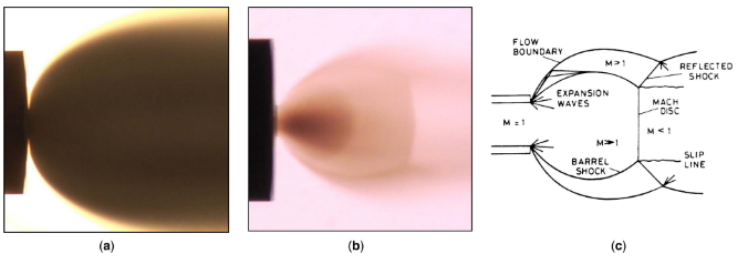

Figure 6.8: Backlit images of CO_2 expansion jets from (a) liquid feed phase, (b) gas feed phase. (c) a schematic of the typical shock structure in an under expanded jet (Pursell, 2012). Contains public sector information licensed under the Open Government Licence v3.0.

Backlit images capturing the structure of the jet can be seen in Figure 6.8 and clearly show the higher solid proportion resulting from a liquid phase release, with the dark, opaque jet containing a larger proportion of solid particles. For case (b) using the gaseous feed phase the shock structures are clearly visible and match well with the sketch. For the image in (a) from the liquid feed the higher proportion of solid phase CO_2 makes it very difficult to see any of the jet's internal structure which is a common problem with CO_2 jet visualisation. Obtaining the outline of the jet flow still allows

for estimations of the length of the expansion zone and the resulting effective diameter of the flow after expansion. Both expansion length and effective diameter depended on the nozzle width and increased for the larger diameter. The effective diameter also depended on the initial feed phase with liquid feed phase diameters giving roughly 30% larger values than seen for initial gas phase diameters.

The structure of CO_2 jets were shown to depend on the feed reserve pressure by Ahmad et al. (2013). The change in structure over time, whilst a reservoir is reducing in pressure was recorded by Ahmad et al. (2013) with the use a high speed camera. Images taken very early in the jet release showed evidence of a superheated liquid jet, before the boiling near the nozzle changed the structure to that of a diverging jet within 1 second of the release beginning. This is consistent with the work of Li et al. (2014) who also described a fully developed flow after 1 second.

Temperature profiles for a CO_2 jet were recorded by Toesse et al. (2013) who found that the location of minimum temperature was approximately 80mm away from the nozzle in the case of 1mm nozzle diameter and CO_2 reservoir conditions of 6MPa and 293K. There was however very little difference in temperature from the minimum (205K) location to very close to the nozzle where temperatures of 210K were recorded and the temperature only began to rise again significantly after distances of over 100mm. The effect of reservoir pressure on minimum temperature value and location was investigated by Ahmad et al. (2013). Vessel pressure was varied between 40 and 105 bar. For all experiments there was only nominal effect on the distance from the nozzle where the minimum temperature was recorded, though the thermocouple density was perhaps not high enough to be sure. The initial pressure gave very similar minimum value temperatures for three measurements in the range of 30-75 bar, however the test with 105 bar pressure in the vessel showed a significantly higher minimum temperature (approx -40°C compared to -80°C). One suggested explanation for this given by Ahmad et al. (2013) is that there is a delayed boiling effect observed at the start of the release.

Pursell (2012) also studied temperature fields while varying nozzle diameters. In addition Pursell also compared the temperatures when the reservoir contained different phases - saturated vapour phase and saturated liquid phase. Using pressures of ≈50 bar and nozzle diameters of 2 and 4 mm the author found minimum temperatures of ≈ -80°C for both nozzles using a liquid feed phase which is in good agreement with the results of Toesse et al. (2013). For the gas phase, the minimum recorded temperature was significantly higher for both nozzles, as can be seen in Figure 6.9. The liquid feed phase results also exhibit a low temperature for a greater downstream distance than their gaseous counterparts.

Analysis of solid CO_2 particle size was presented by Toesse et al. (2013) for a free jet from a 6MPa reservoir and an orifice of size 1mm using close up images

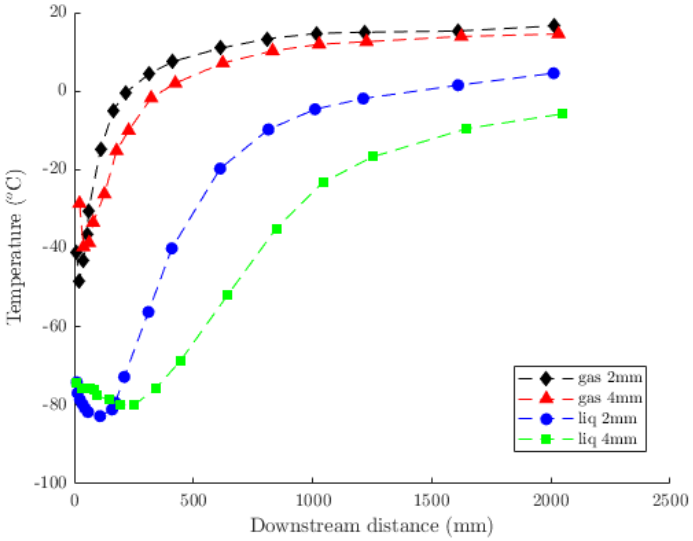

Figure 6.9: Temperature in the expanding jet of CO_2 recorded by Pursell (2012)

of various sections of the jet structure. Some particles between sizes 20-80μm were observed in the outer part of the jet but the centre was shown to be opaque, making assessment of particle sizes and velocities using close up images impossible. Laser diffraction analysis was instead used to investigate this region and found a peak of particles with characteristic size around 1μm. This result showed good agreement with the values measured by Liu et al. (2012) who found that primary particles ejected from the nozzle were about 1μm under similar experimental conditions to those used by Toesse. Lui et al also observed significant agglomeration of the particles to sizes of around 100μm.

Teng et al. (2018) researched the evolution of particle size as they travelled further away from the nozzle and found that they decreased in size as sublimation begins to take place and the solid phase transitions to gas (Figure 6.10).

The vast majority of the research concerning CO_2 de-pressurisation and expansion including the works on temperature fields and shock structures has focused on free jets where the jet expands into free space. For the application to machining, which is the primary motivation of the CO_2 work in this thesis, the under-expanded CO_2 jets will be impinging on the complex tool and workpiece geometries.

A study by Kim & Dongsu (2017) used compressed CO_2 and N2 to investigate the heat transfer of under-expanded impinging jets. The focus of Kim & Dongsu's study was to investigate a relationship between heat transfer and shock structure for under-expanded impinging jets therefore the bulk of the work involved nitrogen due to the visualisation difficulties with CO_2. The initial state of the CO_2 was gas in these experiments since pressures remained below the 5.1 bar triple point value so there was

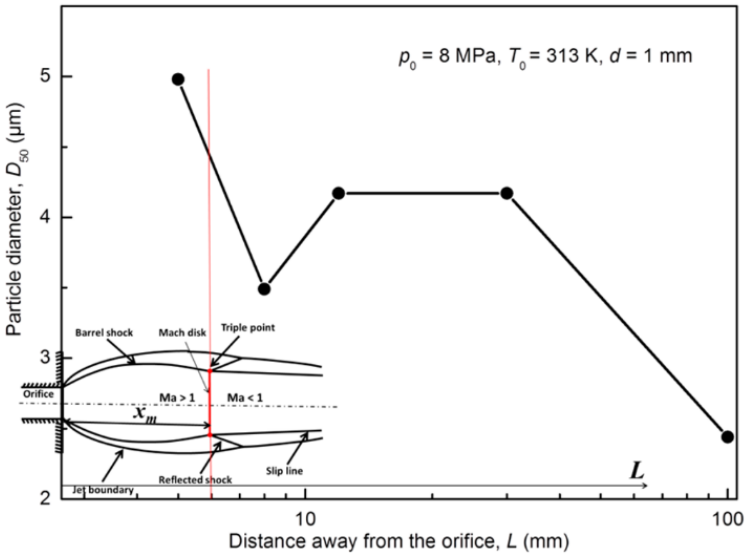

Figure 6.10: Dry ice particle sizes dependent on distance from nozzle in high pressure CO_2 release. Reprinted with permission from Teng et al, 2018. Copyright 2018 American Chemical Society

no liquid-vapour to solid-vapour transition although the expansion still generated solid CO_2 particles. These sublimating particles were predicted to enhance heat transfer due to the increased energy absorbed as they change phase from solid to gas.

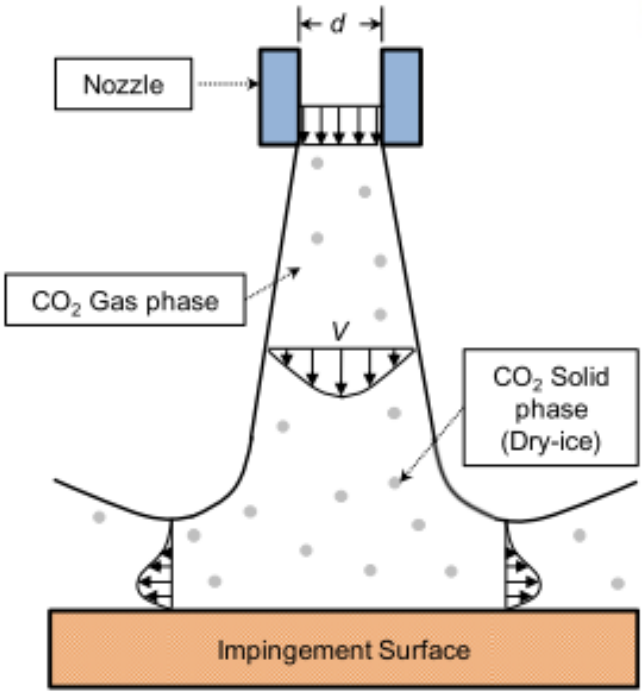

Figure 6.11: Multiphase CO_2 gas-solid jet observed by Kim & Dongsu (2017). Reproduced under creative commons license CC BY-NC-ND 2.0 KR

The experimental rig design, which is shown in Figure 6.11, consisted of an

adjustable nozzle fed by pipes from the compressed gas storage vessels and a copper block embedded and sitting above a heating element. Both the distance to the test block and the diameter were adjustable. Pressure and temperature were recorded at the converging nozzle and the temperature of the block was recorded using an array of embedded thermocouples as well as an infra-red camera directed at the surface.

Kim assumed a uniform 1D heat flux with no thermal spreading and used Fourier's law to evaluate the surface temperatures in both the CO_2 and N2 experiments using thermocouple readings from the copper block. Images taken using an infrared camera show that there were variations in temperature across the surface of the block (Fig 6.12), but with a discernible cold spot in the block centre where the jet was focused.

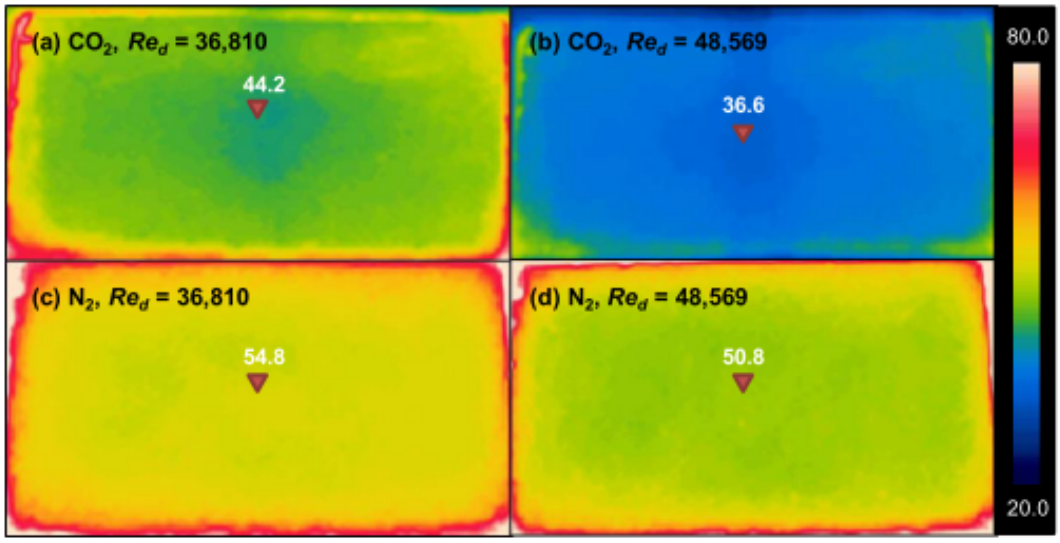

Figure 6.12: IR camera results for CO_2 and LN2 jets block temperatures (Kim & Dongsu, 2017). Reproduced under creative commons license CC BY-NC-ND 2.0 KR

For the thermocouples embedded at the same height in the copper block only small variation was found in temperatures recorded compared to the differences between the block temperature and nozzle inlet and outlet temperatures. This could be for several reasons, the copper block has a high thermal conductivity so it is possible that there was enough heat transfer in a horizontal direction as well as a vertical one to maintain similar temperatures at this depth in the block. Another explanation is that the surface temperatures themselves were also fairly uniform with less localised spot cooling than expected.

A parametric study on Reynolds number and nozzle to block distance by Kim & Dongsu showed a large reduction in temperature for an increase in Reynolds number for all distances, L, away from the copper block as can be seen in Figure 6.13a. There is a consistent decrease in stagnation temperature recorded as the nozzle gets closer to the

impingement plate however this is most exaggerated at the highest Reynolds numbers shown. To accompany this the heat transfer coefficients increase with Reynolds number and the highest is found when the nozzle is closest to the block.

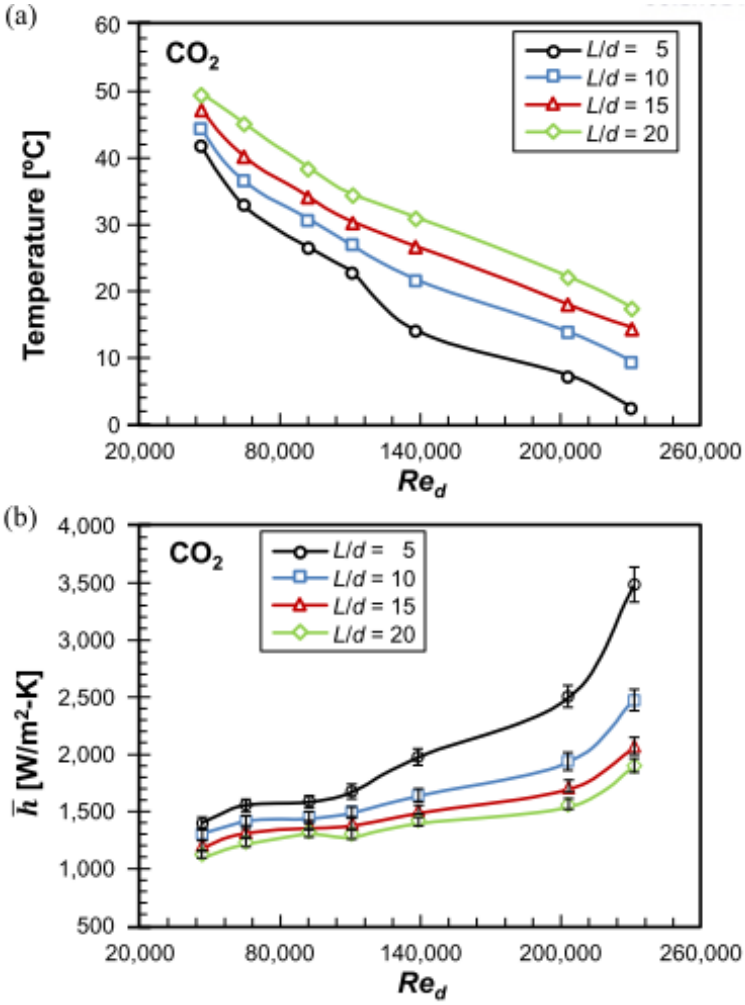

Figure 6.13: Temperature and calculated heat transfer coefficient for varying Reynolds numbers using an under- expanded CO_2 jet (Kim & Dongsu, 2017). Reproduced under creative commons license CC BY-NC-ND 2.0 KR

6.4.2 Modelling the Decompression of Carbon Dioxide

The thermodynamics and fluid dynamics involved in the release of CO_2 is challenging to both measure experimentally and model (Toesse et al., 2013). Historically, there has been interest in the modelling of CO_2 expansion from within the CCS field. In these settings, large quantities of highly pressurised dense phase CO_2 are transported in pipelines and there are safety concerns associated with this process since pipes can rupture or crack causing a release of CO_2. As such, the mechanisms around these CO_2 releases have been studied in detail, both experimentally and through the development

of specialised models (Pham & Rusli, 2016). The modelling methodology for a CO_2 release from a pipe orifice has a similar physical conditions to that of CO_2 application as coolant through small channels or converging nozzles. In this section, CO_2 release modelling methods are reviewed and assessed for suitability to industrial applications of cooling in machining cases.

The modelling of CO_2 release in CCS can be broadly split into three main disciplines, the decompression of the CO_2 filled pipeline, the near-field modelling which captures the complex expansion region, usually with a substantial pressure drop and phase change, and the far-field dispersion modelling which concentrates on the transport and concentration of CO_2 in the environment. An extensive review of the modelling approaches applied in all three disciplines can be found in Pham & Rusli (2016). Modelling approaches have included varying levels of computational complexity, with the key differences usually in the equations of state applied to the calculation of physical properties, and the multiphase model utilised.

Equations of State

An Equation of State (EoS) is a constitutive equation providing a mathematical relationship between state variables (ρ, T, V) for a substance. It is required to close the system of equations when a compressible flow is modelled since the density of the fluid is then assumed to be variable. Early work on equations of state trace back to 1662 as Boyle and Mariotte investigated the relationships between pressure, P, volume, V, and temperature, T, of air at low temperatures and derived the Boyle-Mariotte Law which was later combined by Clapeyron with the equations of Charles-Gay-Lusac to find the first statement of the ideal-gas law.

$$PV = R_0 T \tag{6.2}$$

Victor Regnault applied Avogadro's hypothesis from there to get the ideal gas law,

$$PV = nRT, \tag{6.3}$$

with the ideal gas constant R and number of moles n which has been a well established and widely used EoS since its derivation. While the ideal gas equation gives a reasonable level of accuracy for gases at low pressures and higher temperatures, it becomes increasingly inaccurate at higher pressures and low temperatures (Poling et al. (2001), Orbey & Sandler (1998)). This can make it a less suitable choice for simulations of a carbon dioxide expansion from high pressure.

Many Equations of State have been developed which modify the the ideal gas

equation to better represent gases in other thermodynamic regions (Liu, 2016). Most early EoS described either gases or liquids but there is now the capability to describe two-phase regions. The Redlich–Kwong (RK) EoS, an analytical cubic equation developed by Redlich & Kwong (1949), is a popular choice due to its ease of use and simple form:

$$p = \frac{RT}{V-b} - \frac{a/T_r^{0.5}}{V(V+b)} \tag{6.4}$$

$$T_r = \frac{T}{T_c}$$

$$a = 0.42748\frac{R^2T^2}{p_c}$$

$$b = 0.08664\frac{RT_c}{p_c}$$

T_c, p_c, V, R are the critical point temperature and pressure, molar volume and universal gas constant. It was the modifications of Soave (1972), however, in an updated SRK EoS that allowed the RK-equation to better stand on its own in modelling vapour-liquid equilibria (Tsonopoulos & Heidman, 1985). Soave replaced the $T_r^{0.5}$ term with a function $\alpha(\omega, T)$ where ω is the acentric factor and with this modification improved the vapour-liquid modelling so that the SRK EoS can be used to predict CO_2 properties in gas, liquid and supercritical state (Liu, 2016).

The Peng-Robinson (PR) EoS is a cubic equation of state developed in 1976 which has been shown to predict carbon dioxide properties well and is widely used since it is simple to implement (Liu, 2016). The Peng-Robinson EoS,

$$p = \frac{RT}{V-b} - \frac{a}{V^2+2bV-b^2)}, \tag{6.5}$$

$$a = 0.45724\frac{R^2T_c^2}{p_c}\left(1+\kappa(1-\sqrt{T/T_c})\right)^2,$$

$$b = 0.0778\frac{RT_c}{p_c},$$

$$\kappa = 0.37464 + 1.54226\epsilon - 0.26992\epsilon^2, \tag{6.6}$$

has similar form to the SRK EoS and gives similar performance in the gaseous phase but has been shown to be superior in predicting liquid densities in many cases (Perrot, 1998). It remains widely used in industrial settings, however, it often fails to predict pressure well in the liquid phase. Later developed by Martynov et al. (2013) the PR can be extended below the triple point to model the solid-vapour equilibrium that

is often observed in the multiphase jet upon release. This is managed by applying the usual equations (6.5) above the triple point but modifying coefficients a and b below this to those which better reflect the solid-vapour equilibrium line.

An EoS that does represent the gas and liquid properties of CO_2 well is the Span & Wagner (1996) EoS which is a complex equation built using a fit to all available data for CO_2. Having approximately 50 terms, it is not favourable for numerical methods implementation due to the computational expense associated with evaluating it, however, the fit to the data is good and where realistic to use, it is accepted to provide very accurate predictions (Liu, 2016). The applications of SW EoS are also somewhat limited due to the fact that the experimental data used to fit the model does not take into account data below the triple point, which limits its accuracy in this region.

As much interest arose in Equations of State for natural gases and mixtures of substances an EoS was developed by the European Gas Research Group / Groupe Europeeen de Reserches Gazieres (GERG) for single component systems or mixtures of up to 21 components including carbon dioxide, methane, hydrogen, etc, known as the GERG-2008 EoS (Kunz & Wagner, 2012). Valid for a wide range of temperatures and pressures and for gas and liquid phases the GERG-08 EoS is widely accepted as one of the most accurate to use (Wareing et al. (2013b), Liu (2016)).

The various equations of state developed over the years for CO_2 each have strengths and weaknesses. The very accurate models such as those of Span & Wagner (1996) and the GERG-2008 are complex and computationally expensive whereas the cubic equations are often inaccurate at certain pressures or in the multiphase saturation region. A composite EoS developed by Wareing et al. (2013b) incorporates the strengths of each by applying the PR EoS to model the gaseous phase and using tabulated Span & Wagner (1996) data in the liquid and equilibrium regions.

Multiphase modelling approaches

As CO_2 is released from high pressure, it can be seen from the phase diagram, shown previously in figure 6.1, that a change of state is expected if the CO_2 is previously held at a pressure over 5.1 bar. The presence of multiple physical states of CO_2 has been included in several modelling approaches of both decompression, near field and far-field releases. The most popular approach is to incorporate a Homogeneous Equilibrium Mixture (HEM) model. This model assumes that the phases are in the same conditions of velocity, temperature, and pressure, so that the conservation equations for any fluid present can be added together, as seen for liquid and vapour here for a mass, momentum and energy equation:

$$\frac{\partial \rho}{\partial t} + \frac{\partial \rho u}{\partial z} = 0 \tag{6.7}$$

$$\frac{\partial \rho u}{\partial t} + \frac{\partial \rho u^2 + p}{\partial z} = 0 \tag{6.8}$$

$$\frac{\partial E}{\partial t} + \frac{\partial u(E+p)}{\partial z} = 0 \tag{6.9}$$

as functions of time, t, and space, z. E represents the total mixture energy defined as $E = \rho(e + 1/2u^2)$.

The properties of the mixture with vapour mass fraction x_v, and liquid mass fraction x_l are taken as:

$$\frac{1}{\rho} = \frac{x_v}{\rho_v} + \frac{x_l}{\rho_l}, \tag{6.10}$$

$$e = x_v e_v + x_l e_l, \tag{6.11}$$

The assumptions of thermal and mechanical equilibrium associated with the HEM model are reasonable provided the dense phase CO_2 liquid drops or solid particles are sufficiently small (Woolley et al., 2013), however it is limited in some applications due to the neglecting of phase-slip and non-equilibrium liquid/vapour transition (Benintendi, 2014), (Woolley et al., 2013), (Brown et al., 2013). Non-equilibrium two-phase models which can capture a delay in phase changes and be utilised when particle sizes are found to be sufficiently large have been developed using a relaxation of the thermodynamic equilibrium by the introduction of a vapour mass fraction term. This relaxation approach, the Homogeneous Relaxation Mixture (HRM) model, adds a scalar transport equation to the HEM model:

$$\frac{\partial x}{\partial t} + u\frac{\partial x}{\partial z} = \frac{\Gamma}{\rho}. \tag{6.12}$$

The Γ term represents the interface mass exchange per unit volume, and is calculated as follows,

$$\Gamma = K(\phi - \phi_{eq}), \tag{6.13}$$

from a relaxation parameter, K and variable ϕ, which can be chosen as phase fraction, pressure, enthalpy or any other relevant thermodynamic variable(Brown et al. (2014), Zheng et al. (2017), Woolley et al. (2013)).

For the solid phase CO_2 particles, the HEM model could still be applied to find the concentration of solid particles in a dispersion setting. To more accurately model particle interactions and behaviours, an alternative Lagrangian particle tracking method could be used. Particles were explicitly tracked by Wareing et al. (2015a) in their modelling of turbulent particle-laden sonic CO_2 jets.

Combined CO_2 CFD modelling approaches

A range of these modelling approaches has been applied in different combinations in the literature, across all regimes of the CO_2 high pressure release. Several modelling approaches have been used to consider the decompression in pipes. This modelling usually only requires a simple quasi-one dimensional system, though the modelling tools can be complex and computationally expensive. Martynov et al. (2018), for example, included conjugate heat transfer modelling between the CO_2 and pipe walls, and physical properties calculated from the complex GERG2004 equation of state for liquid and vapour phases, and the extended Peng-Robinsion equation of state (Martynov et al., 2013) for vapour and solid CO_2 phases from along the sublimation line. A series of published work by Mahgerefteh (2006, 2008, 2012) presents a pipeline decompression model using the HEM mode for pipeline full bore ruptures and puncture failures. Properties near the wall such as heat transfer coefficients and friction are applied using standard correlations and the Peng-Robinson Gas EoS is used to calculate fluid properties. The conservation equations are used in wave form and solved using a method of characteristics. The modelling approach has been validated against multiple data-sets, including the National Grid CO_2 pipeline decompression tests (Cosham et al., 2012). A similar modelling approach was used by Teng et al. (2016) who modelled and experimentally investigated decompression over different flow conditions. Pressure monitor profiles were well validated for a vapour initial flow condition, but began to deviate from each other in both liquid and supercritical flow condition tests. For a comprehensive review of pipeline decompression modelling, the reader is referred to Zheng (2018). In further work these modelling approaches could be highly useful in application to the depressurisation of CO_2 in the supply pipelines in machining tools, since there is a release to atmospheric pressure at the end of the tool channel, and to predict and tailor the conditions here would be beneficial in enhancing the cooling control and understanding. For the current work, this is out of the scope and the focus is on the CO_2 cooling of the tool edge upon application, and the models applied have been almost exclusively using a quasi-one dimensional approach which would be too limiting for machining studies which have intricate 3D geometries.

There has also been significant interest in the dispersion and far-field modelling of the CO_2 releases as this is the element of the CO_2 release which can be a serious hazard to a widespread area. The UK Health and Safety Executive (HSE) have published a number of papers on CO_2 release and dispersion modelling. In-house tools and specialist codes are common in the modelling of CO_2 since it is a complex physical modelling problem with significant industrial interest. One heavily used software is PHAST, a hazard analysis suite which includes multiple models for CO_2 dispersion and consequence analysis. The software has been used for analysis of discharge and atmospheric dispersion of carbon dioxide, over a wide range of scenarios includ-

ing high-pressure cold releases (liquid storage) and high-pressure supercritical releases (vapour storage) from vessels, short pipes or long pipes (Witlox et al., 2011). The PHAST software has been validated against experimental results (Witlox et al., 2014), (Gant et al., 2014) with the flow rate predicted accurately by the PHAST discharge models (within the accuracy at which the experimental data were measured), and the concentrations found to be predicted within a factor of two accurately by the PHAST dispersion model. Commercial codes such as Fluent have also been used to successfully model the dispersion. Liu et al. (2014) used a turbulent flow HEM model with a PR EoS to predict the downwind concentration of CO_2. Hill et al. (2011) used the CFX CFD package to study the effects of particle size on the dispersion a the released CO_2 mixture. It was shown that the particle size has negligible impact on the prediction of downwind concentration, however the temperature of the plume retains a lower value nearer to the sublimation temperature for longer as particles are included in the model, and as they increase in size. The significant amount of research into far-field modelling is useful to some extent in machining processes, as the presence of solid dry ice particles could contribute to the heat transfer in the cutting region.

Modelling of the near-field region is less prevalent in CCS applications, and usually only seen as a means of generating the input parameters for dispersion modelling instead of being a core focus in its own right. It is also a particularly complex region to model due to the need to incorporate the expansion and shock behaviours of the CO_2, as was needed in the pipeline decompression, with a more real-world geometry in 2D or 3D. A specialised in-house code developed at the University of Leeds has been widely used to generate inputs for dispersion modelling. First presented by Wareing et al. (2013a), a composite two-phase method is developed and used to predict the thermodynamic physical properties of carbon dioxide (CO_2) above and below the triple point. RANS modelling was used to study a CO_2 release from typical storage conditions and the sonic CO_2 jet that forms was found to require a three-phase equation of state including the latent heat of fusion to accurately simulate its characteristics. This work was then validated (Woolley et al., 2013) using both data available in the literature and new experimental results. Excellent agreement with experimental data was achieved for the fluid and sonic structure and temperature measurements, and good agreement with respect to composition data. Later work by this group has included the incorporation of Lagrangian particle tracking to more accurately model the solid CO_2 within the expanded jet ((Wareing et al., 2013c), (Wareing et al., 2015b)), and extended the applications to both ruptures (Wareing et al., 2015a) and punctures (Wareing et al., 2014) of pipes and the flow of CO_2 from craters. The in-house nature of this code can make it difficult to access and apply across a breadth of other CO_2 modelling cases however, and there are limitations to the geometry and meshing capabilities of the software. An advanced mesh refinement algorithm, which refines the mesh along regions of steep gradients in physical properties, is used as part of the numerical modelling. The

geometry to solve for CO_2 applications numerically however is configured in an input file for the code and as a result is not currently suitable for running on complex 3D tool and geometries at this time. The code has been successfully applied to a machining application using simplified tool geometries to model a free jet from a nozzle using machining conditions however and would be a valuable tool in predicting the near field expansion upon tool coolant channel exit in future work.

Another near field model was implemented by Wang et al. (2021) which used commercial package Fluent and a computationally cheaper mixture model to account for the different thermophysical properties between phases. The Peng-Robinson EoS was used to accurately predict the jet shape and shock structures for the gas phase release experimental results of Pursell (2012). Fluent provides the built-in implementations of Peng-Robinson EOS, however it is limited to use under saturation conditions (Fluent, 2018). A User-Defined Real Gas Model (UDRGM) for Peng-Robinson EOS was implemented instead. This model captures many of the key features of the CO_2 jet release, however the minimum temperatures predicted along the jet centre-line were identified by Wang et al. as being unrealistically low who suggested this could be due to the use of the PR EoS which is not valid across the solid phase.

One of the main interests from a machining perspective is to model the heat transfer near to the cutting edge. Although the expansion, development and dispersion of CO_2 flow is considered in the extensive CCS work available, there is no heat transfer component considered. Predicting the jet temperature accurately is likely to be the most essential component in successfully modelling impinging CO_2 heat transfer. The temperatures in the CO_2 jet release are often predicted with some accuracy but impingement and conjugate heat transfer modelling are not considered, and temperature predictions in the jets have proved less reliable than other jet properties.

Outside of the CCS industry, two phase jet impingement and its potential for increased heat transfer are of increased interest. A CFD model for CO_2 sublimation cooling was presented by Kwak & Lee (2018). Combining a Euler-Euler multiphase model in Fluent which treats the solid phase as a pseudo-fluid and an incorporated sublimation model, heat transfer of a sublimating jet on a heated block was predicted. The modelling was configured to correspond to the experimental study of Kim & Lee (2016). The gas phase carbon dioxide was modelled as a compressible ideal gas. A simple carbon dioxide sublimation rate model was assumed with the sublimation rate taken as a linear function of temperature difference between the solid phase CO_2 and the surrounding gaseous phase. The CFD modelling predicted an increased heat transfer coefficient when the sublimation model was included, compared to the values observed without it. The predicted average temperature of the heated block being used as an impingement surface was also reduced when the sublimation model was included. As is often the case in the CO_2 modelling recorded here, some level of assumption is required

when setting initial and boundary conditions for the models. The amount of vapour and solid phase was presumed to be 90-10% and a constant CO_2 particle size of 100μm was assumed based on experimental observations of Kim & Lee (2016). Although these simulations were set up to match the experimental rig of Kim & Lee (2016), it should be noted that no results were compared between the model output and the experimental results as of yet.

6.5 Chapter Conclusions

In this chapter, a review of CO_2 cooling in machining operations, and more specifically, milling operations, was presented. In collection and comparisons of published work in the literature, the variability of CO_2 as a coolant was established and discussed. As has been shown in many works, CO_2 has viability as a coolant to both match and exceed the current standards for tool life and producibility observed in the utilisation of conventional emulsion coolants.

A gap in the literature in explanations of CO_2 behaviour near to the cutting edge has been identified. This behaviour is likely a culmination of its heat transfer, lubrication and flow field features. The following work in this thesis will seek to contribute to understanding of CO_2 flow fields and heat transfer in the cutting region, with both experimental and CFD modelling methods.

To support this, the chapter has also presented an introduction to the physical processes involved in the release of carbon dioxide from high pressure, and a range of modelling approaches previously applied to CO_2 CFD modelling. Much of the experimental work around CO_2 releases has considered the evaluation of an unobstructed CO_2 jet expansion, however a vapour phase release of CO_2 as an impinging jet for heat transfer applications was studied in detail by Kim & Dongsu (2017). If extended to high pressure liquid phase releases, this configuration would be applicable to machining research. The CFD modelling work available in the literature details many advanced techniques, some of which have even been applied to machining studies. There is often a difficulty in setting correct initialisation conditions for these modelling approaches, especially in far-field dispersion work. This is accompanied by a heavy reliance on initial conditions, often provided by difficult to validate and complex modelling of the expansion region of the jet. There is a gap in the literature for a model which can be applied to the full complexity of machining simulations and 3D meshes, such as those used in Chapters 3 and 4. The physical modelling would likely need to be simplified in order to attain reasonably efficient computational results. A simple and robust model which can be applied with a manageable computational expense to complex geometries is required for the modelling of CO_2 to be valuable and efficient in industrial machining

applications. A valid contribution to the literature would be to identify if such a model could capture the physical reality of the CO_2 coolant application.

Chapter 7

Experimental investigations into a high pressure release CO_2 jet for heat transfer applications

Contents

In Chapter 6, the use of CO_2 coolant in machining applications was discussed in a review of the available literature. Experimental studies of CO_2 coolant in machining settings have shown it to be a viable alternative to conventional oil-water emulsion coolants under the right conditions. Although significant improvements in thermal cutting wear have been observed in machining tests with liquid CO_2 compared to emulsion coolant, this has been very inconsistent and varies depending on cutting parameters, coolant application, and machining operation.

The heat transfer potential of CO_2 as a coolant is relatively little understood compared to the machining industry standards of water, emulsions and even the moderately new MQL. In this chapter, to obtain a more fundamental understanding of the

CO_2 flow and heat transfer an experimental rig has been designed and tested which removes the complexity of the machining geometries and will provide an opportunity to investigate the physics at play in a simplified setting. This experimental work will both provide essential validation data for a CO_2 CFD model and novel experimental results for the heat transfer of CO_2 cooling jets with studies on the effect of key experimental parameters.

7.1 Experimental Aims

Through these experiments the application of a liquid-fed CO_2 jet to a heated block will be investigated. Heat transfer coefficients will be calculated and their variability under different experimental parameters analysed.
The profile of local heat transfer coefficients will be considered in order to determine the heat transfer profile across the impingement surface.
CO_2 mass flow rates are also of significant interest in relation to the heat transfer coefficient, since the possibility of incorporating CO_2 as a viable coolant in machining applications is desired to be an environmentally friendly alternative to oil emulsions. Where very high flow rates are required for adequate heat transfer, this environmental benefit could be reduced and running costs increased — making the CO_2 an unsustainable option.
The experiments are designed with a geometrically basic set up in order to provide a simplified case to be used in validation of CO_2 conjugate heat transfer CFD modelling. A validated model would then be able to be used in more varied machining cases or to test out new geometries.

The aim of these experimental studies is to provide a set of validation data for a CFD model in a fundamental setting, and to allow for direct observation of the features of a CO_2 impinging jet and record any observations particularly relevant to machining applications.

7.2 Experimental rig design

An experimental rig has been purpose designed and built to investigate the use of CO_2 as a coolant. The outline of the rig design is similar to that built by Kim & Lee (2016). The design includes a CO_2 supply delivered to a heat transfer test bench, which is monitored to investigate heat loss through a series of transient data collections. Where the design of Kim & Lee (2016) investigated a gas feed cooling, the design in this work is modified to include a liquid feed of CO_2. Experimental parameters have also been chosen to more closely correspond with machining conditions than those used by Kim

& Lee (2016), such as an increase in the mass flow rates of CO_2 used to investigate the heat transfer, and a decrease in nozzle diameters, required to regulate the higher pressure liquid phase flow.

CO_2 supply and delivery system

The CO_2 supply to the test bench was required to be regulated and well contained due to the hazardous asphyxiate properties of CO_2 and the large quantities in use here. A liquid feed CO_2 tank is used to supply CO_2 to the test bench via a series of regulating and safety valves through to a converging nozzle.

The CO_2 is drawn from the bottom of the high pressure cylinder to enable liquid supply even as a pressure decreases and the cylinder then begins to hold saturated liquid and vapour phases in equilibrium. A regulator assembly with flexible hose then links to 1/4" Swagelok tubing before passing through a needle valve where this tubing size is reduced to size 1/8" outer diameter (OD) piping for the remaining supply line. The CO_2 is then passed through a safety cryogenic solenoid valve; this valve can be remote operated and can be used to shut down the CO_2 flow in case of an emergency. The solenoid valve requires an electrical supply to operate, and needs a small pressure difference on either side of the valve to be turned on. To facilitate this, a bypass section of tubing surrounds the valve to flood the line with high pressure CO_2 at the beginning of each test set to allow it to be turned on. The bypass line is then closed and the safety valve can operate effectively during the experimental runs.

The final valve in the piping is a Swagelok needle valve which is used more locally to the CO_2 application point and acts to control the flow rates and turn the flow on and off for short periods between tests.

Finally, the CO_2 is passed through connectors to a nozzle. The nozzle is fitted to the tubing using a Female/Female converter to connect to the pipe fitting. In any further experimental work, this would have been the location a pressure monitor could have been included in the rig to capture the CO_2 pressure in the tubing work directly above the nozzle.

The nozzle itself is a converging steel nozzle, the internal nozzle geometry can be seen in Figure 7.1. A selection of 3D printing nozzles were used with nozzle diameters, D, ranging from 0.25 - 0.8mm. The nozzle diameters used here are smaller than the 1 mm diameter nozzle used by Kim et al. (2001) who studied gas feed flow and the 2 and 4 mm nozzles used by Pursell (2012) who measured flow rates of up to 270kg/hr in their liquid-fed work, which are significantly higher than those to be investigated in this work. Pušavec et al. (2019), who studied the cooling of a heated

probe using CO_2 used 0.8mm nozzles in their investigations of liquid CO_2 with flow rates of 6 and 12 kg/hr which align with those seen in machining cooling applications and correspond more closely to the setup in this work. Enhanced nozzles with coatings to reduce friction in the converging internal channels were used to minimise any blockage risk in the case of solid CO_2 formation and promote smooth, steady flow. Decreasing the friction in the nozzle is also important to minimise the pressure drop and limit any transition of the CO_2 to vapour phase.

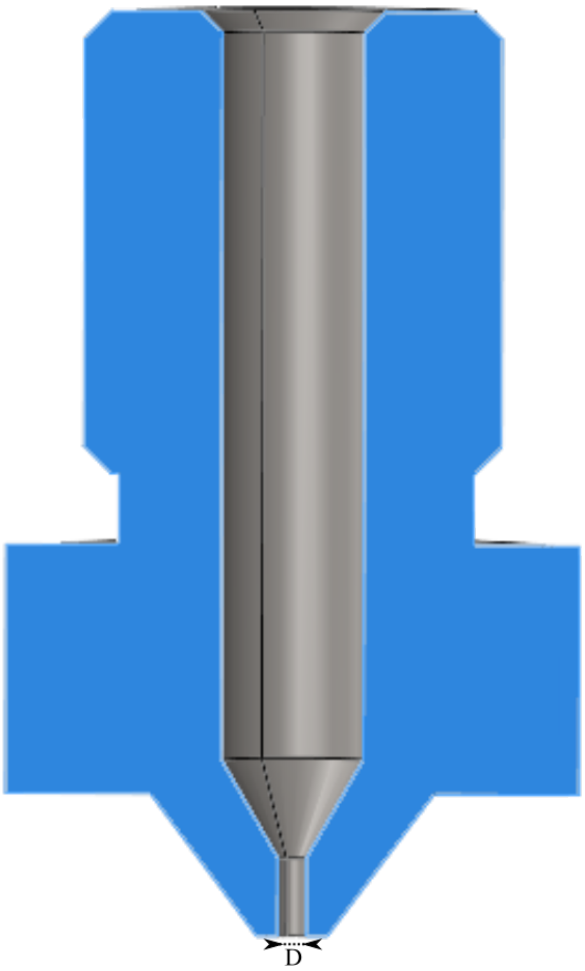

Figure 7.1: CAD drawing detailing the converging nozzle used in the experimental rig. The cut away slice shows the internal profile, with the nozzle converging to a diameter, D. Nozzles used here have diameters varying from $D = 0.25$mm to $D = 0.8$mm.

The converging nature of the nozzle and the high pressures in the tubing is expected to create a choked flow of CO_2 from the nozzles, as was reported by Pursell (2012) for a liquid-fed CO_2 release. Ideally, straight nozzles would have been considered alongside converging nozzles for this heat transfer study, since this is the current standard for through-tool machining channels, however, the choking of the flow is what enables the majority of regulation of the flow rate and keeps the pressure high in the internal pipes. This high pressure is needed to maintain a liquid CO_2 state, which is

preferable in these experiments since it is expected to significantly enhance the heat transfer if a high liquid volume fraction can be delivered to the nozzle. In addition, if a straight nozzle were used and the CO_2 were not regulated elsewhere in the system, the flow rates would be likely significantly higher and unmanageable in the current rig due to the CO_2 levels of the work space. As CO_2 consumption would increase, this would also lead to higher expense and be unsustainable and far less attractive as an option for alternative coolants in machining applications.

During the experiments, the nozzle and piping needs to be supported effectively and fixed in place. To this end, it is attached to aluminium support fittings. During any test runs the nozzle is set to a fixed distance from the heated test bench, H, as seen in Figure 7.2. Over the course of the experimental investigation this distance is varied between 3 and 30mm as part of a parametric study. The changing height of the nozzle fixture is enabled through the loosening of the surrounding fittings to allow the pipework to flow at small angles downwards up to the needle valve instead of being perfectly straight. This method limits any bending or stress on the pipes and valves supplying the CO_2.

The application of CO_2 to the heated test bench is carried out inside of a sealed test cell. This sealing of the application region within a suitable container was required to maintain safe working levels of CO_2 in the vicinity. The adoption of this sealed test environment was a required alteration to the rig design used by Kim & Lee (2016) due to the higher mass flow rates of CO_2 being applied in liquid-fed applications here and the limit on allowable concentrations in laboratories. The approach here is more closely aligned to that of Pursell (2012) who carried out their experiments in a suitable extraction chamber due to the use of liquid-fed CO_2 applications. The test cell is constructed out of clear perspex to retain unobstructed visual access to the CO_2 release point and test bench throughout the experiments and is chosen to be large enough so that the impact of a surrounding container on the flow rate is thought to be reduced to minimal. Sealing the box also provides the opportunity to monitor the flow rate of the CO_2 easily. In order to avoid a significant pressure build up during the test runs an outlet for the expanded CO_2 gas is needed. This outlet has been created in the back wall of the test bench container and has a flow meter fitted to it. As well as providing a safe CO_2 release, which is then easily directed up the ventilation chute in the laboratory, the CO_2 consumption can be monitored accurately using this flow meter.

Two additional holes are required in the panes of the sealed container. These include an 1/8” hole in the top of the box for the CO_2 supply piping, and another access point with a bulkhead seal for electrical cabling. These cables power components in the test bench and relay measurement data to loggers outside the container. The container is well sealed, with sealant applied around all permanent edges and a foam seal used

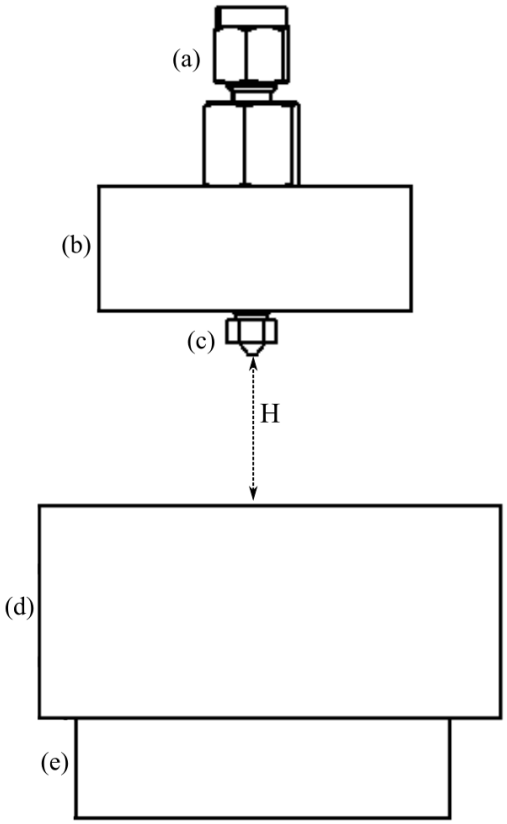

Figure 7.2: A schematic showing the CAD parts as follows. The tube fitting at the top (a) connects to the converging nozzle (b) via a female-female in-house fitting (c). The nozzle directs the flow at a copper test block (d), at a fixed distance, H, which sits over a ceramic heater (e).

on the access door pane which is tightly secured during each run.

The whole experimental rig is operated in a engine test-cell bay as an additional measure to improve safety and reduce CO_2 levels in the operating environment. The CO_2 flow which exits the rig via the flow-meter is well ventilated out of the room using an active ventilation system. For personal safety of anyone operating the rig, a Gas Alarm Systems Ltd CO_2 monitor is used to ensure appropriate working levels of CO_2. The monitor is set up to notify if either the long term working air quality exposure limit of 5000ppm in 8 hours, or the short term exposure limit of 15000 ppm in 15 minutes is reached.

The clear seal-able container, along with test bench and nozzle with fittings can be seen in figure 7.3.

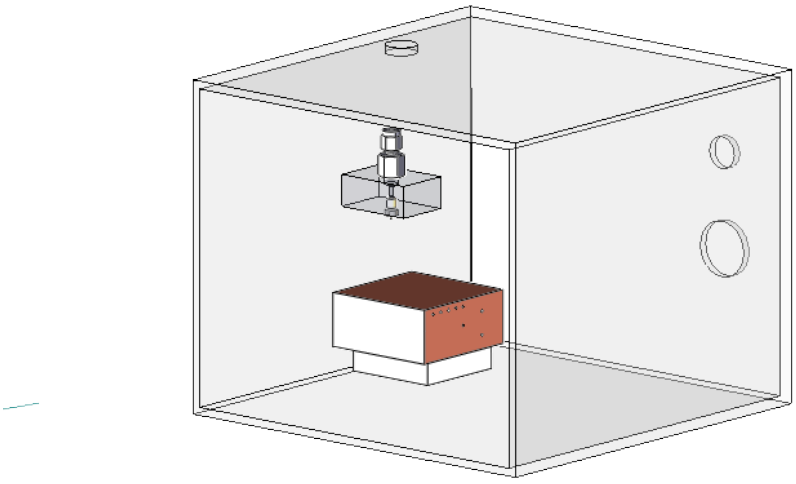

Figure 7.3: CAD model of the experimental rig section. Parts include the clear perspex box which contains the CO_2 application and allows it to be ventilated, the heating element, the copper test block and the nozzle and fittings to the pipework. All parts are in the correct proportions.

7.2.1 Heated test block design

As the CO_2 is released from the nozzle, it is applied to the heat transfer testing apparatus in the rig. This part of the test bench consists of a copper test block which has been pre-heated to a fixed temperature. The cooling rate of the block under application of CO_2 coolant can then be monitored under different experimental set up parameters.

The copper block, heater and nozzle with fittings was shown from a side profile in Figure 7.2. The heater used is a flat, square ceramic heater with a power of 125W. This is a low power supply when compared with the incredibly high power output generated and mostly converted into heat when machining, but there were limitations with size and safety due to surrounding components melting points. The heater used in this work has a higher power than the 12W heater used by Kim & Lee (2016), however was not able to supply a fixed power due to safety limitations when powering the heater element in the laboratory. The top of the ceramic heater is not flush against the copper and a seal of solder was applied to the connections between, along with a thermocouple to monitor the temperature at the interface. The copper block sits over the top of the heater element with a lip to secure the test block in place.

For the heated test plate, copper was chosen as the material to use due to its

high thermal conductivity and melting point. A 74 × 74 × 34 mm block was cut, with a square indent of 4mm height at the base which was used so that it fit over the ceramic heating element more securely. The copper block used in this study has been increased in size compared to the rig design of Kim & Lee (2016) since the use of liquid-fed CO_2 is expected to result in increased expansion of the resulting CO_2 jet and a smaller block could prevent the full expansion being captured. The temperature throughout the block was recorded with 8 thermocouples. Built to order by Thermosense, the thermocouples were J type to withstand both the high and low temperatures they would be exposed to in the rig, with a 50mm probe length, which was long enough to extend from the edge of the block to the middle and take readings in the desired locations, with additional room to remove the high temperature pot seal from the vicinity of the CO_2 flow and insulate from the cold temperatures or any moisture if necessary. A probe diameter of 1.5mm was used, which compromised the need for a small diameter probe in order the limit the interference with heat transfer in the block, and the minimum diameter which could be machined effectively into the copper to such a depth. The thermocouples were embedded in the test block at different locations, shown in the part schematic in Figure 7.4.

Five thermocouples were placed near to the top of the block to capture any difference in surface temperature between the centre where the CO_2 jet is to be applied and the outer edges. A further three were located lower down in the copper, with the goal to map the temperature field over the whole block. As seen in Figure 7.4, all thermocouples were inserted to the same depth, to capture the central plane of the block.

From Figure 7.4, it can be seen that the locations of the thermocouples are spread out to span almost the full width of the block, which is in order to minimise any interference. As the heat transfer is assumed to be approximately axisymmetric, the locations of the thermocouples can be mapped to a single plane running through the middle of the block where the jet is applied. In Figure 7.5, the thermocouple locations are mapped onto such a shared plane to illustrate their radial and vertical locations. Results taken at these locations can be interpolated to analyse the temperatures across the block.

7.3 Initial Testing and Experimental Process Development

Once the experimental rig was designed and built, initial testing was required to establish the best experimental approach and procedure to gather the data investigating heat transfer in this application. The two key areas of iterative development have been focused on the establishing of a suitable CO_2 flow and determination of consistent

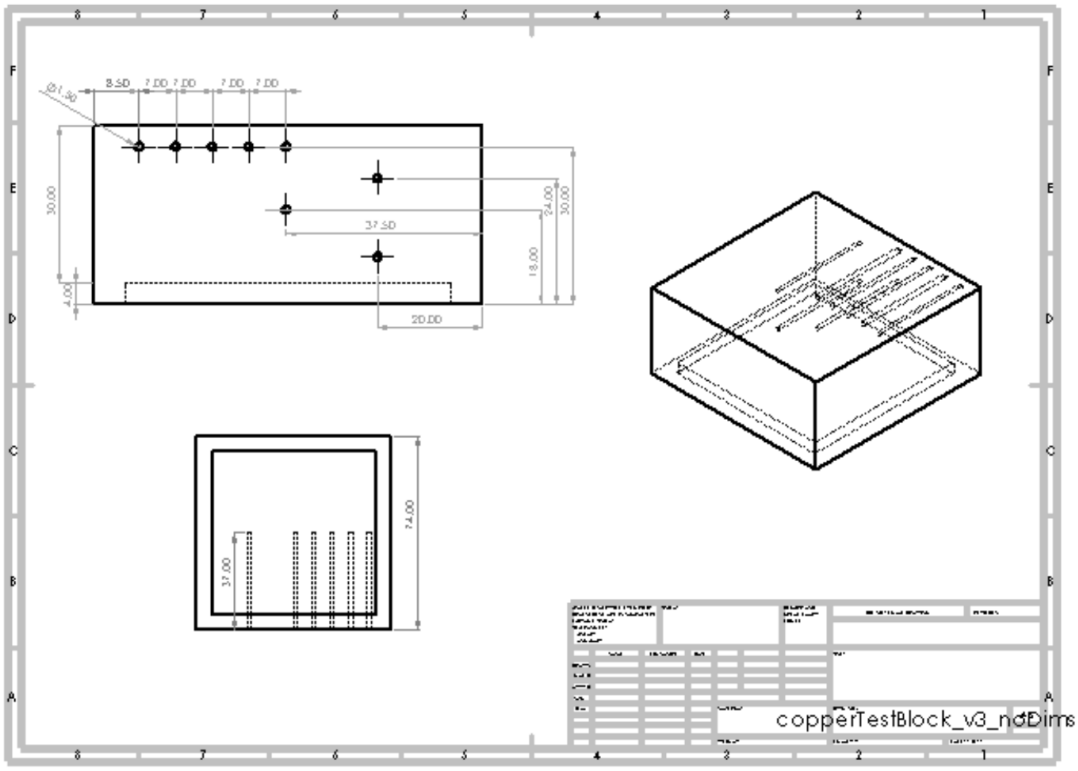

Figure 7.4: Engineering drawing of the copper test block with thermocouple positions shown. The top left drawing shows the block from one side, with the locations of the thermocouple insert holes all shown. The drawing beneath shows the equal depth all the thermocouple insert holes are drilled to in the copper block, and also includes the small square lip at the edge of the block, which allows it to sit over the heater. The third drawing on the right shows an isometric view, and the thermocouple locations are seen drilled into the centre of the copper block.

sampling of the flow rates, and in identifying best practices and temperature ranges to use when setting up the heated test section for each data collection run.

7.3.1 CO_2 Flow Stabilisation

In this heat transfer application, a steady flow of CO_2 is desirable to obtain the clearest data on heat transfer coefficients and the behaviours and capability of CO_2 as a coolant. A flow meter has been used to record the CO_2 volumetric flow rate leaving the sealed box during experimental runs. This flow meter outputs a voltage reading which then needs to be converted into a flow rate for further analysis. Calibrated flow rate data for the voltage to litres per minute (LPM) flow of air is shown in Table 7.1. Values for the volumetric flow of CO_2 are then calculated using a density for CO_2 of 1.96 kg/m^3. With the calibration data calculated for CO_2 flows, an interpolation is fitted for the

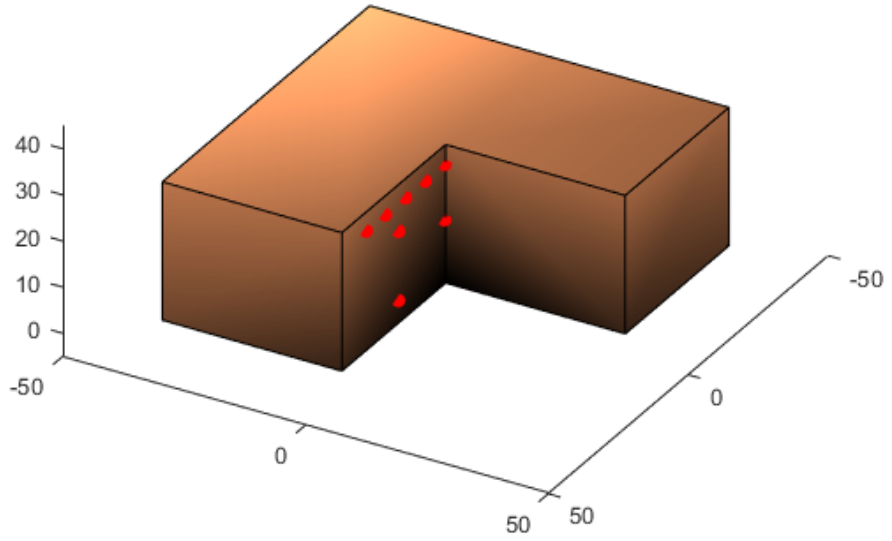

Figure 7.5: Shaded visualisation of the copper block with all thermocouples shown mapped onto one quarter slice plane, assuming even thermal energy transport from the centre of the block.

Flow meter readings (V)	Volumetric flow rate (LPM)
1	1
2.99	25
3.82	50
4.3	75
4.58	100
4.86	150
5	200

Table 7.1: Calibrated flow rate values for the Honeywell Airflow sensor flowmeter, provided in Voltage readings and standard condition Litres per minute flow rate corresponding values.

relationship between volts and flow rate. A Gaussian curve fit of the form

$$f(V) = a_1 e^{-(Vx-b_1)/c_1)^2} + a_2 e^{-((V-b_2)/c_2)^2} \tag{7.1}$$

is used to map the relationship between the voltage, V, and flow rates, f in kg/hr. The fitted parameters are $a_1 = 68.7,\ b_1 = \ 10.05,\ c_1 = 1.603,\ a_2 = 0.0038,\ b_2 = 6.054,\ c_2 = 2.436$.

The fitted curve, along with calibration data points scaled to CO_2 flow in kg/hr is shown in Figure 7.6.

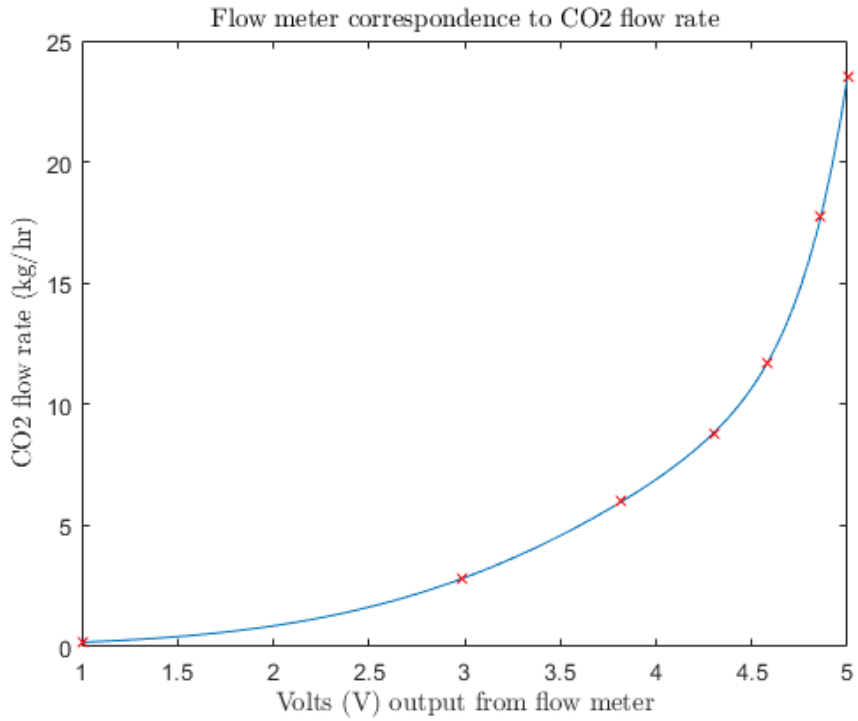

Figure 7.6: Fitted calibration curve to interpolate the Table 7.1 calibration data using a Gaussian curve fit (eqn 7.1). Voltage readings from the Honeywell flow meter output are calibrated to corresponding CO_2 specific mass flow rates in kg/hr.

Flow meter readings were used in the initial testing of the rig to investigate the flow development. It was observed that when the CO_2 supply to the rig was turned on, there would be a consistent flow development sequence. Immediately after turning on, the flow would create an under-expanded jet and show an expansion zone, which was clearly visible, as seen in Figure 7.7.

Shortly after establishing, the jet would then become near transparent and much more difficult to visually observe, although it was still clearly audible, before returning once again to a white, clearly visible jet, and remaining as such until the flow was stopped. It is assumed that the white opaque appearance of the jet is caused by solid phase dry-ice CO_2 particles which are formed on expansion from high pressure in these releases. In releases from both liquid and gas states, Pursell (2012) found that there was a much higher presence of solid particles formed in higher liquid phase fractions than in the case of gaseous releases. It is expected that there is some mechanism occurring while the flow is establishing which causes the pressure to drop for a small time, or an expansion in some of the pipe work upon the initial release which causes, for a short term period, a gas phase expansion resulting in a smaller amount of solid particle formations. Monitoring with the flow meter supports this hypothesis, as the flow rate reduces in the same time window, between two regions of higher flow, as highlighted in Figure 7.8. The development and flow of the CO_2 whilst in the piping

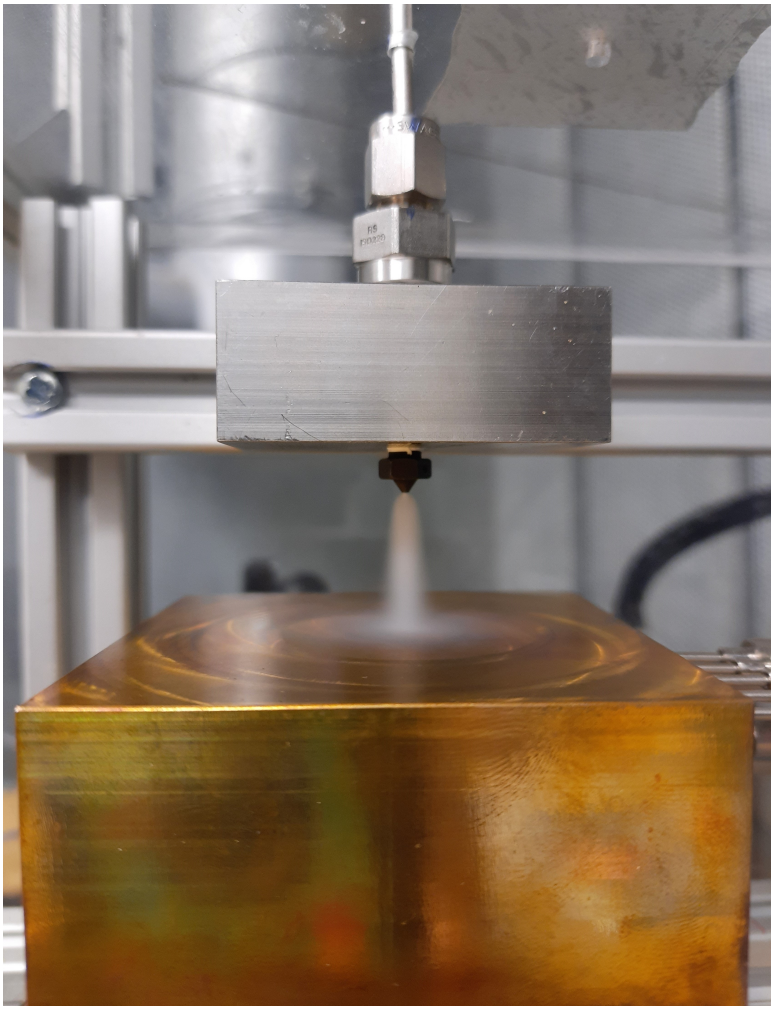

Figure 7.7: Photograph of the experimental rig in use, with the CO_2 supply pipe running through fittings to the nozzle, an expanding clearly visible CO_2 jet, and the copper test block on which it is impinging.

systems is out of scope of these experiments, as they were time limited and there are no measurements taken to provide more insight into these behaviours, but this could be of interest in future work.

The development of the flow, however, must still be taken into account in these experimental studies. Any sampling should be taken over consistent conditions, and so as a result of these observations, all results will be recorded only once the gas phase release period has been observed and finished to show a developed consistent jet.

In observing the flow rate data recorded in an experimental run in Figure 7.8, it can be also seen that there is a level of noise in the readings. Any noise in the readings from the flow meter in volts gets scaled to larger variations when converting into kg/hr due to the exponential terms in the Gaussian fit in equation 7.1.

To reduce any effect of noise of the flow results reported, the experimental

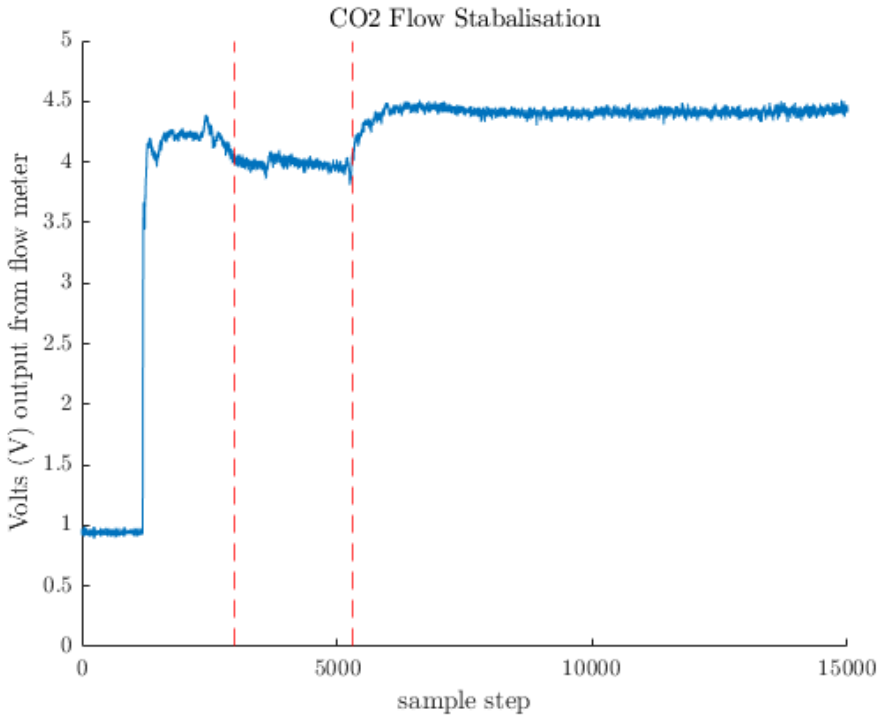

Figure 7.8: A graph of the CO_2 flow rate testing run output in volts over a sample with 15000 data samples. The beginning and end of a short period of reduced flow rate is highlighted between red dashed lines and corresponds to a temporary gas phase release.

process was altered to take a time averaged reading. The flow data will be recorded over the length of any heat transfer test run and a mean value of flow rate calculated and used. In each case, the flow data will be checked to ensure that no lower readings from a shorter term gas release have been included in the test runs. An example of a thirty second sample period with a mean value included is shown in Figure 7.9.

Testing was also completed to determine the level of control possible on flow rates with the needle valve closest to the application point. A series of runs were carried out with the needle valve open to varying extents. In these tests, a significant change in flow rate was observed when the needle valve was restricted to a point which resulted in an expansion and phase change in the tubing and a gas jet release of CO_2 at the nozzle, which exhibited much smaller flow rates. This expansion in the piping over a prolonged experimental run caused a significant temperature decrease in the piping, marked by the air surrounding the rig frosted onto the outside extensively.

There was only nominal control over the flow rate whilst in the liquid phase, with the output being difficult to control as real-time feedback includes only the noisy pre-processed data, making the flow hard to tune to a particular value. A far more effective way of managing the flow of CO_2 was found to be the modification of nozzle

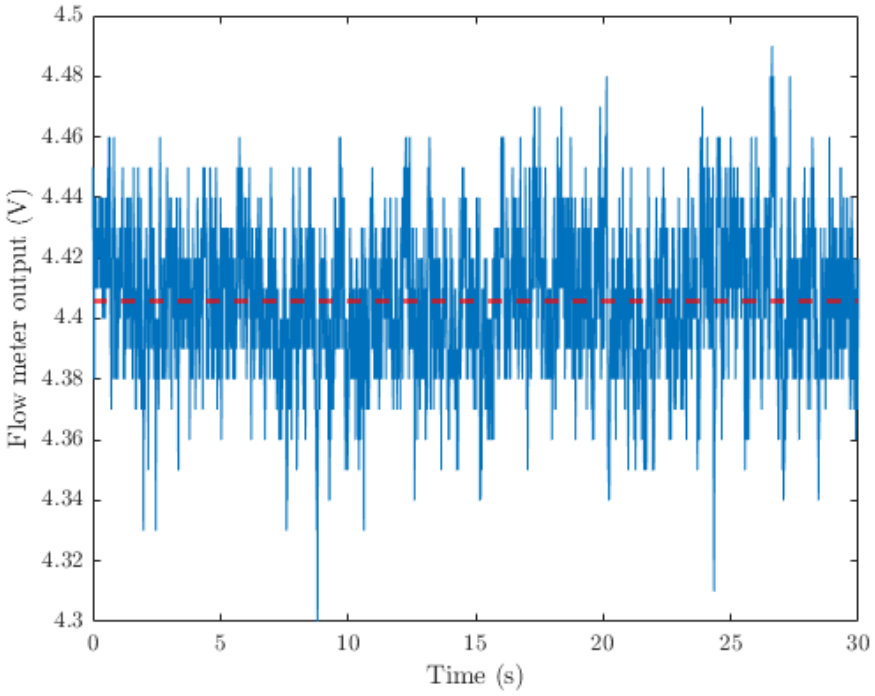

Figure 7.9: A graph of flow meter output in volts during a sampling period in an experimental test run. The sample length is 30 seconds long and is recorded, with an average value calculated which is plotted in red and taken as the mean flow rate for this period.

diameter. A range of nozzles was tested in the initial stages, with diameters of 0.25, 0.3, 0.4, 0.5 and 0.8mm. Flow rates across the varying nozzles was assessed, with the results shown in Figure 7.10.

The flow rates across the smallest four nozzles roughly level off to a steady value, though they appear to take a longer time to reach this developed flow as the nozzle diameters are reduced. The smallest nozzles could be taking longer to develop the liquid-fed jets expected due to the increased likelihood of small blockages, an increased impact of friction along the inside of the nozzle surfaces, or a reduced quality of the nozzle itself as they become more intricate to machine. The largest nozzle is not run long enough to be confident in a levelled off steady value for the flow rate. This was due to the significant increase in CO_2 consumption, which is already evident in the results, causing the safety alarms to register for the short term limit so that the test runs could not be continued.

The 0.25 and 0.3mm nozzles will only be used in limited test cases following these results, since the flow rates are lower then generally used in most machining applications. They also appeared to have very stuttering flows visually, with the jet appearing to fade back to gas for very short periods of time intermittently, though this

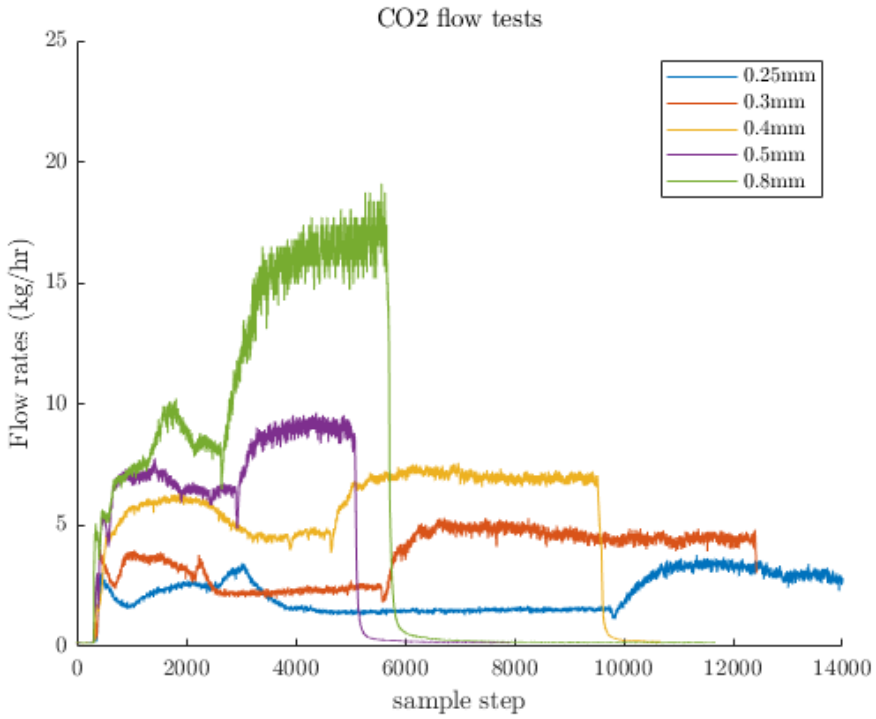

Figure 7.10: Experimental study of the CO_2 mass flow rates observed for five different nozzle diameters tested. The five nozzle diameters, 0.25,0.3,0.4,0.5 and 0.8mm were sampled over periods of varying lengths to establish an estimate of flow rates.

was not pronounced enough to affect the flow readings in these tests significantly, it is not something that is desired in the full test bench runs. The 0.8 mm nozzle appears to allow too high a flow rate for any extended use. It can still be utilised for short tests, but is not suitable for longer tests in this setting.

7.3.2 Heating apparatus

As part of the development of the experimental process, the heating element was used to assess the heat soaking of the copper test block. The planned experimental process involves the cooling of the copper block from a fixed temperature. This temperature would ideally have been as high as possible (around 200°C with this heater), but the heat soak temperature profiles shown in Figure 7.11 highlight the significant lengths of time it would take to soak the copper, and a high temperature would limit the number of runs possible due to time pressure in the laboratories. An initial temperature of 150°C is chosen as the temperature to heat the block to, though there is capacity to reduce this as needed in the experimental programme.

Initial testing was carried out to investigate the possibility of running the experiment to a steady equilibrium, by leaving the heater on, supplying a constant

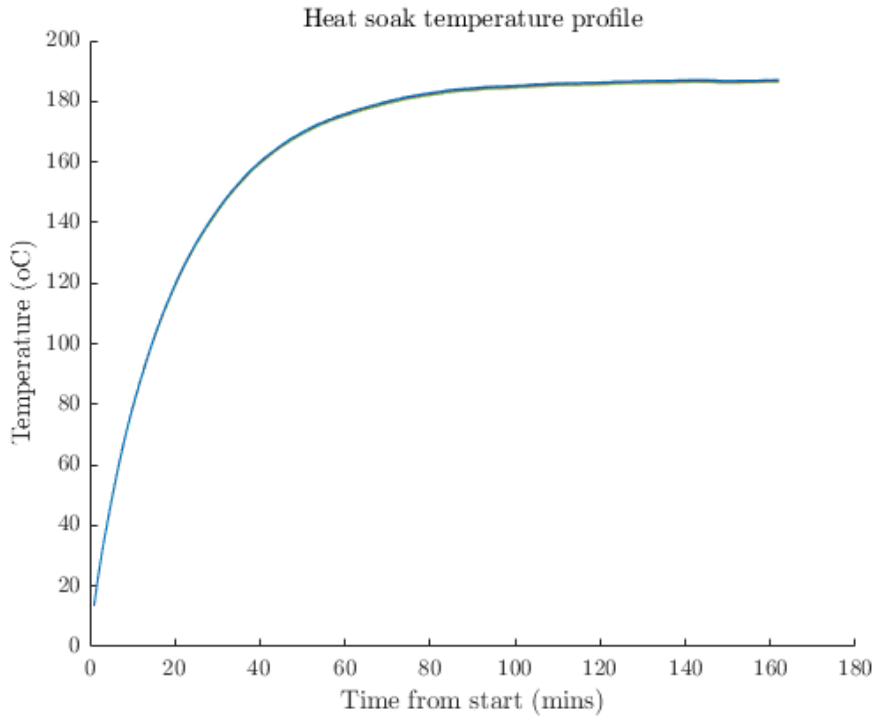

Figure 7.11: Thermocouple temperature profiles for eight different positions in the block during a heat soak test of the copper. The thermocouple profiles are indistinguishable and all show the increase in the temperature of the block. A quick initial increase in temperature is followed by a more gradual approach to the maximum temperature reached of around 180°C.

amount of energy to the test bench, and establishing a steady CO_2 jet until a thermal equilibrium could be reached.In this instance, the amount of thermal energy which was being removed by the CO_2 cooling jet could be established.

In these initial tests the copper block was allowed to heat up to a high temperature and then the CO_2 was applied without turning off the heating element. Results from one such test can be seen in Figure 7.12. The cooling curve, which includes all thermocouples in the copper block, shows a decrease in temperature when the CO_2 is turned on and a decrease of nearly 100°C in 4 minutes. The curve does begin to decrease in gradient and near a steady state towards the end of the run, however at 11 minutes the CO_2 supply had to be turned off due to the CO_2 alarm being triggered at the high limit. There is a small increase in temperature at this 11 minute mark in the results, as the CO_2 supply is removed and the heater remains on.

Even if the CO_2 levels had remained above the short term working exposure limit, both the low temperatures reached (-60°C) and the increase in CO_2 consumption over the extended time span of this experimental run make this approach unsuitable within the scope of this work and rig design. Although most components in the test cell were specifically sourced and rated to work at low temperatures, the flow meter

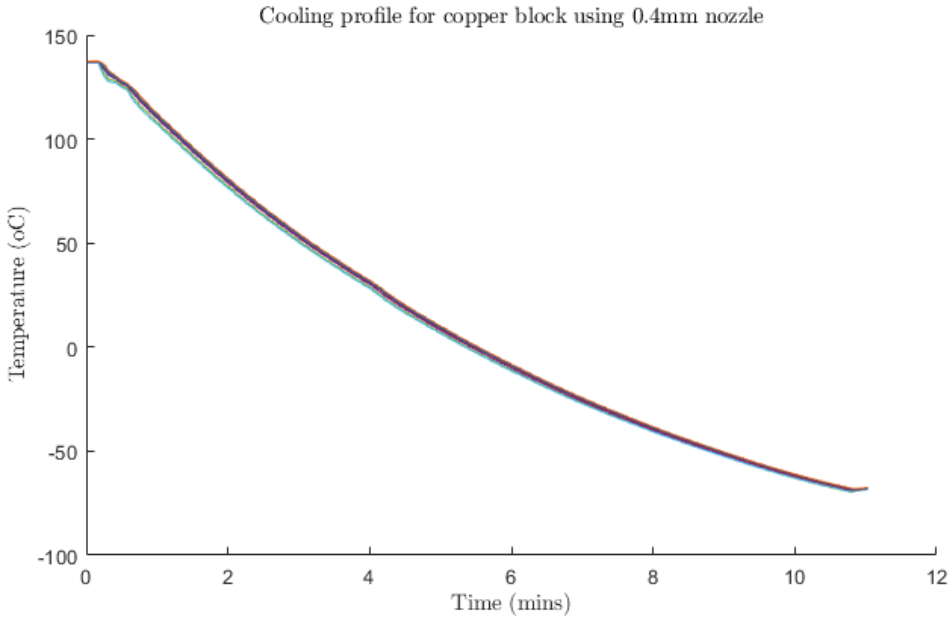

Figure 7.12: Thermocouple profiles showing the temperature decrease of the copper block under the application of a CO_2 impinging jet using a 0.4mm diameter nozzle at a distance of $H = 30$mm between the copper block and nozzle exit. The sample runs for 11 minutes, with a decrease in the block temperature from 140°C to -70°C.

accuracy is reduced at these low temperatures and any water vapour contained in the box when it is sealed for the test run condenses and subsequently freezes onto various points in the box. The proximity of several electrical components and the ceramic heater meant these working temperatures and conditions would ideally be avoided. The quantity of CO_2 used under a steady state experimental process is also a severely limiting factor, as it effectively divides the number of test runs possible by 10 compared to the proposed 1 minute tests.

In any further iterations of this experimental design, one key component to work on improving would be the heating element used here. The goal here was to use a small element since the box is contained and the CO_2 jet and nozzle are small. After observing the cooling capabilities of the CO_2 paired with the thermal conductivity of copper, a larger heated block would likely still be suitable and this would allow for a larger, higher powered heater. The method for using this heater could also be improved. In its current iteration, the heater responds to a thermocouple placed on its surface acting as a thermostat, to ensure it did not exceed the working temperature range. However, the nature of this set-up meant the power supply was not constant and the heater was not on continuously. In reality a continuous supply of power is needed to reach a steady state equilibrium with the CO_2 cooling jet, and the installation/workings of the heater could be addressed. Alternatively, the rig could be improved by modifying it to be closer to a machining setting. The heat/power generated in the rig could be

created in a manner more similar to machining, with a turning part on a motor creating a high friction point against another fixed surface.

Initial testing results providing cooling curves, shown in Figure 7.12, included data from all thermocouples present in the copper test block. The copper block surface and volume are relatively large compared to the apparent area of the CO_2 jet, which can be seen in Figure 7.7. As a result, it was anticipated that differences would be seen in results between the spread-out thermocouples as the temperature of the block decreased upon CO_2 application. Instead, the results are shown to be very similar, and only record a couple of degrees difference in temperature between the hottest and coolest thermocouple data at any point in time. The testing results indicate that the high thermal conductivity of the copper block is managing to conduct the heat through the block quickly.

The results of the thermocouples in the initial cooling tests can be interpolated to visualise the temperature profiles across the copper block's entire volume. The interpolated values, shown as a contour over a cut slice of the block in Figure 7.13, show the small 2°C temperature difference observed. It can also be seen that the lowest temperatures during the cooling region are at the centre of the block, near the top surface where the CO_2 jet is applied. The temperatures then gradually increase moving away from this point, to be warmest at the outside edges.

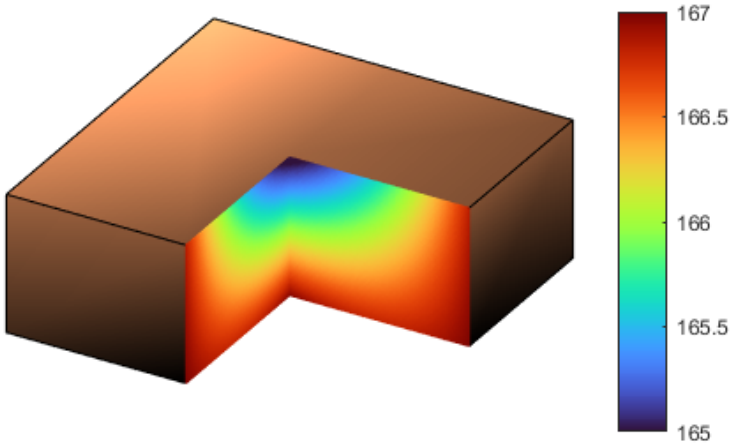

Figure 7.13: Contour plot of the internal temperatures of the copper block, as interpolated values from the thermocouple readings obtained during a cooling curve test.

Due to the small differences in temperatures across the block throughout the cooling tests, the temperature readings in the experimental investigations will be averaged to provide one mean temperature value across the volume of the block.

7.3.3 Final Experimental Methodology

Using the initial testing stages, an experimental methodology has been finalised for this work.

1. The rig will be set up by initially heating the block to a fixed temperature of 150°C.
2. The CO_2 piping will be flooded to achieve high pressure and all safety valves will be turned on.
3. The needle valve near to the test bench container will be turned on to initialise the CO_2 flow
4. Once the jet has developed and returned to a stable, visible appearance a sample can begin
5. Temperate and flow rate data are collected over a sample of at least 30 seconds
6. CO_2 supply is turned off at the needle valve
7. The data is processed to calculate an average flow rate over the sample length and a mean start and end temperature over the copper block volume for the same period.

7.4 Characterisation results

The high pressure release of CO_2 in these experiments develops into a highly under-expanded multiphase jet. The form of the jet is complex compared to a single phase coolant release of oil-water emulsion. Observations of the properties of the jet are recorded here to provide insight into any behaviours and to help investigate or explain the heat transfer results more fully.

The visual inspection of the jet showed it to be visible through the entire core of the jet from the nozzle tip to the impact point on the copper block in Figure 7.7. A high speed camera was used to make additional observations, with a frame shown in Figure 7.14. The camera recorded footage at a frame rate of 8000 fps, which was the

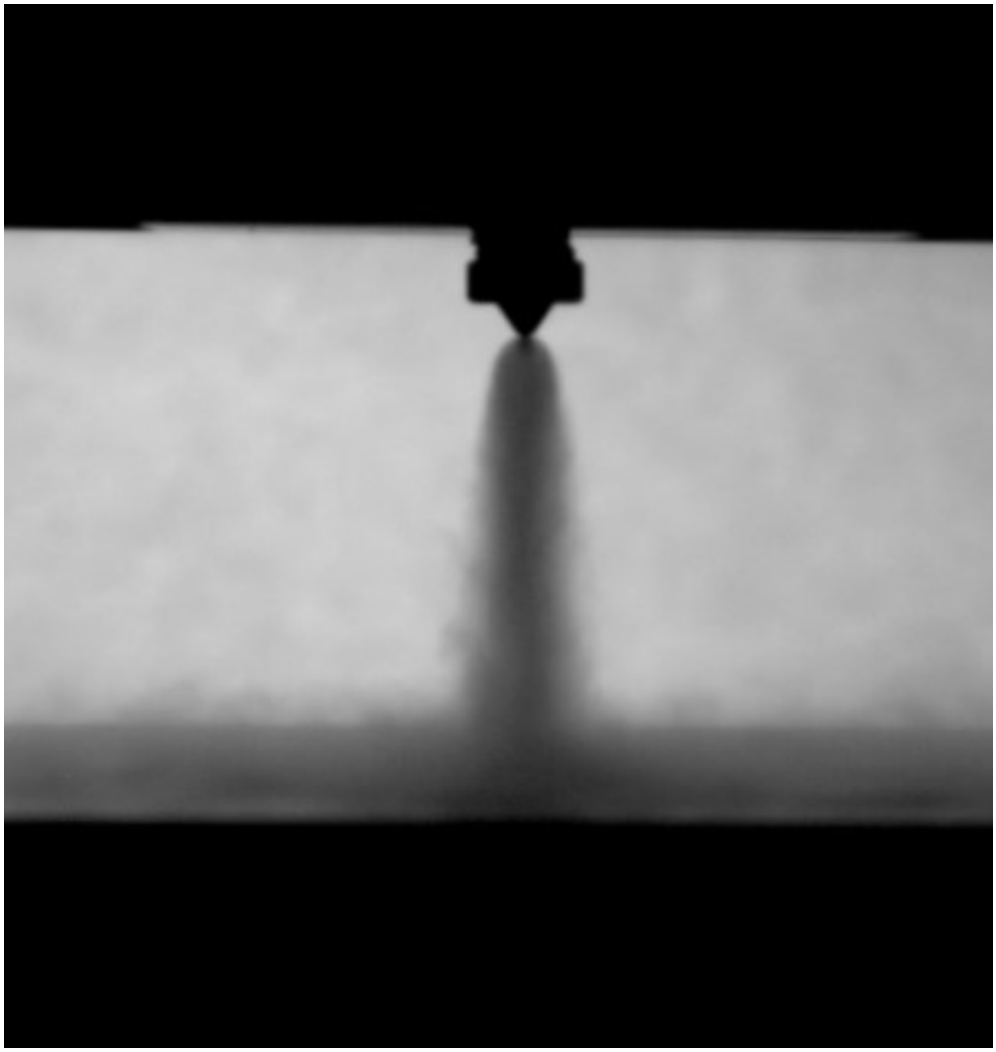

Figure 7.14: A frame from a high-speed camera recording of the application of the CO_2 jet to the copper test block. Illuminated with flood lighting from behind, the shape of the jet is captured to show the outline and expansion of the jet from the nozzle.

upper limit due to the accompanying short exposure times and darkening of the visuals above this fps rate.

The high speed camera images show the shape of the CO_2 jet for application from the 0.4mm diameter nozzle. There is a clear bow shape to the jet as it expands upon exiting the nozzle and at the top of the jet the shape has a clear, sharp outline. The flow further from the nozzle seems to expand slightly still as it interacts with the surrounding air and has softer outlines, while the centre of the jet still appears darker. Upon impacting on the test block, some CO_2 can be seen moving along its surface, outwards towards from the centre of the jet. This is consistent with the shape and behaviours observed by Pursell (2012) for liquid-fed results.

Visual inspection of the CO_2 under expanded jet flow indicates that the cir-

cumference of the jet core that impacts onto the copper block is much greater than the nozzle diameter. In machining applications, where the angle of the coolant channels directed towards the tool's cutting edge is limited by the obstruction of the tool body, this feature of the jets could promote the supply of coolant to otherwise unreachable regions, since the applied CO_2 expands to cool a wider area outside of its direct line and size of application channel. The expansion of the jet can be assessed from the images of the jet releases here, and an expansion ratio for the expansion diameter, D_e, to the nozzle diameter, D, is calculated as $D_e/D = 10.5$ for the jet release in Figure 7.14. This is similar to the liquid release expansion recorded by Pursell (2012), who studied free jet releases, of 9.15 for a 2mm nozzle.

Further to recording of the copper block temperatures, a thermocouple has also been used to collect temperature data from various positions in the core of the under-expanded jet. Multiple readings were taken of the temperature at the base of the jet, where it impacts on the copper block, at a height of H/2, midway between the block and nozzle, and near to the top of the jet, just inside the expanding region. For each height tested, the thermocouple was inserted into the jet multiple times across the jets diameter at that height. The results of each study are plotted as profiles in Figure 7.15.

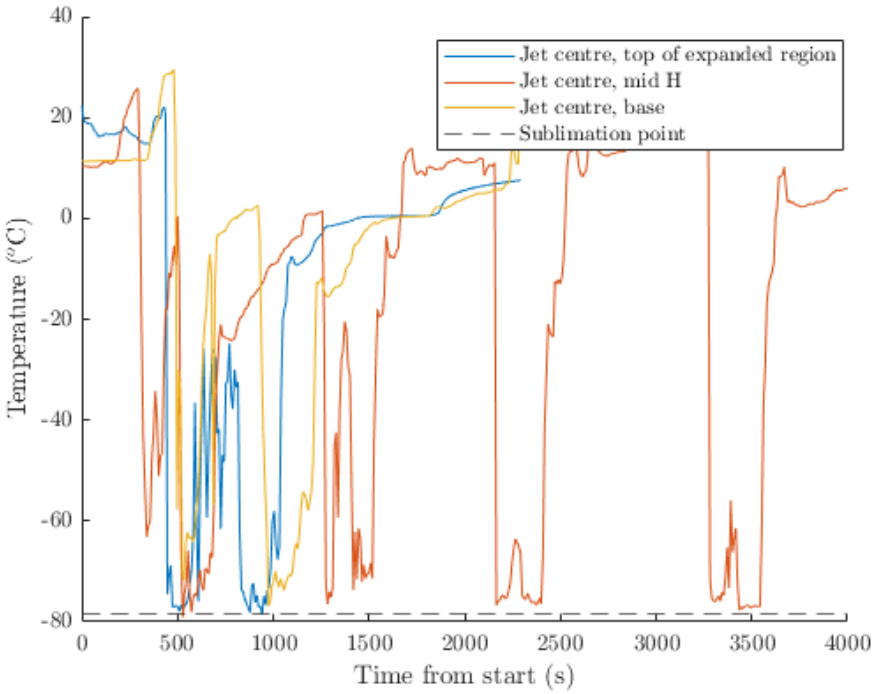

Figure 7.15: Thermocouple temperature profiles for assessments of temperatures inside the core of the CO_2 jet. Different samples at the top, bottom and midpoint of the height of the jet were sampled, with multiple readings taken in each profiled sample site. The sublimation temperature of CO_2 at atmospheric pressure is included for reference.

The temperature profiles show sharp changes as the probe was entered and removed from the CO_2 jet, but across the three heights and different radial positions within the jet where there is a sharp decrease in temperature, the resulting low temperatures are very similar. In all cases the results decrease to around -80°C. This appears to support the proposal that there is a significant quantity of solid dry ice particles within the expanded CO_2 jet. The CO_2, upon expanding from the dense phase liquid release, has formed a gas and solid particle jet, since these are the only two phases which can exist at atmospheric pressure. The temperature at which the CO_2 solid particles sublimate to gaseous form is -78.5°C. The sublimation temperature, added on to Figure 7.15 as a dashed line shows the temperature profiles of the jet touching it at several points and sitting near to it in others, which suggests the gas jet being monitored is made of the gas-solid equilibrium, as expected. The temperature of the jet cools to the sublimation temperature and seems to remain consistently around this value for the length of the jet between the expanded region and the copper test bench. There were some increases to around -60°C as the probe was moved further from the centre of the jet and along the copper block just outside the main skirt of the jet (yellow profile, ≈1250 seconds from start). At this location, the jet is less densely filled with solid particles and mixes with the air more, which could contribute to the higher temperatures. Alternatively, the readings were also taken on the copper block, which had some residual heat (≈40°C) and could have impacted on the readings more outside of the dominant region of the jet.

Readings with other diameters of nozzle were also tested for temperature profiles and revealed the same behaviours, with the minimum value of just above -80°C being encountered throughout the body of the jet. Applying these characterisation analyses to cooling applications, the temperature of the jet appears to be consistent across the range of experimental parameters considered here. Within the small distances from the nozzle (up to H=30mm) and the nozzle diameters considered (0.5mm, 0.3mm), the jet temperatures reduce to around the sublimation temperature (-78.5 °C) across the core of the jet. Similar temperatures have been recorded for under-expanded liquid-fed CO_2 jets by Pursell (2012) who observed a minimum temperature of -82.9°C and -80.8°C for 2 and 4 mm nozzles respectively. Pušavec et al. (2019) recorded a temperature of -71.2°C in the region near to the nozzle outlet in a liquid-fed release. The downstream temperatures recorded by Pursell (2012) showed that the CO_2 jet reached these cold temperatures immediately after the outlet and remained low for a range of over 100 mm in the 2 mm nozzle case and nearly 300 mm in the 4 mm nozzle case. This shows excellent agreement with the findings in this work that the jet remains near sublimation temperature up to the impingement surface, which is only a maximum of 30 mm away from the nozzle outlet. The temperatures recorded for gas phase releases by both Pursell (2012) and Kim & Lee (2016) were higher, with a minimum of -48.3°C recorded.

7.5 Exploration of experimental parameters

To expand on the characterisation experiments carried out, an exploration of some of the experimental rig parameters was completed to determine their effect on the heat transfer using the CO_2 coolant jet. Variables of interest included the nozzle diameter (and therefore the CO_2 flow rate and jet diameter), and the distance, H, between the nozzle and heated plate.

In these experiments, a heat transfer coefficient, h, is calculated which quantifies the convective heat transfer of the CO_2 flow over the copper test block. The thermal energy change, Q of the block during the sample period is calculated as,

$$Q = mC_p(T_f - T_i) \tag{7.2}$$

for the mass of the copper block, m, the specific heat capacity of copper, C_p, and the temperature of the block at the initial and final times, T_i, T_f. The heat flux, q, is then calculated by dividing through by the surface area of the heat transfer region, A, and the length of time, t,

$$q = \frac{Q}{At} \tag{7.3}$$

Finally, a heat transfer coefficient, h can then be calculated by dividing by the difference in temperature between the copper block and the jet.

$$h = \frac{q}{\Delta T} \tag{7.4}$$

Experiments have been repeated at least twice for each configuration to determine reliability, with results of all experimental runs included below.

7.5.1 Variation of nozzle to plate distance, H

The distance between the CO_2 supply nozzle and the copper test block, H, has been varied between 3 and 30mm. Results of the testing with one nozzle diameter, D=0.4mm, are shown in Figure 7.16. They show the calculated heat transfer coefficient and how it varies with the distance, H.

Error bars have been added to the data points to show the uncertainty in the experimental data. The heat transfer coefficients have been calculated using input from multiple independent variables, including thermocouple output and dimensions of heat transfer surfaces, and these have been combined into one value for the uncertainty using the formula for Propagation of Error (Ku et al., 1966) for the standard deviation σ of a function $f(a, b, c)$, of variables a, b and c and the standard deviations of each

variable, σ_a, σ_b and σ_c respectively,

$$\sigma_f = \sqrt{\left(\frac{\partial f}{\partial a}\right)^2 \sigma_a^2 + \left(\frac{\partial f}{\partial b}\right)^2 \sigma_b^2 + \left(\frac{\partial f}{\partial c}\right)^2 \sigma_c^2} \tag{7.5}$$

In these experiments, the measurements which are used to calculate heat transfer coefficients are the measurements of surface area and copper block dimensions, which are determined to have a tolerance of ±0.5 mm, the measurements of temperature, which are from thermocouples with a tolerance ±0.5 K, and the flow rate calculated from the flow meter voltage output.

The flow meter voltage readings are time averaged due to the variance seen in readings over the recorded sample periods for each experimental run (shown in Figure 7.9). For these samples, the standard deviation over the sample period is used in the calculations of error propagation.

The heat transfer coefficients varied between ∼ 380 - 510 W/m^2/K. As far as possible, every experimental variable was kept consistent across these tests apart from the distance, H, however there is significant variation in the results observed. At each value of H the experiment was run twice to assess repeatability and there appeared to be discrepancies across all data points. Repeated data points for a fixed value of H lie outside of the experimental uncertainty for other data points at the same value of H at several locations. Upon analysis, although every effort was made to run the tests with consistent flow rates, the limited control over the flow rates using the needle valve and the absence of real time flow data during the runs made it difficult to control and there was also variation in flow rates observed over the test sets.

Given the spread of the data it is difficult to make statements or draw conclusions on the trends of the data with the variation of H with any strong confidence, however the results for the heat transfer coefficient do seem to increase somewhat at the smallest value of H. To provide more clarity in the results, the flow rate is used to normalise the data in Figure 7.17. Once the heat transfer coefficients, h, have been divided by the flow rates the data is much less scattered and a trend is more obvious. This shows a significant sensitivity in the heat transfer coefficients to the mass flow rate of CO_2, $\dot{m}$. This sensitivity to flow rate of CO_2 in jet cooling has been observed in several studies (Chen et al. (2021), Kim & Lee (2016), Pušavec et al. (2019)). There appears to be a sharp increase in $h/\dot{m}$ as H is decreased and the nozzle moves closer to the test plate. This agrees with the findings of Kim & Lee (2016) who also reported an increased heat transfer coefficient with reduced nozzle to plate distances. The results in this study show a reduction of 4% in the heat transfer coefficient when H/D is increased from 5 to 10, which is the same order of magnitude of the reduction seen by Kim & Lee (2016) of ≈ 7% for the same H/D values. There is an increase in $h/\dot{m}$ again from

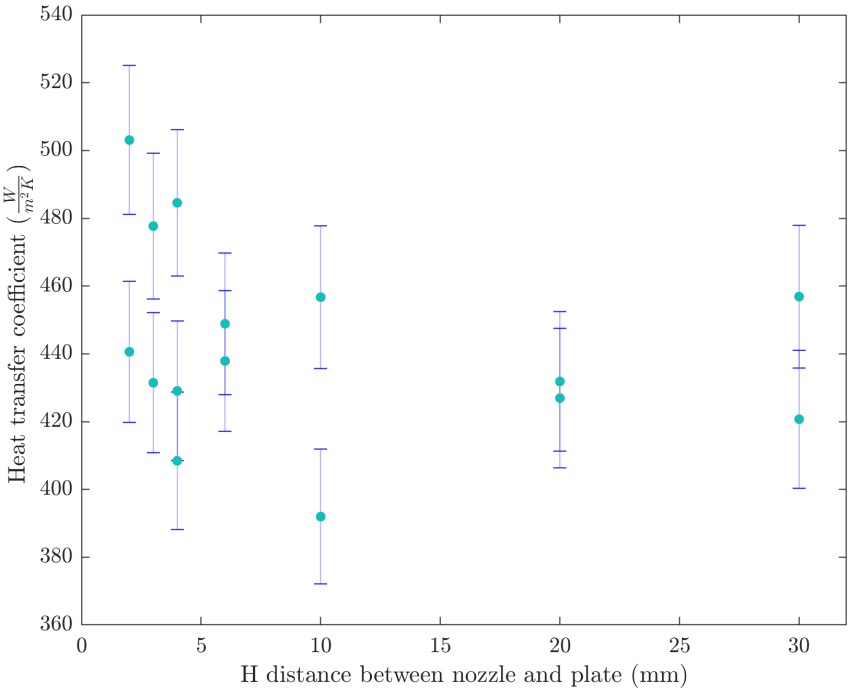

Figure 7.16: Calculated heat transfer coefficients h for experimental study with nozzle diameter, $D = 0.4$mm and distances H varied between 3 and 30mm.

the minimum at around $H = 20$ as H is increased further. This could be a genuine low point in the heat transfer being observed, or a levelling out of the trend. Either way it is not possible to predict with any certainty the behaviour as H increases from 30 in this case. Further work to develop these experiments could include a larger sealed container for the rig which provides the possibility to extend H past 30 and also, with more time a more extensive set of test runs could be run to better establish the trend seen.

For the smallest values of H, where the nozzle and plate are in close proximity, the coolant jet is applied and is still in the near-field expanding phase upon making contact with the heated block. Inside this expansion bow shape, complex jet structures and supersonic flow features could be playing more of a role in the cooling process. In the very top of the jet, there will be significant proportions of dense phase CO_2. If there is a mach disk in the expansion zone then there could be liquid phase present in the core of the jet which would then be applied onto the CO_2. The exact nature and phase composition of the jet cannot be observed within the current set up of the rig, and the impingement on the plate would have an impact on any shock features compared to a free expansion which means there is limited opportunity for further investigation of this possibility.

It is also possible that the increase in heat transfer coefficient at the smal-

lest value of H is largely due to the more targeted application, with less mixing and dispersion of the high speed jet flow before it impacts on the copper block.

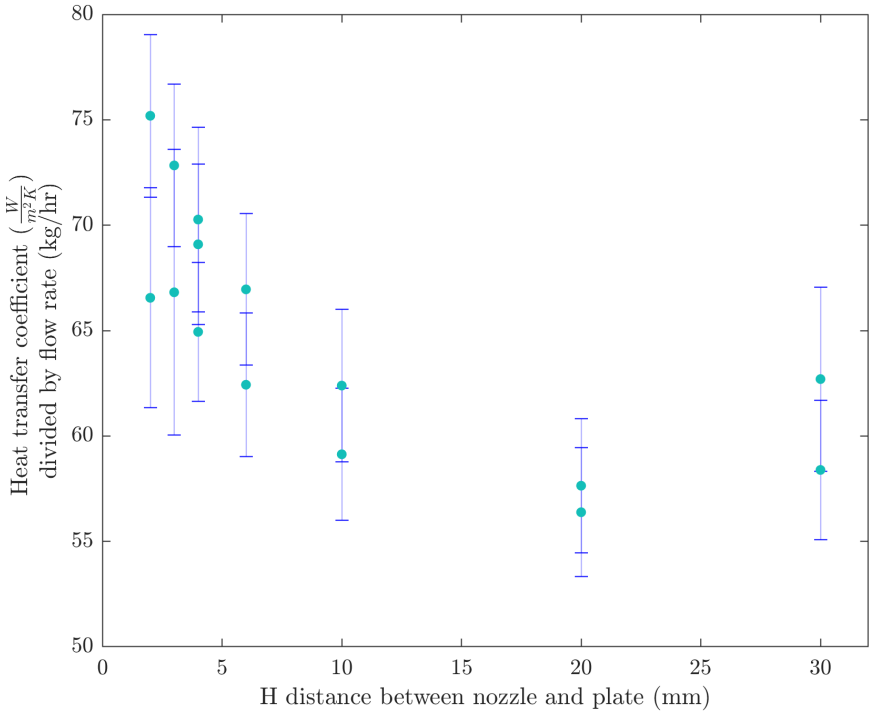

Figure 7.17: Calculated heat transfer coefficients h, normalised by diving by the CO_2 mass flow rate, $\dot{m}$, for experimental configurations with nozzle diameter, $D = 0.4mm$ and distances H varied between 3 and 30mm.

7.5.2 Variation of nozzle diameter and flow rate

Another key parameter which has been varied in the experiments is the nozzle diameter, which in turn leads to variations in CO_2 mass flow rates. The flow rates are of interest, since a requirement for very high quantities of CO_2 in cooling applications in machining is unsustainable and expensive as well as more hazardous to anyone in the working environment.

As seen above, even when varying the distance H, the flow rate of CO_2 had to be taken into account, since it was observed to have a significant impact, even for the small differences in flow rate observed in those cases. Changing of the nozzle diameter, as was shown in Figure 7.10, results in substantial changes to the flow rate, with a change in diameter from 0.3 to 0.5mm resulting in over a 200 % increase in flow rate. Results of the experimental investigation of the effect of nozzle diameter and flow rate on the heat transfer coefficient are shown in Figure 7.18.

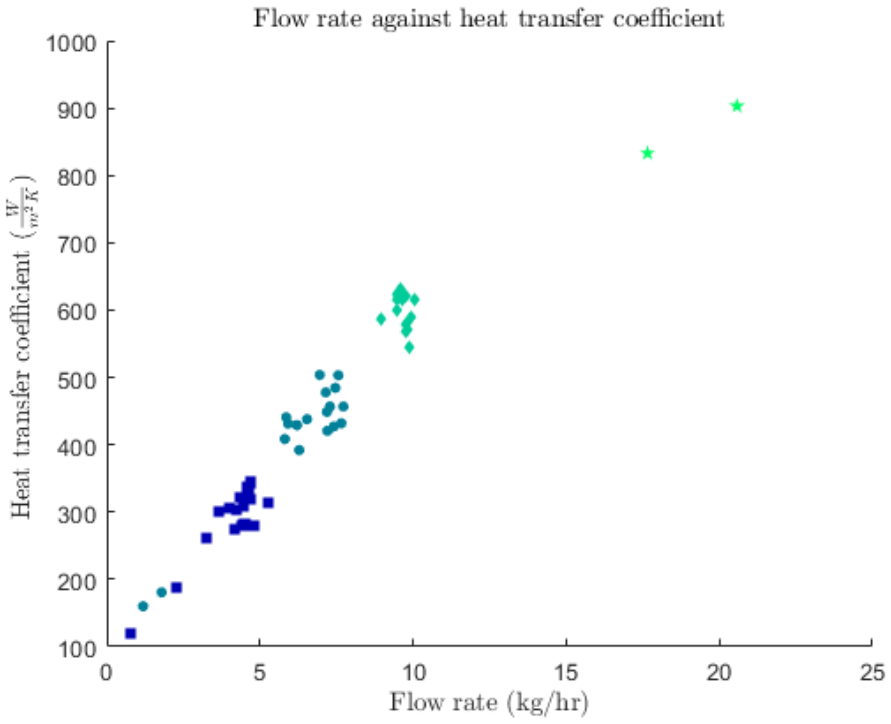

Figure 7.18: Experimental results showing the relationship between CO_2 mass flow rate $\dot{m}$, and heat transfer coefficient, h. The data is coloured and marked according to the nozzle diameter, with the square markers for $D = 0.3$mm, dots for $D = 0.4$mm, diamonds for $D = 0.5$mm, and stars for $D = 0.8$mm.

The graph includes result from four different nozzles (0.3mm, 0.4mm, 0.5mm and 0.8mm), with all data sets distinguishable by markers and colours. There are distinct groups of data which correspond to each individual nozzle and the resulting ranges of flow rates. As observed in the initial testing of nozzles and flow rates (Figure 7.10), as the nozzle diameter is increased there are increases in flow rates. With this increase in D, and accompanying increase in $\dot{m}$, there is an increase in heat transfer coefficient, h, shown in the results. The relationship between the flow rate and heat transfer coefficient seems to be linear, with a clear trend over at least the first three nozzle sizes tested. Two data points using the 0.8mm nozzle have been included, but gathering test data for this nozzle was limited by the supply and safety issues noted in the rig development, so that only two full tests were completed. The trend over these points could indicate a non linear relationship after this point, as the heat transfer coefficients look to be departing from the previous data points linear trend. This, however, would require further study to analyse as the data is limited in this case.

The results shown in Figure 7.18 predominantly include the liquid-fed release CO_2 which is of interest. To extend the graph down to lower flow rates of CO_2, the needle valve was restricted for two tests using both the 0.3mm and 0.4mm diameter nozzles. The results for these tests are included in the graph and they are the four

lowest flow rates, which sit apart from the rest of the data in the bottom left corner of the graph. In these data collections, the flow was restricted, with CO_2 depressurisation and expansion to multiphase flow in the pipes, marked by the freezing around the pipes on and immediately following the needle valve. In these four cases, the jet was not clear to observe, since it seemed to have a significantly reduced solid phase presence indicating the pressure in the pipes after the needle valve had dropped to provide a predominantly gas phase supply to the nozzle. Interestingly, in these four gas phase releases, the flow rate and heat transfer coefficient relationship appears to follow the same behavioural trend as the rest of the high pressure, liquid release experimental data points. This implies that the liquid reaching the tip of the nozzle and the resulting high percentage of sublimating solid particles which are formed may have little significant cooling advantage over the gas phase release. Instead the quantity of coolant supplied has more impact.

In a machining application, where there is potentially more difficulty in controlling the CO_2 supply conditions and a pressure drop or restriction in the delivery conditions is more likely, there could be expansion in the system before the CO_2 reaches the intended supply point. This is especially likely if the CO_2 coolant channels exit the system using straight nozzles and not the converging style nozzle used in this experiment (Figure 7.1). With a straight nozzle, the retaining of the high pressure in the piping needed to maintain liquid phase is difficult and an equilibrium with a lower dense phase fraction would be likely. An analysis of the phase fractions of CO_2 release from different configurations is outside the scope of this work, but it can still be highlighted here that the behaviours of the restricted, gas phase release could still be predicted using the same methods as the liquid as they appear to follow the same behavioural trend in this parameter space.

The data shown in Figure 7.18 was collected over a range of configurations and the distance between the nozzle and plate, H, was varied throughout. Figure 7.19 shows the same data points, this time coloured according to the distance H. The effect of varying H was observed for the 0.4mm diameter nozzle in Figure 7.17 and it was found that the smallest distances between the CO_2 and copper block corresponded to the highest values of the heat transfer coefficient. Here, in Figure 7.19, an extension of this behaviour is seen, and it seems to be observable over the range of flow rates seen. In each set of results, the darkest blue data points are close to the top of the data clusters, and the light green, which represents the largest distance of $H = 30$mm is at the bottom of the data groups. The increased impact of the nozzle to plate spacing, H, with flow rate is observed in Figure 7.19. The range in heat transfer coefficient experimental data increases as the flow rate increases, with the largest variation between the light blue $H = 30$ mm data and the darkest blue $H = 3$ mm data found at the higher flow rates. This agrees with the same behaviour observed by Kim & Lee (2016)

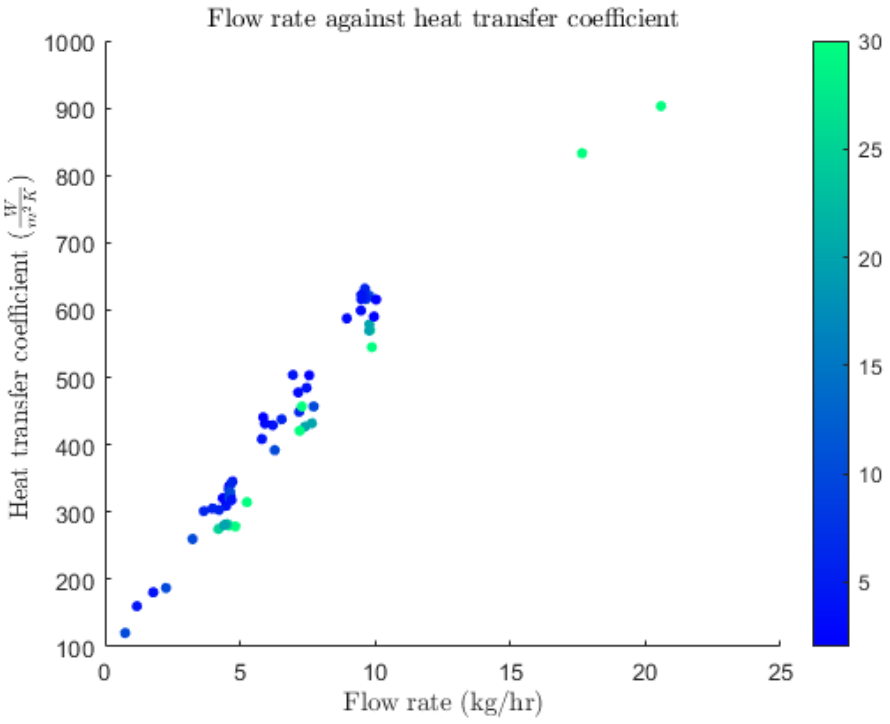

Figure 7.19: Experimental results showing the relationship between CO_2 mass flow rate $\dot{m}$, and heat transfer coefficient, h, replicated from Figure 7.18, but coloured with distance H between the nozzle and copper block for values between 2 and 30mm.

7.5.3 Local heat transfer coefficient predictions

Experimental results to this point have included a heat transfer coefficient, h, which assumes the area of active heat transfer is the entire top surface of the copper block. This area is relatively large compared to the small observable region where the CO_2 jet is impacting on, and very large compared to the nozzle diameter where the CO_2 jet is being applied from. The heat transfer coefficient will be compared to other coolants and applications in the machining industry as a means to assess the benefits of different coolants. The precise application of the CO_2 coolant may mean it is only cooling a relatively small area on the top of the copper block. One of the limitations of using copper as the material for the test block is that the very good thermal conductivity means it is difficult to observe large temperature gradients over the block, making it difficult to know where on the block surface the cooling is most prevalent.

In order to get a more accurate heat transfer coefficient and better understand the local distribution of heat fluxes across the copper block surface around the jet impingement point, a second set of experiments is run. These experiments used the same set up as presented above (section 7.3.3), but controlled the exposure of the top surface area of the copper block with an insulation addition. Different amounts of the copper block surface are exposed over a series of tests, as a circular region is cut out

from the centre of the insulation, centred where the jet impinges. The reference change in temperature of the block while fully covered with insulation is tested and recorded as $(\Delta T)_0$. As the uncovered surface area of copper is extended, the values of the change in temperature of the block over the sample time, ΔT, are recorded and compared to the fully insulated reference value $(\Delta T)_0$. This process, carried out at three different configurations of $H = 6, 10, 30$mm, provides insight into the thermal energy which is removed from the block as the exposed surface of the block is increased. The results are shown in Figure 7.20 show the $\Delta T - (\Delta T)_0$ values, which are the reductions in temperature of the block over the sample time compared to the fully insulated block. These values are plotted against the radius of the circular exposed region of the copper block, r.

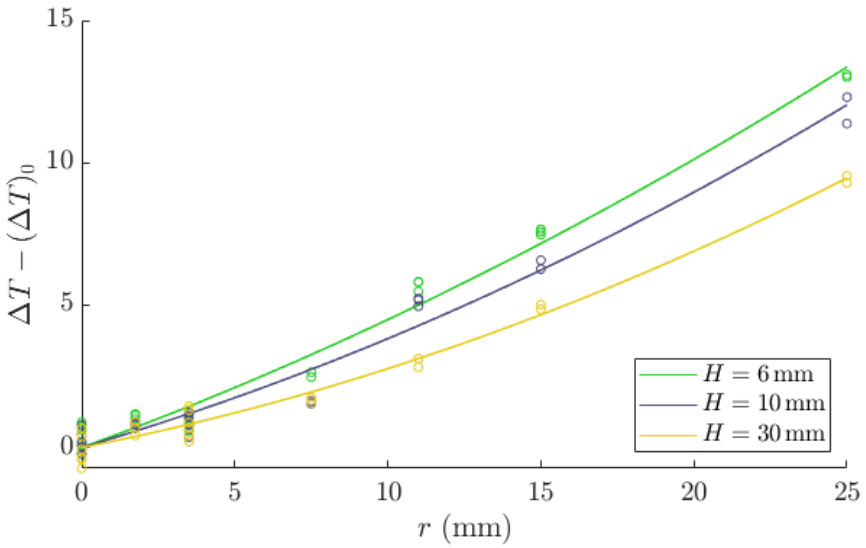

Figure 7.20: Changes in temperature of the copper block for a thirty second sample, for a given amount of circular exposed surface area with radius r, compared to the change in temperature in the fully covered copper block over a thirty second sample. Profiles for three different H configurations are included, with all tests using the nozzle diameter of 0.4mm. Experimental data sets for each value of H have been fitted with a second order polynomial.

The three data sets for the different nozzle to plate distances have each been fit with a quadratic function. This fit provides a prediction for the change in thermal energy corresponding to the exposed surface area of the block up to a radius of 50mm. These values have been used to predict local heat transfer coefficients across the radius of the block. Shown in Figure 7.21, local values of h for each of the distances, H, indicate an increase in heat transfer coefficient very close to the centre of the jet impingement. This value tends to infinity in the calculations here, since the heat transfer coefficient is calculated by estimating the heat flux as the thermal energy removed from the block in the sample time over the exposed area. The exposed surface area tends to 0 as r is decreased faster than the change in thermal energy, causing the steep rise.

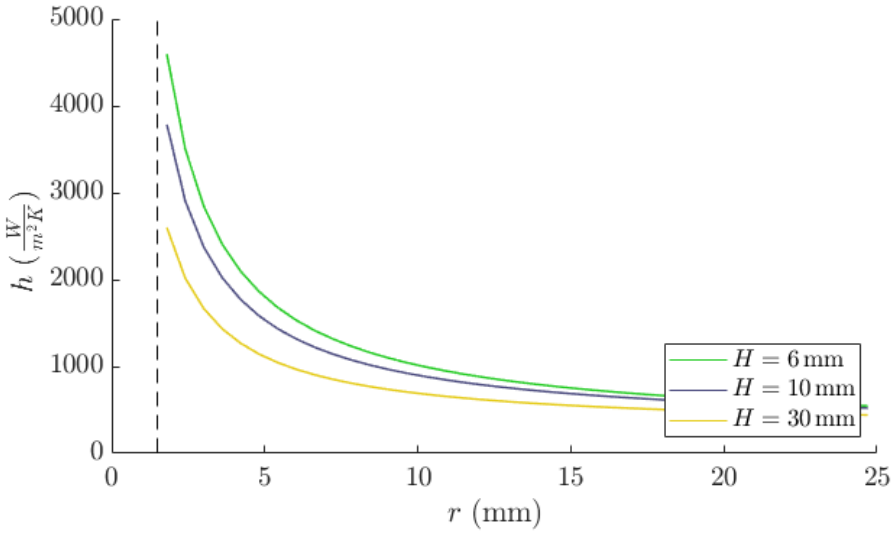

Figure 7.21: Local heat transfer coefficients, calculated from the fitted second order polynomials in figure 7.20, over varying radial positions. Three configurations of H are included. All interpolations are limited to radial values over 1.5mm to exceed the smallest data collection point and avoid extrapolation in regions or high error.

The error at the smallest exposed areas is very high, since the margins of both temperature change ($\approx 1^oC$), and the exposed surface area ($\approx 7 \times 10^{-6} m^2$) are small, so extrapolation of this data towards 0 is unreliable.

The values for the heat transfer coefficient are higher across most of the surface while using these local estimations of heat flux compared to the previous values which have assumed the heat flux over the entire copper block surface. It can be seen that within the data ranges considered, the heat transfer coefficient seems highest at small radial distances from the centre of the jet, with a steep drop off and a levelling out to more consistent values as the radius increases. The results show the levelling out of the local heat transfer coefficient at radial values much higher than the radius of the nozzle diameter, showing that the CO_2 is enabling high rates of heat transfer far beyond its expected impingement point under a non expanding assumption.

The local heat transfer coefficients over the region of interpolation for this data have been plotted as a contour in the context of the copper block surface in Figure 7.22 for the $H = 6mm$ tests.

The local heat transfer coefficients highlight the distribution of the heat flux over the surface and emphasise the differences and increase in heat transfer at the centre of the jet, but they also show that although the values of h decrease towards the edge of the samples taken, a significant amount of heat is still removed from near the edges of the block, even though the CO_2 jet is not as visible in these areas. A high speed flow of cold CO_2 gas is likely spreading over the surface and maintaining a good

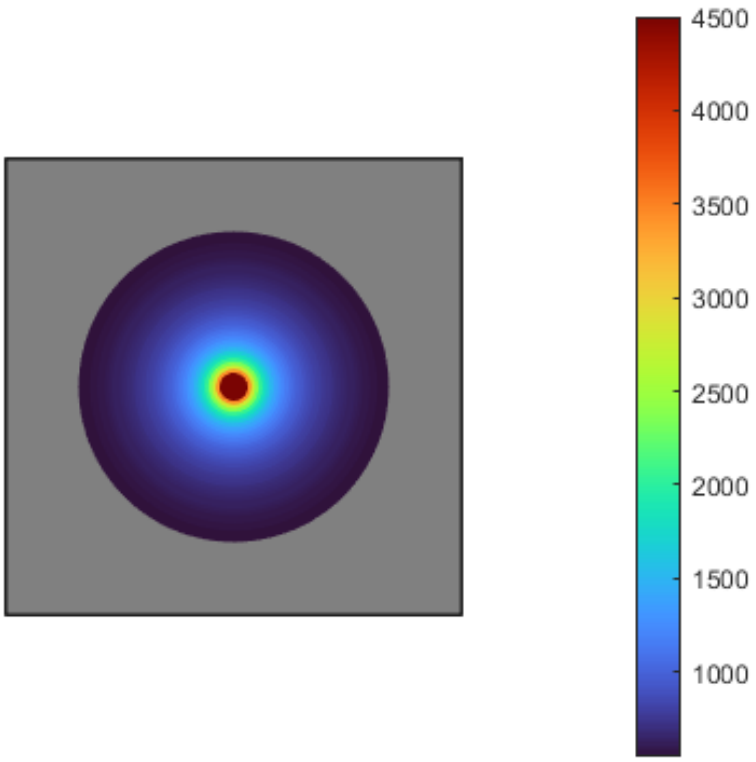

Figure 7.22: Contour plot of the local heat transfer coefficients calculated in figure 7.21, showing the scale and distribution of the local values of h in the context of the copper block used. The contour plot is extended to radial values of 25mm, with the remainder of the block shaded grey.

cooling effect over the whole surface.

7.5.4 Comparisons to gas phase release

Previously, in the discussion of results with low flow rates in Figure 7.18, the behaviour of gas phase release in the context of these liquid-fed results was discussed. The relationship between flow rate and heat transfer coefficient continued out of the liquid phase region and into the gas phase region with no obvious change. Even though there appeared to be a much lower volume fraction of dense CO_2 in the restricted flow rate results set, the experiments remained liquid draw, so that at some point in the system, there was ultimately an expansion. This is expanded on here by comparison with data from the literature which utilised a gas phase release.

The experimental setup of Kim & Lee (2016) was very similar to the rig used in this experiment, with the key differences being that they used a gas feed CO_2 draw

from the cylinder supplies. A smaller copper test block was used by Kim & Lee, a square length of 12.7mm compared to the 74mm used here. The nozzle used by Kim & Lee was fixed at a 1mm diameter, larger than those used here, but the flow rates were roughly similar.

Using the local heat transfer coefficients calculated in section 7.5.3, a comparison between the gas and liquid-fed can be made. The experimental parameters of $H = 6, D = 0.4$mm used in this work correspond to an $L/D = 15$ configuration which was considered by Kim & Lee. An average change in temperature, $\Delta T - (\Delta T)_0$, for an exposed surface area to match the size of the block in the Kim and Lee experiments is interpolated from Figure 7.20. This is used to calculate a heat flux and surface average heat transfer coefficient for the experimental data presented in this work for the same surface area as was used by Kim and Lee.

A plot of heat transfer against flow rate from Kim & Lee (2016) is recreated in Figure 7.23. A curve has been fitted to the data from the gas feed experiments and extrapolated to a higher flow rate of 10 kg/hr. The interpolated value for the heat transfer coefficient for this size of surface area calculated from the liquid-fed results presented in this chapter is included in the plot. The data from this liquid draw CO_2 cooling was not included in the curve fitting for the gas draw data of Kim and Lee, but it can be seen to correspond very well and sit close to the fitted line.

This close correlation between the results for the gas-fed from the literature and the liquid-fed results presented here was unexpected, since it seemed likely that the liquid-fed CO_2 would have different heat transfer behaviours to the gas feed due to the significant expansion zone and high proportion of dense phase remaining at the nozzle outlet. It was noted by Kim & Lee that although the CO_2 used was gas feed, for the highest flow rates of CO_2, the converging nozzle did see a large increase in pressure and a corresponding increase in dry-ice solid particles observed in the jet flow as well as a larger reduction in temperature and an expansion of the CO_2 jet. These features correspond closely with the liquid-fed releases and suggest more similarities than predicted at the outset.

Further comparison between the gas-fed data from the literature and the liquid-fed data in this work would be useful to provide increased confidence in the observations made here, but there is limited cross-over in compatible experimental parameters.

There is a change in gradient observed on the curve fitted to the experimental data of Kim & Lee, with the low flow rates seeing a shallower gradient than the two highest points which were identified as having increased solid particles. The liquid-fed data added from this work lies on the extrapolation of the steeper gradient and it could

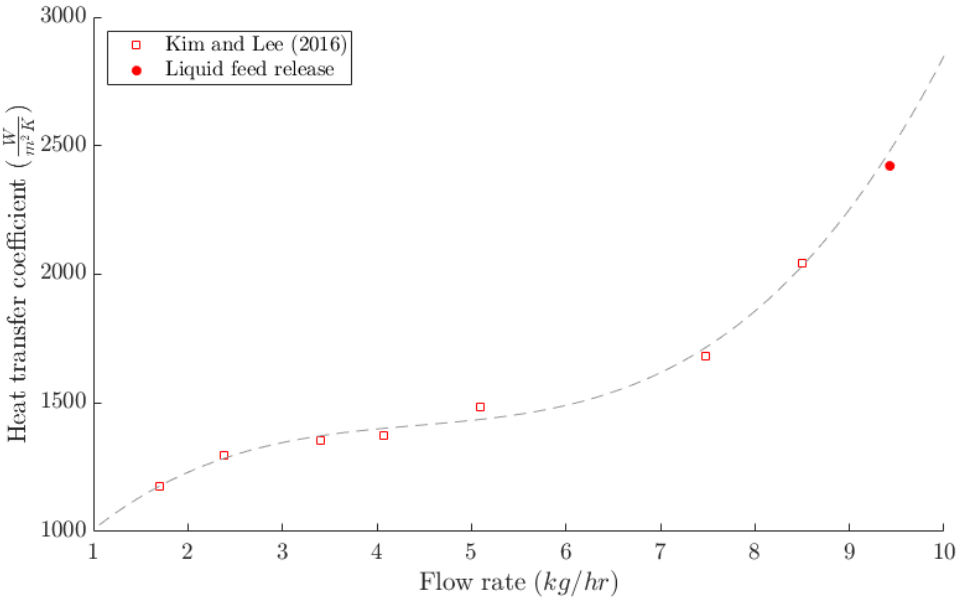

Figure 7.23: Experimental results of Kim & Lee (2016) are shown and fitted with a third order polynomial. A data point from this work, which has been extrapolated to the same surface area as used by Kim & Lee is included to show the correlation between liquid phase and gas phase releases.

be that there is some transition point in the heat transfer coefficient as the pressure is increased building up to the converging nozzle choke point, which would correspond to a higher proportion of dense phase. A larger nozzle of 1mm diameter is used in the study by Kim and Lee, compared to a diameter of 0.4mm which is used in the comparison data point here, which has resulted in higher flow rates than was achievable for gas releases in this work which required restriction of the flow.

Throughout the experimental results presented and discussed in this chapter, it has been the case that the key parameter to have a significant impact on heat transfer coefficient is the mass flow rate of CO_2, $\dot{m}$. In Figures 7.16 and 7.17, the small changes in flow rate had to be taken into account to normalise the flow before being being able to observe the varying values of h for changes in H. Comparing the results here to gas releases from the literature and observing the agreement between the data sets, it can be noted that there is a strong link between the heat transfer coefficients, in spite of the differences in nozzle diameter and phase composition. The collection of findings across the experiments conducted here indicates that mass flow rate is a good predictor of heat transfer coefficient across the range configurations.

In terms of the true level of thermal energy removed from a heat source, liquid CO_2 looks to have an increased level compared to gas phase releases despite having approximately consistent values for h. The difference in temperature between the CO_2 jet from liquid phase and gas phase is potentially large, Kim & Lee noted nozzle inlet

temperatures of -11.1°C to -21.9°C, compared to the consistent -80°C measured here. The colder sublimation temperatures of liquid release CO_2 jets will result in a larger value of $T - T_\infty$, and so for a consistent value of h, a larger heat flux, q. In short, the colder temperature of the liquid phase jet results in a higher heat flux and energy removal, while maintaining a similar value of h.

7.6 Conclusions

The work presented in this chapter includes the design and development of an experimental rig to assess the heat transfer of a CO_2 jet applied from high pressure. The development of the rig provided the environment to conduct novel research into the cooling capability of CO_2. Heat transfer coefficients have been calculated under different cooling configurations, with the distance between nozzle and plate, H, and the nozzle diameter, D and mass flow rate, $\dot{m}$ of CO_2 being varied.

The distance, H, between nozzle tip and heated test plate was varied, and showed an increased heat transfer coefficient for the smallest distances tested, 3mm. Heat transfer coefficient results appeared sensitive to small variations in flow rate, which was the dominant parameter. The importance of flow rate was then examined through the variation of converging nozzle diameters, and a linear relationship was observed between heat transfer coefficient and mass flow rate of CO_2.

A closer study of the heat transfer coefficients was presented which used a secondary set of experimental data with gradually increasing surface areas exposed on the copper test block. From this results set, local heat transfer coefficients were calculated, with the highest values observed towards the centre of the jet, and steep decreases as the radial distance was increased.

A comparison of the liquid-fed results investigated in this experimental configuration were compared to gas feed CO_2 cooling jet results from the literature, and agreement in the trend and relationship between heat transfer coefficient and mass flow rate was found. It was established that the mass flow rate seems to be the experimental parameter with the most significant impact across the range of experimental configurations considered in this chapter, with the phase composition, distance between nozzle and plate and nozzle diameter having relatively low impacts in comparison.

Alongside the results presented for heat transfer coefficients and the effect of experimental parameters, observations were made of temperatures and the expansion and shape of the CO_2 jets. Temperature readings across the profile of the cooling jet were recorded, with a consistent reading near the sublimation temperature point of -78.5°C. These observations can be taken forward and incorporated into simplified CFD

modelling of CO_2 cooling.

Chapter 8

CFD modelling of CO_2 cooling jets

Contents

8.1 Introduction

Accurate CFD modelling of CO_2 cooling processes would be a useful component in the adoption of this cooling technique within wider industry. Despite the clear potential shown for improved machining tool lives and reduced wear found in certain trials (Sadik et al. (2016), Nimel Sworna Ross & Manimaran (2019), Jerold & Kumar (2013)), the improvements are not always significant and can be hard to predict. To realise the potential of CO_2 coolant, the capabilities should be established and maximised. CFD modelling which could accurately predict the cooling capabilities of CO_2 application would be a valuable tool in this process.

The physical properties and processes observed in a CO_2 release from high pressure are complex to capture. Specialised models which include phase changes and supersonic flow and shock features are required to realistically capture the phenomenon, which makes this a computationally challenging problem. In chapter 6, the current state

of this modelling work was reviewed. There are advanced, CO_2 specific, modelling approaches available which have been validated for a variety of features detailed in the literature, however due to either computational costs or geometrical limitations none were identified as immediately suitable for use here. A CFD modelling approach which is computationally inexpensive, open-source and compatible with complex 3D tool geometries is desired to become a part of the suite of tools used to assess CO_2 as a coolant and optimise tool design for this specific application within industry.

Based on the experimental observations in Chapter 7 and the literature, the CO_2 release from high pressure can generally be separated into two main regimes. A highly compressible expansion region, and a multiphase gas-solid jet region. The regions of the jet are highlighted in Figure 8.1 with region (a) marking the expansion near-field region and region (b) marking the high speed jet which is resulting from the depressurisation and expansion.

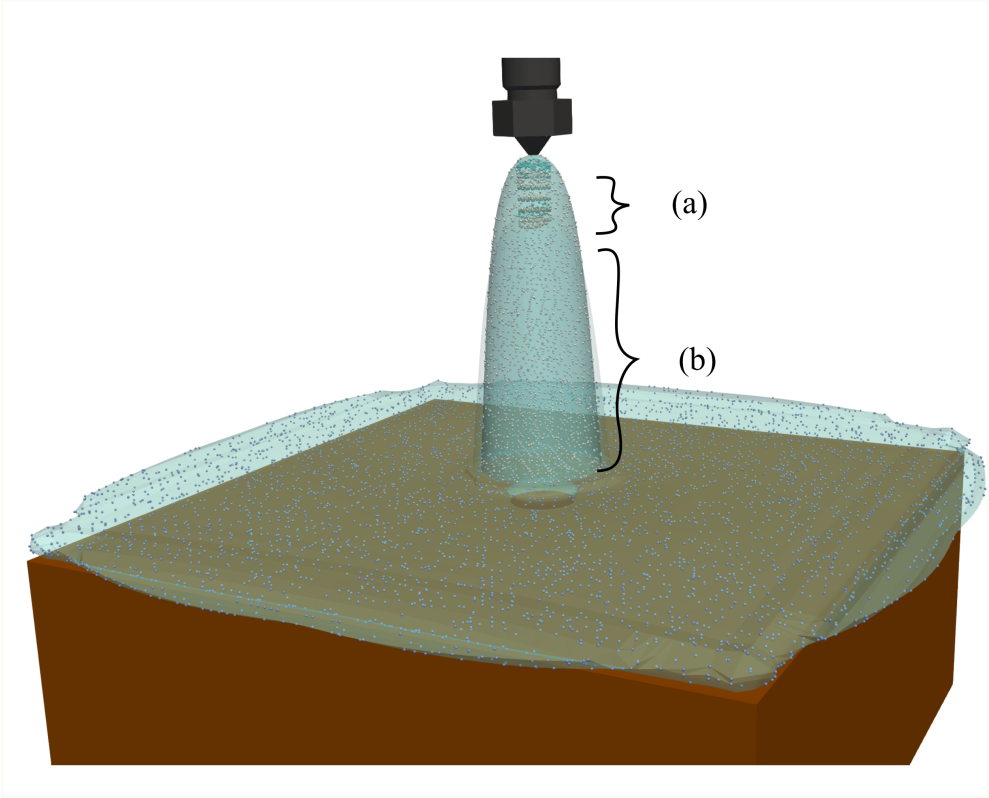

Figure 8.1: Schematic of the under-expanded CO_2 jet development observed in the experimental results. The near-field region (a) contains the CO_2 expansion from the nozzle orifice to atmospheric pressure, with a high presence of dense phase CO_2. Region (b), the far-field region, shows the expansion due to entrainment and interaction with the ambient surroundings up to the point of impingement on the copper block.

The phase change and compressible flow features which are key to determining high pressure CO_2 release are predominantly observed in the expansion, region (a). The compressible region at the nozzle exit is where a CO_2 specific, complex physical model

would be likely essential to capture the expansion region and mach disk sufficiently well. After this point, a more conventional cooling jet is proposed to form in region (b). The main objective of this work is to propose and validate a simplified CFD model which removes much of the complexity usually included in work with CO_2. The secondary region is modelled here to assess whether an assumption of a simplified gas jet can feasibly capture the heat transfer at an impingement surface for CO_2 jets. Once investigated and validated, such a tool would be extremely valuable in the development of tool geometries for CO_2 specific cooling.

In this chapter, a simplified CO_2 modelling approach is firstly introduced and the assumptions made to remove complexity are discussed and analysed for potential limitations. Then the model is validated against the experimental results in chapter 7 in two studies. These validation studies cover both moderate and small distances between the nozzle and heated surface. This is required in order to assess the limitations of the simplified model and ensure that the model can predict the cooling with CO_2, even when the jet has not fully expanded. A sensitivity study is then carried out on certain initial conditions which may be more difficult to observe in other applications. Finally the validated CFD model is utilised in a machining geometry setting, with a variety of flow rates considered and a comparison is made to conventional coolant.

8.2 Modelling heat transfer with CO_2 cold gas jet

A priority when modelling CO_2 from an industrial machining standpoint is to capture the heat transfer capabilities accurately. The compressible expansion and complex phase changes associated with CO_2 application are potentially a crucial part of modelling and predicting this heat transfer correctly, however they are computationally complex to resolve. A simplified model which can both capture the heat transfer behaviours and still be applied to a variety of geometries would be a valuable tool in industrial applications. Such a model could be used to inform tool design and optimise CO_2 coolant delivery using a similar process to that with conventional coolant in Chapter 4. An incompressible simplified model is tested here to assess whether or not this is a feasible tool which can predict the cooling capacities well, while not including any compressible features of the CO_2 coolant application. The study evaluates the effect of this simplification, and will provide insight into whether modelling of CO_2 cooling can proceed while neglecting multi-phase flow and compressibility.

8.2.1 Model

The model used for the CO_2 simulation in the expanded jet region is a multi-region conjugate heat transfer model, with an incompressible single phase CFD model applied for the CO_2 fluid component. Several assumptions have been made to simplify the CFD modelling and make it more feasible for the requirements of industrial applications. The fluid simulated comprises only of CO_2, with any surrounding air or other gases neglected. Although a quantity of air is likely to remain in the vicinity of the simulation regions during real world CO_2 jet cooling, to model the mixing and diffusion of multiple gases adds complexity and reduces computational speed. The quantity of CO_2 applied, and observations from the experiments of the CO_2 gas flow along the copper surfaces surrounding the impingement point suggests there is very little air which would remain in contact with the solid elements due to the high CO_2 flow. The CO_2 flow is applied at high speed from the expansion region, and so is expected to not mix significantly with the air before its application to the heated surfaces. If slower regions of flow were observed this assumption would need to be examined further to consider whether a mixing of air and CO_2 would be necessary to combine the thermal properties.

A second assumption of incompressible flow has been applied to the fluid region in this model. This assumption is being implemented due to the simplicity it allows in the CFD model, with the neglecting of compressible effects. In best practice, the flow should be modelled as compressible even in the secondary region below the expansion point of the jet due to the high speed flows modelled. The Mach number is calculated to around 0.37 at the inlet point, with incompressible assumptions only really advised below a Mach of 0.3 (Maia et al., 2020). One aim in the application of this model is to assess the limitations of a heavily simplified model which would be feasible for quick running simulations in industry. As such, the assumption is included, but is noted as being applied outside of the advisable regime.

This modelling approach for the CO_2 application also simplifies the real world presence of multi-phase equilibrium flow in the CO_2 to instead assume a single phase gas CO_2 flow. An inspection of the experimental operations discussed in Chapter 7 in conjunction with the CO_2 phase diagram (Figure 6.1) indicates that a gas-solid particle equilibrium is formed upon the release of the dense phase CO_2 from the converging nozzles investigated here. Although solid CO_2 particles have been modelled using a variety of implementation methods in the literature, they are neglected from this model in favour of the single phase CO_2 gas jet.

With all the assumptions included above, the modelling of the conjugate heat transfer using a cooling CO_2 jet uses incompressible Reynolds Averaged Navier Stokes (RANS) equations (8.1, 8.2), which are solved for the CO_2 fluid component.

$$\frac{\partial u_j}{\partial x_j} = 0 \tag{8.1}$$

$$\frac{\partial(\rho u_i)}{\partial t} + \frac{\partial}{\partial x_j}(\rho u_j u_i) = -\frac{\partial p}{\partial x_i} + \frac{\partial \tau_{ij}}{\partial x_j} + \rho g_i + f_{\gamma i}, \tag{8.2}$$

A $k-\omega$ SST turbulence model is applied, due to its success in modelling near-wall turbulence features which are key in heat transfer applications (Menter & Esch, 2001), with additional equations for the length scale and turbulent dissipation as follows,

$$\frac{\partial \rho k}{\partial t} + \frac{\partial \rho k \overline{u_j}}{\partial x_j} = \tau_{ij}\frac{\partial u_i}{\partial x_j} - \beta^* \rho \omega k + \frac{\partial}{\partial x_j}\left[(\mu + \sigma_k \mu_t)\frac{\partial k}{\partial x_j}\right], \tag{8.3}$$

$$\frac{\partial \rho \omega}{\partial t} + \frac{\partial \rho \omega \overline{u_j}}{\partial x_j} = \frac{\gamma}{\nu_t}\tau_{ij}\frac{\partial u_i}{\partial x_j} - \beta \rho \omega^2 + \frac{\partial}{\partial x_j}\left[(\mu + \sigma_\omega \mu_t)\frac{\partial \omega}{\partial x_j}\right] + 2(1-F_1)\frac{\rho \sigma_{\omega 2}}{\omega}\frac{\partial k}{\partial x_j}\frac{\partial \omega}{\partial x_j}, \tag{8.4}$$

$$\mu_t = \frac{\rho a_1 k}{max(a_1 \omega, \Omega F_2)}. \tag{8.5}$$

For full details of the $k-\omega$SST turbulence modelling please refer back to section 3.4.1.

The conjugate heat transfer model for the simulations solves an energy equation in both the liquid (Eq 8.6) and solid regions (Eq 8.7):

$$\rho\frac{Dh}{Dt} + \rho\frac{DK}{Dt} - \nabla(\alpha_{\text{Eff}} \cdot h) = \rho U g + r, \tag{8.6}$$

$$\frac{\partial T}{\partial t} = \frac{\lambda}{\rho C_p}\nabla^2 T. \tag{8.7}$$

The fluid energy equation 8.6 in the model solves for enthalpy, h, and kinetic energy, K. Terms include, α_{Eff}, the effective thermal diffusivity, r, the heat source terms, and $\rho U g$ to include any buoyancy effects.

The liquid and solid regions are paired with a mapped OpenFOAM boundary condition `compressible::turbulentTemperatureRadCoupledMixed` to maintain consistent temperatures and heat fluxes between regions.

8.3 Validation study

In this section the CFD model outlined in section 8.2 is validated against experimental data from the test rig described in section 7.2. The model is outlined in the previous section. Initial and boundary conditions, along with the geometry, are taken to be corresponding to the experimental configuration and data, given below.

Geometry

A multi-region 3D geometry is used, with a solid copper region and a fluid CO_2 region, as shown in Figure 8.2.

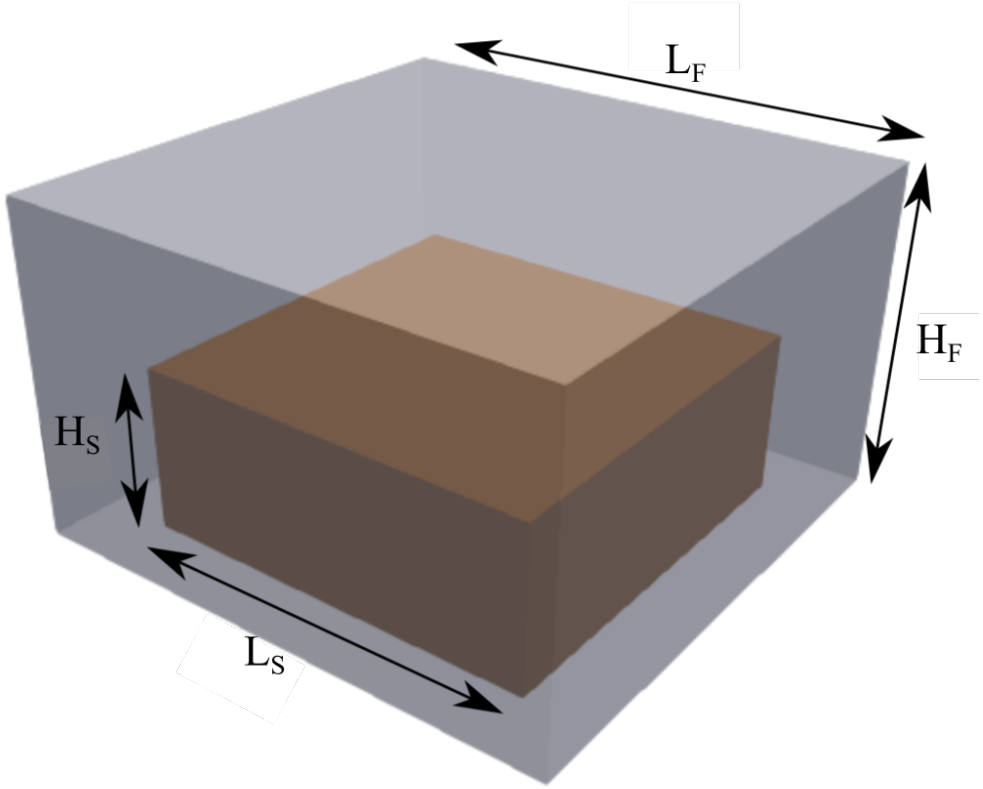

Figure 8.2: Multi region fluid and solid geometry used for CO_2 validation simulations. The fluid region has a square width of L_F and the solid region sits centrally inside this square, with a width of L_S. The height of the solid region from the base of the domain is denoted H_S, and the height of the fluid domain from the same base is denoted H_F.

The solid copper region is defined as a rectangular block with dimensions of L_S x L_S x H_S (74 x 74 x 30 mm) to correspond to the size of the copper test block cut for the experiments. The CO_2 region geometry is defined based on the experimental configuration we are validating against. The domain does not extend to the walls of the perspex box to capture the entire flow region due to computational limitations and

the additional resources this would require, but the region defined is presumed large enough to not heavily impact on the modelling and simulation of the CO_2 flow around the block. It is sized to surround the copper block, with cross sectional area of L_F x L_F (100 x 100 mm), with the copper block located in the centre. The height of the outer fluid region, H_F, is determined by the distance, H, between the nozzle and block in the experiments, so that the CO_2 geometry outer diameter is 100x100x(H+30)mm. An inlet boundary is defined by splitting the top patch of the defined geometry into an inlet and surrounding region using the features of experimental results in this case. Combining fixed experimental parameters, such as the distance between the nozzle and copper block, H, with visual results provided by high speed camera images (shown in Figure 8.3), the diameter of the jet can be calculated. The dashed horizontal line in the figure marks the jet diameter at the end of the expanding region, at a distance of H_e from the nozzle. At this point, the jet becomes less defined at the boundaries and begins to mix and interact with the surrounding air more.

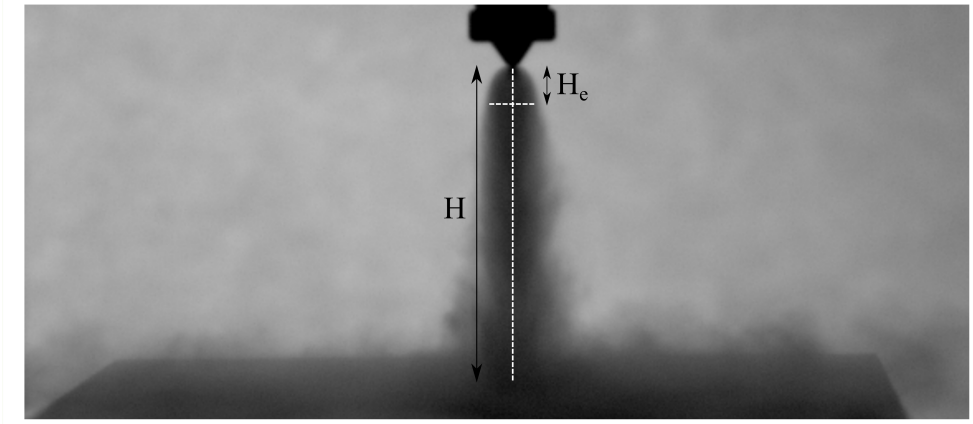

Figure 8.3: High speed camera image of the experimental CO_2 jet expansion. The height of the jet from nozzle exit to impinging on the block is denoted H, with the height of the near field expansion region noted H_e. The width of the expanded jet at the distance H_e from the nozzle is indicated with a horizontal dashed line.

H_e is used to define the circular inlet geometry for the CFD model, defined in the centre of the top patch, directly over the middle of the copper solid region. The model becomes limited when using this method of defining the inlet since it is taken from additional experimental observations. A well validated compressible expansion model could be used to inform this input alternatively.

Mesh

A regular hexahedral mesh is generated for both the solid and fluid regions. An initial mesh of $\approx 380,000$ cells is created, with a grading of the cells to refine the mesh near to the centre of the domain along the core of the jet. The mesh covers a rectangular

block of dimensions L_F x L_F x H_F, as shown in Figure 8.2. This mesh is then split to the two regions, copper and CO_2, and further refinement is added to the CO_2 mesh. Layers are introduced using the OpenFOAM `snappyHexMesh` tool along the boundary where the CO_2 region meets the copper block, with the refinement shown in a clipped section of the mesh for the CO_2 region in Figure 8.4. The copper block is shown in grey with the mesh outline of part of the CO_2 region in blue. The CO_2 region was clipped to highlight the meshing features as the two regions meet. In the three boxes below the main image, more detail of the layers added to the CO_2 region on the surface and around the corners of the copper block are included and show the heavy refinement in this region. A final image of the meshing refinement features is included to highlight the additional refinement localised around the core of the jet, with the initial hexahedral block mesh refined near to the centre for both the CO_2 and copper regions where the core of the jet is located.

Layers were required in the CO_2 region to ensure sufficient y^+ values in the simulation and resolve the region near to the wall for the highly turbulent, fast moving fluid flow. A total of 15 layers were added to the wall to reduce the y^+ values to around 1, which resulted in a mesh of $\approx$ 440,000 elements.

Initial and boundary conditions

The validation simulation cases are set up to replicate the experimental conditions outlined in section 7.2. An initial condition is set with a hot copper block at constant temperature, T_H, which is taken as the starting temperature of the cooling curve in the experimental sample data which is being compared against. The surrounding CO_2 fluid is initialised at a temperature of 273K, with the inlet set to a fixed value of 195K, around the sublimation temperature of CO_2, which was recorded in the experiments.

Initially, the fluid domain consists of stationary CO_2 which fills the space. The inlet conditions are taken from experimental results, and mass flow rate data recorded in the experimental test run used to configure the inflow of CO_2. The mass flow rate is used to set a corresponding fixed velocity at the inlet, with a constant value applied over the boundary. Compressible CFD modelling of CO_2 flow in the literature indicate a slow region in the core of the jet which follows the mach disk (Wareing et al., 2013c), whereas in most developed flows a higher velocity would be expected in the core of the jet, as the outer regions are slowed by interactions with the slower flowing surrounding fluid. The fixed velocity used over this boundary is chosen due to the desired simplicity of the model and the limitations when employing a potentially more sophisticated inlet condition. In the experimental study, it was not possible to record the velocity profile across the jet, although no dramatic temperature changes were observed in the core of the jet near to the expansion region which would correspond to the slow flow region

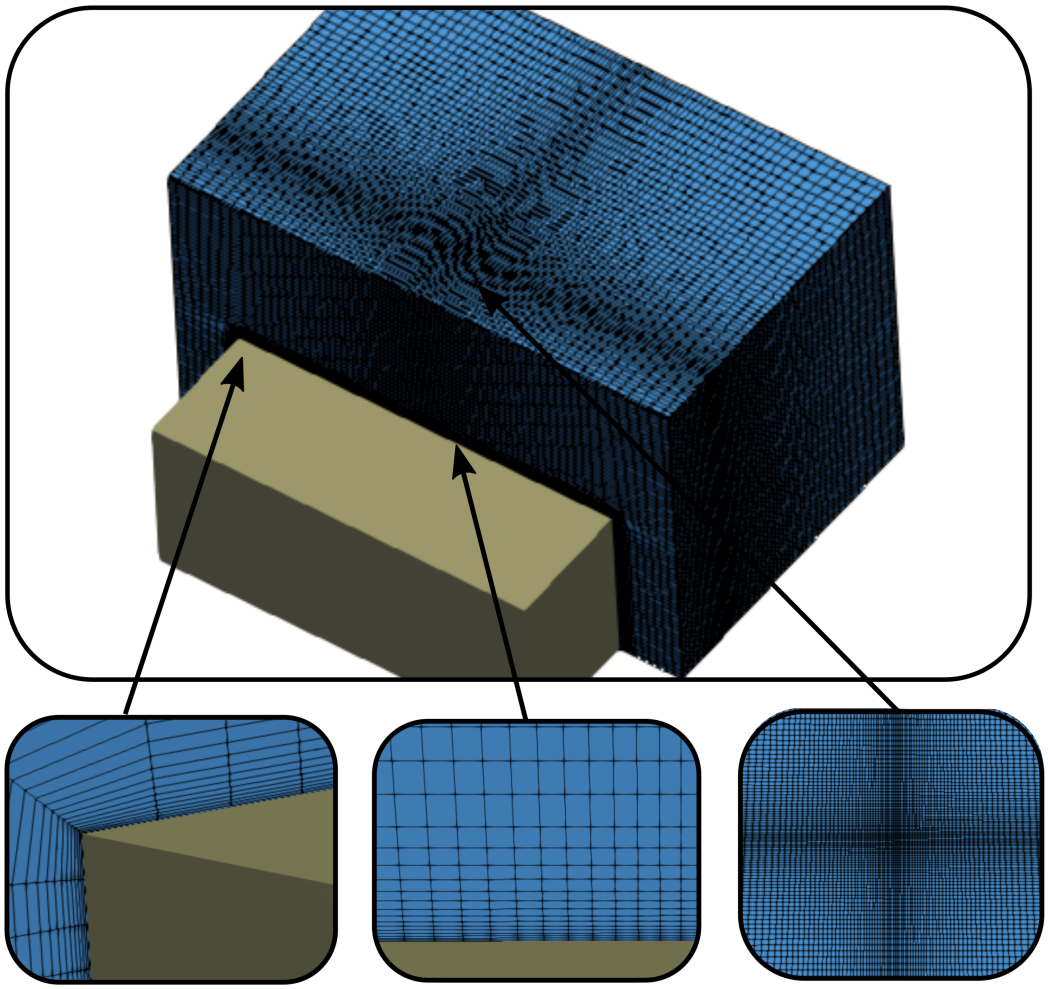

Figure 8.4: CO_2 validation simulation mesh features. The mesh of the fluid region is shown at the top, partly cut away to show the placement of the solid region within. Features of the meshing approach are highlighted below. These three images include the refinement of the mesh around the corners of the copper block (left), and the top/sides of the copper block (centre) using the addition of layers. These mesh layers were added to reduce the y+ values sufficiently in the simulations and remove the need for wall functions with the turbulence model. The mesh was also refined through the height of the domain around the centre of the jet (right) since this is the region with much of the development of the high speed flow.

seen in the compressible simulations in the literature. In CFD modelling of coolants in machining, an accurate and well validated inlet profile would likely be even more difficult to establish, and therefore the simplified profile is taken here as part of the feasibility study for a reduced complexity model.

The remainder of the domain exterior is defined as an outlet boundary, with flow allowed to leave the region in any direction. In the experimental rig, a larger contained volume was provided in the perspex test call than that modelled here, but

CO_2 was still contained in a closed volume, with recirculating flow observed as CO_2 flowed with high speed along the top of the copper block and into the perspex surroundings. From there, it was recirculated back towards the heater surface and could interact with the sides of the copper block. A `zeroGradient` flow condition is applied to the outlet, which allows CO_2 to return into the domain as well as be removed from it. The temperature of the flow re-entering through an outlet boundary is fixed at 243K, which is chosen based on the cooling of the surrounding CO_2 in the box during the sample period and experimental observations of these surrounding temperatures and the incoming flow being predominantly from redirected cold high speed flow which is directed by the boundaries of the experimental setup.

8.3.1 Results for H=30mm, D=0.5mm

A validation of the model for a configuration with nozzle diameter, D, of 0.5mm and a distance, H, of 30mm between nozzle and block is carried out. The results are shown in Figure 8.5, with experimental data points from thermocouple location 1 plotted with black markers, and the CFD cooling curve plotted in red.

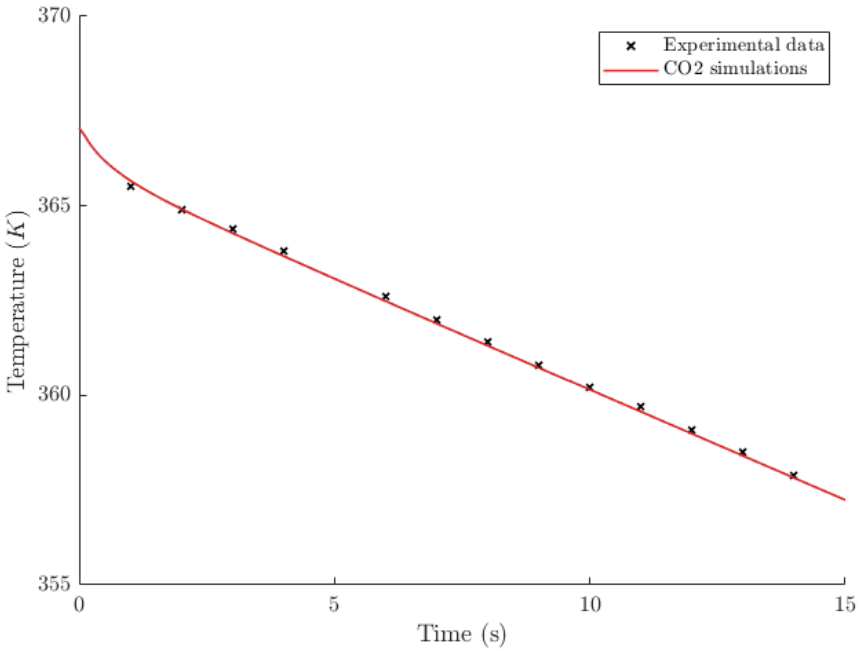

Figure 8.5: Plot of validation study results for tool temperature, with the experimental data from marked in black crosses and the CO_2 simulation data plotted alongside taken from the same location within the copper block.

Good agreement is found between the experimental results and the cooling predicted by the CFD model, the CFD simulation cooling curve can be seen to match well with the experimental data, and sits within the points with a similar gradient.

The simplified model appears to capture the cooling rate well, which indicates that this model would be feasible for use in industrial applications. Simplifying the model by only considering the incompressible flow and removing the multiphase physical features does not appear to lead to a compromise on accuracy in this instance. The configuration tested in this study modelled the largest distance possible between nozzle and plate, and assumptions may be less valid as this distance decreases and the jet is not fully expanded before impacting on the copper block.

Along with cooling curves, local heat transfer coefficients were also calculated from experimental data. The HTC values presented using the experimental data in Chapter 7 results were limited, with errors increasing significantly nearest to the centre of the jet impingement. Heat transfer coefficients calculated from CFD simulations are compared to the experimental results for a distance of H=30mm and shown in Figure 8.6. Throughout the radial distances included, the results from the CFD data fall within the predicted error range of the experimental data, although they are consistently at the bottom of this range instead of nearer to the experimental predictions.

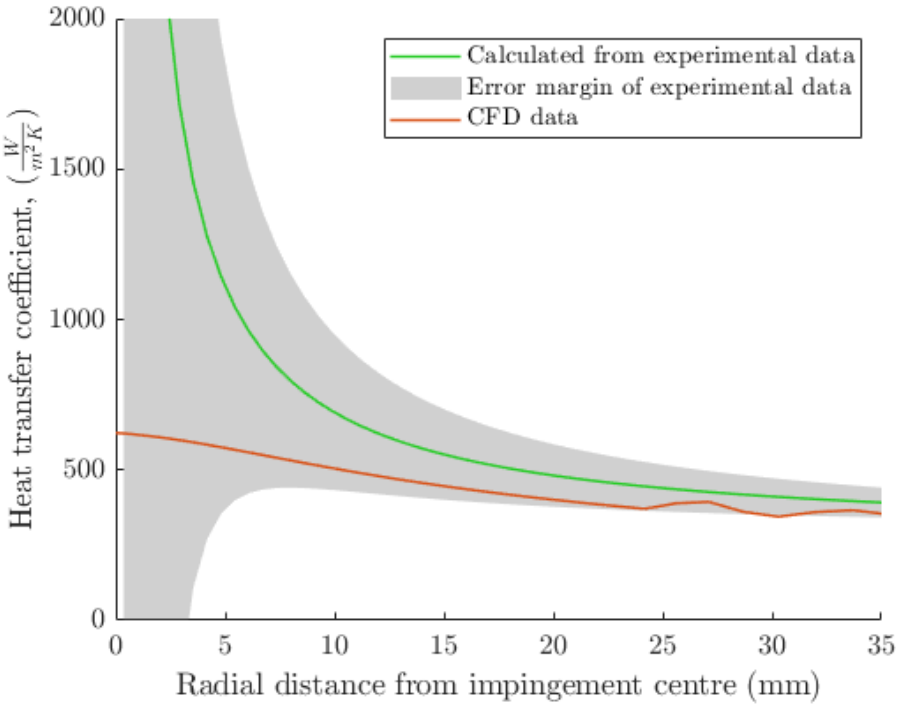

Figure 8.6: Comparison of heat transfer coefficients from the experimental data and CFD results. The values calculated from experimental results tend to infinity as the distance from the centre of the jet increases, and the margin of error also becomes very large in this region. The CFD results, shown in red lie within the error predictions of the experiments, which are shown in a shaded grey region.

The predicted heat transfer coefficients show markedly different trends at the smallest distances from the jet centre, with the experimental interpolated results in-

creasing towards an infinite value as the surface area is reduced and the CFD results rising by a much smaller amount to a finite value peak at the centre of the jet. The experimental predictions were expected to be limited in accuracy at these impingement regions, and could have been heavily impacted on by small misalignments in the application of the jet or disruptions to surface flow caused by the insulation applied to the copper surface. Where these effects are expected to have smaller impacts and the error is lower, the CFD and experiments show reasonable agreement, with the CFD results predicting a slightly lower value then the experimental results. With a validated model, these more reliable HTCs from the CFD can be used to analyse the locations of cooling on the surface of the block, and on machining surfaces in the future. The HTC values remain high relatively far away from the peak value at the centre of the jet, with the outwards CO_2 flow over the surface having a potentially significant effect.

8.3.2 Results for H=3mm, D=0.5mm

The CFD modelling results were shown to match the experiments very well for the validation case shown previously with a nozzle to plate distance of 30mm. The successful validation showed that the simplified model could be applied to the expanded region of the jet. When the model was proposed and limitations discussed in the sections above, it was considered that the model may only be valid in the expanded region of the jet and therefore limited to use at larger nozzle to plate distances. Here, this model has been applied at a much smaller nozzle plate spacing of H=3mm. In experimental observations of the jet shapes shown in Figure 7.14, the expansion distance is considered to be larger than this distance of 3mm, so that in this case the jet impinges on the heated copper block before it is fully expanded. Comparing the CFD model against such an experimental case means the limitations of the model can be examined and any breakdown of the modelling assumptions in the expansion region can be identified. These distances are also much closer to distances seen in tool design, which makes it especially important to identify any limitations at this proximity.

The details of the model remain largely consistent with those used in the previous case described in section 8.3.1. The only modifications are to reduce the domain height to reflect the new configuration with a nozzle to copper block distance of H=3mm. The inlet diameter and coolant velocity is maintained as the full width of the jet, despite the fact that the simulation now begins in the narrower, still expanding region for this validation case. The results for the H=3mm validation study are shown together with the results from the H=30mm validation case in Figure 8.7.

The figure shows there is still excellent agreement in the results for the H=3mm case, with the gradients matching very well. The thirty second sample is taken at different points in the two cases shown according to when the flow stabilised in the

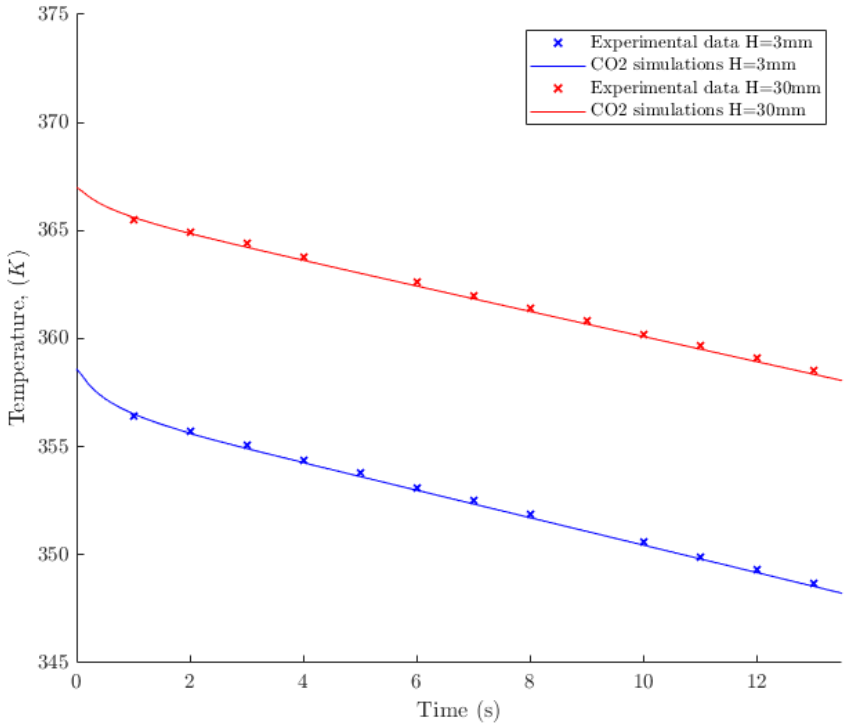

Figure 8.7: Validation results graph for both the nozzle to plate distances of H=30mm and H=3mm. Experimental and CFD simulation temperature results are extracted from the same fixed location in the copper block.

experiments, hence the different temperatures. Otherwise, the actual rates of cooling are also very similar in these two nozzle to plate distances. Each case shows a very smooth decrease in temperature for the thermocouple reading of $\frac{\Delta T}{\Delta t} = -0.58$ for H=30 mm and $\frac{\Delta T}{\Delta t} = -0.63$ for H=3 mm.

The validation of the model has now been extended to smaller nozzle to plate distances, which indicates that this simplified modelling approach can be used across a variety of machining cases, even when the impingement point may lie inside the expansion region.

8.3.3 Sensitivity study to inlet conditions

In the validation studies conducted in this chapter, CFD boundary conditions were calculated and applied based on experimental observations. The most important condition to model was the CO_2 jet at the inlet. The temperatures of the CO_2 jet were found to be close to the sublimation temperature of -78.5°C across a range of nozzle diameters and distances from the nozzle, seeming to not be sensitive to changes in configurations and making the inlet conditions easier to predict. An extraction of the dimensions of

the jet in Figure 8.3 was applied to calculate the size of the inlet boundary, which determines the speed of flow for a fixed mass flow rate inlet. A limitation of separating the compressible and incompressible parts of the simulation, is that the expansion region diameter becomes an additional parameter for the incompressible model. Although experimental results were available in this instance to set up the CO_2 case, this is not necessarily a sustainable practise in other cases, such as when the model will be applied to machining cases.

Mass flow rate is a quantity that is consistently monitored and regulated in CO_2 coolant testing in machining cases, however, the diameter of the expanded region of the jet could vary dependent on orifice diameter and outlet conditions of the coolant channels on the tool flutes. A discrepancy between the expected expanded jet diameter and that which is physically developed directly impacts the coolant velocity in the jet and could have a significant impact on cooling.

A sensitivity study is presented here to examine the impact of error in the jet diameter in the H=30mm validation case. A CFD case is setup with the diameter of the CO_2 inlet jet boundary increased by 10%, and the velocity of the jet reduced accordingly to ensure an equal mass flow.

By increasing inlet diameter by 10% the results show a reduction in cooling in Figure 8.8. The gradient, $\frac{\Delta T}{\Delta t}$, is 8.4% smaller, showing that the cooling rate is sensitive to inlet jet diameters and flow speeds.

An accurate compressible region model would benefit by determining inlet diameter for the incompressible model, although achieving a 10% margin of error would potentially be challenging with the complexity of the flow at hand, and experiments observing the jets diameter across a range of machining tools would be needed and used for either validation purposes or to be used directly in incompressible models. Even the use of a compressible CO_2 specialised model in the expansion near-field region here would require inlet conditions, however, and since the supply system of CO_2 to the tool channel exit positions is not easily comparable to a simple pipeline system, there would likely still be inaccuracies or difficulty in the modelling. CO_2 supply lines are dependent on individual tools and supply systems and therefore also vary considerably between uses. The greater contribution of any further work could be to increase the measurement capability of CO_2 flow at the tool channel exit or vicinity.

8.4 Modelling of CO_2 cooling in machining applications

A CFD model for conjugate heat transfer and cooling with CO_2 jets has been proposed and validated against experimental results in this chapter in order to provide a tool for

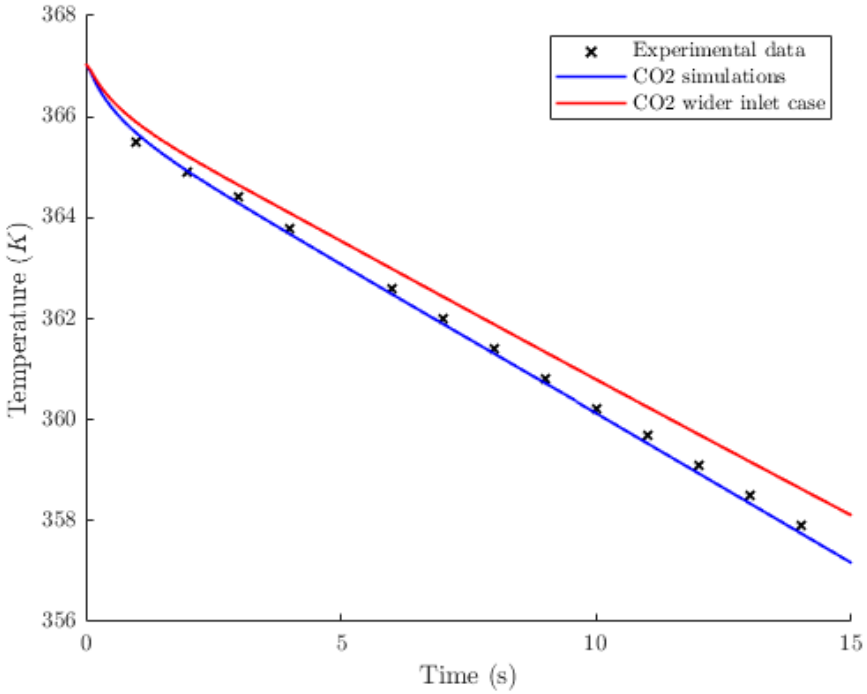

Figure 8.8: CFD sensitivity results to the jet diameter at the inlet. CFD results from the original simulation and the new sensitivity results are plotted together with the experimental results. In this case a wider inlet is included and shows a slower decrease in the temperature then the original inlet and experimental results.

use in machining applications. This model is now used here to simulate cooling with compressed CO_2 in a machining application.

8.4.1 Simulation configurations

A pilot study for CFD simulations of CO_2 cooling in a milling process has been modelled using geometries provided by Sandvik Coromant, consistent with the approach used for conventional coolant modelling in chapter 3. The CoroMill Plura solid carbide end mill for High Feed Side milling tool, which can be used in a range of milling operations, is used in this study. The tool geometry used directs the coolant close to the cutting edge, which was found in chapter 4 to improve the cooling of the cutting edge region. In this study the geometry of the CoroMill Plura, which will be called Geometry 1, is modified to direct coolant towards the flank edge, known as Geometry 2. In trials with CO_2 cooling in milling, it was found by Pittalà (2018) that the optimum configuration for conventional coolant channels were not the best geometry for CO_2 cooling. Instead, a coolant supply near to the flank side of the cutting edge reduced the wear by over 30%. Both models are considered together here across a range of flow rates to investigate this further.

The CO_2 flow conditions in the central core of the tool are not possible to experimentally measure and are difficult to predict. Due to regulation of the flow in the supply system between the high pressure CO_2 cylinders and the tool, a significant pressure drop is expected compared to the feed pressure. There are also complex features on the inside of the tool such as the central coolant supply channel splitting into six smaller channels. Ultimately, this leads to the pressure of the CO_2 supply in the smaller delivery channels being difficult to predict without the aid of direct physical monitoring. As such, the expansion of the CO_2 from the channel outlet is difficult to predict and should an area of further study to develop the understanding of CO_2 flow in machining tools. There is no convergence at the end of these smaller coolant channels to choke or limit the CO_2 flow at the outlet, and a opaque CO_2 expansion with significant solid particle presence is not reported in test cases, though they appear to be present in smaller quantities. An approximate expansion needs to be determined for this study in order to set the inlet boundary condition appropriately. Without experimental observation data, the expansion is loosely here presumed to have a diameter of between D and $2D$ for the coolant channel diameter, D. If there is significant pressure decrease further back in the CO_2 supply system, a cold gas with minimal expansion at the channel outlet is expected. The upper estimate of an expansion of 100% requires further attention in any later study, as it was noted that the diameter size has a observable impact on cooling rates. Here is it is used as an estimate and to demonstrate the use of the CO_2 modelling in milling but a well justified expansion should be finalised in any further work before application of this model for cutting tool development studies. To cover the D - 2D expansion range for this plot study, CFD cases are run for a zero expansion configuration, using a tool geometry with a regular inlet of diameter D, and for CFD cases where expansion is included to double the effective jet diameter to 2D are configured with a tool geometry with an channel diameter increased accordingly, as seen in Figure 8.9.

The workpiece geometry is a solid metal block which is in the process of being milled, and engaged with the tool at an axial engagement of 16 mm and a radial engagement of 4 mm, as was studied in the conventional coolant analysis in chapter 3.

Following the methodology for machining simulations in chapter 3, a multi-region mesh is created, covering the tool, workpiece and CO_2 regions. A hexahedral mesh is used as a base covering all the regions of interest, and then refined and transformed to conform to the geometrical features of the tool and workpiece. The OpenFOAM tool `snappyHexMesh` automates this process, and the refined mesh is then split to allow for simulation over the solid and fluid regions as needed.

The simulation is run as steady state, with a heated contact region between tool and workpiece fixed at 500°C. A CO_2 single phase gas jet is applied through the coolant channel at the sublimation temperature of -78.5°C. Since CO_2 cooling in milling

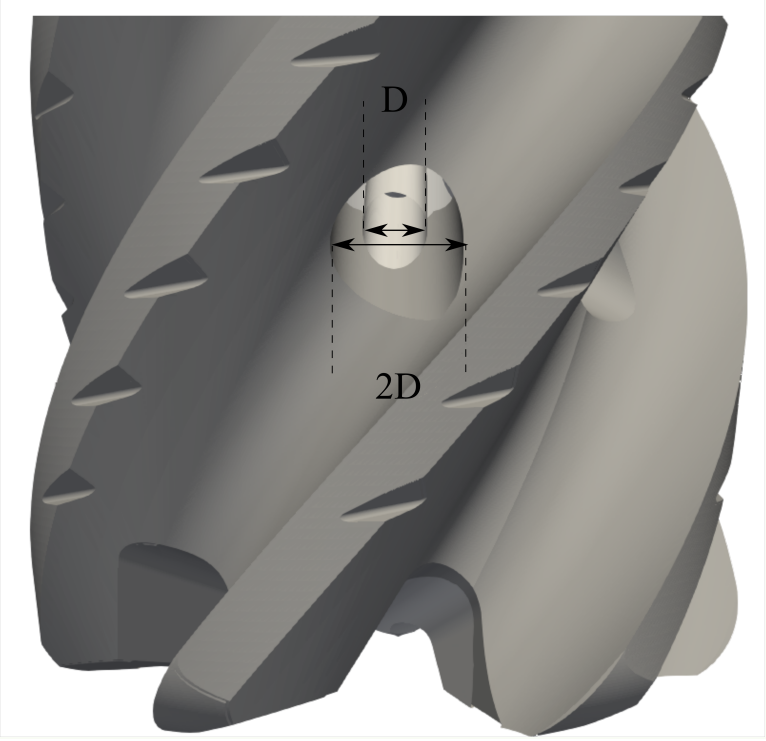

Figure 8.9: Geometry modifications to the tool to represent an expansion of the jet of 100% by increasing the coolant channel diameter outlet from D to 2D.

is a relatively new process, appropriate flow rates are still being experimentally trialled. For these modelling cases mass flow rates of 1, 4, and 10 kg per minute are tested, which have all been used in experimental machining in the literature (Grguraš et al. (2019), Pittalà (2018) Cordes et al. (2014)). These are presumed to flow evenly between the six flutes here, so that one sixth of the total flow is supplied to each cutting edge.

A no slip condition is applied at all walls along the tool and workpiece in the simulation, and an `inletOutlet` condition is used at the outlet boundaries so that CO_2 can leave the cutting region. Along each region boundary, the conjugate heat transfer model solves to ensure consistent temperatures and heat fluxes to conserve energy in the simulation.

8.4.2 Tool temperature results under CO_2 cooling

Tool temperatures near to the cutting edge have been extracted and averaged across all CFD models and the results are presented in Figure 8.10. The two geometries, Geometry 1 directing the coolant flow to the rake side of the cutting edge, which is preferred in conventional coolant, and Geometry 2 which directs the coolant to the flank side of the cutting edge, are included with both a minimal and 100% expansion of the CO_2 jet at the tool channel outlet. All four configurations are shown with average tool temperature results for the three CO_2 flow rates tested, 1, 4 and 10kg/min.

The first thing to note is that the results show significantly higher tool temperatures across all CFD results for the CO_2 cooling simulations compared to conventional coolant. Conventional coolants for these tool geometries resulted in a 341°C average tool temperature for Geometry 1 and 343°C for Geometry 2. In all the CFD results shown in Figure 8.10, the tool temperatures are above 450°C.

The improvements in tool life for CO_2 coolant compared to conventional coolant in milling trials could be due to reduced thermal shock based on these results. The tool cutting edge is being cooled to some extent, but the effect is much more subtle than in the conventional coolant cases, and this could limit the extremes of the thermal cycling which is inherent in milling operations and often contributes heavily to thermal wear (Yellowley & Barrow, 1976).

Until more studies have been carried out on the pressure in coolant channels and expansion of CO_2 at the exit, the real world expansion diameter of CO_2 cooling jets is difficult to predict with confidence in the CFD modelling. Here both Geometry 1 and 2 are shown with results presuming both 0% and 100% expansion, and the improvement in the cooling for the wider diameter cooling jet is clear for the cases with expansion. The increased diameter jet results in application directly towards the cutting edges in each model and covers a wider region. It would be beneficial to take this into account when designing the CO_2 coolant channels for any new specialised tools if the aim is to increase the cooling of the tool. Even increasing the flow rate by ten fold for the 0% expansion cases from 1kg/min to 10kg/min was not able to cool the tool as efficiently as the wider diameter jet in these cases. If a converging nozzle was included in the tool geometry somehow through additive manufacturing or another advanced technique and a high pressure choking of the flow was achieved as the coolant exited the tool, the amount of CO_2 required could potentially be reduced while maintaining good cooling, which would be an effective use of CO_2's physical properties. With a straight coolant channel currently used in internal cooling methods, a smaller pressure drop is expected and significantly reduced expansion. Interestingly, it was found in the results presented in Figure 8.8 that a wider (more expanded) inlet actually contributed to reduced cooling. In the results here, this indicates that the reduced temperatures

achieved under the 100% expansion cases are likely solely due to the additional hot contact region which is now targeted under the expanded jet.

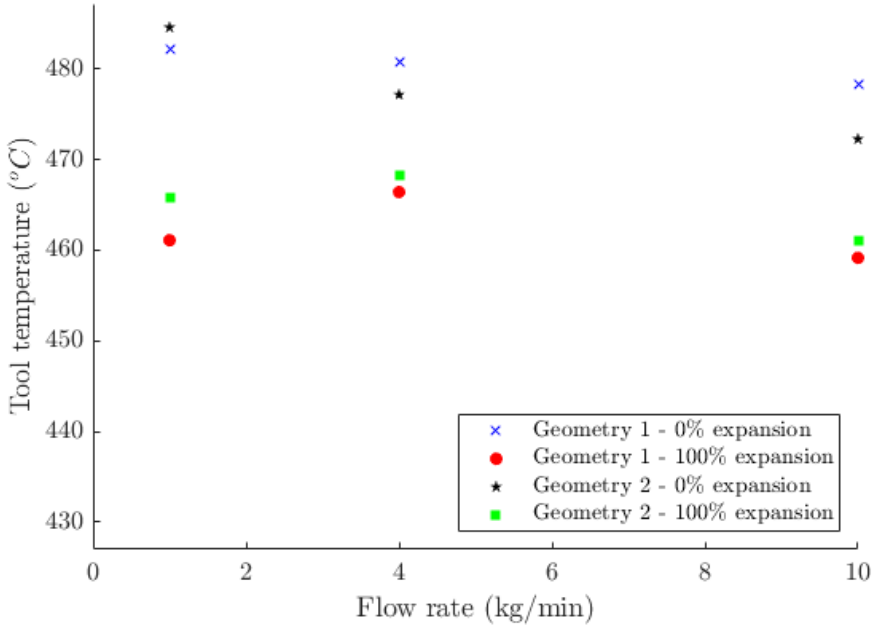

Figure 8.10: CO_2 machining modelling results for tool temperature. Two models are shown for cases both with and without an enlargement of the coolant channel to imitate expansion, and a range of flow rates.

Another interesting result from the CO_2 behaviour is the cooling of the tool under minimal expansion as the flow rates increase. At the lowest flow rate of 1kg/min, the Geometry 1 which is near optimal for conventional coolant results cools the tool the most, however at both of the higher flow rates of 4 and 10kg/min the Geometry 2 tool provides the lower average temperature. This would qualitatively agree with the findings of Pittalà (2018), that the optimum coolant channel location for CO_2 cooling may be closer to the rake as this cools the tool better. The reason for this improved cooling is not obvious, though the CO_2 may spread out more evenly when impacting high in the domain, while requiring high volumes to still provide enough CO_2 to the regions. The improved cooling for Geometry 2 is not observed for cases which include a 100% jet expansion. The Geometry 1 results have lower average tool temperatures over all flow rates considered, though the differences between the two geometries is reduced to less than 2 degrees for the higher flow rates. For both model 1 and model 2 under the 100% expansion inlet condition, the tool temperature does not consistently decrease with flow rate increases, which was the pattern in the results with minimal expansion. Instead, the tool temperatures actually increase as the flow rate rises from 1 to 4kg/min. The reasoning for this trend is unclear, though with the wider diameter cooling jets, a larger stagnation region under impingement would be expected and this could potentially be located over the warmest regions. This should be explored further

in any further research which considers the cooling of these expanded jets.

To further analyse the locations across the tool geometry which were seeing effective cooling by the CO_2 jet, heat fluxes were post processed from the CFD results and plotted as contours over the tool surface within the domain for all tool set ups under a flow rate of 1kg/min. The contour plots for the four CO_2 jet configurations are shown in Figure 8.11, with a fifth contour plot showing the heat fluxes over the same surface for the conventional emulsion cooling with the standard geometry, Geometry 1.

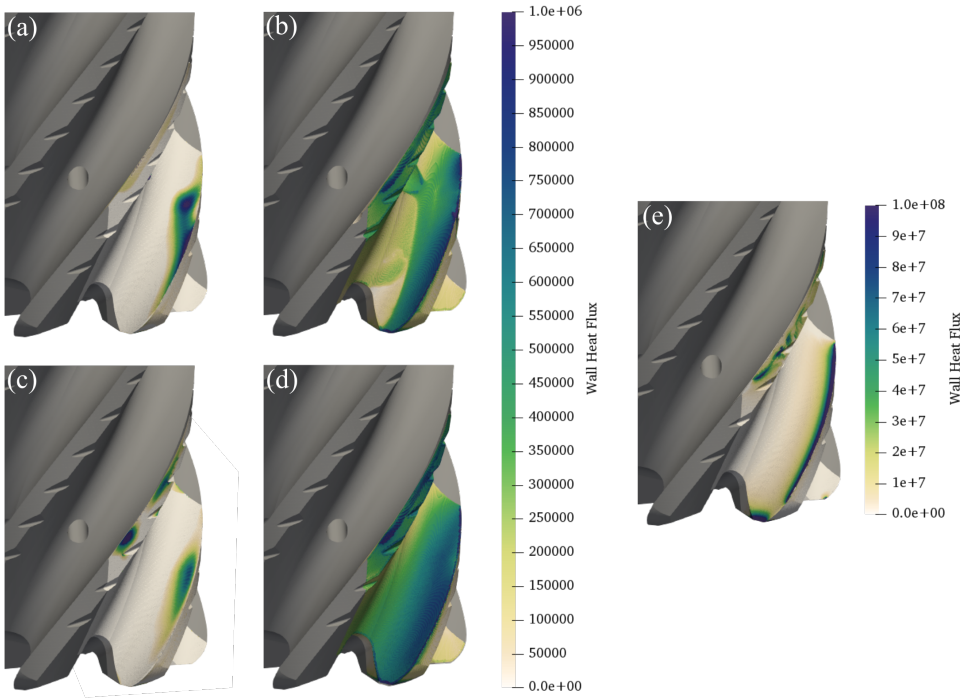

Figure 8.11: Contour plots of wall heat flux (W/m^2) on the tool for (a) Geometry 1, 0% expansion, (b) Geometry 1, 100% expansion, (c) Geometry 2, 0% expansion, (d) Geometry 2, 100% expansion, (e) Geometry 1, conventional coolant. The tool geometry is included with the contours for context.

The heat fluxes for the CO_2 results are two orders of magnitude lower than that for the conventional coolant results, which was expected due to the significantly increased cooling observed in the conventional coolant CFD results compared to the CO_2 simulations. What is of more interest in these results is the cooling regions, and how they differ across the set of results. In the un-expanded cases (a) and (c), which use Models 1 and 2 with inlet diameter, D, the cooling on the rake side of the cutting edge is highest around the middle of the region, and does not extend across the length of the cutting edge. This is different to the cooling regions observed when conventional coolant is observed in case (e) where a high level of cooling is seen across the length of the cutting edge. The specific heat capacity of water is approximately 5 times higher than that of CO_2 gas, so as the energy is transferred from the tool to the fluid, the CO_2 will heat up much quicker than the water, and be less effective in cooling the tool in

regions away from the impingement. In the expanded cases, (b) and (d) for Models 1 and 2 respectively, the cooling is spread much more evenly across the tool surface than either the un-expanded or water cases. The most even cooling over the tool surface is seen for case (d) which is the Geometry 2 expanded case, directing the coolant to the flank side with the expansion effect included.

8.5 Conclusions

In this chapter, a CFD model for CO_2 cooling jets applied to impingement surfaces was proposed, validated, and applied to a pilot machining study. The model incorporates several assumptions to simplify the approach, including the assumption of largely incompressible, single phase flow after the expansion region of the jet between the nozzle and return to atmospheric pressure. The assumptions have been detailed and justified and the CFD model has subsequently been validated against experimental data collected using the rig detailed in Chapter 7. The model predicted the cooling rate of a copper block for both high and low nozzle to plate distances, which supports its use in machining applications.

The results were found to be sensitive to inlet conditions, which are difficult to produce with great accuracy either experimentally or computationally in a machining setting. A pilot study with estimated inlet conditions was carried out for CO_2 cooling of a milling operation. Results for tool temperatures and heat fluxes across the tool rake face indicated that an expanded jet would offer significant cooling benefits over a CO_2 application without expansion. The results of this pilot study are informative for tool design processes. Any method or modification to the tools manufacture to include or enhance a convergence in the tool channel geometries at the outlet would encourage this expansion and offer this benefit.

Further work in this area could include the development of the machining models by implementing more realistic inlet conditions. This would require experimental monitoring of CO_2 conditions at the coolant channel outlets and the expanded region, or the development of a pipeline and expansion mode for the CO_2 internal supply system to the tool spindle. With the availability of more reliable input data for the tool channel outlet, the model could be applied to investigate specialised optimal tool designs for CO_2 cooling conditions. Modelling could also be extended to incorporate and assess the simplifications made in this work. The incorporation of sublimating solid particles and their impact on the heat transfer would be useful to quantify fully.

Chapter 9

Conclusions

Contents

9.1 Thesis Conclusions

In this thesis, a collection of modelling tools and methods have been developed and applied to investigate the application of coolant in milling operations. The work has presented novel modelling results of oil-water emulsion coolant applications in milling, with both coolant distribution and flow studied, as well as tool temperatures. A simplified modelling approach for new CO_2 coolant applications is also presented, with a pilot study highlighting its potential and experimental and CFD validation work presented. In this chapter a brief summary of the thesis' key results is presented. Following this, avenues for further work are discussed.

In Chapter 3, the application of conventional water-oil emulsion coolant in milling operations has been modelled. Extending on work in the literature, CFD modelling of both coolant flow and distribution as well as tool temperature has been presented for a milling tool application. These results and methodologies provide a valuable tool to aid in the improved understanding of coolant flow in milling and pave the way for increasingly informed milling tool designs with targeted coolant applications. The visualisations of coolant flow along the cutting edge show the interaction of the applied flow with the rake and flank edges of the tool, which has not been previously observed due to the highly obstructed nature and high temperatures and forces in the cutting region during the cutting process. The combination of the visualisations presented and the quantitative results extracted at the rake cutting edge confirm that this Sandvik tool model has excellent coolant coverage at the cutting edge where the lubrication is most required.

In Chapter 4, the coolant channel design space for a milling tool was explored in two studies, using the CFD model presented in Chapter 3. Quantitative results for

coolant application and tool temperatures were analysed across a range of horizontal and vertical coolant channel angles and coolant inlet velocities, which allowed the precise targeting of coolant to different positions within the cutting environment. The first study investigated a design space with two design variables, $\hat{u_i}$ and $\hat{\theta_h}$ and it was found that the coolant inlet velocity, $\hat{u_i}$, had a significant impact on the tool temperatures and vertical coolant velocity along the cutting edge, with higher inlet speeds resulting in lower tool temperatures and higher magnitude downwards coolant flow. The inlet velocity had significantly reduced impact on the wetting of the tool, which was instead heavily dependent on the horizontal coolant channel angle, $\hat{\theta_h}$, with the highest levels of wetting achieved for small values of $\hat{\theta_h}$, which directs the coolant as far as possible towards the cutting edge. When both the horizontal and vertical coolant channel angles were considered together in the second study of the design space, results showed dependence on both design variables for all the response surfaces analysed, coolant coverage, vertical coolant velocity and tool temperature. The highest levels of wetting were found for small values of $\hat{\theta_h}$ and $\hat{\theta_v}$ when the coolant is directed at the cutting edge, however for large values of $\hat{\theta_h}$ the variation with $\hat{\theta_v}$ was significantly reduced compared to the steeper decrease in wetting as $\hat{\theta_v}$ increases at very low $\hat{\theta_h}$. Tool temperatures were found to generally decrease as $\hat{\theta_h}$ decreases, and the coolant is directed further towards the cutting edge, with the highest levels of wetting. One of the key findings of this work, however, was in the identification of a change of behaviour in the coolant wetting and tool temperature response as the coolant flow was directed very close to the cutting edge. As the coolant was directed straight towards the cutting edge, with a minimum horizontal angle on the coolant channel angle in the tool design, the coolant flow followed the line of the cutting edge with high quantities applied to this edge and significantly reduced spread over the remainder of the tool surface, compared to other tool designs. This concentrated coolant distribution at the cutting edge coincided with higher tool temperature in the simulation results, showing that a good coolant coverage over a larger heat transfer area on the tool has provided better cooling here than a concentrated application to the cutting edge alone, using these modelling assumptions.

The application of full slot milling was modelled using the multiphase fluid model in Chapter 5, with more detailed analysis of the impingement location of the coolant jet and resultant coolant flow direction along the cutting edge presented and discussed. The standard tool geometry was found to direct most of its coolant downwards to the cutting edge below the impingement point, driven by the high vertical angle of the coolant channel. Detailed results of the vertical coolant velocity component along both the rake and flank edges were extracted for a full slot milling case which highlighted a dramatic change in coolant velocity direction across the impingement point. The novel work investigating coolant flow in full slot milling included the modelling of a new tool design concept with an additional axial coolant channel along-

side radial coolant channels. The new tool design concept was developed and tested with both internal and external coolant modelling and showed promising results, with a significantly reduced downwards coolant velocity near to the tool tip. For one of the designs tested, with a reduced radial coolant channel exit height of 5mm, the height of the impingement point was also lower than the standard model, resulting in an improvement for upwards coolant flow along the majority of the tool cutting edge and an attractive candidate tool for further analysis and development.

Further to contributions in the modelling of conventional coolants for milling tool operations, early technology readiness work on the coolant behaviours of CO_2 coolant have been explored, with experimental results presented in Chapter 7 following the development of a purpose built rig, and a validated CO_2 conjugate heat transfer model presented in Chapter 8. Experimental results in Chapter 7 include observations of the CO_2 jet shape, temperature, and composition, all of which contribute to better understanding of CO_2 jet releases onto impingement surfaces. Observations of the experimental features of the CO_2 releases was also crucial to inform the development of a simplified CO_2 CFD model. Alongside characterisation experiments, analysis of the heat transfer in the experimental rig under varying conditions including the nozzle diameter, D, and distance between CO_2 jet release point and heated impingement surface, H, was presented. A significant dependence on CO_2 flow rate was observed in the heat transfer results during the experiments, with higher flow rates of CO_2 enabling the greatest rates of cooling. Improved cooling with the CO_2 jets was also shown for reduced nozzle to impingement surface distances, which can be applied to tool design processes.

The CFD modelling of CO_2 application for heat transfer in Chapter 8 provides a simplified model of the complex processes which comprise cooling with CO_2 from high pressure releases. Assumptions of incompressible, single phase flow from the point of expansion have allowed the development of a model which could now be used in tool design applications in industry. The simplifications make the simulation more robust and computationally cheaper than more physically realistic models of the expansion region and phase changes which are detailed in the literature. This is especially valuable in this industrial application since the model will be used with intricate meshes which are needed to capture the tool geometries accurately. The validation of this model in a heat transfer application using the results of the experiments collected in Chapter 7 showed excellent agreement and has provided confidence that this modelling approach captures the fundamental cooling behaviours of the CO_2 coolant. An initial pilot study utilising the CO_2 model in a milling application presented a technique for incorporating the CO_2 jet expansion by increasing the coolant channel inlet size to create a representation of the expanded jet. The results of this study highlighted that the cooling with CO_2 jets in milling is significantly enhanced if some expansion of the

coolant around the cutting edge can be achieved. This corresponds to similar findings in Chapter 4 which highlighted that an improved coolant coverage area across the tool surfaces was very important for heat transfer. Maintaining the high-pressure feed of CO_2 to the coolant channel outlet by means of a restriction in the channel diameter near to this point would be a good candidate for a tool design since it would enhance the expansion, which has been shown to be beneficial here, while maintaining a similar CO_2 consumption.

9.2 Further work

Through this work, the modelling of milling processes has investigated a fully engaged milling tool in a static configuration with a workpiece. A short study on the impact of rotational engagement position in section 3.2.2 highlighted the intermittent coverage of coolant as the tool moved through a rotation. In future work, the behaviour of coolant coverage through a full tool rotation and the variation of tool temperatures through multiple cycles would be of significant interest. Rotation could be incorporated into the modelling and would provide an understanding of the cyclic temperatures in the tool edges which can cause thermal shock and increased tool wear in intermittent milling operations.

Further developments of the modelling for targeted chip evacuation research could be supported by the extension of this work to include a mechanism for predicting the transportation of generated chips near or away from the cutting edge where they are formed, adding a solid fluid interaction element to the modelling and tracking the evacuation trajectories of various chip sizes and shapes. There is also scope to improve the realistic fixing of thermal boundary conditions along the cutting edge in the conjugate heat transfer modelling presented in this work. The amount of friction and heat generated at the cutting edge is known to depend on a variety of machining parameters, as was discussed in Chapter 2, but there is also expected to be a significant benefit taken from successful lubrication of the full cutting edge by the applied coolant. In the work presented in this thesis, the tool temperature boundary is fixed independently of coolant application in the vicinity. Experimental studies of machining operations, or a deeper assessment of the tribological effects of the coolant on the high temperatures generated, could be incorporated into new boundary condition which would calculate the fixed temperature condition based on a correlation with the successful wetting with coolant in that local region.

The optimisation of tool coolant channels could be extended with the introduction of more sample points to calculate the response surface in the regions of high variation and to explore areas with high potential for improved tool design in more

detail. This work could resolve the response surface more accurately and tailor the investigation to a specific tool and machining process with individual design requirements to accompany the broader design space exploration presented in this work. Since the requirements when using coolants differ depending on tool-workpiece pairings, material properties and cutting parameters such as cutting speed and feed, sweeping conclusions are more difficult to draw from this overview. For a selection of isolated machining cases, the methods presented could be tailored to the specific configuration and any improvements validated with tool prototypes to provide further proof of concept for the machining industry.

A continuation of this work to extend the CO_2 CFD model presented to a more detailed machining case would require experimental observations of the CO_2 jet flow from internal tool coolant channels under a range of flow settings and conditions, or the accompaniment of a validated model of the decompression stage, aligning with the advanced CO_2 modelling presented for simpler geometries discussed in the literature. Work to create a thorough understanding of the quality and physical properties of the CO_2 which is delivered to the cutting region would be essential to the wide application of the CFD model successfully tested here, since it has been shown to be sensitive to inlet conditions. An adaptation of the experimental rig developed in this work to supply the CO_2 into the environment using through-tool coolant channels or a collection of observations gathered in industrial CO_2 machining settings with thermocouples and flow visualisations would be beneficial. A review and tailored study of CO_2 flow in the supply lines in the industrial setting would also be valuable since it is difficult to replicate in experimental rigs accurately and could be having a significant impact on CO_2 physical properties at the point of delivery to the cutting edge.

The CO_2 CFD model could also be developed to incorporate more complexity, for example the presence of sublimating solid phase particles could be included. The omission of the solid phase and lack of a sublimation model may limit the accuracy of the model in cases where extensive sublimation is occurring near to the hot cutting edge. An advanced equation of state such as the GERG 2008 (Kunz & Wagner, 2012) equation could be tabulated and incorporated into a compressible model to capture the expansion region of the CO_2 jet.

Bibliography

Abele E., Fröhlich B., 2008, *"High speed milling of titanium alloys"*, Advances in Production Engineering

Abukhshim N. A., Mativenga P. T., Sheikh M. A., 2006, *"Heat generation and temperature prediction in metal cutting: A review and implications for high speed machining"*, International Journal of Machine Tools and Manufacture, 46, 782

Adesta E., Hamidon R., Riza M., F A Alrashidi R. F., F S Alazemi A. F., 2018, *"Investigation of tool engagement and cutting performance in machining a pocket"*, iopscience.iop.org

Agapiou J. S., Stephenson D. A., 1994, *"Analytical and experimental studies of drill temperatures"*, Journal of Engineering for Industry, 116, 54

Aggarwal A., Singh H., Kumar P., Singh M., 2008, *"Optimization of multiple quality characteristics for CNC turning under cryogenic cutting environment using desirability function"*, Journal of Materials Processing Technology, 205, 42

Ahmad M., Osch M. B.-v., Buit L., Florisson O., Hulsbosch-Dam C. E. C., Spruijt M., Davolio F., 2013, *"Study of the thermohydraulics of CO2 discharge from a high pressure reservoir"*, International Journal of Greenhouse Gas Control, 19, 63

Akhtar W., Sun J., Sun P., Chen W., Saleem Z., 2014, *"Tool wear mechanisms in the machining of Nickel based super-alloys: A review"*, Frontiers of Mechanical Engineering 2014 9:2, 9, 106

An Q. L., Fu Y. C., Xu J. H., 2006, *"The Application of Cryogenic Pneumatic Mist Jet Impinging in High-Speed Milling of Ti-6Al-4V"*, Key Engineering Materials, 315-316, 244

Astakhov V., 2006, *"Tribology of metal cutting"*. https://books.google.com/books?hl=en&lr=&id=GZk6tuMKhU8C&oi=fnd&pg=PR4&ots=4AtX-ygMzT&sig=sJ_BwPlYUTO623cOtmvihEQFAww

Attalla M., Salem M., 2014, *"Heat transfer from a flat surface to an inclined impinging jet"*, Heat and Mass Transfer/Waerme- und Stoffuebertragung, 50, 915

Attia M. H., Cameron A., Kops L., 2002, *"Distortion in thermal field around inserted thermocouples in experimental interfacial studies, Part 4: End effect"*, Journal of Manufacturing Science and Engineering, Transactions of the ASME, 124, 135

Augspurger T., Koch M., Klocke F., Döbbeler B., 2019, in Procedia CIRP. Elsevier B.V., pp 33–38, doi:10.1016/j.procir.2019.02.007

Baradie M., 1996, *"Cutting fluids: Part I. characterisation"*, Journal of materials processing technology

Bardina J. E., Huang P. G., Coakley T. J., 1997, *"Turbulence modeling validation"*, 28th Fluid Dynamics Conference

Baughn J. W., Shimizu S., 1989, *"Heat Transfer Measurements From a Surface With Uniform Heat Flux and an Impinging Jet"*, Journal of Heat Transfer, 111

Benintendi R., 2014, *"Non-equilibrium phenomena in carbon dioxide expansion"*, Process Safety and Environmental Protection, 92, 47

Bermingham M. J., Palanisamy S., Morr D., Andrews R., Dargusch M. S., 2014, *"Advantages of milling and drilling Ti-6Al-4V components with high-pressure coolant"*, Int J Adv Manuf Techno

Biermann D., Abrahams H., Metzger M., 2015, *"Experimental investigation of tool wear and chip formation in cryogenic machining of titanium alloys"*, Advances in Manufacturing, 3

Bird R. B., 2002, *"Transport phenomena"*, Applied Mechanics Reviews, 55, R1

Boussinesq J., 1877, *"Essai sur la théorie des eaux courantes"*. https://books.google.com/books?hl=en&lr=&id=QAuWqaSZqvEC&oi=fnd&pg=PA1&dq=Essai+sur+la+th%C2%B4eorie+des+eaux+courantes&ots=QyINcOTi88&sig=hdYOTUpSgL5L4CF6x-idfMPyGA4

Brackbill J. U., Kothe D. B., Zemach C., 1992, *"A continuum method for modeling surface tension"*, Journal of Computational Physics, 100, 335

Brown S., Martynov S., Mahgerefteh H., Proust C., 2013, *"A homogeneous relaxation flow model for the full bore rupture of dense phase CO2 pipelines S."*, International Journal of Greenhouse Gas Control, 17, 349

Brown S., Martynov S., Mahgerefteh H., Chen S., Zhang Y., 2014, *"Modelling the non-equilibrium two-phase flow during depressurisation of CO 2 pipelines"*, International Journal of Greenhouse Gas Control, 30, 9

Byrne G., Scholta E., 1993, *"Environmentally Clean Machining Processes — A Strategic Approach"*, CIRP Annals, 42, 471

Cai C., Liang X., An Q., Tao Z., Ming W., Chen M., 2020, *"Cooling/Lubrication Performance of Dry and Supercritical CO2-Based Minimum Quantity Lubrication in Peripheral Milling Ti-6Al-4V"*, International Journal of Precision Engineering and Manufacturing - Green Technology, pp 1–17

Catherine L., Abdul Hamid D. B., Ibrahim M., Zakaria A., 2018, *"Computational Fluid Dynamic Analysis of Coolant Flow in Milling of Titanium grade-2 under Multiple Nozzle"*, IOP Conference Series: Materials Science and Engineering, 429, 012069

Cavazzuti M., 2013, *"Optimization methods: From theory to design scientific and technological aspects in mechanics"*, Optimization Methods: From Theory to Design Scientific and Technological Aspects in Mechanics, pp 1–262

Chen K., Xu R.-N., Jiang P.-X., 2021, *"Experimental study of jet impingement boiling cooling with CO2 at subcritical pressures and comparisons with at supercritical pressures"*, International Journal of Heat and Mass Transfer, 165, 120605

Chowdhury S., Islam M., Boswell B., 2014, in Proceedings of the World Congress on Engineering.

Cordes S., Hübner F., Schaarschmidt T., 2014, *"Next Generation High Performance Cutting by Use of Carbon Dioxide as Cryogenics"*, Procedia CIRP, 14, 401

Cosham A., Jones D. G., Armstrong K., Allason D., Barnett J., 2012, in Volume 3: Materials and Joining. ASME, p. 447, doi:10.1115/IPC2012-90461, http://proceedings.asmedigitalcollection.asme.org/proceeding.aspx?doi=10.1115/IPC2012-90461

Cui X., Jiao F., Zhao B., Guo J., 2017, *"A review of high-speed intermittent cutting of hardened steel"*, International Journal of Advanced Manufacturing Technology, 93, 3837

Da Silva R., Vieira J., Cardoso R., Carvalho H., Costa E., Machado A., De Ávila R., 2011, *"Tool wear analysis in milling of medium carbon steel with coated cemented carbide inserts using different machining lubrication/cooling systems"*, Wear, 271, 2459

Daymi A., Boujelbene M., Ben Salem S., Hadj Sassi B., Torbaty S., 2009, *"Effect of the cutting speed on the chip morphology and the cutting forces"*, researchgate.net, 1, 77

De Lacalle L. N., Lamikiz A., Sanchez J. A., Cabanes I., 2001, *"Cutting conditions and tool optimization in the high-speed milling of aluminium alloys"*, Proceedings of the Institution of Mechanical Engineers, Part B: Journal of Engineering Manufacture, 215, 1257

Deshpande S. S., 2014, *"A Computational Study of Multiphase Flows"*, PhD thesis

Deshpande S. S., Anumolu L., Trujillo M. F., 2012, *"Evaluating the performance of the two-phase flow solver interFoam"*, Computational Science and Discovery, 5, 014016

Donachie M. J., Donachie S. J., 2002, *"Superalloys: a technical guide"*. ASM international

Dou R., Wen Z., Zhou G., Liu X., Feng X., 2014, *"Experimental study on heat-transfer characteristics of circular water jet impinging on high-temperature stainless steel plate"*, Applied Thermal Engineering, 62, 738

Evdokimov D. V., Skuratov D. L., Fedorov D. G., 2015, *"Thermal fields in the end milling of VT6 titanium alloy with cooling"*, Russian Engineering Research, 35, 773

Ezugwu E., Bonney J., Yamane Y., 2003, *"An overview of the machinability of aeroengine alloys"*, Journal of Materials Processing Technology, 134, 233

Fabritius B., Tabor G., 2016, *"Improving the quality of finite volume meshes through genetic optimisation"*, Engineering with Computers, 32, 425

Fallenstein F., Aurich J. C., 2014, *"CFD based investigation on internal cooling of twist drills"*, Procedia CIRP, 14, 293

Fan W., Ji W., Wang L., Zheng L., Wang Y., 2020, *"A review on cutting tool technology in machining of Ni-based superalloys"*, The International Journal of Advanced Manufacturing Technology, 110, 2863

Fernández D., Sandá A., Bengoetxea I., 2019, *"Cryogenic milling: Study of the effect of CO 2 cooling on tool wear when machining Inconel 718, grade EA1N steel and Gamma TiAl"*, Lubricants, 7

Forrester A. I. J., Sóbester A., Keane A. J., 2008, *"Engineering design via surrogate modelling : a practical guide"*

Gant S. E., Narasimhamurthy V. D., Skjold T., Jamois D., Proust C., 2014, *"Evaluation of multi-phase atmospheric dispersion models for application to Carbon Capture and Storage"*, Journal of Loss Prevention in the Process Industries, 32, 286

Grguraš D., Sterle L., Krajnik P., Pušavec F., 2019, *"A novel cryogenic machining concept based on a lubricated liquid carbon dioxide"*, International Journal of Machine Tools and Manufacture, 145

Gross D., Appis M., Hanenkamp N., 2019, *"Investigation on the productivity of milling ti6al4v with cryogenic minimum quantity lubrication"*, MM Science Journal, 2019, 3393

Grzesik W., 2008a, *"Advanced machining processes of metallic materials: theory, modelling and applications"*. Grzesik2008, https://books.google.com/books?hl=en&lr=&id=j-_QA3u1D5EC&oi=fnd&pg=PP1&ots=iugqwceaRP&sig=hJLa3i53X6tJEtllGlQZF8ADOxQ

Grzesik W., 2008b, *"Metal Cutting Operations and Terminology"*, Advanced Machining Processes of Metallic Materials, pp 5–15

Gu J., Tung S., Barber G., 1998, in , Wear Processes in Manufacturing. ASTM International, 100 Barr Harbor Drive, PO Box C700, West Conshohocken, PA 19428-2959, pp 31–31, doi:10.1520/STP15737S, http://www.astm.org/doiLink.cgi?STP15737S

Halim N. H., Haron C. H., Ghani J. A., Azhar M. F., 2019, *"Tool wear and chip morphology in high-speed milling of hardened Inconel 718 under dry and cryogenic CO 2 conditions"*, Wear, 426-427, 1683

Hill T. A., Fackrell J. E., Dubal M. R., Stiff S. M., 2011, *"Understanding the consequences of CO2 leakage downstream of the capture plant"*, Energy Procedia, 4, 2230

Hirt C. W., Nichols B. D., 1981, Technical report, *"Volume of Fluid (VOF) Method for the Dynamics of Free Boundaries*"*

Hong S., 2006, *"Lubrication mechanisms of LN2 in ecological cryogenic machining"*, Machining Science and Technology, 10, 133

Hong S., Ding Y., 2001, *"Cooling approaches and cutting temperatures in cryogenic machining of Ti-6Al-4V"*, International Journal of Machine Tools

Hong S. Y., Zhao Z., Hong S. Y., Zhao Z., 1999, Technical report, *"Thermal aspects, material considerations and cooling strategies in cryogenic machining"*

Huang K., Yang W., 2016, *"Analytical model of temperature field in workpiece machined surface layer in orthogonal cutting"*, Journal of Materials Processing Technology, 229, 375

Iqbal A., Suhaimi H., Zhao W., Jamil M., Nauman M. M., He N., Zaini J., 2020, *"Sustainable Milling of Ti-6Al-4V: Investigating the Effects of Milling Orientation, Cutter's Helix Angle, and Type of Cryogenic Coolant"*, Metals, 10, 258

Iqbal A., Zhao G., Suhaimi H., Nauman M. M., He N., Zaini J., Zhao W., 2021, *"On Coolant Flow Rate-Cutting Speed Trade-Off for Sustainability in Cryogenic Milling of Ti–6Al–4V"*, Materials 2021, Vol. 14, Page 3429, 14, 3429

Islam A. K., Mia M., Dhar N. R., 2017, *"Effects of internal cooling by cryogenic on the machinability of hardened steel"*, The International Journal of Advanced Manufacturing Technology, 90, 11

Jamil M., et al., 2021, *"Sustainable milling of Ti–6Al–4V: A trade-off between energy efficiency, carbon emissions and machining characteristics under MQL and cryogenic environment"*, Journal of Cleaner Production, 281, 125374

Jasak H., 2009, *"OpenFOAM: Open source CFD in research and industry"*, International Journal of Naval Architecture and Ocean Engineering, 1, 89

Jawahir I. S., et al., 2016, *"Cryogenic manufacturing processes"*, CIRP Annals - Manufacturing Technology, 65, 713

Jebaraj M., Pradeep Kumar M., 2019, *"Effect of cryogenic CO ¡sub¿2¡/sub¿ and LN ¡sub¿2¡/sub¿ coolants in milling of aluminum alloy"*, Materials and Manufacturing Processes, 34, 511

Jebaraj M., Pradeep Kumar M., Yuvaraj N., Anburaj R., 2019, *"Investigation of surface integrity in end milling of 55NiCrMoV7 die steel under the cryogenic environments"*, Machining Science and Technology

Jebaraj M., Pradeep Kumar M., Anburaj R., 2020, *"Effect of LN2 and CO2 coolants in milling of 55NiCrMoV7 steel"*, Journal of Manufacturing Processes, 53, 318

Jebaraj M., Pradeep Kumar M., Anburaj R., 2021, *"Investigations on milling SKT4 steel by using cryogenic carbon-dioxide"*, https://doi.org/10.1080/10426914.2021.1914847, 36, 1414

Jerold B. D., Kumar M. P., 2012, *"Machining of AISI 316 Stainless Steel under Carbon-Di-Oxide Cooling"*, Materials and Manufacturing Processes, 27, 1059

Jerold B., Kumar M., 2013, *"The influence of cryogenic coolants in machining of Ti–6Al–4V"*, Journal of Manufacturing Science and Engineering

Johns A., Merson E., Royer R., Thompson H., Summers J., 2018, *"A Numerical Investigation of Through-Tool Coolant Wetting Behaviour in Twist-Drilling"*, Journal of Fluid Flow, Heat and Mass Transfer

Johnson M. E., Moore L. M., Ylvisaker D., 1990, *"Minimax and maximin distance designs"*, Journal of Statistical Planning and Inference, 26, 131

Kalyan Kumar K., Choudhury S., 2008, *"Investigation of tool wear and cutting force in cryogenic machining using design of experiments"*, Journal of Materials Processing Technology, 203, 95

Kao Y.-T., Takabi B., Hu M., Tai B. L., 2017, in Volume 2: Additive Manufacturing; Materials. ASME, p. V002T03A031, doi:10.1115/MSEC2017-3060, http://proceedings.asmedigitalcollection.asme.org/proceeding.aspx?doi=10.1115/MSEC2017-3060

Kato T., Fujii H., 1997, *"Temperature measurement of workpiece in surface grinding by PVD film method"*, https://manufacturingscience.asmedigitalcollection.asme.org/article.aspx?articleid=1433622

Kikuchi M., 2009, *"The use of cutting temperature to evaluate the machinability of titanium alloys"*, Acta Biomaterialia, 5, 770

Kim D., Dongsu 2017, *"Experimental Investigations for Heat Transfer Characteristics of Under-expanded Impinging Jet"*

Kim D., Lee J., 2016, *"Experimental investigation of CO2 dry-ice assisted jet impingement cooling"*, Applied Thermal Engineering, 107, 927

Kim S., Lee C., Lee D., Kim J., Jung Y., 2001, *"Evaluation of the thermal characteristics in high-speed ball-end milling"*, Journal of Materials Processing Technology, 113, 406

Klocke F., Krämer A., Sangermann H., Lung D., 2012, in Procedia CIRP. pp 295–300, doi:10.1016/j.procir.2012.04.053, www.sciencedirect.com

Komanduri R., Hou Z. B., 2001, *"Thermal modeling of the metal cutting process — Part II: temperature rise distribution due to frictional heat source at the tool–chip interface"*, International Journal of Mechanical Sciences, 43, 57

Kovacevic R., Cherukuthota C., Mazurkiewicz M., 1995, *"High pressure waterjet cooling/lubrication to improve machining efficiency in milling"*, International Journal of Machine Tools and Manufacture, 35, 1459

Ku H. H., et al., 1966, *"Notes on the use of propagation of error formulas"*, Journal of Research of the National Bureau of Standards, 70

Kui G. W. A., Islam S., Reddy M. M., Khandoker N., Chen V. L. C., 2021, *"Recent progress and evolution of coolant usages in conventional machining methods: a comprehensive review"*, The International Journal of Advanced Manufacturing Technology 2021 119:1, 119, 3

Kumar P., Pradeep M., Ramakrishna K. N., Amarnath K., Sunil Kumar M., 2015, *"Study on Tool Life and its Failure Mechanisms"*, IJIRST-International Journal for Innovative Research in Science & Technology—, 2

Kunz O., Wagner W., 2012, *"The GERG-2008 Wide-Range Equation of State for Natural Gases and Other Mixtures: An Expansion of GERG-2004"*, Journal of Chemical & Engineering Data, 57, 3032

Kwak S., Lee J., 2018, *"Eulerian multiphase analysis for heat transfer enhancement by CO2 sublimation in slot jet impingement"*, International Journal of Multiphase Flow, 107, 182

Lai W.-H., 2000, *"Modeling of Cutting Forces in End Milling Operations"*, Tamkang Journal of Science and Engineering, 3, 15

Launder B., Spalding D., 1983, in , Numerical Prediction of Flow, Heat Transfer, Turbulence and Combustion. Elsevier, pp 96–116, doi:10.1016/b978-0-08-030937-8.50016-7

Leschziner M., Launder B., 1993, *"Two-equation models for high-Reynolds-number flow"*, ui.adsabs.harvard.edu

Li K., Zhou X., Tu R., Xie Q., Jiang X., 2014, *"The flow and heat transfer characteristics of supercritical CO2 leakage from a pipeline"*, Energy, 71, 665

Liu B., 2016, *"Modelling of CO2 release from high pressure pipelines"*, PhD thesis, http://ro.uow.edu.au/theses/4950http://ro.uow.edu.au/cgi/viewcontent.cgi?article=5972&context=theses

Liu Y.-H., Calvert G., Hare C., Ghadiri M., Matsusaka S., 2012, *"Size measurement of dry ice particles produced from liquid carbon dioxide"*, Journal of Aerosol Science, 48, 1

Liu X., Godbole A., Lu C., Michal G., Venton P., 2014, *"Source strength and dispersion of CO2 releases from high-pressure pipelines: CFD model using real gas equation of state"*, Applied Energy, 126, 56

Liu Z. Y., Li C., Fang X. Y., Guo Y. B., 2018, *"Cumulative energy demand and environmental impact in sustainable machining of inconel superalloy"*, Journal of Cleaner Production, 181, 329

López de Lacalle L., Angulo C., Lamikiz A., Sánchez J., 2006, *"Experimental and numerical investigation of the effect of spray cutting fluids in high speed milling"*, Journal of Materials Processing Technology, 172, 11

Machai C., Biermann D., 2011, *"Machining of β-titanium-alloy Ti–10V–2Fe–3Al under cryogenic conditions: Cooling with carbon dioxide snow"*, Journal of Materials Processing Technology, 211, 1175

Mahgerefteh H., Oke A., Atti O., 2006, *"Modelling outflow following rupture in pipeline networks"*, Chemical Engineering Science, 61, 1811

Mahgerefteh H., Denton G., Rykov Y., 2008, *"A hybrid multiphase flow model"*, AIChE Journal, 54, 2261

Mahgerefteh H., Brown S., Martynov S., 2012, *"A study of the effects of friction, heat transfer, and stream impurities on the decompression behavior in CO2 pipelines"*, Greenhouse Gases: Science and Technology, 2, 369

Maia A. A., Kapat J. S., Tomita J. T., Silva J. F., Bringhenti C., Cavalca D. F., 2020, *"Preconditioning methods for compressible flow CFD codes: Revisited"*, International Journal of Mechanical Sciences, 186, 105898

Mansour N. N., Kim J., Moin P., 2012, *"Near-wall k-epsilon turbulence modeling"*, https://doi.org/10.2514/3.10222, 27, 1068

Martynov S., Brown S., Mahgerefteh H., 2013, *"An extended Peng-Robinson equation of state for carbon dioxide solid-vapor equilibrium"*, Greenhouse Gases: Science and Technology, 3, 136

Martynov S., Zheng W., Mahgerefteh H., Brown S., Hebrard J., Jamois D., Proust C., 2018, *"Computational and Experimental Study of Solid-Phase Formation during the Decompression of High-Pressure CO2Pipelines"*, Industrial and Engineering Chemistry Research, 57, 7054

Mazurkiewicz M., Kubala Z., Chow J., 1989, *"Metal Machining With High-Pressure Water-Jet Cooling Assistance—A New Possibility"*, Journal of Engineering for Industry, 111, 7

Mazzoldi A., 2009, *"Leakage and atmospheric dispersion of CO2 associated with carbon capture and storage projects"*

McCoy J. S., 2017, in , MetalWorking Fluids

Menter F. R., 1994, *"Two-equation eddy-viscosity turbulence models for engineering applications"*, AIAA Journal, 32, 1598

Menter F. R., 2012, *"Influence of freestream values on k-omega turbulence model predictions"*, https://doi.org/10.2514/3.11115, 30, 1657

Menter F., Esch T., 2001, in 16th Brazilian Congress of Mechanical Engineering (COBEM). p. 650

Morris M. D., Mitchell T. J., 1995, *"Exploratory designs for computational experiments"*, Journal of Statistical Planning and Inference, 43, 381

Mulyana T., Rahim E. A., Md Yahaya S. N., 2017, *"The influence of cryogenic supercritical carbon dioxide cooling on tool wear during machining high thermal conductivity steel"*, Journal of Cleaner Production, 164, 950

Najiha M. S., Rahman M. M., 2014, *"A computational fluid dynamics analysis of single and three nozzles minimum quantity lubricant flow for milling"*, International Journal of Automotive and Mechanical Engineering, 10, 1891

Najiha M., Rahman M., Kamal M., Yusoff A., Kadirgama K., 2012, *"Minimum Quantity Lubricant Flow Analysis in End Milling Processes: A Computational Fluid Dynamics Approach"*, JOURNAL OF MECHANICAL ENGINEERING AND SCIENCES, 3, 340

Nalbant M., Yildiz Y., 2011, *"Effect of cryogenic cooling in milling process of AISI 304 stainless steel"*, Transactions of Nonferrous Metals Society of China, 21, 72

Navascues G., 1979, Technical report, *"Liquid surfaces: theory of surface tension"*

Nimel Sworna Ross K., Ganesh M., 2019, *"Performance Analysis of Machining Ti–6Al–4V Under Cryogenic CO2 Using PVD-TiN Coated Tool"*, Journal of Failure Analysis and Prevention, 19, 821

Nimel Sworna Ross K., Manimaran G., 2019, *"Effect of cryogenic coolant on machinability of difficult-to-machine Ni–Cr alloy using PVD-TiAlN coated WC tool"*, Journal of the Brazilian Society of Mechanical Sciences and Engineering, 41, 44

O'Sullivan D., Cotterell M., 2001, *"Temperature measurement in single point turning"*, Journal of Materials Processing Technology, 118, 301

O'Sullivan D., Cotterell M., 2002, *"Workpiece temperature measurement in machining"*, Proceedings of the Institution of Mechanical Engineers, Part B: Journal of Engineering Manufacture, 216, 135

Oezkaya E., Beer N., Biermann D., 2016, *"Experimental studies and CFD simulation of the internal cooling conditions when drilling Inconel 718"*, International Journal of Machine Tools and Manufacture, 108, 52

Orbey H., Sandler S. I., 1998, *"Modeling vapor-liquid equilibria : cubic equations of state and their mixing rules"*. Cambridge University Press, https://books.google.co.uk/books?hl=en&lr=&id=Gl9C1trxMDYC&oi=fnd&pg=PR11&dq=Modeling+vapor-liquid+equilibria+:+cubic+equations+of+state+and+their+mixing+rules+&ots=7yL1Esxl1p&sig=KDHSn51MBBjcQxoZBaAkrD0BJeo#v=onepage&q=Modelingvapor-liquidequilibria%253

Ozcelik B., Kuram E., Simsek B. T., 2011, *"Comparison of Dry and Wet End Milling of AISI 316 Stainless Steel"*, Materials and Manufacturing Processes, 26, 1041

Özel T., Altan T., 2000, *"Process simulation using finite element method - prediction of cutting forces, tool stresses and temperatures in high-speed flat end milling"*, International Journal of Machine Tools and Manufacture, 40, 713

Pabst R., Fleischer J., Michna J., 2010, *"Modelling of the heat input for face-milling processes"*, CIRP Annals, 59, 121

Park K.-H., Yang G.-D., Lee D. Y., 2015a, *"Tool Wear Analysis on Coated and Uncoated Carbide Tools in Inconel Machining"*, INTERNATIONAL JOURNAL OF PRECISION ENGINEERING AND MANUFACTURING, 16, 1639

Park K.-H., Yang G.-D., Suhaimi M. A., Lee D. Y., Kim T.-G., Kim D.-W., Lee S.-W., 2015b, *"The effect of cryogenic cooling and minimum quantity lubrication on end milling of titanium alloy Ti-6Al-4V"*, Journal of Mechanical Science and Technology, 29, 5121

Patil P., Polishetty A., Goldberg M., Littlefair G., Nomani J., 2014, *"Slot machining of Ti6Al4V with trochoidal milling technique"*, yadda.icm.edu.pl, 14

Pereira O., Català P., Rodríguez A., Ostra T., Vivancos J., Rivero A., López-de Lacalle L., 2015, *"The Use of Hybrid CO2+MQL in Machining Operations"*, Procedia Engineering, 132, 492

Pereira O., Rodríguez A., Ayesta I., García J. B., Abia A. I. F., Lacalle L. N. L. D., 2016, *"A cryo lubri-coolant approach for finish milling of aeronautical hard-to-cut materials"*, International Journal of Mechatronics and Manufacturing Systems, 9, 370

Pereira O., Rodríguez A., Barreiro J., Fernández-Abia A. I., Norberto López De Lacalle L., 2017a, *"Nozzle Design for Combined Use of MQL and Cryogenic Gas in Machining"*, INTERNATIONAL JOURNAL OF PRECISION ENGINEERING AND MANUFACTURING-GREEN TECHNOLOGY, 4, 87

Pereira O., Urbikain G., Rodríguez A., Fernández-Valdivielso A., Calleja A., Ayesta I., de Lacalle L. L., 2017b, *"Internal cryolubrication approach for Inconel 718 milling"*, Procedia Manufacturing, 13, 89

Perri G. M., Bräunig M., Di Gironimo G., Putz M., Tarallo A., Wittstock V., 2016, *"Numerical modelling and analysis of the influence of an air cooling system on a milling machine in virtual environment"*, The International Journal of Advanced Manufacturing Technology, 86, 1853

Perrot P., 1998, *"A to Z of Thermodynamics"*. Perror1998, https://books.google.co.uk/books?hl=en&lr=&id=EBSbdNLmD-oC&oi=fnd&pg=PA1&dq=Perrot,+Pierre+(1998).+A+to+Z+of+Thermodynamics.+Oxford+University+Press&ots=kLoXJMByjh&sig=EG5mf4It76Qo5Vo73hkyEwsymIA

Pham H. H. P. L., Rusli R., 2016, *"A review of experimental and modelling methods for accidental release behaviour of high-pressurised CO2 pipelines at atmospheric environment"*, Process Safety and Environmental Protection, 104, 48

Pittalà G. M., 2018, *"A study of the effect of CO2 cryogenic coolant in end milling of Ti-6Al-4V"*, Procedia CIRP, 77, 445

Poling B. E., et al., 2001, *"THE PROPERTIES OF GASES AND LIQUIDS Fifth Edition McGRAW-HILL"*,] 10.1036/0070116822

Pursell M., 2012, *"Experimental investigation of high pressure liquid CO2 release behaviour"*, Harzards symposium series, pp 164–171

Pušavec F., Grguraš D., Koch M., Krajnik P., 2019, *"Cooling capability of liquid nitrogen and carbon dioxide in cryogenic milling"*, CIRP Annals, 68, 73

Rahman M., Senthil Kumar A., Choudhury M. R., 2000, *"Identification of effective zones for high pressure coolant in milling"*, CIRP Annals - Manufacturing Technology, 49, 47

Ravi S., Kumar M. P., 2011, *"Experimental investigations on cryogenic cooling by liquid nitrogen in the end milling of hardened steel"*, Cryogenics, 51, 509

Ravi S., Kumar M. P., 2012, *"Experimental Investigation of Cryogenic Cooling in Milling of AISI D3 Tool Steel"*, Materials and Manufacturing Processes, 27, 1017

Redlich O., Kwong J. N. S., 1949, *"On the Thermodynamics of Solutions. V. An Equation of State. Fugacities of Gaseous Solutions."*, Chemical Reviews, 44, 233

Reznikov A., Zhivoglyadov N., 1989, *"How Internal Cooling Affects the Temperature and Life of Cutting Tools"*, Stanki i Instrument

Richardson D., Keavey M., Dailami F., 2006a, *"Modelling of cutting induced workpiece temperatures for dry milling"*, International Journal of Machine Tools and Manufacture, 46, 1139

Richardson S., Saville G., Fisher S., Meredith A., Dix M., 2006b, *"Experimental Determination of Two-Phase Flow Rates of Hydrocarbons Through Restrictions"*, Process Safety and Environmental Protection, 84, 40

Roebuck J. R., Murrell T. A., Miller Vol E. E., R Roebuck B. J., Miller E. E., 1925, Technical Report 2, *"The Joule-Thomson Effect in Carbon Dioxide"*, https://pubs.acs.org/sharingguidelines. https://pubs.acs.org/sharingguidelines

Rojas-Sola J. I., García-Baena C., Jesús Hermoso-Orzáez M., Rojas-Sola J. I., García-Baena C., Hermoso-Orzáez M. J., 2016, *"A REVIEW OF THE COMPUTATIONAL FLUID DYNAMICS SIMULATION SOFTWARE: ADVANTAGES, DISADVANTAGES AND MAIN APPLICATIONS *"*, Journal of Magnetohydrodynamics, Plasma and Space Research, 23, 417

Roller D. H. D., Thilorier M., 1952, *"Thilorier and the First Solidification of a "Permanent" Gas (1835)"*, https://doi.org/10.1086/349402, 43, 109

Rusche H., 2003, *"Computational fluid dynamics of dispersed two-phase flows at high phase fractions - Google Search"*, PhD thesis, https://www.google.com/search?channel=fs&client=ubuntu&q=Computational+fluid+dynamics+of+dispersed+two-phase++flows++at++high++phase++fractions

Sadik M. I., Isakson S., Malakizadi A., Nyborg L., 2016, *"Influence of Coolant Flow Rate on Tool Life and Wear Development in Cryogenic and Wet Milling of Ti-6Al-4V"*, Procedia CIRP, 46, 91

Sagot B., Antonini G., Christgen A., Buron F., 2008, *"Jet impingement heat transfer on a flat plate at a constant wall temperature"*, International Journal of Thermal Sciences, 47, 1610

Sales W. F., Guimarães G., Machado R., Ezugwu E. O., 2002, *"Cooling ability of cutting fluids and measurement of the chip-tool interface temperatures"*, Industrial Lubrication and Tribology, 54, 57

Sankar M. R., Choudhury S. K., 2015, *"Experimental Study and Modeling of Machining with Dry Compressed Air, Flood and Minimum Quantity Cutting Fluid Cooling Techniques"*, Procedia CIRP, 31, 228

Sarikaya M., Gupta M. K., Tomaz I., Pimenov D. Y., Kuntoglu M., Khanna N., Yildirim C. V., Krolczyk G. M., 2021, *"A state-of-the-art review on tool wear and surface integrity characteristics in machining of superalloys"*, CIRP Journal of Manufacturing Science and Technology, 35, 624

Schmidt A., 1949, *"Distribution of heat generated in drilling"*, ASME

Senthil Kumar A., Rahman M., Ng S. L., 2002, *"Effect of high-pressure coolant on machining performance"*, International Journal of Advanced Manufacturing Technology, 20, 83

Shah P., Khanna N., Chetan 2020, *"Comprehensive machining analysis to establish cryogenic LN2 and LCO2 as sustainable cooling and lubrication techniques"*, Tribology International, 148

Shaw M., Cookson J., 2005, *"Metal cutting principles"*. http://www.academia.edu/download/51746613/Metal_Cutting_Principles_2nd_Edition_-_By_Milton_C._Shaw.pdf

Shokrani A., Dhokia V., Newman S. T., 2012a, in 22nd international conference on flexible automation and intelligent manufacturing.

Shokrani A., Dhokia V., Newman S. T., 2012b, *"Environmentally conscious machining of difficult-to-machine materials with regard to cutting fluids"*, International Journal of Machine Tools and Manufacture, 57, 83

Shokrani A., Dhokia V., Muñoz-Escalona P., Newman S. T., 2013, *"State-of-the-art cryogenic machining and processing"*, International Journal of Computer Integrated Manufacturing, 26, 616

Shokrani A., Dhokia V., Newman S. T., 2016, *"Comparative investigation on using cryogenic machining in CNC milling of Ti-6Al-4V titanium alloy"*, Machining Science and Technology, 20, 475

Shore H., 1924, *"Tool and chip temperatures in machine shop practice"*

Singh D., Doom J. J., 2017, in 55th AIAA Aerospace Sciences Meeting. American Institute of Aeronautics and Astronautics, Reston, Virginia, doi:10.2514/6.2017-0751, http://arc.aiaa.org/doi/10.2514/6.2017-0751

Singh A., Aravind S., Srinadhi K., Kannan B. T., 2020, *"Assessment of Turbulence Models on a Backward Facing Step Flow Using OpenFOAM®"*, IOP Conference Series: Materials Science and Engineering, 912, 042060

Sivaiah P., Chakradhar D., 2018, *"The Effectiveness of a Novel Cryogenic Cooling Approach on Turning Performance Characteristics During Machining of 17-4 PH Stainless Steel Material"*, Silicon 2018 11:1, 11, 25

Soave G., 1972, *"Equilibrium constants from a modified Redlich-Kwong equation of state"*, Chemical Engineering Science, 27, 1197

Spalart P. R., 2000, in International Journal of Heat and Fluid Flow. Elsevier Science Inc, pp 252–263, doi:10.1016/S0142-727X(00)00007-2

Span R., Wagner W., 1996, *"A New Equation of State for Carbon Dioxide Covering the Fluid Region from the Triple-Point Temperature to 1100 K at Pressures up to 800 MPa"*, Journal of Physical and Chemical Reference Data, 25, 1509

Su Y., He N., Li L., Li X., 2006, *"An experimental investigation of effects of cooling/lubrication conditions on tool wear in high-speed end milling of Ti-6Al-4V"*, Wear, 261, 760

Su Y., He N., Li L., 2011, *"Investigation Into the Effect of Cryogenic Minimum Quantity Lubrication in High-Speed Milling of Titanium Alloys"*, Advanced Science Letters, 4, 2289

Sun J., Wong Y. S., Rahman M., Wang Z. G., Neo K. S., Tan C. H., Onozuka H., 2006, *"EFFECTS OF COOLANT SUPPLY METHODS AND CUTTING CONDITIONS ON TOOL LIFE IN END MILLING TITANIUM ALLOY"*, Machining Science and Technology, 10, 355

Sun S., Brandt M., Dargusch M. S., 2009, *"Characteristics of cutting forces and chip formation in machining of titanium alloys"*, International Journal of Machine Tools and Manufacture, 49, 561

Tapoglou N., Lopez M. I. A., Cook I., Taylor C. M., 2017, *"Investigation of the Influence of CO2 Cryogenic Coolant Application on Tool Wear"*, Procedia CIRP, 63, 745

Taylor F., 1906, *"On the Art of Cutting Metals..."*

Teng L., Li Y., Zhao Q., Wang W., Hu Q., Ye X., Zhang D., 2016, *"Decompression characteristics of CO2 pipelines following rupture"*, Journal of Natural Gas Science and Engineering, 36, 213

Teng L., Li Y., Zhang D., Ye X., Gu S., Wang C., Wang J., 2018, *"Evolution and Size Distribution of Solid CO 2 Particles in Supercritical CO 2 Releases"*, Industrial & Engineering Chemistry Research, 57, 7655

Tennekes H., Wyngaard J. C., 1972, *"The intermittent small-scale structure of turbulence: Data-processing hazards"*, Journal of Fluid Mechanics, 55, 93

Thepsonthi T., Hamdi M., Mitsui K., 2009, *"Investigation into minimal-cutting-fluid application in high-speed milling of hardened steel using carbide mills"*, International Journal of Machine Tools and Manufacture, 49, 156

Toesse S., Vaagsaether K., Lundberg J., Gaathaug A. V., Bjerketvedt D., Nilsen S., Jayarathna C. K., 2013, *"Experimental study of CO 2 releases from a saturated liquid reservoir"*, Energy Procedia, 37, 4818

Tsonopoulos C., Heidman J. L., 1985, *"From Redlich-Kwong to the present"*, Fluid Phase Equilibria, 24, 1

Tyler C. T., Schmitz T. L., 2014, Technical report, *"Examining the effects of cooling/lubricating conditions on tool wear in milling Hastelloy X"*, https://coefs.uncc.edu/tschmit4/files/2011/11/CO2_NAMRC_2014_r1.pdf. https://coefs.uncc.edu/tschmit4/files/2011/11/CO2_NAMRC_2014_r1.pdf

Uhlmann E., Riemer H., Schröter D., Sammler F., Richarz S., 2017, *"Substitution of coolant by using a closed internally cooled milling tool"*, Procedia CIRP, 61, 553

Ulutan D., Lazoglu I., Dinc C., 2009, *"Three-dimensional temperature predictions in machining processes using finite difference method"*, Journal of Materials Processing Technology, 209, 1111

Versteeg H. K., et al., 2007, Technical report, *"An Introduction to Computational Fluid Dynamits Second Edition"*, https://books.google.com/books?hl=en&lr=&id=RvBZ-UMpGzIC&oi=fnd&pg=PA7&dq=verstaag+2007+reynolds+number&ots=u3wXw9zqFc&sig=2I9ffPyswMwTxgWHcT-x9qkXMbY. https://books.google.com/books?hl=en&lr=&id=RvBZ-UMpGzIC&oi=fnd&pg=PA7&dq=verstaag+2007+reynolds+number&ots=u3wXw9zqFc&sig=2I9ffPyswMwTxgWHcT-x9qkXMbY

Vieira J. M., Machado A. R., Ezugwu E. O., 2001, *"Performance of cutting fluids during face milling of steels"*, Journal of Materials Processing Technology, 116, 244

Wang X., Song Z., Pan X., Zhang L., Zhu X., Mei Y., Jiang J., 2021, *"Simulation study on near-field structure and flow characteristics of high-pressure CO2 released from the pipeline"*, Journal of Loss Prevention in the Process Industries, 71, 104481

Wareing C., Woolley R., Fairweather M., Falle S., Cleaver R. P., 2013a, *"Large-scale validation of a numerical model of accidental releases from buried CO2Pipelines"*, Computer Aided Chemical Engineering, 32, 229

Wareing C., Woolley R., Fairweather M., Falle S., 2013b, *"A composite equation of state for the modeling of sonic carbon dioxide jets in carbon capture and storage scenarios"*, AIChE Journal, 59, 3928

Wareing C. J., Fairweather M., Peakall J., Keevil G., Falle S. A. E. G., Woolley R. M., 2013c, in AIP Conference Proceedings. American Institute of Physics, pp 98–102, doi:10.1063/1.4825430, http://aip.scitation.org/doi/abs/10.1063/1.4825430

Wareing C., Fairweather M., Falle S. A., Woolley R. M., 2014, *"Modelling punctures of buried high-pressure dense phase CO 2 pipelines in CCS applications"*, International Journal of Greenhouse Gas Control, 29, 231

Wareing C., Fairweather M., Falle S. A., Woolley R. M., 2015a, *"Modelling ruptures of buried high-pressure dense-phase CO 2 pipelines in carbon capture and storage applications – Part II. A full-scale rupture"*, International Journal of Greenhouse Gas Control, 42, 712

Wareing C., Woolley R., Fairweather M., Peakall J., Falle S., 2015b, *"Numerical Modelling of Turbulent Particle-laden Sonic CO2 Jets with Experimental Validation"*, Procedia Engineering, 102, 1621

Webber D., 2011, *"Generalising two-phase homogeneous equilibrium pipeline and jet models to the case of carbon dioxide"*, Journal of Loss Prevention in the Process Industries, 24, 356

Weller H. G., Tabor G., Jasak H., Fureby C., 1998, *"A tensorial approach to computational continuum mechanics using object-oriented techniques"*, Computers in Physics, 12, 620

Wertheim R., Rotberg J., Ber A., 1992, *"Influence of High-pressure Flushing through the Rake Face of the Cutting Tool"*, CIRP Annals, 41, 101

West J. B., 2014, *"Joseph Black, carbon dioxide, latent heat, and the beginnings of the discovery of the respiratory gases"*, American Journal of Physiology-Lung Cellular and Molecular Physiology, 306, L1057

Wika K. K., Litwa P., Hitchens C., 2019, *"Impact of supercritical carbon dioxide cooling with Minimum Quantity Lubrication on tool wear and surface integrity in the milling of AISI 304L stainless steel"*, Wear, 426-427, 1691

Wilcox D. C., 1988, *"Reassessment of the scale-determining equation for advanced turbulence models"*, AIAA Journal, 26, 1299

Witkowski A., Majkut M., Rulik S., 2014, *"Analysis of pipeline transportation systems for carbon dioxide sequestration"*, Archives of Thermodynamics, 35, 117

Witlox H. W., Stene J., Harper M., Nilsen S. H., 2011, *"Modelling of discharge and atmospheric dispersion for carbon dioxide releases including sensitivity analysis for wide range of scenarios"*, Energy Procedia, 4, 2253

Witlox H. W., Harper M., Oke A., Stene J., 2014, *"Phast validation of discharge and atmospheric dispersion for pressurised carbon dioxide releases"*, Journal of Loss Prevention in the Process Industries, 30, 243

Woolley R., Fairweather M., Wareing C., Falle S., Proust C., Hebrard J., Jamois D., 2013, *"Experimental measurement and Reynolds-averaged Navier-Stokes modelling of the near-field structure of multi-phase CO 2 jet releases"*, International Journal of Greenhouse Gas Control, 18, 139

Woon K. S., Tnay G. L., Rahman M., Wan S., Yeo S. H., 2016, *"A computational fluid dynamics (CFD) model for effective coolant application in deep hole gundrilling"*, International Journal of Machine Tools and Manufacture, 113, 10

Yang Y., Zhu W., Yang Y., Zhu W., 2014, *"Study on cutting temperature during milling of titanium alloy based on FEM and experiment"*, Int J Adv Manuf Technol, 73, 1511

Yellowley I., Barrow G., 1976, *"The influence of thermal cycling on tool life in peripheral milling"*, International Journal of Machine Tool Design and Research, 16, 1

Yildiz Y., Nalbant M., 2008, *"A review of cryogenic cooling in machining processes"*, International Journal of Machine Tools and Manufacture, 48, 947

Yuan S. M., Yan L. T., Liu W. D., Liu Q., 2010, *"Effects of cooling air temperature on cryogenic machining of Ti-Al6-4V alloy"*, Journal of Materials Processing Tech., 211, 356

Yusof S. N. A., Asako Y., Sidik N. A. C., Mohamed S. B., Japar W. M. A. A., 2020, *"A Short Review on RANS Turbulence Models"*, CFD Letters, 12, 83

Zheng W., 2018, *"Numerical Modelling of the Rapid Depressurisation and Outflow of High Pressure Containments in the Framework of Carbon Capture and Sequestration"*, Doctoral thesis, UCL (University College London).

Zheng Yang K., et al., 2022, *"Application of coolants during tool-based machining – A review"*, Ain Shams Engineering Journal

Zheng W., Mahgerefteh H., Martynov S., Brown S., 2017, *"Modeling of CO ¡sub¿2¡/sub¿ Decompression across the Triple Point"*, Industrial & Engineering Chemistry Research, 56, 10491

Zhiyin Y., 2015, *"Large-eddy simulation: Past, present and the future"*, doi:10.1016/j.cja.2014.12.007

Zhu G., Yuan S., Chen B., 2018, *"Numerical and experimental optimizations of nozzle distance in minimum quantity lubrication (MQL) milling process"*, The International Journal of Advanced Manufacturing Technology

Zou L. T., Zhang S., Chen W. D., Zhao G. Q., Zhao B., 2013, *"CFD Analysis of Cryogenic Oil Mist of Milling Cutters with Different Interior Channels"*, Key Engineering Materials, 589-590, 317